Improving imaging performance in planar superlenses

Mikkel Schøler

Department of Electrical and Computer Engineering

University of Canterbury

A thesis submitted for the degree of

Doctor of Philosophy

28th of June 2011

Thesis timeline:

Project start date: 1st of February 2007.

Submission date: 28th of June 2011.

Defense date: 14th of September 2011.

Corrections performed by: 14th of November 2011.

Examination panel:

Supervisor: Professor Richard J. Blaikie, University of Canterbury, New Zealand.

Examiner: Dr. Chris Mack, University of Texas, Austin TX, USA.

Examiner: Dr. Tim Davis, CSIRO, Melbourne, Australia.

Defense coordinator: Professor Pat Bodger, University of Canterbury, New Zealand.

Abstract

The aim of this project was to improve the imaging performance of planar superlenses for evanescent near-field lithography. An experimental investigation of the performance of superlenses with reduced surface roughness was proposed. Such an investigation poses significant requirements in regards to process control in thin film deposition of silver onto dielectric substrates. Thin film deposition of silver films, onto silicon dioxide substrates, achieved films with root mean square surface roughness as low as 0.8 nm. While these experiments provided good understanding of the deposition process, significant variability of the surface roughness parameter remained an issue. The difficulty of achieving consistent control of surface roughness led to a finite element method simulation study where this parameter could be readily controlled. An improved understanding of how surface roughness affects superlens imaging performance was obtained from the results of this investigation. Furthermore, it was shown that in order to conduct an experimental investigation to verify the simulation results, it would be necessary to improve the imaging capability of super-resolution lithography protocols to achieve 3σ line edge roughness (LER) of $<$20 nm. Resist-scheme optimisation was identified as an important factor in this regard. Thus, a novel calixarene-based photoresist was formulated and characterised. The resist demonstrated superior imaging capabilities through interference lithography and evanescent near-field optical lithography, capable of resolving 250-nm period half-pitch line gratings with 3σ LER below 10 nm. The development of this novel photoresist will enable future lithographical investigations to be conducted with improved resolution and imaging fidelity.

Preface

This project was performed at the Department of Electrical and Computer Engineering, at the University of Canterbury, under the supervision of Professor Richard J. Blaikie and the co-supervision of Assoc. Prof. Maan Alkaisi. It builds upon results achieved by past PhD-students at this department, most notably Dr. D.O.S. Melville and Dr. S.J. McNab. Almost all experimental work described herein was conducted at the nano-fabrication laboratory at the Department of Electrical and Computer Engineering. The one exception is the calixarene-synthesis, which was done at the Department of Chemistry, also at the University of Canterbury. Financial support for the project and related activities was provided by the MacDiarmid Institute. I must express my gratitude these people and institutions since they form the stable fundament upon which this particular house of cards have been constructed.

I was fortunate to make the acquaintance of Richard through an introduction from a friend. Richard's ability to remain focused on the positive has been nothing short of inspirational. I freely admit that after having spent the better (or worse) part of a year in the lab, mainly glued to the atomic force microscope, analysing silver surfaces as bereft of features as possible–without much progress and even less consistency–my motivation was ever so slightly depleted. Somehow I managed not to throw in the towel and Richard deserves a significant share of the credits in this regard.

I began working on the project described within these pages on February 1st 2007. Experimental work was brought to an abrupt stop when Christchurch was struck by a magnitude 7.1 earthquake in the early hours of September 4, 2010. The quake closed the University of Canterbury for three weeks and caused continuing disruption of laboratory operations. At that point I decided to focus solely on the writing of this thesis. Since the initial seismic event the city has been pummelled by aftershocks–notably the fatal 6.3 aftershock of February 22, 2011 which caused the death of 182 people and shut

down the campus for another six weeks. More recently the 6.3 aftershock of June 13, 2011 caused the university to shut down for another week. At times it has felt as if the very fabric of reality was opposed to the completion of this thesis.

Parts of the work described within this thesis has been published and presented at international conferences. National and intra-departmental presentations have been a regular and educational part of doing a PhD within the MacDiarmid Institute. These contributions are outlined below. Furthermore, I propose that this project may also be considered anecdotal evidence in support of Hofstadter's law.

Mikkel Schøler, 28th of June, 2011.

Journal publication

- M. Schøler and R. J. Blaikie. "Resonant surface roughness interactions in planar superlenses". *Microelectronics Engineering* **87**(5–8): 887-889, 2010.

- M. Schøler and R. J. Blaikie. "Simulations of surface roughness effects in planar superlenses". *Journal of Optics A: Pure and Applied Optics* **11**(10): 105503, 2009.

International Conference Presentations – Orals

- **M. Schøler**, D. J. Garrett and R. J. Blaikie. "Novel Calixarene-Based UV-Sensitive Photoresist for Evanescent Near-Field Optical Lithography". Fifth International Conference on Advanced Materials and Nanotechnology (AMN-5); Wellington, New Zealand; February 11, 2011.

- **M. Schøler** and R. J. Blaikie. "Simulations of surface roughness effects in planar super-lenses". NANOMETA-2009; Seefeld, Austria; January 8, 2009.

International Conference Presentations – Posters

- **M. Schøler**, D. J. Garrett and R. J. Blaikie. "Super-resolution lithography using a novel calixarene-based photoresist". 37th International Conference on Micro & Nano Engineering (MNE); Berlin, Germany; September 19, 2011.

- **M. Schøler** and R. J. Blaikie. "Resonant Surface Roughness Interactions in Planar Superlens Imaging". 35th International Conference on Micro & Nano Engineering (MNE); Ghent, Belgium; September 30, 2009.

- **M. Schøler** and R. J. Blaikie. "Simulations of surface roughness effects in planar super-lenses". Fourth International Conference on Advanced Materials and Nanotechnology (AMN-4); Dunedin, New Zealand; February 11, 2009.

Local Presentations

- **M. Schøler**, D. J. Garrett and R. J. Blaikie. "Novel calixarene-based UV-Sensitive photoresist for evanescent near-field optical lithography". *Poster.* Annual MacDiarmid Institute Student and Postdoc Symposium; Wellington, New Zealand; November 19, 2010.

- **M. Schøler**. "Calixarene-based photoresist development". *Oral.* Group meeting; Christchurch, New Zealand; February 22, 2010.

- **M. Schøler**. "An Introduction to Thin Film Deposition at ELEC UC". *Oral.* Annual MacDiarmid Institute Student and Postdoc Symposium; Wellington, New Zealand; November 10, 2008.

- **M. Schøler**. "Silver thin films for planar lensing". *Oral.* Group meeting; Christchurch, New Zealand; December 10, 2007.

- **M. Schøler** and R. J. Blaikie. "Enabling Technologies for Planar Super Lenses". *Poster.* Annual MacDiarmid Institute Student and Postdoc Symposium; Palmerston North, New Zealand; November 26, 2007.

- **M. Schøler**. "Some stuff about nanolithography". *Oral.* Group meeting; Christchurch, New Zealand; February 19, 2007.

Acknowledgements

To list all the people who have, in one way or the other, helped with the creation of this thesis is impossible. Thus, I must restrict my attention here to those who have affected the process directly.

I must first express my gratitude and appreciation towards my supervisor Professor Richard Blaikie, who has been a great support throughout this project – be it providing financial support or identifying new directions. Richard has never failed to impress me with his uncanny ability to answer emails within few hours - no matter what the subject or the time of the day. His ability to remain positive and provide constructive feedback has been immeasurably helpful.

I thank Helen Devereux and Gary Turner, the nano fabrication lab could not run without them. Without Helen we'd quick be out of supplies and up to our ears in our own mess and without Gary none of the equipment would work. Thank you for doing a great job and for freely sharing your knowledge and expertise.

Pieter Kikstra deserves thanks, partly for helping me navigate the university's labyrinthian IT system and being my enabling hardware-pusher. Partly, and perhaps more importantly, for always being up for a chat - and in doing so providing open-minded and positive perspectives.

I am also grateful to David Healy for sharing his expertise in all things mechanical in both thesis-related and unrelated projects.

When I began this project Matthew Arnold was a postdoc in our group, his help in relation to the numerical simulations, undertaken as part of this project, has been very valuable. Trey Holzwarth joined our group as a postdoc and set up the laser laboratory in which the interference lithography experiments were conducted. For this I owe him thanks, but also for being a good person to bounce ideas off.

Without David Garrett the work on the calixarene resist would not have happened. The knowledge and experience in chemistry he brought to this process can not be overestimated. Working with Dave allowed me to gain a new appreciation of the mystical world of chemistry. For all of this I owe him my gratitude.

During my time working on this project I have enjoyed the fortune of having good colleagues. A big 'thank you' to my fellow PhD students Volker Nock, John Foulkes, Ciaran Moore and Prateek Mehrotra. Volker had a bit of a head start, but stayed on as a postdoc - in that capacity he has also been a great help in all things lab-related. John started his PhD shortly after me and has been my personal Matlab-helpdesk. John and Volker have also often kept me company during lunch (pizza or curry? - the most important question of the day) – engaging in stimulating and abstract discussions on topics far removed from our projects, this has been helpful insofar it assisted me in retaining my sanity. Ciaran has been very helpful in providing assistance with Matlab and COMSOL - especially his tool for extracting AFM data was of great help to my simulation work. Prateek is the newest addition to our group and shows great promise – he even likes beer now. Thank you all for the time we have shared.

Amongst my friends there are a few that deserves a special mention here. First, Julian Maclaren, a former PhD student at this department, who put me in contact with Richard in the first place. Stewart Hardie, also a former PhD-student at this department, deserves thanks for impressing upon me, on several occassions, that it was worthwhile to keep pushing on with the project. Kylie Hills deserves kudos for telling me to "HTFU and just do it!" at a time when it was needed.

Last and most importantly I must thank my lovely partner Berit for her unwavering support, on so many levels, throughout this project. It's been a long, and at times hard, road and if it hadn't been for her it would not have happened at all. Thank you for everything.

Contents

List of Figures

LIST OF FIGURES

List of Tables

1

Introduction

This chapter provides a brief summary outlining the motivation for this project and the circumstances from which it originates. The summary presented here is expanded significantly upon in Chapter 2. Then follows a statement of the project's initial aim and its evolution during the project. Finally a thesis outline presents a short description of the contents of the remaining chapters.

1.1 Motivation

Since the invention of the semiconductor transistor, huge advancements in several areas, especially information technology, have been achieved through an ongoing miniaturisation process [1]. One of the key enabling technologies for the miniaturisation process is that of photolithography, which relies on altering the chemical and/or physical properties of a resist layer through selective exposure to electromagnetic (EM) radiation [2]. The strength of this technology lies in it being a parallel definition process utilising reusable masks, which allows for high throughput fabrication at comparatively low costs. Its main weakness is that it relies on diffraction-limited optics and so the achievable resolution is proportional to the wavelength of the radiation utilised. Improvements in resolution have been facilitated mainly by using radiation with shorter wavelength, corresponding to higher photonic energy. The transition to higher photonic energies introduces additional complications pertaining to both masking and radiation sources [3, p. 30]. As a consequence improving photolithography resolution becomes more and more expensive to the point where costs become prohibitive. However, in

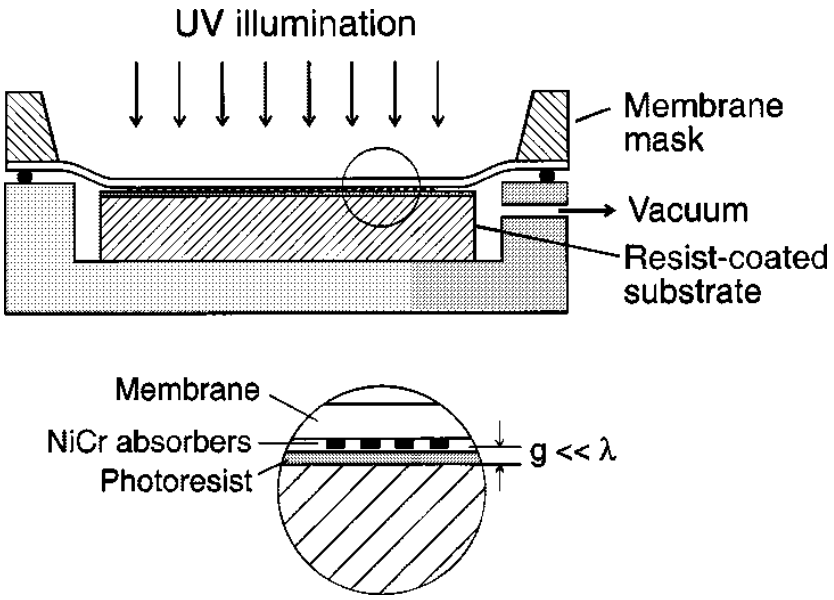

Figure 1.1: "Schematic diagram illustrating the evanescent near-field optical lithography (ENFOL) process." Reproduced from [6, FIG. 1.].

recent years developments within the fields of evanescent near-field optical lithography [4] and superlensing [5] have demonstrated promising potential.

1.1.1 Evanescent near-field optical lithography

EM radiation incident on apertures with dimensions comparable to the wavelength of the radiation undergo diffraction. As a result, the sub-wavelength information contained in a pattern of such apertures (e.g. an exposure shadow mask) does not propagate beyond the masking layer, but is contained within the evanescent near-field which decays exponentially. Provided that the mask is kept in intimate contact with the resist, sub-wavelength information may be transferred to the resist layer through this evanescent near-field [6], as shown in Fig. 1.1.

While recent achievements in evanescent near-field optical lithography (ENFOL) show great promise [4, 7–10] an important issue remains: lifetime of the exposure mask. Intimate contact between the mask and substrate will increase the risk of contamination of and damage to the masking pattern for each exposure. This becomes even more important for masks with sub-wavelength features since these are significantly more

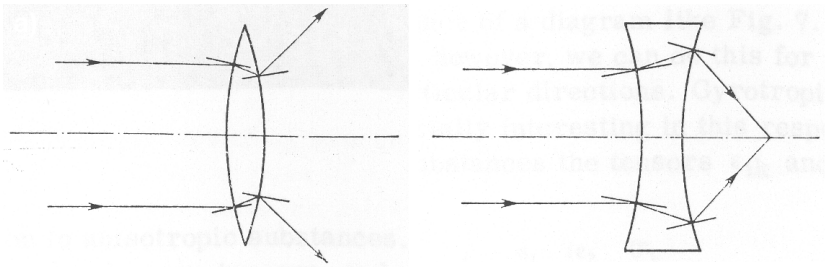

Figure 1.2: "Paths of rays through lenses made of left-handed substances, situated in vacuum." Reproduced, in modified form, from [12, FIG. 5.]

expensive to produce than regular photolithography shadowmasks. Unfortunately, due to the evanescent character of the nearfield any spacing of the mask and resist layer will cause a loss of the sub-wavelength information. A controversial solution to this problem was proposed in 2000 [11], a solution based upon an idea formulated in 1968 [12].

1.1.2 Super optics

In 1968 Victor Veselago conducted a theoretical investigation of wavepropagation in lossless materials with simultaneous negative electric permittivity (ϵ) and magnetic permeability (μ) [12]. His analysis was based upon the dispersion equation and Maxwell's equations and led to a range of interesting observations. One of these concerned the refractive properties of such a material; Veselago showed that in the case where both ϵ and μ are negative the refractive index, n, must also be negative. Veselago referred to such a material as a "Left-handed" substance since the electric field E, magnetic field H and wave-vector k form a left-handed set in such materials unlike in normal materials where they form a right-handed set. As a consequence, in left-handed materials the Poynting vector and wave-vector are anti-parallel, i.e. the direction of wave propagation is opposite to the direction of energy flow. Light propagating through an interface between two materials with differing refractive indices will experience refraction as according to Snell's law as shown in Fig. 1.2. For refraction at the interface between a right-handed and a left-handed material both the incoming and refracted ray will be the same side of the normal. As a result, a simple slab of left-handed material is capable of focusing an object point onto an image point, as illustrated by Fig. 1.3.

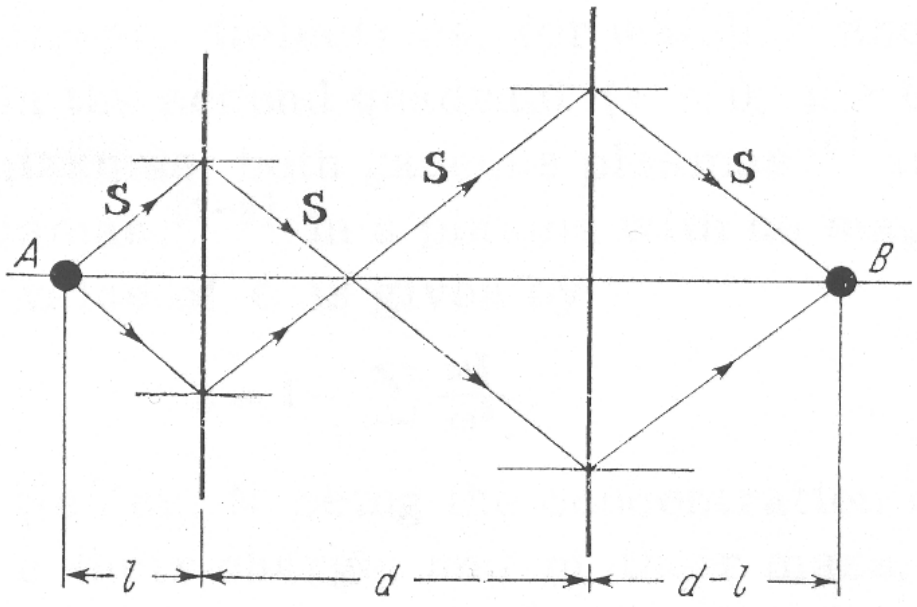

Figure 1.3: "Passage of rays of light through a plate of thickness d made of a left-handed substance. A – source of radiation; B – detector of radiation." Reproduced, in modified form, from [12, FIG. 4.]

In 2000 John Pendry published a controvesial paper entitled "Negative Refraction Makes a Perfect Lens" [11]. In this paper it was shown that a slab of left-handed material would, under the right conditions, act like a perfect lens capable of amplifying and transmitting evanescent field components of electromagnetic signals. This allows a projection of the near-field some distance away from the masking layer, effectively allowing for non-diffraction-limited optics. Such a "superlens" would enable physical separation of masking and resist layers in ENFOL without loss of high-frequency information, hereby solving the dominant problem pertaining to the technique. Furthermore, Pendry identified various metals which exhibit plasma-like behaviour for electromagnetic waves at optical frequencies and went on to calculate the contrast of a super-resolving planar silver lens.

In the time following Pendry's publication negative refraction in metamaterials was demonstrated. First for microwaves [13, 14], later for infra-red (IR) [15, 16] and ultimately near-UV radiation [17, 18]. For microwaves, it is a comparatively simple matter to fabricate a metamaterial consisting of sub-wavelength elements since such radia-

tion has wavelengths in the order of centimeters. Making a mesh of wire lattices and split-ring resonators yields a material with simultaneous negative ϵ and μ for a given range of frequencies [19]. Fabricating a superlens for optical frequencies is much more difficult owing to the shorter wavelengths involved (400-700 nm). While it is possible to achieve negative ϵ through plasmonics, no metamaterial with negative μ, for optical wavelengths, has been presented to date. However, it is still possible to realise a super-resolving planar lens provided the distance between the object and image planes are kept smaller than the wavelength. Image-transfer through such super-resolving planar lenses, fabricated by stacking silver and dielectric thin films, were presented in 2005 and demonstrated to be capable of projecting ENFOL images containing sub-wavelength information [17, 18].

1.1.3 In media res

The project described within the present thesis springs from superlensing experiments conducted by Melville, described in his 2006 PhD thesis "Planar Lensing Lithography: Enhancing the Optical Near Field" [20]. Melville developed an experimental protocol that allowed the demonstration of the proof-of-principle for superlensing at optical wavelengths. While the principle has been demonstrated there are still unanswered questions which present fundamental obstacles to furthering the field of optical superlensing.

Melville's thesis documents superlens image projection of 145-nm period grating structures. This result was achieved using planar silver lenses with interfacial roughness of $\sim$1 nm Root-Mean-Square (RMS). The performance of such planar lenses is very sensitive to surface roughness at the interface between the silver and dielectric layers. Roughness induced losses within the system occur due to the resonant nature of the plasmon-driven image transfer mechanism. Consequently it can be concluded, qualitatively, that to improve superlens imaging it is necessary to reduce interfacial surface roughness within the lens stack. However, the quantitative connection between image transfer performance and interfacial roughness in superlenses is not understood.

In order to conduct an experimental investigation of this subject two requirements must be fulfilled; first a reliable protocol for performing superlens experiments must be

available and second good control of the surface roughness parameter during superlens fabrication is required. Melville satisfied the first requirement. The second requirement becomes complicated due to the thermodynamics involved in thin film deposition of metals onto dielectric substrates. A good understanding of the mechanics behind thin film deposition and thorough optimisation of the deposition process is necessary in order to achieve consistent silver thin films with reduced surface roughnesses (i.e. <1 nm RMS).

1.2 Project aims

The initial aim of this project was:

> To conduct experimental studies to qualify and quantify the relationship between interfacial surface roughness and imaging performance in planar silver superlenses for the optical spectrum.

Following extensive investigations of the thin film deposition process, this initial aim was modified for reasons explained in Chapter 3. Subsequently a new aim was formulated:

> To investigate the relationship between interfacial surface roughness and imaging performance in planar superlenses through finite element method simulation studies.

Results obtained from these studies were published in 2009 [21, 22]. The results indicated that in order to properly evaluate the correlation between interfacial roughness and imaging fidelity in superlens experiments it would be necessary to increase the imaging performance of existing experimental near-field lithography protocols. Thus an additional aim was identified:

> To formulate and characterise a novel high-performance photoresist scheme for use in near-field lithography experiments.

1.3 Thesis outline

Work towards these aims is described herein according to the following schedule:

Chapter 1: Brief summary of motivation and origin for present thesis. Statement of project aims and thesis outline.

Chapter 2: In-depth presentation of the background of the thesis; fundamental limitation of photolithography, near-field imaging, superlensing and plasmonics.

Chapter 3: Thin film deposition; fundamental theory and experimental results. Highlights the issues of depositing smooth silver films on dielectric substrates.

Chapter 4: Motivation, methodology and results of finite element method modelling studies of surface roughness effects in superlens imaging.

Chapter 5: Expansion of work presented in Chapter 4 by spatial-frequency analysis of resonant coupling to surface roughness in superlenses.

Chapter 6: Experimental formulation and development of a novel calixarene-based photoresist for high-resolution UV photolithography experiments.

Chapter 7: Super-resolution interference and evanescent near-field lithography experiments conducted utilising the photoresist described in Chapter 6.

Chapter 8: Summary, outlook and conclusion.

2

Background

This chapter provides a background for the present project. It begins with a brief introduction to the field of lithography in relation to micro- and nanotechnology and the fundamental limitations pertaining to conventional optical lithography specifically. This is followed by an introduction to evanescent near-field optical lithography (ENFOL), its capabilities and constraints. Then follows a presentation of the topics of superlensing and its enablers; negative refraction and photon-plasmon interactions.

2.1 Optical lithography

The word *lithography*, which comes from the Greek words *lithos*, meaning 'stone', and *graphein*, meaning 'to write', originally described a specific type of printing method invented by Alois Senefelder in 1796 [23]. The word lithography has since been adopted as the accepted term describing most patterning techniques utilised in micro- and nanofabrication [24]. The most prolific type of lithography process used in this context is that of optical lithography, which has arguably been the most important technological enabler for the miniaturisation process.

While there are many other types of lithography techniques, e.g. electron-beam lithography [25], nano-imprint lithography [26], scanning probe lithography [27], etc., no other lithography techinique has been able to match optical lithography in regards to commercial viability. The subject of photolithography has been covered in several encompassing works of literature, one recent work is that of Mack from 2007 [2]. Com-

mon to all lithography techniques is the need for a recording medium and a definition mechanism capable of transferring spatial information into the medium. In the case of photolithography the recording medium is a photosensitive film, typically a polymer, which is referred to as the photoresist. Spatial information is transferred to the photoresist through selective photonic irradiation. This selective irradiation was first achieved by insertion of a patterned absorption plate, known as a shadow mask, into the path of a collimated beam of UV light. Generally there exists a distinction between two different shadow mask exposure techniques: contact and proximity exposure. As the etymology infers, in contact lithography the mask-resist separation is minimal where as for proximity exposures, a significant gap exists between mask and resist. A third exposure method, projection lithography, also exists wherein the mask pattern is projected onto the substrate through sophisticated optical systems. Projection photolithography further allows image reduction (e.g. 4-5x) thereby relaxing resolution demands on mask fabrication, and this is the method of choice for current commercial integrated-circuit lithography applications.

In all cases the resulting physical image is achieved by alteration of the chemical and/or physical characteristics of the exposed photoresist relative to unexposed regions. In a subsequent development step, one of these two regions is dissolved using a developer. When the exposed region is dissolved the process is referred to as being positive. Conversely, if the unexposed regions are dissolved the process is considered negative. This fundamental operational model is illustrated by Fig. 2.1.

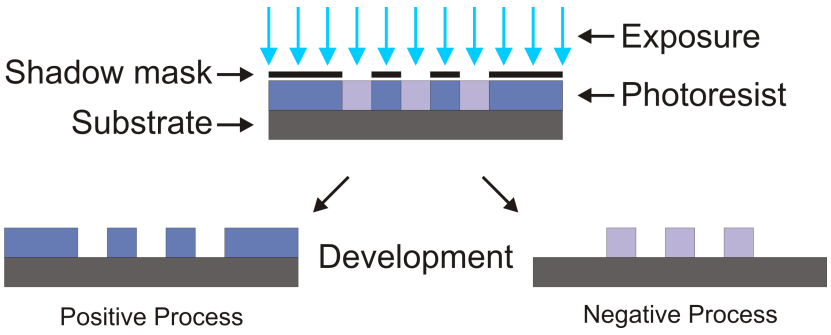

Figure 2.1: Photolithography, the basic concept.

2.1.1 Ultra-violet lithography and Moore's Law

The advances in micro-device density, and consequently lithographical performance, up until today were famously predicted by Intel co-founder Gordon E. Moore in 1965 [1]. Moore's law states that the device density of integrated circuits doubles approximately every two years as illustrated by Fig. 2.2(top). As device density scales with the square of the resolution of lithography, it follows that the resolution must double approximately every four years to fulfil Moore's Law. This rapid advance in lithographic resolution does however present cosiderable challenges in regards to technological development.

The main limitation on photolithographic resolution is that it depends upon diffraction-limited optics. Consequently the ultimate resolution achievable is directly proportional to the wavelength of the exposure source. Until recently improvements in photolithographic resolution have been achieved, in part, through a gradual transition towards exposure sources operating at shorter wavelengths. From the 1960's through to the mid-1980's mercury gas-discharge lamps were used as exposure sources, operating at the spectral G-, H- and I-lines with wavelengths of 435.8, 404.7 and 365.4 nm respectively. Development of the excimer laser in 1982 [30] enabled the transition to deep UV (DUV) wavelengths of 248 and 193 nm for krypton flouride and argon flouride lasers respectively. In recent years the drive has been towards extreme ultraviolet lithography (EUVL) operating at 13.5 nm [31]. This development in exposure wavelength is mapped together with the resolution improvements necessary to realise Moore's law in Fig. 2.2(bottom).

The transition to shorter wavelengths, and the corresponding higher photonic energies, introduces other complications. Commercial requirements for a viable lithography system demands state-of-the-art optics, high-performance photoresists, massive throughputs and bright and reliable exposure sources. EUVL has been the subject of studies since the late 1980's with increasing amounts of funding being invested to bring the technology to maturity. EUVL development has been facing considerable challenges in many crucial areas due to complications arising from the high photonic energies involved. A review of the subject of EUVL by Wu and Kumar in 2007 [31] concluded that EUVL would "'be seen in the next few years"'. However, so far there are still no

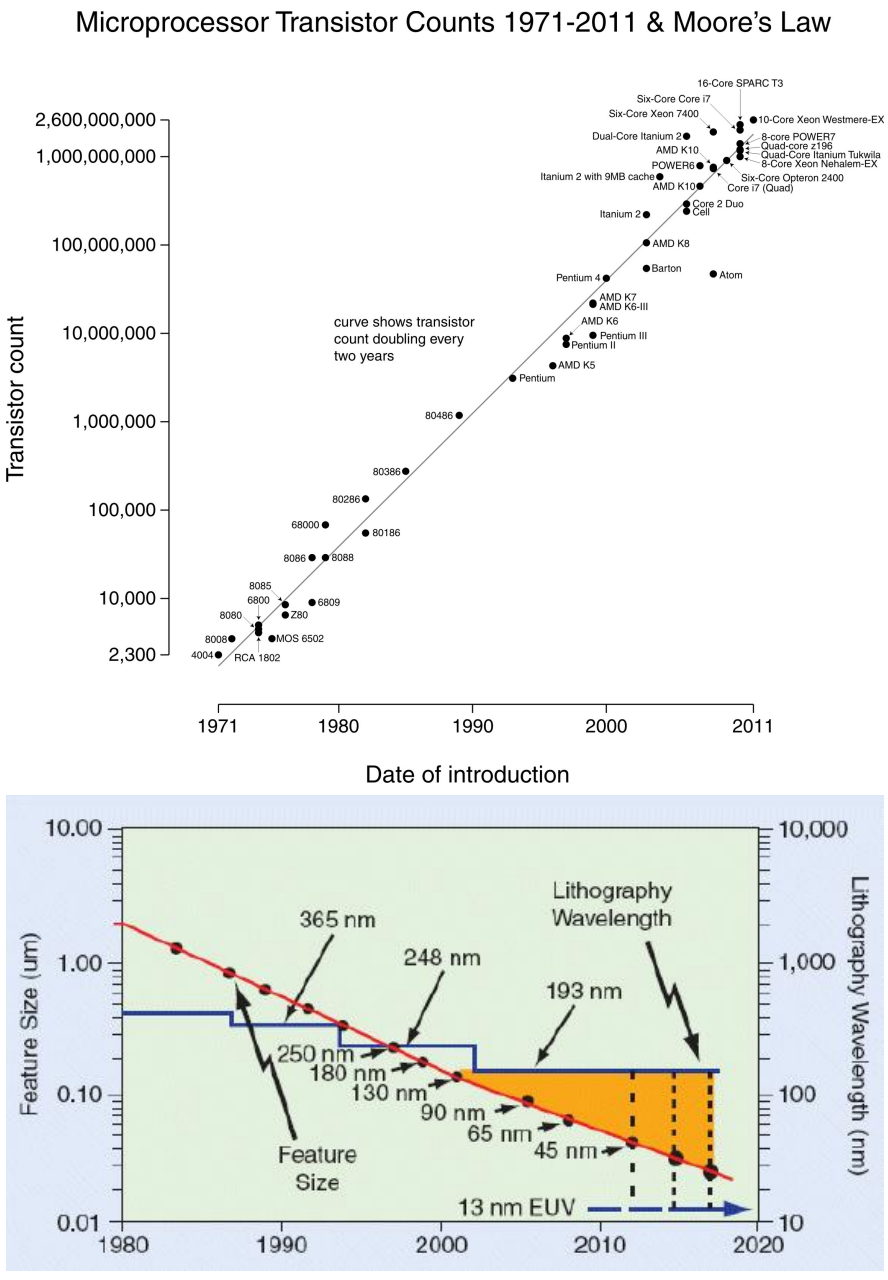

Figure 2.2: Moore's law and the lithographical challenge. Reproduced from (top) [28, Moore's law] and (bottom) [29].

viable commercial EUVL tools available despite the billions of dollars that have been invested in the technology. In the meantime DUV lithography operating at the 193 nm wavelength has managed to enable Moore's law through solutions such as immersion, double patterning and computational lithography techniques [31–34]. However, DUV lithography is now beginning to reach the point where futher refining the technology becomes difficult and expensive.

2.1.2 The diffraction limit

Diffraction occurs as a consequence of wave mechanics whenever a wave is caused to interfere either with another wave or with itself through spatial confinement. As a phenomenon it is closely related to, and arguably indistinguishable from, that of interference. In relation to this project the main issue is that it dictates the limits as to how tightly it is possible to spatially confine an electromagnetic wave signal without losing coherence due to interference effects. Fig. 2.3 illustrates the diffraction patterns that arise when a wave passes through (left) a single slit with a width comparable to the wavelength and (right) passes through a double slit with a separation comparable to the wavelength.

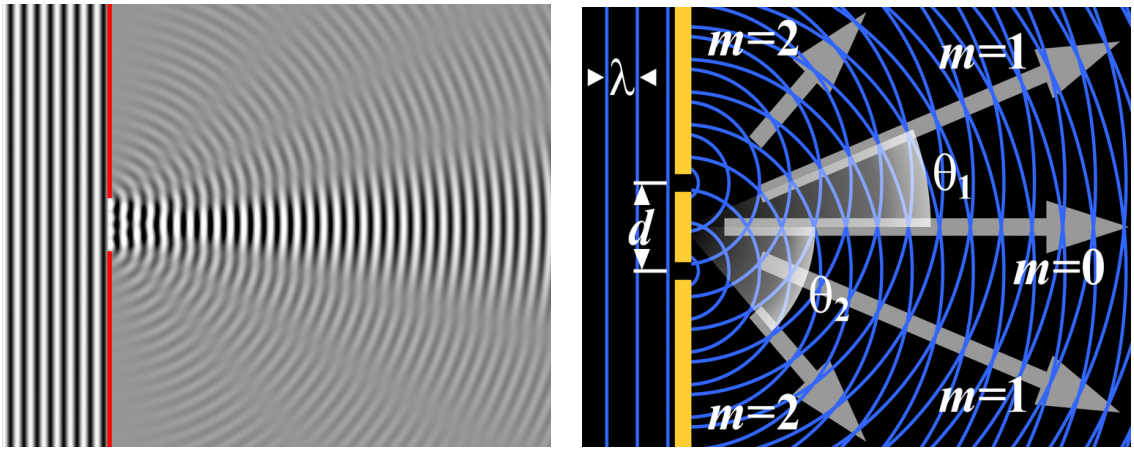

Figure 2.3: Illustrations of the diffraction patterns arising from a single slit (left) and a double slit (right). Reproduced from [28, Diffraction].

In 1883 Ernst Abbe published a paper showing that the smallest feature size, d, that could be imaged by a microscope operating at a given wavelength, λ, could be expressed by the formula presented in Eq. 2.1 [35].

$$d = \frac{\lambda}{2n\sin\phi} = \frac{\lambda}{2NA} \tag{2.1}$$

In this equation n is the refractive index and ϕ is the maximum convergence angle. The numerical aperture, $NA = n\sin\phi$, is a figure of merit which describes an imaging system's ability to project an image as illustrated by Fig. 2.4.

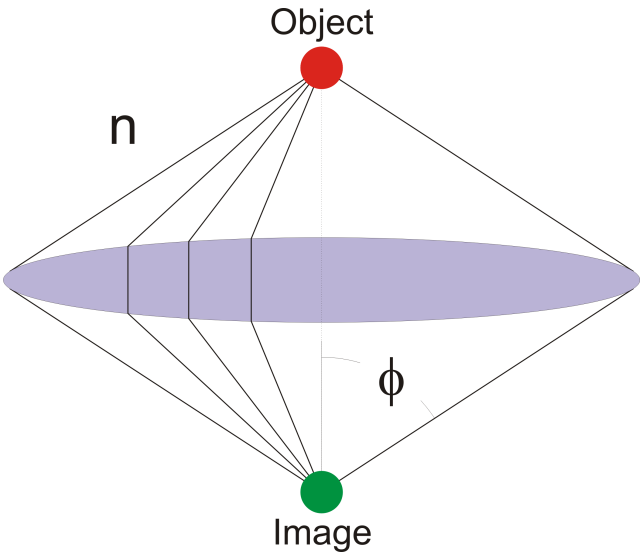

Figure 2.4: Light being captured by a lens characterised by a numerical aperture $NA = n\sin\phi$. n is the refractive index of the medium surrounding the lens and ϕ is the maximum angle of incidence from the lens for a ray propagating towards the image.

Abbe's conclusion can be expressed in more general terms, and more applicable to the subject of optical lithography, as the modified Rayleigh equations [2]:

$$R = k_1\frac{\lambda}{NA} \tag{2.2}$$

$$DOF = k_2\frac{\lambda}{NA^2} \tag{2.3}$$

Here R is the maximum resolution, DOF is the depth of focus of a feature at the resolution limit and the constants k_1 and k_2 are measures of the performance of the lithography system.

The diffraction limit can be understood through an analysis of diffraction from a periodic grating. Any signal can be expressed as a superposition of its Fourier components. Consequently consideration of a plane wave passing through a diffraction grating yields valuable insight into the influence of diffraction upon image formation in lithography. Fig. 2.5 illustrates how a plane wave, with wavelength λ, passing through a diffraction grating, with period Λ, is diffracted for the 0th, -1st, -2nd and higher order modes ($m \in [0, \pm 1, \pm 2, ...]$) and the corresponding propagation vectors k_m and their angular deviation, θ_m, from the z-axis.

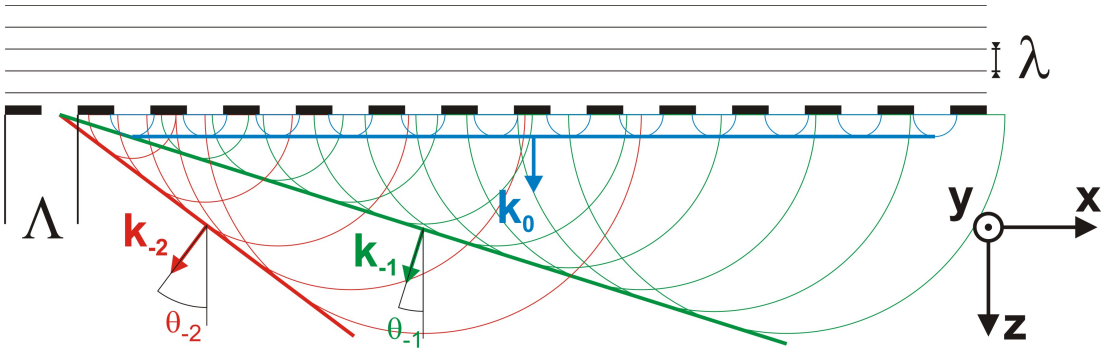

Figure 2.5: Plane wave passing through a diffraction grating.

Consider a plane wave $\mathbf{E}$, with angular frequency ω, propagating through space as given by Eq. 2.4.

$$\mathbf{E}(\mathbf{r}, t) = \mathbf{E_0} \cdot e^{i(\mathbf{k}\cdot\mathbf{r} - \omega t)} \tag{2.4}$$

Here the propagation vector, $\mathbf{k}$, is given by Eq. 2.5 and the corresponding wave number, $|\mathbf{k}|$, for a wave propagating through a medium with refractive index n, by Eq. 2.6 (in the following n is assumed to be 1).

$$\mathbf{k} = k_x\hat{\mathbf{x}} + k_y\hat{\mathbf{y}} + k_z\hat{\mathbf{y}} \tag{2.5}$$

$$|\mathbf{k}| = \frac{\omega n}{c} = \frac{2\pi n}{\lambda} = \sqrt{k_x^2 + k_y^2 + k_z^2} \tag{2.6}$$

A diffraction grating is situated at the object plane at $z = 0$. The grating is assumed to be infinite in the x-direction with a grating period of Λ, infinitely thin in the z-direction and made from a perfectly absorbing material. As a plane wave propagating along the

z-axis ($k_x = k_y = 0$ and $\mathbf{k} = k_z\hat{\mathbf{z}}$), with wavelength λ, passes through the grating a number of diffracted waves are generated. These diffracted orders, m, propagate into the space beyond the object plane at characteristic angles, θ_m, with regards to the z-axis, as given by the grating equation Eq. 2.7.

$$m\lambda = \Lambda \sin\theta_m, \ m \in \mathbb{Z} \tag{2.7}$$

$$\sin\theta_m = \frac{m\lambda}{\Lambda} \tag{2.8}$$

Given that $\sin\theta_m \leq 1$ it can be seen that the highest propagating order diffracted by the grating is given by $m_{max} = \Lambda/\lambda$. The wave propagation vector for the m-th diffraction order is given by Eq. 2.9.

$$\mathbf{k_m} = k_{x,m}\hat{\mathbf{x}} + k_{y,m}\hat{\mathbf{y}} + k_{z,m}\hat{\mathbf{z}} \tag{2.9}$$

The electric field beyond the grating can be expressed as a summation of the diffracted orders as shown in Eq. 2.10.

$$\mathbf{E}(\mathbf{r}, t) = \sum_{m=0} \mathbf{E_m} \cdot e^{i(\mathbf{k}_m \cdot \mathbf{r} - \omega t)} \tag{2.10}$$

For the 2D case considered here $k_{y,m} = 0$ and the x- and z-components of the diffracted propagation vector are given by Eqs. 2.11 & 2.12.

$$\begin{aligned} k_{x,m} &= \frac{\omega}{c} \cdot \sin\theta_m \\ &= \frac{\omega}{c} \cdot \frac{m\lambda}{\Lambda} \end{aligned} \tag{2.11}$$

$$\begin{aligned} k_{z,m} &= \frac{\omega}{c} \cdot \cos\theta_m \\ &= \frac{\omega}{c}\sqrt{1 - \left(\frac{m\lambda}{\Lambda}\right)^2} \\ &= \sqrt{\left(\frac{\omega}{c}\right)^2 - k_{x,m}^2} \end{aligned} \tag{2.12}$$

It is a requirement for a wave propagating into the space beyond the object plane, that $k_{z,m}$ is both positive and a real number. Thus, Eq. 2.12 imposes the condition given by Eq. 2.13.

$$\Lambda > m\lambda \tag{2.13}$$

In the case where the requirement in Eq. 2.13 is not fulfilled, that is $\Lambda < m\lambda$, k_z is imaginary and given by Eq. 2.14.

$$k_{z,m} = +i\frac{\omega}{c}\sqrt{\left(\frac{m\lambda}{\Lambda}\right)^2 - 1} \tag{2.14}$$

In the case of an imaginary wave vector the resulting expression for the electric field beyond the object plane is given by a decaying exponential function. This exponentially decaying field is called the evanescent near-field and it contains, as will be shown, high-frequency spatial information from the object plane. Even in the circumstance where $\Lambda \gg \lambda$ high-frequency spatial information will be contained within the non-propagating diffraction orders where $m > m_{max}$ and consequently some information is lost in the far-field image. Conversely, when $\Lambda < \lambda$ only the 0-th diffraction order, which is a plane wave, containing no information about the object, will propagate beyond the object plane. The highest spatial frequency, $k_g = 2\pi/\Lambda$, where any information about the object is retained in the far-field, i.e. the 1st order is diffracted at the propagation limit ($m\lambda = \Lambda$), is given by Eq. 2.15.

$$k_g = \frac{2\pi}{\Lambda} = \frac{2\pi}{\lambda} = \frac{\omega}{c} = |\mathbf{k}| \tag{2.15}$$

This illustrates the diffraction limit; that the upper limit for information transfer of high transverse spatial frequencies is inversely proportional to the wavelength. It has also been shown that sub-wavelength information, contained by the evanescent near-field, decays exponentially beyond the object plane.

2.2 Evanescent near-field optical lithography

Evanescent near-field optical lithography (ENFOL) is capable of surpassing the diffraction limit by capturing the evanescent near-field. This is achieved by eliminating the separation between object and image planes. In practice the photoresist is placed in intimate contact with the shadow mask, enabling evanescent near-field information transfer, see Fig. 2.6. Experimental investigations of this principle have illustrated great imaging potential for this technique as well as significant issues complicating commercial applications [36, Ch. 17, pp. 395-422].

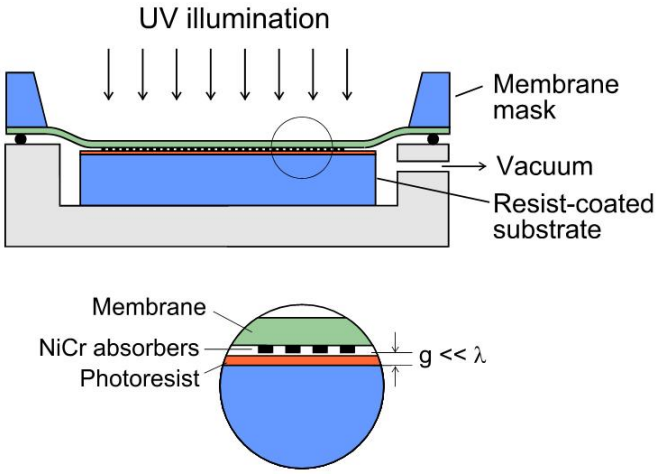

Figure 2.6: Schematic representation of an ENFOL imaging system utilising a combination of flexible masks and vacuum to achieve conformable contact. Reproduced from [36].

2.2.1 Imaging beyond the diffraction limit

In Section 2.1.2 it was shown how diffraction imposes a limit upon the transverse spatial frequency, k_x, that a propagating wave signal can convey. It was shown that information beyond this cut-off is contained within the exponentially decaying near-field.

Here follows a brief analysis of the implications of attempting to image beyond the diffraction limit.

Eq. 2.6 shows that k_z becomes imaginary when the transverse component $k_x^2 + k_y^2$ becomes larger than $\frac{\omega}{c}$. In the 2D case, where $k_y = 0$, k_z is given by Eq. 2.16.

$$k_z = i\sqrt{k_x^2 - \left(\frac{\omega}{c}\right)^2} = i\sqrt{k_x^2 - \left(\frac{2\pi}{\lambda}\right)^2} \tag{2.16}$$

The electric field for an evanescent mode in the space beyond the object plane varies with z as shown in Eq. 2.17.

$$\begin{aligned} \mathbf{E}(z,t) &= \mathbf{E_1} \cdot e^{i(k_z z - \omega t)} \\ &= \mathbf{E_1} \cdot e^{-\sqrt{k_x^2 - \left(\frac{2\pi}{\lambda}\right)^2} z} \cdot e^{-i\omega t} \end{aligned} \tag{2.17}$$

The exponential decay will cause the electric field to fall to e^{-1} of its initial value at the some evanescent decay length z_e given by Eq. 2.18.

$$z_e = \frac{1}{\sqrt{k_x^2 - \left(\frac{2\pi}{\lambda}\right)^2}} \tag{2.18}$$

As seen from this equation the decay length for the evanescent wave depends upon the spatial frequency, k_x, of the information transferred and the wavelength of the source. Fig. 2.7 show z_e as a function of $\frac{2\pi}{k_x}$ for the three wavelengths (365.4 nm, 193 nm and 13.5 nm) corresponding to UV, DUV and EUV exposure sources. As seen from this figure, the conformal contact requirement for achieving sub-wavelength resolution becomes more rigorous at shorter exposure wavelengths.

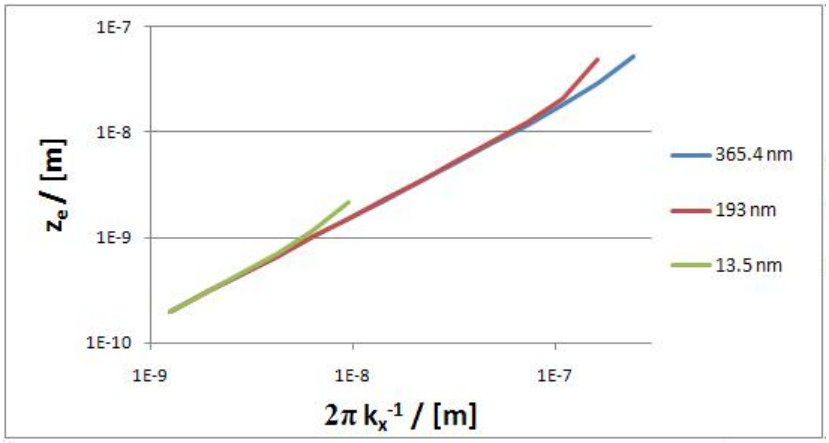

Figure 2.7: The evanescent decay length, z_e, as a function of $\frac{2\pi}{k_x}$. It can be inferred from the graph that depth of field in ENFOL for sub-wavelength features is largely independent of wavelength and scales linearly with the feature size.

The decay length for the evanescent field drops linearly with increasing spatial resolution given a constant exposure wavelength. To give one example, imaging a 60-nm-period grating at an exposure wavelength of 365 nm yields a decay length of ∼10 nm. The decay length defined here may be considered analogous to the depth of focus for a conventional imaging system. Furthermore, note that the decay length approaches ∼1 Å when trying to resolve features smaller than 1 nm. At very high resolution ($k_x \gg 2\pi/\lambda$) the decay length is equal to k_x^{-1}, independent of exposure source wavelength.

2.2.2 Developments in near-field lithography

Due to the significantly limited depth of focus of the evanescent field beyond the object plane initial capture and subsequent pattern transfer of the exposure pattern becomes very difficult. As the depth of field decreases linearly as a function of the spatial frequency of the object features, increasing the resolution of ENFOL places high demands on process parameters. The first critical issue is ensuring intimate contact between mask and photoresist as well as achieving a very high degree of planarisation. The second issue is that, to achieve good pattern transfer, the thickness of the photoresist layer itself must be on the order of the near-field decay length to produce a high-contrast resist image. Using such thin photoresist layers means that a multi-layer resist process may be required to achieve high aspect ratio pattern transfer.

In 1974 Smith demonstrated near-field image transfer using a conformal shadow mask and an exposure spectrum consisting of the mercury lamp G-, H- and I-lines to produce 400-nm half-pitch gratings [37, 38]. Smith identified some of the complications associated with near-field exposures and also proposed that much higher resolution should be achievable. Fischer reported in 1981 submicroscopic imaging through conformal contact lithography; here 100-nm features were defined in a negative photoresist using an exposure wavelength of 400 nm [39]. Embedded-amplitude masks (EAM), characterised by a topographically flat object-plane as illustrated by Fig. 2.8 were proposed for ENFOL by Gooberlet in 2000 [40, 41]. Using such EAMs, Goodberlet demonstrated definition of 100-nm features in a tri-layer resist, exposed at a wavelength of 220 nm. These results were further improved upon in 2002 when 45-nm wide lines and dots were defined [42]. Experimental studies of ENFOL have also been conducted at the University of Canterbury. In 1999, 50 nm wide lines and 140 nm period gratings were defined using a broadband source of radiation (365-600 nm) [6, 43].

EAM have several implicit advantages over normal amplitude masks in regards to ENFOL; higher degree of planarisation, less flexion stress from forces during mask-resist contact as well as increased transmission through apertures due to the absence of glass-air interfaces [44]. Additional optical confinement can be achieved using recessed metal absorbers or even absorber-less phase-shift masks. One example of this concept is the

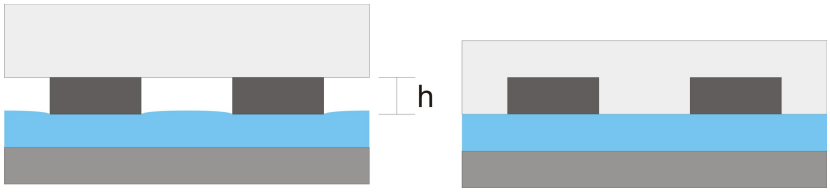

Figure 2.8: Left: Conventional shadow mask with protruding absorbers, more likely to cause deformation due to stress during contact. Right: Planarised embedded-amplitude mask (EAM) with intimate mask-resist contact.

light-coupling masks, relying on wave-guiding principles and intimate mask-resist contact. These were proposed by Schmid in 1998 and were used to define 100-nm features exposed at 256 nm [45].

Reports of extensive process optimisation studies for near-field lithography were published by a research group at Canon Inc., Japan, between 2005 and 2007 [4, 7–10, 46]. Initially 50-nm half-pitch gratings, exposed at a wavelength of 365.4 nm, were defined using a chemically amplified positive tone resist. Through utilisation of a tri-layer resist process an aspect ratio of 2.4 was achieved for these structures [7]. In 2006 simulation and experimental studies evaluating chromium and amorphous silicon (a-Si) as shadow mask absorption materials were presented [8]. Further, improvements were made in the way of 32-nm half-pitch resist patterns with aspect ratios of up to 3.75. Resolution of 22-nm half-pitch patterns was achieved in 2007 using a non-chemically amplified photo-deprotection resist based on photolysis of o-nitrobenzyl phenol ether [4]. Other publications by the group in 2007 dealt with resist process optimisation [46], the potential of the technique as a prototype nano-fabrication tool [10] and the chemical performance of the photoresist used in various experiments [9]. At present these results constitute the state-of-the-art in the field of ENFOL. The most recent achievements are showcased in Figs. 2.9 and 2.10.

However, while these results are encouraging, important issues in regards to utilising ENFOL for commercial applications remain unsolved. The lifetime of the shadow mask is significantly compromised relative to that of a projection mask due to the intimate contact requirement. The contact between mask and photoresist increases the risk of contamination and damage of the shadow mask with each exposure. Shadow mask life-

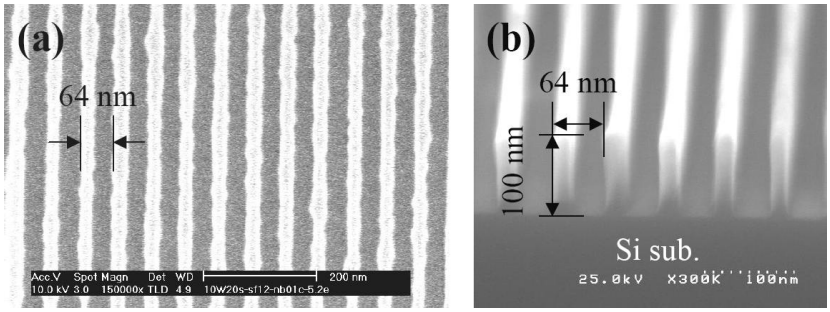

Figure 2.9: SEM micrograph of 32-nm half-pitch lines defined through ENFOL by the Canon group. Top-down (a) and cross-section (b). Reproduced from [4].

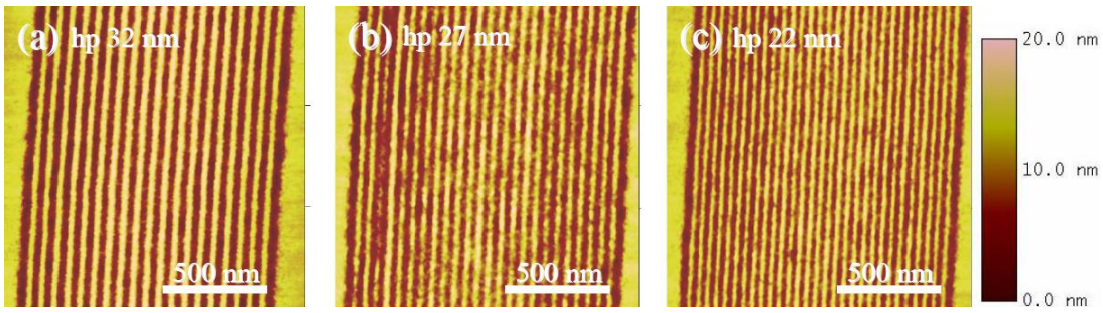

Figure 2.10: AFM surface map of line patterns defined through ENFOL by the Canon group. 32-nm half-pitch (a), 27-nm half-pitch (b) and 22-nm half-pitch (c). Reproduced from [4].

time becomes even more important for masks with sub-wavelength features since these will be significantly more expensive to produce than regular photolithography shadow masks.

2.3 The superlens

As illustrated by Section 2.2 ENFOL allows for the imaging of high-resolution patterns. Unfortunately, the near-field requirement, that the resist and mask are in conformal contact, severely limits the potential applications of the technique. In 2000 Pendry published the paper "Negative Refraction Makes a Perfect Lens" which presented a potential solution to this inherent problem of ENFOL [11]. Pendry showed that a planar lens with super-resolution capability could be positioned as a spacer between a shadow mask and photoresist while still transferring the evanescent field. While Pendry's proposal was new and controversial it was based on an idea presented by Veselago in 1968 [12]. These works are reviewed below.

2.3.1 Negative refraction and the perfect lens

In 1968 Victor Veselago conducted a theoretical investigation of wave propagation in lossless materials with simultaneous negative permittivity (ϵ) and permeability (μ) [12]. Veselago referred to such a material as a "left-handed substance" due to the fact that the vectors E, H and k form a left-handed set in such materials, as opposed to the right-handed set characteristic of natural materials. His analysis was based upon the dispersion equation and Maxwell's equations and led to a range of curious observations. One of these concerned the refractive properties of such materials. Veselago showed that in the case where ϵ and μ are both negative the refractive index, n, must also be negative. Consequently, light propagating through an interface between two materials with differing refractive indices will experience refraction in accordance with Snell's law. For refraction at the interface between a right-handed (RHM) and a left-handed material (LHM) both the incoming and refracted ray will be the same side of the normal. As a result, a rectangular slab of left-handed material will focus an object onto an image as shown in Fig. 2.11. Another controversial observation made by Veselago was that the wave propagation vector, $\mathbf{k}$, and the Poynting vector, $\mathbf{S}$, are anti-parallel in a left-handed medium.

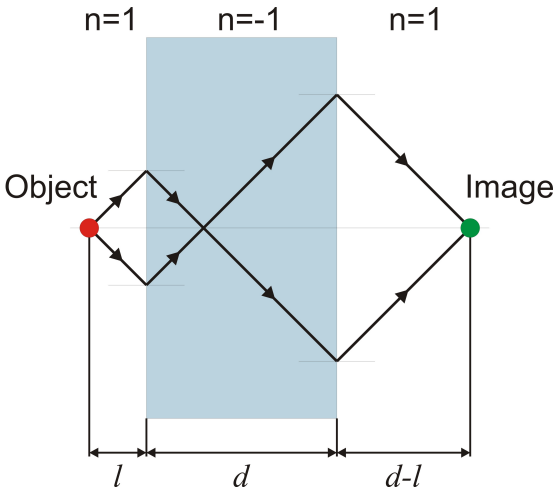

Figure 2.11: Ray tracing for a planar lens with a refractive index of -1.

In 2000, 32 years later, John Pendry's controversial paper entitled "Negative Refraction Makes a Perfect Lens" [11] was published. In this paper it was shown that a planar lens with $\epsilon_r = -1$ and $\mu_r = -1$ would act as a perfect lens. Such a lens would be capable of amplifying the evanescent field components of electromagnetic waves, allowing the projection of the near field an arbitrary distance away from the object plane, effectively allowing for non-diffraction-limited optics. A perfect lens would enable separation of the masking layer and the resist, hereby solving the dominant problem pertaining to ENFOL. However, no naturally occurring materials have the property $\epsilon_r = \mu_r = -1$.

For engineered meta-materials, composed of sub-wavelength elements, it is possible to tune the electric and magnetic properties so that for a given frequency the condition $\epsilon_r = \mu_r = -1$ may be fulfilled. However, fabricating large arrays of complex sub-wavelength elements for optical frequencies presents an astounding challenge due to the length-scales involved. Some metals behave as perfect plasmas at frequencies just below their plasma frequency. Consequently it is possible to achieve negative ϵ_r at optical frequencies by choosing a metal with an appropriate plasma frequency. While no metals are known to exhibit $\mu_r = -1$, Pendry proposed that in the electrostatic limit transfer of the evanescent field would still be possible for TM polarised light at frequencies where the real component of ϵ_r is close to -1. It was hypothesised that plas-

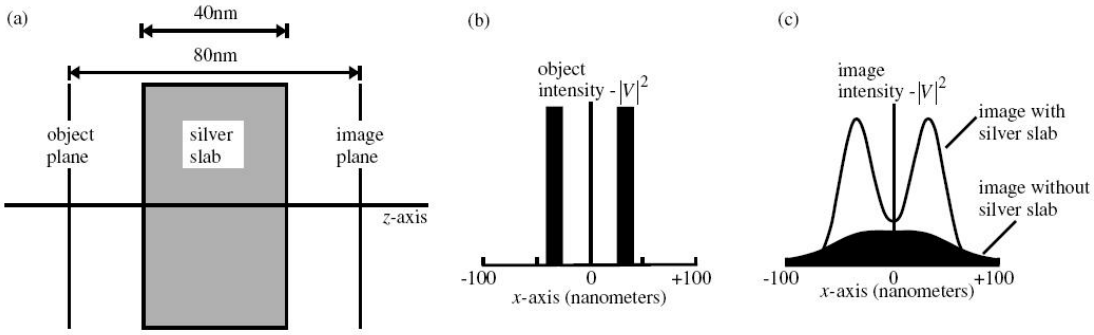

Figure 2.12: Calculations of image transfer in a silver superlens. Reproduced from [11].

monic interactions could be the mediating mechanism for high-frequency information transfer. Pendry finally simulated the transmission of sub-wavelength information for a planar silver lens under these assumptions, the results of which are shown in Fig. 2.12.

Pendry's paper sparked both great interest in, and considerable controversy over, the concept of negative refraction and perfect lensing. Not long after Pendry's publication, the principle of negative refraction in meta-materials was demonstrated for microwaves [13, 14]. The realisation of these negative refractive index metamaterials built upon earlier works by Pendry and Smith, predating "Negative Refraction Makes a Perfect Lens", dealing with tuning the electromagnetic response of micro-structured materials composed from split-ring-resonators (SRR) and thin wire networks [19, 47, 48].

Several theoretical papers contesting Pendry's hypothesis were published. Valanju argued that in LHM the group fronts refracts positively while the phase fronts refract negatively resulting in dispersing and inhomogeous waves [51]. This anti-thesis was later considered and dismissed by Pendry and Smith [52, 53]. Garcia argued that in real LHMs there would be no evanescent field amplification due to loss-effects [54]. Pendry et al. addressed this assertion and presented both a theoretical analysis of non-planar superlens geometries [55] as well as discussions about the limitations of planar superlens [56]. While loss was identified as a limitation in super-resolution imaging there have been considerations around reversing losses in meta-materials by introducing a gain medium [57]. Garcia also questioned whether the results on microwaves

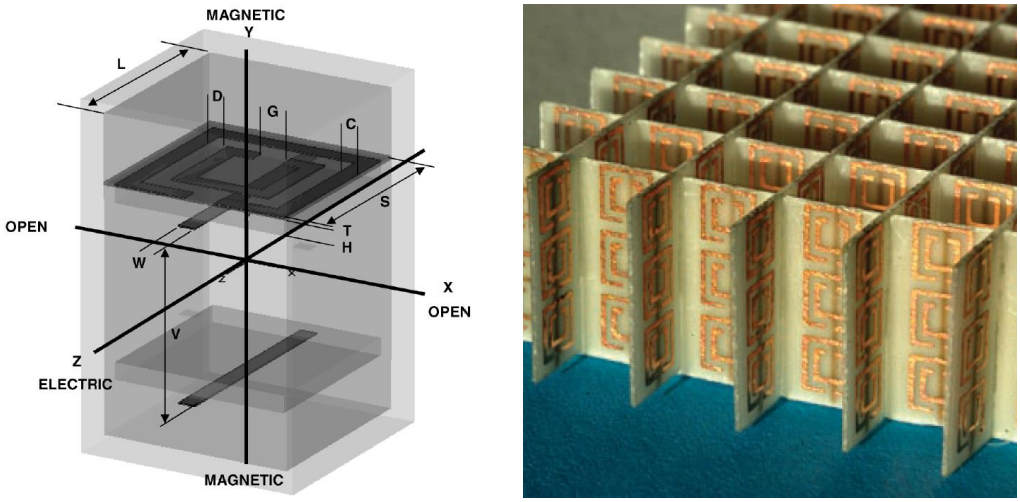

Figure 2.13: Metamaterial yielding both negative permittivity and permeability for microwaves. Left: Schematic overview of LHM components; split-ring-resonators for magnetic and wires for electric control. Right: A photograph of a real LHM for microwave frequencies. Reproduced from (left) [49] and (right) [50].

presented by Shelby [14] in fact did demonstrate negative refraction [58]. Soukoulis responded to this argument through numerical analysis of transmission losses in LHM and comparison with experimental results [59].

With more recent experimental results adding weight to the findings of negative refraction in metamaterials at microwave frequencies [49, 60], the debate on the viability of negative refraction appears diminished. Negative refraction and metamaterials for the IR and visible parts of the spectrum have also been investigated [16, 61]. Superlenses based upon silver for applications in the near-UV has been an area of much interest and is the focus of the next section.

2.3.2 Silver super lenses

The material requirements for surface plasmon driven superlensing dictates that the real component of the complex permittivity be negative ($\epsilon' < 0$) and that the loss component relatively small ($\epsilon'' < \epsilon'$). The optical properties of a material can be described by the complex refractive index, $\tilde{n}$, given by the real refractive index, n, and the extinction coefficient, k, as per Eq. 2.19.

$$\tilde{n} = n + ik \tag{2.19}$$

Given the parameters n and k the complex relative permittivity, $\tilde{\epsilon_r}$, can be calculated as shown in Eq. 2.20.

$$\begin{aligned} \tilde{\epsilon_r} &= \epsilon' + i\epsilon'' \\ \epsilon' &= n^2 - k^2 \\ \epsilon'' &= 2nk \end{aligned} \tag{2.20}$$

Due to dispersion these optical constants vary as a function of frequency, ω. Experimental measurements of n and k were carried out for copper, silver and gold at optical frequencies in the early 1970's by Irani, Huen & Wooten [62] as well as Johnson & Christy [63]. Their findings, for frequencies corresponding to wavelengths near the mercury I-line (365.4 nm), are summarised in Table 2.1 along with the corresponding values for ϵ' and ϵ''. As can be seen ϵ' is negative and its magnitude approximately one order of magnitude higher than ϵ''. Consequently the requirement for superlensing is fulfilled for silver at wavelengths in this region of the spectrum.

Source:	Irani, Huen & Wooten [62]	Johnson & Chrisy [63]
Wavelength:	366.2 nm	368.2 nm
n	0.087	0.07
k	1.564	1.657
ϵ'	-2.44	-2.74
ϵ''	0.27	0.23

Table 2.1: Components of the complex n and ϵ_r of silver at wavelengths close to the mercury I-line.

Here follows a review of the advances made in the field of silver superlens enhanced imaging in the near-UV spectrum. Planar superlens geometries will be presented in the form [t_1-t_2-...-t_n] where t_n is the thickness of the n-th layer of the lensing stack. In reporting on such geometries only the number of silver layers $(n-1)/2$ are considered. Thus, a single-layer superlens will consist of a single layer of silver surrounded by two dielectric spacers, while a double-layer superlens will consist of two silver layers and three dielectric spacers as illustrated by Fig. 2.14.

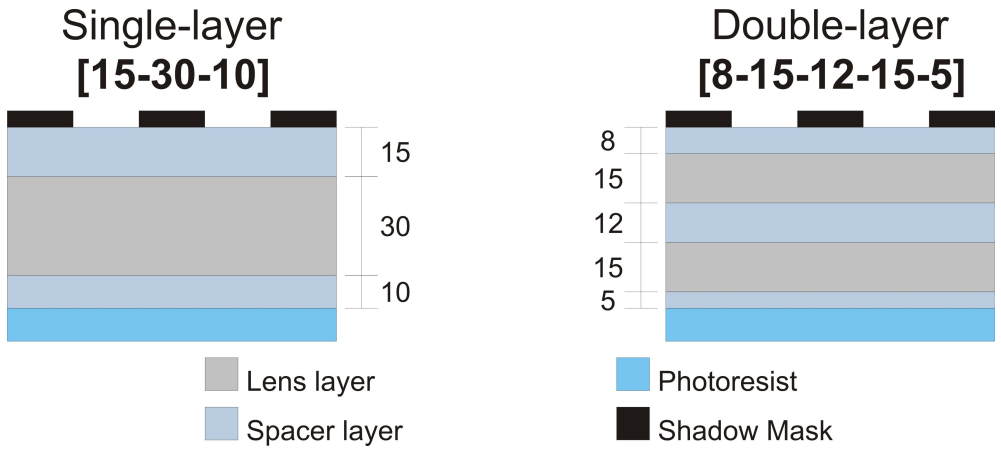

Figure 2.14: Schematic overview of superlens geometries. Left: Single-layer [15-30-10] geometry - i.e. a superlens stack consisting of three layers, proceeding along the optical axis: a 15-nm thick spacer layer, a 30-nm thick lens layer and a 10-nm thick spacer layer. Right: Double-layer [8-15-12-15-5] geometry - i.e. a superlens stack consisting of five layers, proceeding along the optical axis: an 8-nm thick spacer layer, a 15-nm thick lens layer, a 12-nm thick spacer layer, a 15-nm thick lens layer and a 5-nm thick spacer layer.

Pendry identified silver as a potential material for superlenses operating at optical to near-UV wavelengths and suggested surface plasmons as the mechanism [11]. Initial simulation results indicated that a 40-nm silver film should be able to transmit 50-nm features using an exposure wavelength of 341 nm [64]. In 2003 Zhang presented experimental evidence for evanescent field enhancement on silver thin-film surfaces and showed that the effect depended strongly on film thickness with a maximum observed at 50 nm [65].

The following year Melville initially demonstrated definition of 350-nm half-pitch gratings exposed at 365 nm using a [60-120-60] nm geometry consisting of a silver film surrounded by planarised PMMA spacer layers [66]. These results were elaborated and improved upon by resolving 250-nm half-pitch gratings using silver lensing layers with thicknesses in the range 85-120 nm as well as demonstrating loss of image fidelity for a dielectric spacer in the absence of silver ([60-0-60] nm geometry) [67].

In 2005 Zhang expanded upon earlier findings [65] and reported experimental and simulation studies of the surface plasmon based transmission enhancement of evanescent waves in silver films for illumination wavelengths in the range 351.1-514.4 nm [18]. Melville demonstrated resolution of 72.5 nm half-pitch gratings, exposed by a 365-nm wavelength source, using a [25-50-10] nm PMMA/Ag/SiO_2 planar lens geometry [17, 68]. Zhang reported resolution of 60-nm half-pitch gratings using a [40-35-0] nm PMMA/Ag geometry and a negative resist exposed at 365 nm and demonstrated the benefits of a planar silver lens relative to a dielectric spacer of similar thickness ([35-40-0] nm PMMA/PMMA) [18, 69]. Example results from these publications are presented in Fig. 2.15.

Melville compared imaging performance for various single- and double-layered silver superlens geometries ([25-50-10] nm, [30-60-30] nm PMMA/Ag/SiO_2 and [15-30-30-30-10] nm , [25-50-50-50-10] nm PMMA/Ag/SiO_2/Ag/SiO_2) in 2006, reporting increased resolution for double-layered lenses at the cost of pattern fidelity [70].

The most recent results were presented in 2010 when Chaturvedi et al. reported formation of 30-nm half-pitch lines in a negative photoresist using a [6-(1)15-0] nm geometry

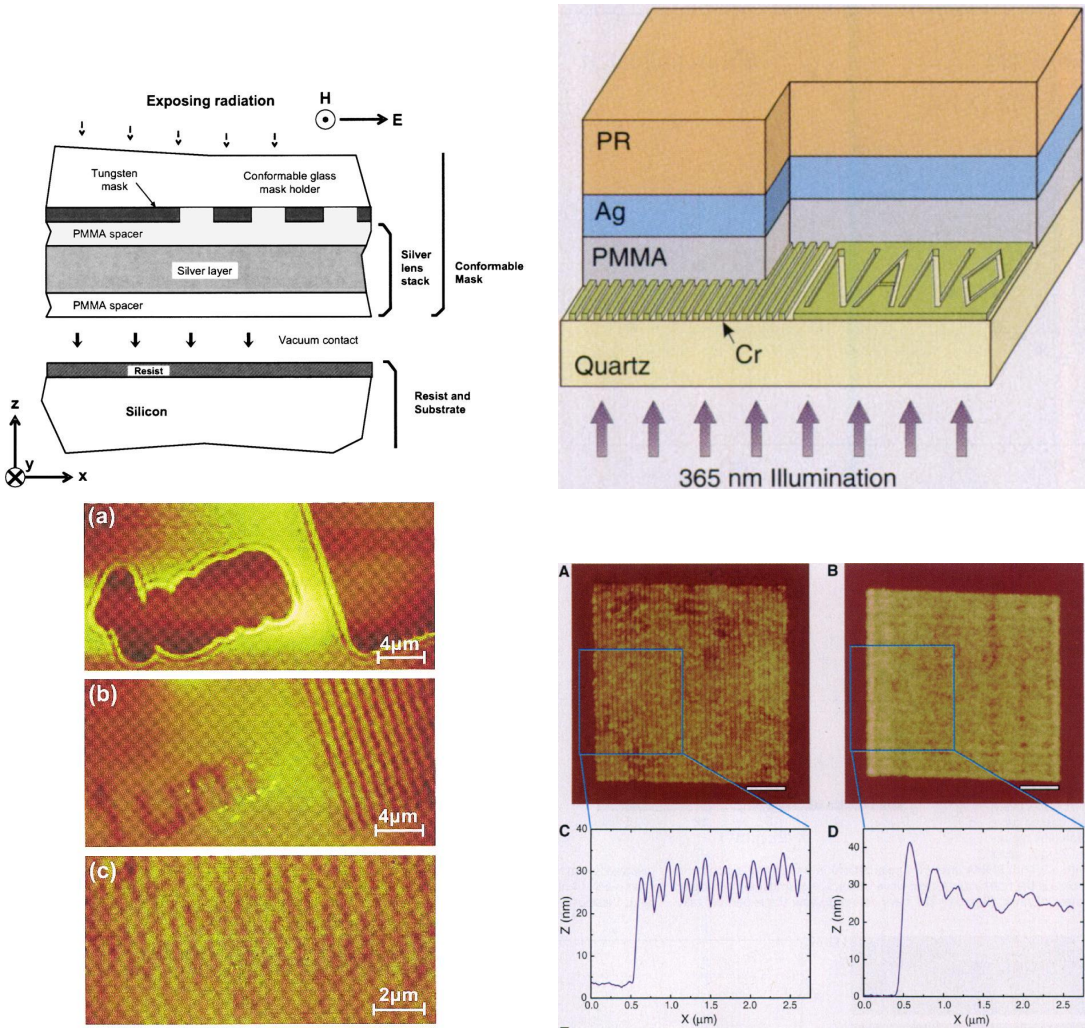

Figure 2.15: Early superlens geometries (top) and results (bottom) as presented by (left) Melville [66] and (right) Zhang [18].

with reduced silver surface roughness achieved by introduction of a 1-nm thick germanium wetting layer [5], as shown in Fig. 2.16(left). The surface roughness figures for the silver films used by Chaturvedi were reported as <0.8 nm RMS compared to earlier values of ∼1.2 nm RMS. However, there are indications that germanium can have a detrimental impact upon plasmonic systems [71] and consequently the utilisation of germanium wetting layers may not be ideal.

The principle of superlensing has been applied to other geometries than planar lensing. Theoretical calculations for various non-planar geometries were performed by Pendry and Ramakrishna [55, 72, 73]. In 2007 Zhang presented the hyperlens, a semi-cylindrical geometry consisting of alternating 35-nm thick layers of silver and alumina, which facilitated the far-field imaging of sub-wavelength objects situated on the inner surface of such a hyperlens [74–77], with results shown in Fig. 2.16(right).

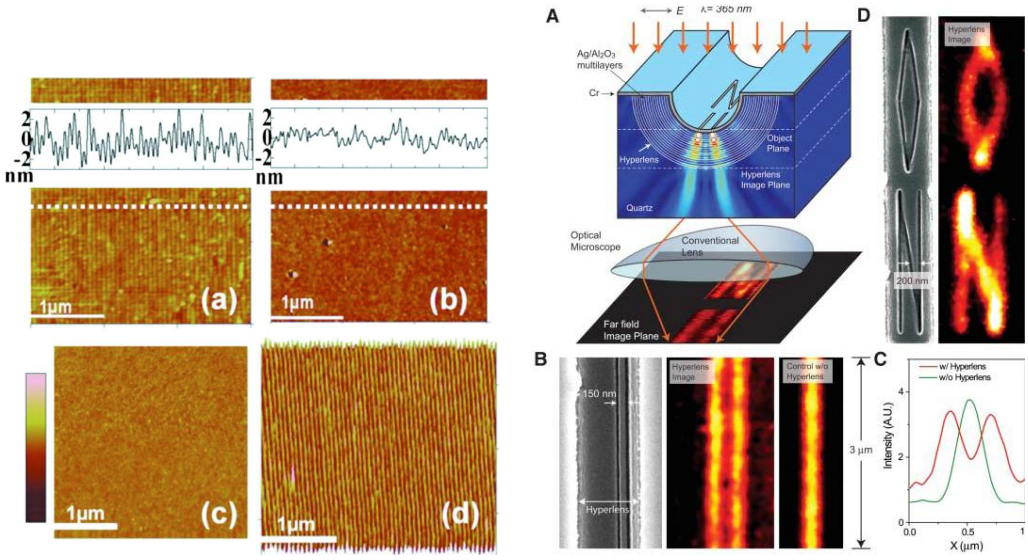

Figure 2.16: Recent developments within the field of optical superlensing. Left: 30-nm half-pitch lines resolved by smooth silver superlens as reported by Chaturvedi [5]. Right: The optical hyperlens proposed by Zhang in 2007 [74].

Other investigations pertaining to the field of superlenses have been conducted; e.g. optimum selection of dielectric spacer material [78], plasmonic alloys to facilitate tuning of operational wavelength [79], thin-film surface modification for plasmonic applications

[80], etc. Another idea related to superlensing is to introduce a plasmonic reflector layer under the photoresist which, through photon-plasmon coupling, improves the depth-of-focus for evanescent waves [81].

2.3.3 Plasmonics

The extraordinary transmission of planar superlenses is facilitated by coupling of the evanescent field into surface plasmons on the metal-dielectric interface, the plasmon-plasmon coupling between interfaces in a thin-film and the subsequent decoupling of the plasmon into an evanescent field beyond the lens interface. In order to understand the fundamental mechanics of the superlens an understanding of plasmonics is necessary.

A plasmon can be considered as a quasi-particle, a quantum of charge density oscillation in a plasma-like medium. The classic case is that of Langmuir waves: charge density oscillations in an ionised gas, a true plasma, which were discovered by Irving Langmuir and Lewi Tonks in the 1920s [82]. In a metal the free electron gas will behave in a plasma-like manner inside a certain range of frequencies. A plasma resonance occurs at a specific frequency known as the plasma frequency, ω_p, given by Eq. 2.21.

$$\omega_p = \sqrt{\frac{n_e e^2}{m^* \epsilon_0}} \tag{2.21}$$

Here n_e is the electron density, e the charge of the electron, m^* is the effective mass of the electron and ϵ_0 is the electric permittivity of vacuum. Plasma oscillations can occur both inside the bulk of a metal as well as at the interfaces. Plasma oscillations at interfaces between media are called surface plasmons and are generally divided into two distinct categories: Surface plasmon polaritons (SPP) and localised surface plasmons (LSP). LSPs typically describe plasmons on spatially confined surfaces, such as those of nano-scale particle. SPP describe plasmons propagating at semi-infinite interfaces and is the analytical approach most suited to characterise the plasmon-interactions in superlenses. The behaviour of surface plasmons depends upon various factors such as scattering, retardation, resonance and coupling effects [83].

In his 1988 book "Surface Plasmons on Smooth and Rough Surfaces and on Gratings" [84], Raether conducts a thorough theoretical analysis of plasmon behaviour on

both smooth and rough surfaces as well as photo-excitation of SPPs with attenuated total reflection (ATR) and grating coupling. Key results from Raether's work pertaining to the mechanics of superlenses are presented below.

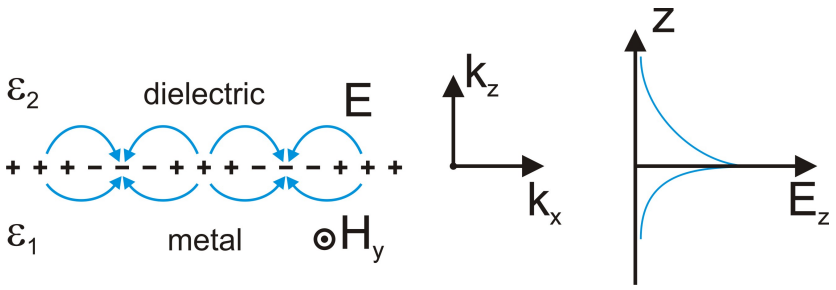

Figure 2.17: Schematic representation of a surface plasmon.

Consider a metal-dielectric interface situated at $z = 0$, with the metal occupying the region $z < 0$ and the dielectric the region $z > 0$. The dielectric constants for the metal and dielectric are given by ϵ_1 and ϵ_2 respectively. Here the dielectric constant for the metal is a complex entity given by $\epsilon_1 = \epsilon_1' + i\epsilon_1''$. The electric field of a SPP on the interface can, for the case of TM polarisation, be expressed as Eq. 2.22.

$$E = E_0^{\pm} \cdot e^{+i(k_x x \pm k_z z - \omega t)} \tag{2.22}$$

In Eq. 2.22 + holds for $z \geq 0$ and − for $z \leq 0$ and k_z is imaginary, describing exponential decay of the electric field in the z-direction moving away from the interface. The propagation of the SPP along the interface is described by k_x, characterised by a plasmon wavelenth $\lambda_p = 2\pi/k_x$. The general dispersion relation for the SPP can be found through application of Maxwell's equations and is given by Eq. 2.23.

$$k_x^2 + k_{zi}^2 = \epsilon_i \left(\frac{\omega}{c}\right)^2, i = 1, 2 \tag{2.23}$$

The requirement that the components of the electric and magnetic fields parallel to the surface must be continuous at the interface results in the condition presented in Eq. 2.24. Further, dispersion relations for the z-components of the SPP propagation vector in either z-region (i) as function of k_x are given by Eq. 2.25.

$$-\frac{k_{z1}}{\epsilon_1} = \frac{k_{z2}}{\epsilon_2} \tag{2.24}$$

$$k_{zi}^2 = \epsilon_1 \left(\frac{\omega}{c}\right)^2 - k_x^2, i = 1, 2 \tag{2.25}$$

Eqs. 2.24 and 2.25 combines to provide the dispersion relation for k_x given by Eq. 2.26.

$$k_x = \left(\frac{\omega}{c}\right)\left(\frac{\epsilon_1\epsilon_2}{\epsilon_1+\epsilon_2}\right)^{1/2} \tag{2.26}$$

Under the assumption that ω and ϵ_2 are both real and that $\epsilon_1'' < |\epsilon_1'|$ the transverse plasmon propagation vector k_x becomes a complex entity, $k_x = k_x' + ik_x''$ with real and imaginary components given by Eqs. 2.27 and 2.28.

$$k_x' = \left(\frac{\omega}{c}\right)\left(\frac{\epsilon_1'\epsilon_2}{\epsilon_1'+\epsilon_2}\right)^{1/2} \tag{2.27}$$

$$k_x'' = \left(\frac{\omega}{c}\right)\left(\frac{\epsilon_1'\epsilon_2}{\epsilon_1'+\epsilon_2}\right)^{3/2}\frac{\epsilon_1''}{2(\epsilon')^2} \tag{2.28}$$

$$\tag{2.29}$$

Given that ϵ_2 is real and positive, Eq. 2.24 imposes the requirement that $\epsilon_1' < 0$. Consequently, if k_x' is to be a real number $|\epsilon_1'| > \epsilon_2$. The imaginary component, k_x'', expresses SPP attenuation due to internal dampening and cause plasmons to decay exponentially as they propagate along a surface. This loss is characterised by the propagation length L_i, which is defined as the distance over which a plasmon decays by a factor of $1/e$. For SPPs on a smooth interface L_i given by Eq. 2.30.

$$L_i = (2k_x'')^{-1} \tag{2.30}$$

This spatial decay is related to the temporal lifetime of the SPP, T_i, by the relation $L_i = T_i v_g$ where $v_g = d\omega/dk$ is the SPP group velocity.

Given the constraints placed upon ϵ_1 and ϵ_2, k_x will always be larger than ω/c. Consequently no direct coupling between propagating light waves and surface plasmons at a smooth interface is possible. As shown earlier, high-frequency spatial information contained within the near-field have transverse frequency components where $k_x > \omega/c$. Provided that a metal-dielectric interface capable of sustaining SPPs is placed close enough to the object plane that the evanescent field has not decayed completely, coupling between the near-field high-frequency components and SPPs is possible given the right material parameters. Furthermore, in the case of successive metal-dielectric interfaces situated along the z-axis, separated by Δz, SPP-coupling between interfaces is possible as long as $|\epsilon_i'|\Delta z \leq 1/k_{zi}$. This coupling between interfaces both affects the

dampening, $k_x'' \propto \Delta z^2$, and causes mode-splitting of the SPP into a high-low-frequency doublet $\omega^{\pm}$. Theoretical analysis of this situation has shown that the group velocity, v_g, of the asymmetric high-frequency mode, ω^{+}, can be negative for high k_x' in very thin films [85].

2.3.4 Surface roughness in superlenses

SPPs propagating along non-smooth surfaces are subject to loss due to scattering and radiation. Raether [84, Section 2.9] analyses SPP behaviour on metal-dielectric interfaces with surface roughness profiles characterised by root-mean-square (RMS) magnitude, δ, and correlation length, σ. In this case the propagation lengths for radiation, L_{rad}, and scattering, L_{sc}, loss are given by Eqs. 2.31 and 2.32 respectively.

$$L_{rad} = \frac{2}{3}\frac{|\epsilon_1'|}{(\omega/c)^5}\frac{1}{\sigma^2\delta^2} \tag{2.31}$$

$$L_{sc} = \frac{3}{4}\frac{|\epsilon_1'|^{1/2}}{(\omega/c)^5}\frac{1}{\sigma^2\delta^2} \tag{2.32}$$

As seen, the loss in rough films is proportional to the square of both surface roughness RMS magnitude and correlation length. Surface topology analysis can be performed by consideration of the corresponding power-spectral-density (PSD) function. Each of the PSD fourier components is characterised by its spatial frequency, k_r. For a periodic function, the correlation length σ_r is equivalent to a period given by $a = 2\pi/k_r$. Consequently, surface plasmon loss effects on rough interfaces depends not only on the RMS magnitude of the roughness, but also upon the spectral distribution of the roughness.

The results presented by Raether pertains to loss-mechanisms for surface plasmons. As shown above there are internal losses for surface plasmons even on perfectly smooth interfaces, which give rise to a characteristic propagation length L_i, given by Eq. 2.30. The presence of surface roughness gives rise to additional losses due to scattering and radiative decoupling, which can be expressed by the corresponding propagation lengths L_{rad} and L_{sc} given by Eqs. 2.31 and 2.32. These loss-mechanisms only describe the transverse attenuation of surface plasmons. Importantly, they do not infer any quantitative information about how the surface characteristics of a thin metal film would affect its ability to reliably project an evanescent near-field. However, the fidelity of

an image reconstructed from its Fourier components will be limited by the spatial frequency band-width of components available. Consequently, the transverse attenuation of surface plasmons in superlens imaging must be assumed to directly result in information loss in image formation. This relationship between plasmonic losses and superlens image fidelity is largely unexplored and an understanding of this is important when seeking to improve superlens imaging.

2.4 Summary

Diffraction imposes an implicit resolution limitation upon conventional lithography. This diffraction limit can be overcome through ENFOL which relies on evanescent fields to achieve non-diffraction-limited resolution. However, the strong dependence upon object-image separation distance in ENFOL imposes rigorous demands on planarisation and a requirement for intimate mask-resist contact. While planarisation is achievable, the requirement for mask-resist contact invariably reduces the life-time of shadow masks.

Superlenses are capable of capturing and transmitting near-field information and will allow ENFOL image transfer while acting as a buffer layer separating mask and resist. The superlens operates through excitation of SPPs and SPP-coupling between closely spaced metal-dielectric interfaces. Plasmonics depend strongly on ϵ of the lens materials and silver exhibit the desired characteristics at UV frequencies. However, SPP behaviour also depends strongly on the surface morphology of the lens, where roughness-induced loss effects occur. The impact of these mechanisms upon the fidelity of image transfer in superlenses is difficult to quantify.

While the principle behind superlensing has been demonstrated both theoretically and experimentally, many aspects of the subject remain unexplored. One aspect is how nanoscale surface roughness on the lens interfaces impacts the imaging characteristics of a superlens system. Experimental reports of silver superlensing to date all show poor image fidelity, relative to theoretical expectations, with high degrees of line-edge roughness (LER) observed in the resulting photoresist images. The cause of this increased LER has not been thoroughly investigated to this date and this is a major focus of

the present thesis. While lens surface roughness will have some impact in this regard, other factors could also have a detrimental effect.

Experimental investigation of the effect of surface roughness on superlens imaging demands a high degree of control of the surface roughness parameter in metal-dielectric films. However, thin film deposition of metal-dielectric stacks with smooth interfaces poses significant challenges as will be described in Chapter 3. Another way of analysing the problem is numerical modelling, solving Maxwell's equations for complex surface geometries. Such investigations are presented in Chapters 4 and 5. Chapters 6 and 7 details development, characterisation and application of a novel high-resolution resist for near-field imaging.

3

Thin film deposition

As identified in Chapter 1, and further expanded upon in Chapter 2, surface roughness on a superlens surface is expected to have a detrimental, albeit unknown, impact upon the imaging performance of the superlens imaging system. In an attempt to experimentally qualify and quantify the impact of such surface roughness upon the performance of silver superlenses, operating at the mercury I-line, an initial series of thin film deposition (TFD) experiments were undertaken using the facilities available at the University of Canterbury nanofabrication laboratory (UCNFL). The goals of these experiments were:

1. To identify how various process parameters affect silver thin film surface roughness using the UCNFL facilities.

2. To establish the attainable range of surface roughnesses achievable for silver thin-films of a given thickness.

3. To establish a deposition protocol for production of silver thin films with consistent film thickness and surface roughness.

Upon achieving the third goal, further experiments were to be undertaken to explore the relationship between superlens surface roughness and imaging performance.

This chapter begins with a brief introduction to the mechanisms underpinning thin film deposition. This is followed by a discussion highlighting the specific issues associated with the deposition of smooth thin-films in general and in the specific case of

alternating stacks of silver and dielectric thin films. Then follows a presentation of the method behind and the results gained from the experimental investigation itself. Finally there is a summary and conclusion section which also provides an outlook for future thin film deposition investigations.

3.1 Thin film deposition fundamentals

Thin film deposition is one of the key technologies in micro- and nanoscale fabrication. It is one of the fundamental tools in the planar fabrication "toolbox" alongside ultraviolet photolithography (UVL) and reactive ion etching (RIE). Thin film deposition techniques such as electro-plating have been used since the early 19th century. However, with the advent of the solid-state transistor and the ensuing miniaturisation process, thin film deposition has, since the 1960s, become an important field of research and development. Today there are numerous different deposition techniques available, each of which has its merits and limitations depending upon the actual application.

The theoretical framework that follows here is based upon 'Thin-film deposition: Principles and practice' by Donald L. Smith [86]. A rigorous consideration of this theoretical foundation is beyond the scope of present thesis. Thus, only selected key results and considerations that dictate the surface roughness characteristics of a resulting thin-film will be presented here. More specifically, focus will be on the kinetics that govern the seeding and growth of thin-films and how these will affect the resulting surface morphology; both in the general case and in the specific case of silver-dielectric stacks.

A thin-film deposition process can, from a general perspective, be broken into three different deposition stages:

1. Source
2. Transport from source to substrate
3. Deposition on substrate and film growth

These deposition stages are illustrated by the schematic overview in Fig. 3.1.

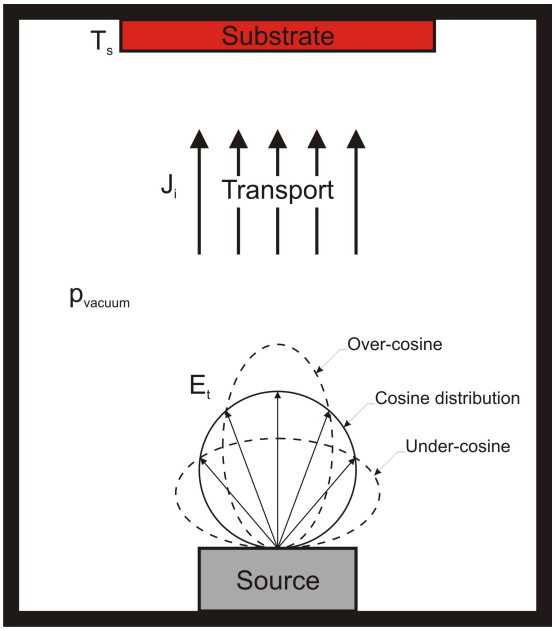

Figure 3.1: Schematic overview illustrating the general concepts of thin-film deposition. Physical vapour deposition usually takes place in a low- to high-vacuum environment, characterised by the vacuum pressure, p_{vacuum}. Source output flux distributions typically have cosine, over- or under-cosine distribution. Kinetic energy, E_t, distribution and the ionisation state of species produced by the source varies significantly between different source technologies. Incident flux of species i, J_i, upon the substrate depends on various transport conditions: source-substrate geometry, vacuum pressure, kinetic energy distribution, etc. Substrate temperature, T_s, has a significant impact upon thin-film growth kinetics.

The source material comes in one of the three physical phases: solid, liquid and gas. Solid sources require the initial vaporisation of the source material, e.g. thermal, photonic-, electron- and ion-bombardment, and are generally catagorised as physical vapour deposition (PVD). In comparison, liquid and gas sources are often catagorised as chemical vapour deposition (CVD). Principal considerations in regards to the source are contamination and supply rate. Dependent upon the source technology depositant species will have certain size, kinetic energy and directional distributions.

In transportation of depositant material from source to substrate, controlling the arrival characteristics across the substrate is imperative to achieve thin films with the desired properties. In general terms, transport from source to substrate takes place

either in a high vacuum or a fluid environment. Most PVD techniques operate in high vacuum where the depositant species have a long mean free path, l. When the atomic diameter, a, temperature, T, and pressure, p, are all known, the mean free path can be calculated as shown in Eq. 3.1. In this equation R is the gas constant and N_A is the Avogadro constant.

$$l = \frac{RT}{\sqrt{2}\pi a^2 p N_A} \tag{3.1}$$

Consequently vacuum transport is mainly dependent upon geometric considerations and the characteristics of the source. Fluid transport environments are encountered more often in CVD techniques and here the transport depends upon flow conditions and diffusion. In the case of plasma processes, such as magnetron sputtering, the transport kinetics may be considered as having both vacuum and fluid character, with either mechanism dominating the other depending upon the process pressure. The transport environment can be characterised by the Knudsen number, Kn, which is given by Eq.3.2.

$$Kn = l/L \tag{3.2}$$

Here l is the mean free path of the depositant species and L is a characteristic length for the deposition system (i.e. source to substrate distance). For $Kn > 1$ the transport can be considered ballistic and this situation is called the molecular flow regime. Conversely, if $Kn < 0.01$ the transport is considered fluidic.

Deposition is the formation of the thin film itself on the substrate surface. Deposition is a complex thermodynamical process that depends upon many factors including the source and transport components. However, in general terms the deposition step depends upon substrate surface conditions, reactivity of the arriving material and energy input. Growth kinetics will be considered in greater detail in section 3.2 as it is predominant stage in determining the morphology of the resultant thin film.

In order to verify that a thin film with the desired properties has been produced it is imperative to conduct quantitative thin film analysis following the deposition process. Analysis of the deposited thin-film varies strongly depending upon the desired properties for the specific application. A vast range of very diverse techniques are

employed to measure film characteristics ranging from surface topolgraphy and crystallinity to conductance and stoichiometry. In this project two analytical techniques were applied; atomic force microscopy (AFM) and profilometry, to measure film surface roughness and film thickness, respectively.

3.2 Thin film deposition kinetics

The deposition stage of the thin-film deposition process can be considered as six distinct mechanisms: adsorption/desorption, diffusion, bond formation, nucleation, structural development and internal reconfiguration. Fig. 3.2 illustrates some of these mechanisms and provides a visual representation of some of the parameters that will be discussed in this section.

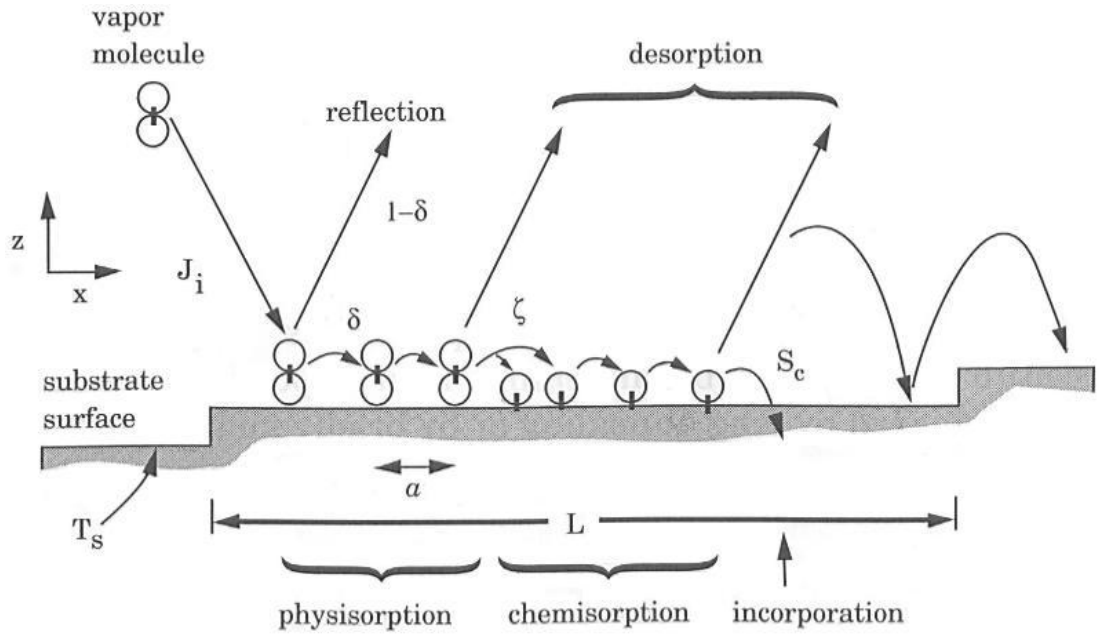

Figure 3.2: Adsorption processes and quantities. A vertical connecting bar denotes a chemical bond. Figure reproduced, in modified form, from [86, p. 120].

However, these mechanisms do not necessarily occur in a straight-forward point by point sequence. Adsorbed species may desorp from the deposition substrate before actually being incorporated into the thin-film and diffusion may still take place even after bond formation with the substrate has occurred, although with highly reduced mobility.

In some cases bond formation with the substrate will not be possible and in others no appreciable diffusion will occur due to thermal quenching. As a result, the dynamics of film growth is a complex consisting of several interacting, even competing, mechanisms.

In this section main considerations and key results relevant to the present project are presented. In the following the TFD mechanisms will be treated under four individual topics: 1) adsorption -how the depositant species arrives at and interacts with the substrate surface, 2) diffusion - the depositant species' surface mobility, 3) wetting and nucleation - how the thin-film seeding occurs and the kinetics governing the formation of the first couple of monolayers, and 4) film growth - considerations of how the structure of the film develops during film growth beyond the initial seed layer.

3.2.1 Adsorption

The depositant species arriving at the substrate surface will have spatial, size and kinetic energy distributions as dictated by the source and transport characteristics for the system. The incoming species will adsorp onto the surface, through van der Waals forces, in a weakly-coupled physical adsorption state. While in this weakly-bound, physiosorped state the depositant species are quite mobile and may yet desorp from the surface depending upon substrate temperature and the surrounding pressure.

A more strongly-bound state also exists as the depositant species may form chemical bonds with the substrate and enter into a chemical adsorption state. In this chemisorped state the depositant is much more strongly bound, surface mobility is significantly reduced and the probability of desorption is very low, except when substrate temperatures, T_s, approach the melting point, T_m, of the film material. However, depending upon the characteristics of the adsorped species there may be a potential energy barrier that needs to be overcome - e.g. dissociation from a molecular bond in the incoming species before chemical bonding with the surface is possible. As an example consider the CVD growth of polycrystaline silicon onto a silicon substrate using silane gas (SiH_4). The energies of the different adsorption states are illustrated by the potential energy curve presented in Fig. 3.3.

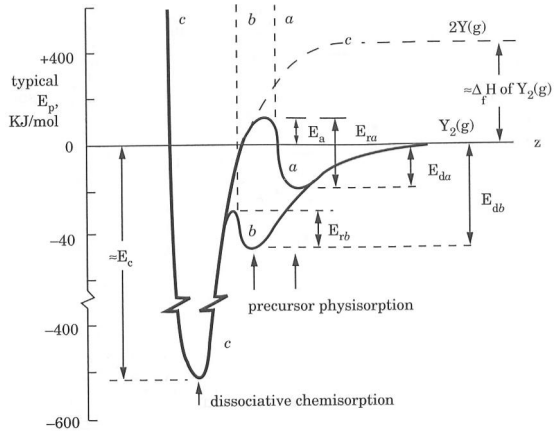

Figure 3.3: Energetics of the precursor adsorption model. Energy scale is typical only. Figure reproduced from [86, p. 123].

Physiosorped and chemisorped states are not necessarily energetically viable for all combinations of depositants and substrates. In some cases bond formation between the depositant species and the substrate surface molecules are not thermodynamically viable given the deposition conditions. Conversely, in some cases there is no potential energy barrier between the physiosorped and chemisorped states. In this case the adsorped species will immediately form the more energetically favourable chemical bond with the substrate.

The utilisation of the adsorption process can be described by the sticking coefficient, S_c. It is defined as the ratio of the incoming species that remain on the surface for the duration of the experiment relative to the total number of incoming species:

$$S_c = R_r / J_i, \tag{3.3}$$

where R_r is the reaction, or incorporation, rate and J_i the impingement flux of depositant species i.

3.2.2 Diffusion

The adsorped species are subject to thermal diffusion across the substrate surface. Diffusion allows the species to move around the surface from one adsorption site to another, which in turn allows them to find and bond to more energetically favourable

surface sites. The transition from one site to another is characterised by a potential energy barrier, E_s, which depends upon the adsorption state as is illustrated by Fig. 3.4.

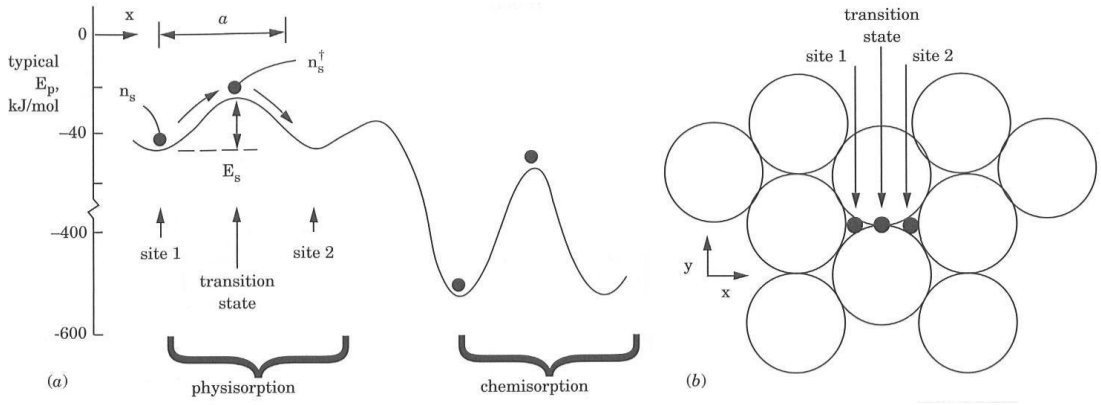

Figure 3.4: Surface diffusion: (a) potential energy vs. position x along the surface, and (b) typical adsorption sites on a surface lattice. Figure reproduced, in modified form, from [86, p. 130].

The mobility of the depositants is characterised by the diffusion length, Λ, given by Eq. 3.4.

$$\begin{aligned} \Lambda &= a\sqrt{k_s t} = 2\sqrt{D\,t} \\ D &= \frac{1}{4}\,v_{os}\,a^2\,e^{-E_s/RT} \\ &= D_0\,e^{-E_s/RT} \end{aligned} \tag{3.4}$$

In this equation a is the distance from one surface "site" to the next, k_s is the translation rate constant, t is the time, D is the diffusivity, v_{os} is a pre-exponential frequency factor which can be calculated by considering the quantum mechanics for a harmonic oscillator. R is the ideal gas constant and T the absolute temperature. As can be seen from this equation, the diffusion rate depends upon a potential energy barrier, E_s, which describes the work required to move from one surface site to another, as well as the inter-site distance, a. The diffusion length increases with higher substrate temperatures. However, as the temperature approaches a certain point the rate of desorption increases and consequently the diffusion length begins to decrease as illustrated by figure 3.5. Thus Eq. 3.4 only holds for the lower temperature burial regime.

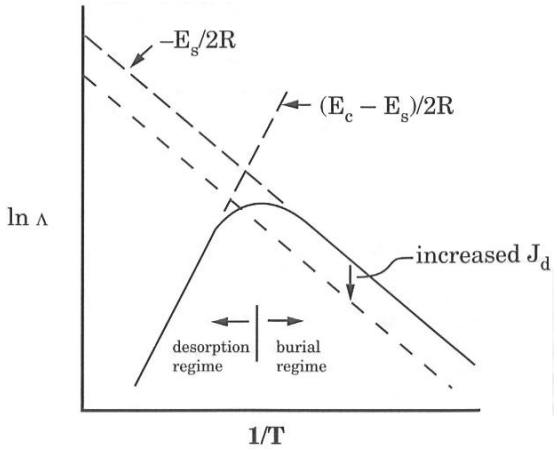

Figure 3.5: Behaviour of surface diffusion length, Λ, with substrate T. Figure reproduced from [86, p. 135].

Consequently, if a long diffusion length is desired for the deposition of a thin-film, stringent substrate temperature control is necessary. A long diffusion length ($\Lambda \gg a$) is often beneficial in growing smooth and homogeneous thin-films. Emperically it has been found that the temperature at which this benefit is highest is just below the re-evaporation temperature. In some other circumstances a negligible diffusion length ($\Lambda < a$) is desired and here cryogenic substrate temperatures will dramatically reduce the surface mobility of the depositant species. Deposition where the diffusion length is limited is called quenched growth. These two distinctly different deposition situations give rise to very different film growth characteristics as will be discussed in section 3.2.4. In the non-quenched case the initial seeding of the thin-film depends upon the balance of the surface energies involved.

3.2.3 Surface wetting and nucleation

Considerations of the relationships between the surface energies of the free surface of the depositant, γ_f, the interface beween the substrate and the film material, γ_i, and the free surface of the substrate, γ_s, allows some predictions of the seeding and growth behaviour of the film deposition process. It is important to note that the surface energies of crystalline solids are dependent upon the crystallographic plane along which the surface is formed. Additional complications arise in regards to determining surface

energies of curved surfaces.

By analogy to the interaction of fluids and surfaces, the balance between the surface energies can be expressed as a figure of merit called the wetting angle, θ. The energy balance and θ are illustrated by figure 3.6.

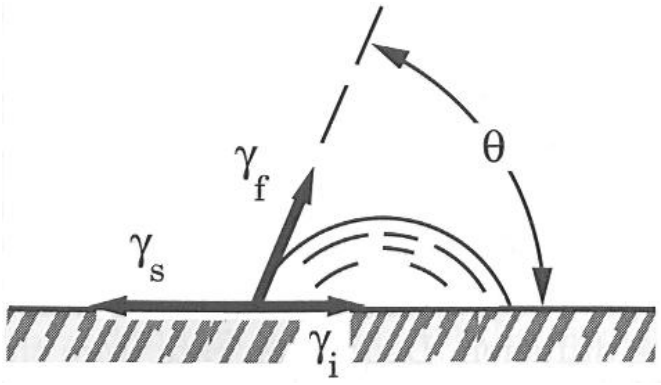

Figure 3.6: Wetting angle of a liquid nucleus. Figure reproduced from [86, p. 154].

The relationship between the surface energies and the wetting angle illustrated by figure 3.6 can be expressed by Eq. 3.5.

$$\gamma_i + \gamma_f \cos\theta = \gamma_s \tag{3.5}$$

When θ is low the material is said to wet the surface. Conversely, when the θ is high the material does not wet the surface. While the wetting angle originally described the behaviour of fluids in contact with surfaces, the wetting angle is a singular measure which characterises the balance between surface energies. Consequently, inferences about the growth behaviour during thin film deposition may be made by consideration of θ.

Growth behaviour can be categorised into two distinctly different modes and a third composite mode. These growth modes, as illustrated by figure 3.7 are:

- Frank-Van der Merwe - layer-by-layer growth
- Volmer-Weber - island growth
- Stranski-Krastanov - layer-and-island growth

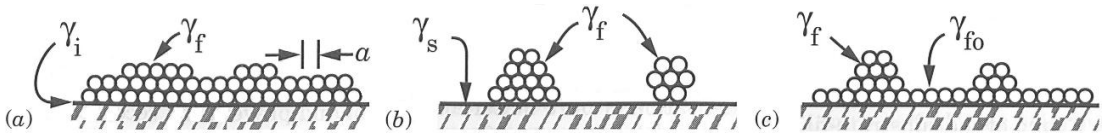

Figure 3.7: Film growth modes: (a) Frank-Van der Merwe (layer), (b) Volmer-Weber (island), and (c) Stranski-Krastanov. Figure reproduced, in modified form, from [86, p. 144].

The requirement for achieving Frank-Van der Merwe growth is that it must be energetically favourable to form both the film free surface and the film-substrate interface relative to having the free exposed substrate surface. This situation can be expressed as an inequality as shown in Eq. 3.6.

$$\gamma_f + \gamma_i < \gamma_s \tag{3.6}$$

By substitution Eq. 3.6 into Eq. 3.5 it can be shown that the inequality is only satisfied when the wetting angle is equal to zero, i.e. the material completely wets the surface.

The Volmer-Weber growth mode occurs when it is thermodynamically favourable to form a free surface of the depositant material as well as a free surface of the substrate rather than just forming an interface between the two. In this case the film material is not wetting (i.e. $\theta = 180°$) the surface and a surface energy relation describing this condition is shown in Eq. 3.7.

$$\gamma_i > \gamma_f + \gamma_s \tag{3.7}$$

The Stranski-Krastanov growth mode is characterised by the initial formation of layered structures, but as the film increases in thickness the growth characteristics, to some extent, tend towards the formation of islands. This mode can be considered as an intermediate growth mode.

The character of the initial interaction between the depositant species and the substrate strongly depends upon the wetting characteristics described above. When wetting of the surface occurs, direct bonding between the depositant and substrate is possible and diffusion will allow depositant species to travel to the most favourable growth sites. The kinetics of this situation is described by 2D nucleation. If, on the other hand, the

film-substrate interaction is characterised by poor surface wetting, that is the Volmer-Weber growth mode is dominant, 3D nucleation will dictate the initial seeding of the film layer. In this case, once seed sites have been established the film will grow from these sites and the completion of the seed layer can be described by the 2D nucleation kinetics as depending upon seed site distribution and film mono-layer coverage.

3D nucleation is the formation of a stable nucleus of the depositant material with contributions from both the vapour phase and diffusing surface particles. Figure 3.8(left) illustrates the in- and out-fluxes of material contributing to the formation of a 3D nucleus as well as the surface areas and energies involved, assuming an isotropic γ_f. In the non-wetting case the area of the depositant-substrate interface, A_i, may be considered small and the geometry of the nucleus can be assumed to be spherical with radius r.

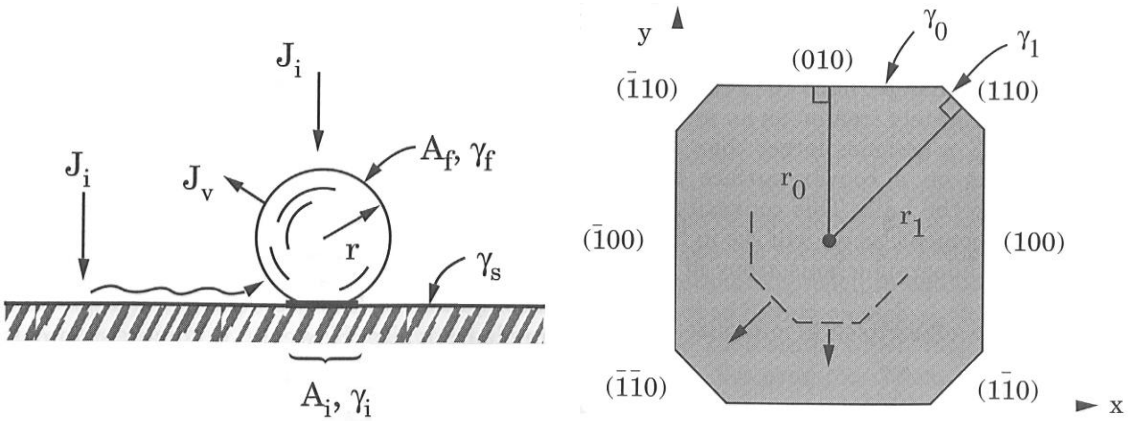

Figure 3.8: Left: Geometry of condensate nucleus formation on nonwetting substrate. Right: Wulff construction for a needle crystallite oriented along the z axis (perpendicular to the paper). Figures reproduced, in modified form, from [86, pp. 146 & 152].

The change in the Gibbs free energy, ΔG, associated with the formation of a 3D seed nucleus of radius, r, surface area A_f and volume, V, is given by Eq. 3.8.

$$\Delta G = -(\mu_v - \mu_c)\frac{V}{V_{mc}} + \gamma_f A_f = -RT \ln\left(\frac{p}{p_v}\right)\frac{[4/3]\,\pi r^3}{V_{mc}} + \gamma_f\, 4\pi r^2 \tag{3.8}$$

In this equation μ_v and μ_c are the chemical potentials of the vapour and condensate phases and V_{mc} is the molar volume of the condensate. p_v and p are the vapour

pressure of the depositant and the partial pressure of the depositant in the vapour phase respectively. By consideration of this equation it can be seen that there will be a local maximum in ΔG as r increases. This means that there is some critical radius, r^*, under which the nucleus will be thermodynamically unstable. This critical radius is found by setting $d(\Delta G)/dr$ equal to zero and yields the expression shown in Eq. 3.9.

$$r^* = \frac{2\gamma_f}{\left[\frac{RT}{V_{mc}} \ln\left(\frac{p}{p_v}\right)\right]} \tag{3.9}$$

Inserting this result into Eq. 3.8 yields an expression for the critical energy, required to form a stable nucleus, as shown in Eq. 3.10.

$$\Delta G^* = \frac{(16/3)\pi\gamma_f^3}{[\frac{RT}{V_{mc}} \ln\left(\frac{p}{p_v}\right)]^2} \tag{3.10}$$

For crystalline solids, γ_f will exhibit at least some degree of anisotropy. It is possible to predict the nucleation shape in these circumstances by considering the lattice structure as well as the energies of the individual crystal planes. The Wulff theorem states that for a crystalline nucleus, for which the surface energy is minimised, the relation given by Eq. 3.11 will hold for all crystal planes.

$$\gamma_k/r_k = constant, \tag{3.11}$$

where γ_k is the surface energy of the k-th crystal plane and r_k is the distance from the centre of the nucleus to the k-th crystal plane. With this relationship it is possible to construct the 3D shape of a cystalline nucleus of a given volume provided that the surface energies of the different crystal planes are known. A 2D example of a Wulff construction with $\gamma_1 = 1.2\gamma_0$ is shown in figure 3.8(right).

Once seed sites have been established upon the substrate, either through chemical bonding between depositant and substrate or through the formation of stable 3D nuclei, the initial film layer will grow and fill out the substrate surface. This planar expansion can be predicted through requirements for the minimisation of the free energy, similar to those that dictated the initial film seeding. Provided that the diffusion length is large, depositant species will preferentially attach to the already existing structure at the energetically favourable positions. Analogous to the surface energy of a 3D geometry,

in the 2D case it is the edge energy, β, which is minimised. While these mechanisms may favour the formation of smooth film layers, in some cases, depending upon the deposition conditions, the result can be the formation of intricate three dimensional structures [87].

Fig. 3.9 illustrates the 2D planar geometry of the layer formation process. The denoted kink site is the preferable growth site since the edge length remains constant. Generally, the more neighbouring atoms a growth site has the lower the edge energy.

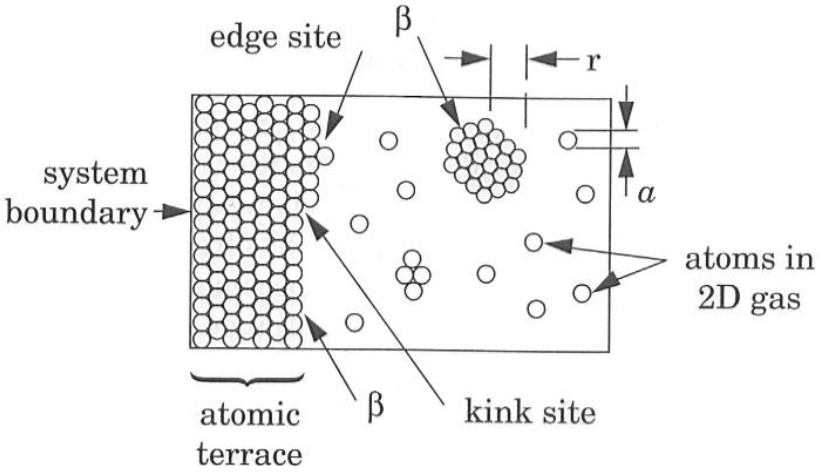

Figure 3.9: Geometry of 2D nucleation, looking down at the surface. Figure reproduced from [86, p. 155].

Analogous to the case of 3D nucleation, a critical nucleus radius, at which the transport to-and-from the nucleus balances out, can be expressed for the 2D case, as shown in Eq. 3.12.

$$r^* = \frac{\beta}{a\,\frac{RT}{V_{mc}}\ln\left(\frac{n_s}{n_v}\right)} \tag{3.12}$$

Here a denotes the size of the "atomic step", or inter-site distance, n_s and n_v are the 2D saturation and actual vapour concentrations on the surface.

3.2.4 Film structure growth

Once a complete film coverage of the substrate surface has been achieved the bulk film structure will begin to develop. The kinetics of this growth phase is strongly dependent

upon the ratio of substrate temperature, T_s, to melting point, T_m, of the film material. Three distinct growth regimes, or structural zones have been identified. These zones, characterised by increasing T_s/T_m are denoted Z1, Z2 and Z3. An intermediate transitional zone, ZT, located between Z1 and Z2, has been identified for energy enhanced deposition processes. These structural zones are illustrated by Fig. 3.10.

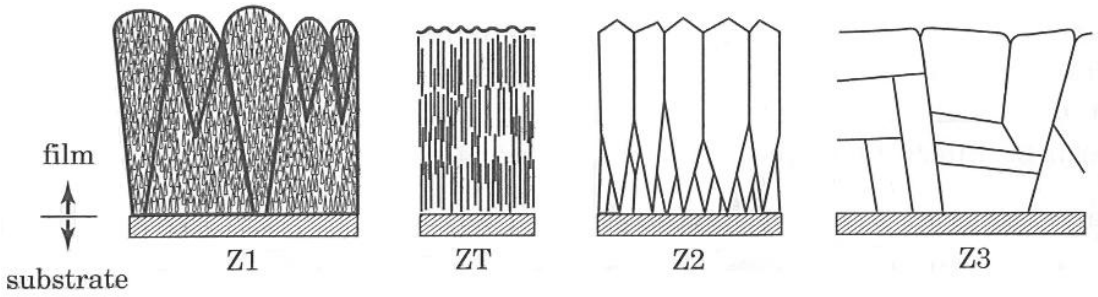

Figure 3.10: Characteristics of the four basic structural zones and of whiskers, in cross section. The ratio of substrate T to film melting T (T_s/T_m) increases in the direction Z1→ZT→Z2→Z3. Figure reproduced, in modified form, from [86, p. 160].

Quenched growth

The Z1 structural zone is characterised by short diffusion lengths ($\Lambda < a$) and is also referred to as quenched growth. This can be achieved by keeping the substrate temperature low, thereby dramatically reducing the diffusion length. As a result the thermodynamical properties of the materials have less influence upon the structural development. In this case the transport characteristics (kinetic energy, angular and arrival distribution) of the incoming species are the dominating factors in determining how the structure of the film evolves. However, even for a completely uniform arrival distribution with low kinetic energies at normal incidence, significant surface roughness will occur with increasing film thickness due to statistical variation. This is illustrated by Fig. 3.11.

Fig. 3.11 is generated by considering a steady rate of arrival at normal incidence across a linear array of evenly spaced seed sites. The adatoms are required to stick wherever they land, whether on-top of a pillar or bottom of a trench. The landing site is chosen arbitrarily for each of the arriving adatoms to illustrate the statistical variation within

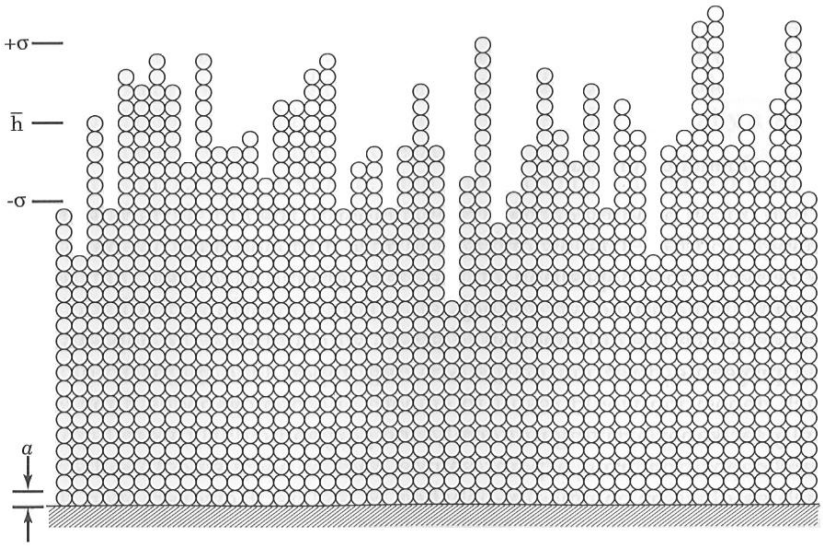

Figure 3.11: Statistical roughening in random ballistic deposition of a 25-atom-thick film. (Pascal solution courtesy of Jared Smith-Mickelson.) Figure reproduced from [p. 162][86].

incident vapour flux. No lateral interactions or boundary conditions between seed sites are allowed and a vertical collumnar packing geometry is assumed. In the figure $\bar{h}$ denotes the average film thickness and σ the standard deviation around $\bar{h}$. σ is an expression of the film surface roughness and is equivalent to the RMS surface roughness when $\bar{h}$ is used as the zero-plane reference. Eq. 3.13 shows the relationship between σ and $\bar{h}$ for the situation illustrated by Fig. 3.11.

$$\frac{\sigma}{a} = \left(\frac{\bar{h}}{a}\right)^{\beta} \tag{3.13}$$

In this equation the growth exponent β depends upon the assumptions behind the model. For the case illustrated by Fig. 3.11 β is equal to $\frac{1}{2}$. By applying the condition that pillar heights can only vary by $\pm a$ between neighbours, β becomes $\frac{1}{3}$ in the 2D case and $\frac{1}{4}$ in the 3D case. However, these models do not take void formation into account and experimental results for Z1 growth indicate a growth exponent of $\frac{3}{4}$ [88, 89].

The situation illustrated by figure 3.11 only shows the variation due to purely statistical factors given a completely homogeneous arrival distribution at normal incidence. Further complications due to various geometrical considerations may also arise as illustrated by figure 3.12.

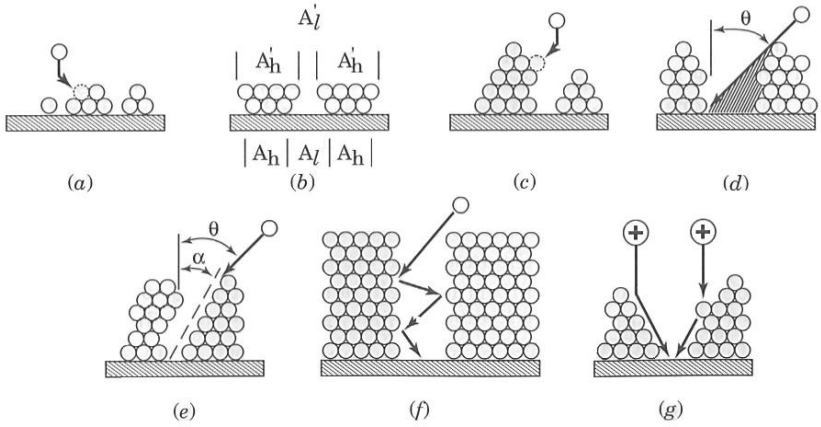

Figure 3.12: Atomistic processes in quenched-growth structure development: (a) ballistic aggregation, (b) finite-size effect, (c) sideways attraction, (d) oblique shadowing, (e) tilt effect, (f) low sticking coefficient, (g) void-filling by energetic particles due to enhanced mobility (left) and forward sputtering (right). Figure reproduced, in modified form, from [86, p. 164].

The structural transition zone

It is possible to affect the internal composition of the thin film, both during and following the deposition process. Post-deposition processing for modifying film morphology will be given brief consideration in section 3.3.1.

Internal reconfiguration during the film deposition itself can be induced either through bombardment of energetic species or through thermally activated growth. The ZT structural zone may be achieved through the combination of quenched diffusion and energy enhanced particle bombardment, either in the form of additional ions or depositant species with high kinetic energy. Fig. 3.13 shows 2D simulations of molecular-dynamics for deposition using energy enhanced species. As can be seen the presence of internal voids decreases as the ratio of kinetic energy, E_t, of the incoming particles relative to the binding energy, E_c, of the depositant increases.

Thermally activated growth

Thermally activated growth, which results in the Z2 structural zone, occurs at temperatures where the diffusion length, Λ, is larger than the distance between growth sites,

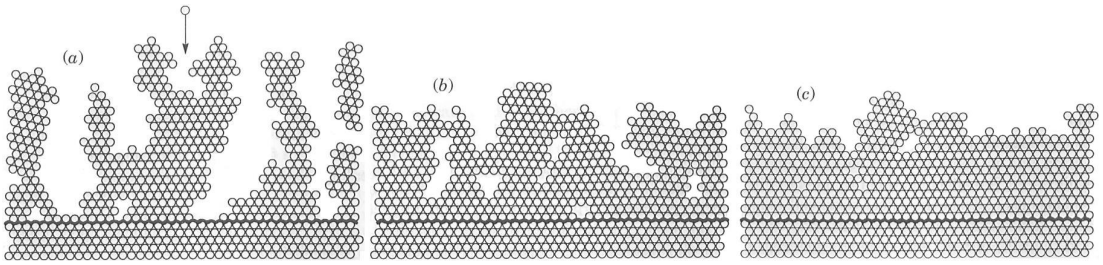

Figure 3.13: Two-dimensional molecular-dynamics simulation of the deposition of energetic atoms impinging perpendicularly onto a substrate held at 0 K. The horizontal line is the substrate interface. Normalized impinging energy E_t/E_c, as defined in text, is (a) 0.02, (b) 0.5, and (c) 1.5. (Source: Reprinted from Ref. 19 by permission.) Figure reproduced, in modified form, from [86, p. 168].

a. Growth like this is characteristic of the structural growth zone Z2 as shown in figure 3.10. In this case the depositant species have enough surface mobility during deposition to reach and occupy the energetically favourable growth sites that could form the basis for a bulk vacancy in a quenched growth situation. Figure 3.14 shows 2D simulations of film formation at varying temperatures for depositant species with a low kinetic energy and an impact angle of 30° relative to the normal. The higher mobility at elevated temperatures signifcantly reduces the presence of bulk film vacancies. Emperically the transition temperature, where such thermally activated growth is observed, occurs at approximately $T_s = 0.3T_m$.

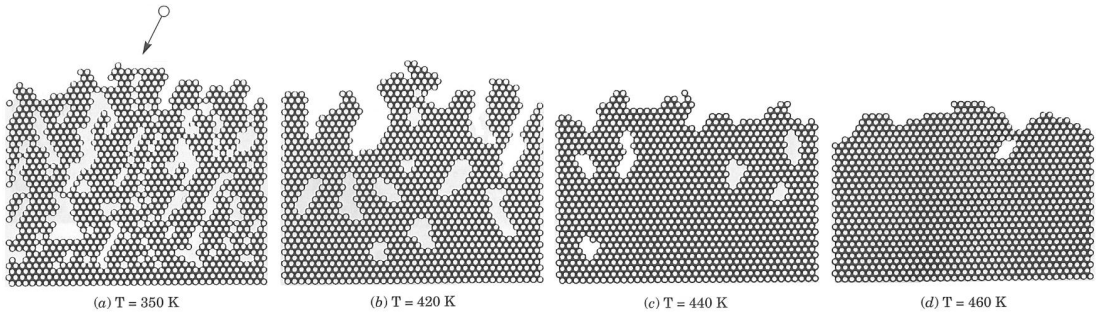

Figure 3.14: Two-dimensional computer simulation of the effect of substrate T on void filling by surface diffusion. (Source: Reprinted from Ref. 22 by permission.) Figure reproduced, in modified form, from [86, p. 171].

Due to surface energy considerations at grain boundaries grooves will develop along these boundaries as illustrated by figure 3.15. Such grooves will be produced during annealing as well, which is why this phenomenon is also known as thermal grooving.

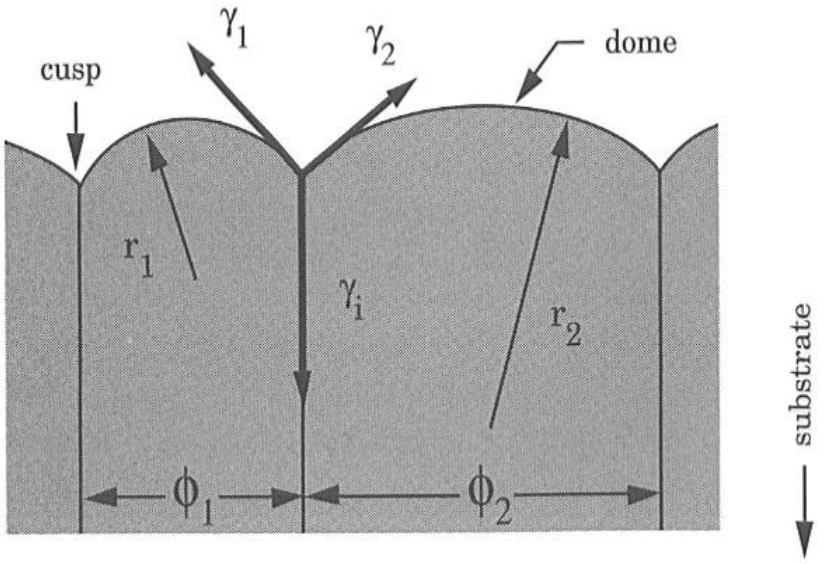

Figure 3.15: Geometry and surface energetics of columnar grain growth. Figure reproduced from [86, p. 174].

From considerations of surface and interfacial energies it can be shown that lateral growth of grains will favour the transport of material from small towards large grains. This is illustrated by figure 3.16. If the radius of the smaller central grain shrinks by dr the decrease in interface length of the small grain is equal to $2\pi dr$ while the boundary increase of the three surrounding grains is only $3dr$, yielding a net decrease in grain boundary length and consequently the associated boundary energy.

The Z3 structural zone is only observed in certain instances and typically will only occur when $T_s/T_m >\sim 0.5$. In the Z3 zone the film undergoes bulk annealing during the deposition which may yield smoother surfaces in some cases. However, deeper grooves tend to form at grain boundaries resulting in smooth grain surfaces separated by deep trenches.

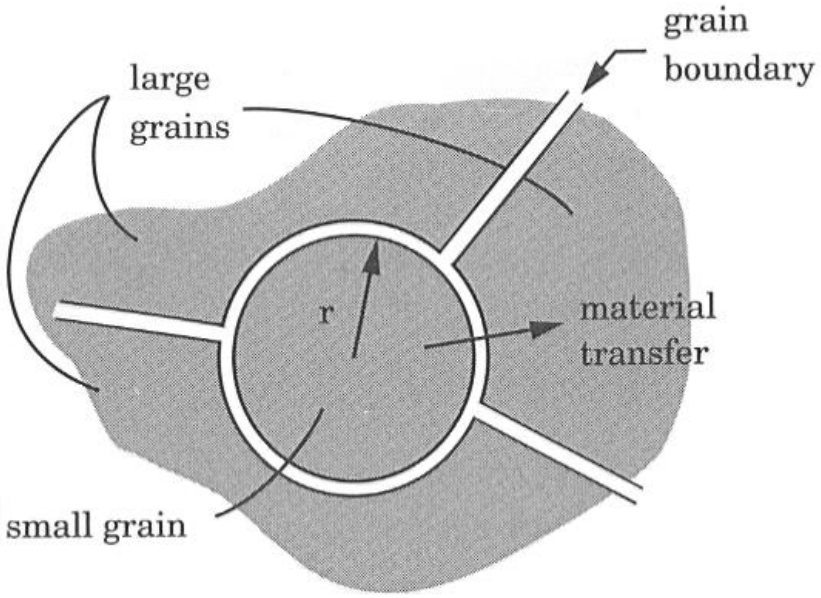

Figure 3.16: Film section parallel to the substrate showing how lateral grain growth occurs. Figure reproduced from [86, p. 176].

Summary

In short, it is possible to distinguish between two different types of surface roughness inducing mechanisms during the structural development of the film: a thermodynamical and a statistical driven mechanism. As a result it is only possible to grow truly smooth thin-films when three conditions are met: 1) the thermodynamic characteristics of the deposition process must favour a smooth film, 2) the diffusion length of the depositant species must be high enough that migration to the favoured growth sites is possible and 3) the arrival rate must be low enough that statistical self-shadowing effects do not degrade the structural development.

3.3 Deposition of smooth thin films

This section deals with the deposition of thin films with low surface roughness. First it provides a quick overview of the current state-of-the-art of the field. Then follows an overview regarding the specific deposition of stacks consisting of alternating layers of silver and dielectric materials. This includes an outline of the fundamental issues

surrounding such an endeavour based upon the theoretical considerations provided in section 3.2. Finally there is presentation of the thin-film deposition technologies available at the UCNFL, including their capabilities and limitations.

3.3.1 State-of-the-art

When trying to achieve smooth, i.e. low surface roughness, thin-films there are a number of approaches available. At one end of the spectrum is molecular beam epitaxy (MBE) where precise control of deposition parameters and lattice matching allows for epitaxial growth of compound materials. At the other end are inherently rough films subjected to post-deposition processes to try and reduce surface roughness.

MBE is basically an advanced thermal evaporation PVD process [90]. However, by using Knudsen effusion cells in an ultra high vacuum it is possible to achieve a very low rate of deposition while still retaining high purity [86]. Through stringent substrate temperature control and lattice-matching of substrate and depositant material, it is possible to achieve epitaxial growth of mono-crystalline compound materials. Formation of ultra-smooth (RMS surface roughness $\sim$0.2 nm) epitaxial films has been reported for a wide range of material combinations, e.g. GaAsBi on Zn-doped (001) GaAs substrates [91], MgO on graphene [92] and GaAs homoepitaxy [93].

Non epitaxial deposition of thin films with very smooth interfaces is also achievable when good matching of depositant and substrate material is ensured. The formation of Mo/Si-stacks for extreme ultraviolet (EUV) reflectors by either sputtering [94] or electron beam evaporation [95] is one such combination that has garnered a lot of interest due to the lithography industry pushing the EUV technology. The reflectivity of EUV mirrors based upon Mo/Si multilayers have been shown to have significant dependence on interfacial surface roughness [96]. Very low interfacial surface roughness (0.06-0.10 nm RMS) for these stacks can be achieved, although the interfacial roughness is observed to increase as the number of layers increases past 30 [96]. Ion assisted deposition has been shown to be of considerable benefit in depositing such multilayers, especially when depositing the critical film onto a rough (>0.3 nm RMS) substrate [96, 97]. Other material combinations for multi-layered stacks with smooth interfaces have also been demonstrated. A couple of examples are: the growth of Nb/Si stacks

to evaluate the impact of various process parameters upon interface characteristics [98] and the growth of alternating layers of cubic boron nitride and hexagonal boron nitride for surface coatings (RMS surface roughness 0.1-0.125 nm) [99].

Promotion of the wetting characteristics between the substrate and depositant species is another method of improving thin-films smoothness. This may be achieved through the introduction of an intermediate wetting layer. An example is an intermediate titanium layer to increase the adhesion of gold onto dielectric surfaces, an approach often applied in preparing insulating samples for SEM. Logeeswaran et al. [100, 101] have reported an improvement in surface roughness from ∼10 nm RMS, for a film deposited without wetting layer, to ∼0.7 nm RMS for a 15 nm thick silver film deposited on a ∼1-2 nm thick germanium wetting layer. Both films were deposited using electron beam evaporation and subsequently analysed through AFM across a 1x1 μm^2 area.

Fabrication of metal-dielectric stacks with silver layers exhibiting very low surface roughness (0.3 nm RMS, 20 nm thickness) has been demonstrated [102]. These films were fabricated by sputtering of silver onto spin-coated layers of glassy amorphous polycarbonate (0.2 nm RMS, 95 nm thick) and are the smoothest silver films reported to date. The stacks in this investigation were used as planar lenses in a near-field scanning optical microscope, using an argon-line illumination source operating at 488 nm. In this regard it should be noted that polycarbonates typically exhibit poor transmission in the UV-range with wavelengths shorter than 400 nm.

As mentioned briefly in section 3.2.4, in situ ion bombardment of the deposition surface is another mechanism for reducing surface roughness as well as achieving denser films. The impact of this technique depends upon both the kinetic energy of the impinging ions and the incident angle as has been reported for Mo/Si multilayer systems [97]. However, most thin-film deposition equipment does not feature ion assisted deposition. A less controllable, but more easily achieved, method of ion-bombardment can be realised by partially immersing the deposition substrate into the plasma discharge during an AC plasma deposition process.

There are various post-deposition processes available that may alter the properties of a thin-film. A well-known technique in this category is annealing. Through controlled heating and cooling of a material it is possible for the material to undergo internal reconfiguration. Other techniques include chemical-mechanical polishing, template-stripping, etching and pressure-induced surface deformation, which can be applied to reduce the surface roughness of an existing thin-film through direct physical manipulation of the film topography [80, 103].

3.3.2 Deposition of smooth silver-dielectric stacks

As covered in Chapter 2, superlenses require a smooth metal-dielectric interface to sustain the surface plasmon polaritons that drives the superlensing effect. Furthermore, the layers that make up the metal-dielectric stack, that is the superlens, needs to be thin enough that the plasmonic oscillation at one interface is close enough to the next interface to allow the signal to cascade through the lens stack.

Thus, the fabricational challenge in making a good superlens is the ability to form stacks consisting of alternating layers of metals and dielectrics, where layers are required to be thin and have low surface roughness. Furthermore, the wavelength of the illumination source used for lithographical exposure must be attuned to the plasmon frequency of the metal.

In the case of the mercury lamp I-line, emitting at a wavelength of 365.7 nm, silver is a good match, having a bulk plasmonic frequency around 360 nm. For the dielectric layers, choosing a material with a low absorption coefficient at this wavelength is important. The transmission coefficients for dielectrics vary substantially, it is not uncommon for the transmission coefficients of polymers to drop off in the UV spectrum, typically between 400 and 250 nm, whereas dielectrics such as silicon dioxide exhibits high transparency at wavelengths above 160 nm. To minimise losses within the lens system the dielectric material must be chosen with these considerations in mind.

Fundamental complications

As discussed in section 3.2, the ability of a thin-film material to form smooth layers is dependent upon the interaction with the substrate material. In the ideal situation the

thermodynamics will favour the Frank-Van der Merwe growth mode while retaining high diffusion mobility. Alas, in the case of a silver-dielectric interface the combination of two materials that have very differing characteristics suggests, qualitatively, that the mechanisms dominating the formation of the film will be the Volmer-Weber growth mode due to weak metal-insulator interaction [104]. In this growth mode weak depositant-substrate interactions and 3D nucleation will characterise the seeding of the layer. Due to the low adsorption energy the diffusion length is expected to be large during the seeding of the film unless cryogenic substrate temperatures are applied. Considering the diffusion length as given by Eq. 3.4 given $v_{os}) = 10^{13}$ s^{-1}, $a = 2.05$ Åand a representative diffusion energy barrier $E_s = 20$ kJ/mol the diffusion length for a physisorped adatom at $T = 300$ K would for $t = 1$ s be in the order of 10 μm.

The critical nucleation radius, given by Eq. 3.9, can be calculated provided the surface energy, vapour pressure and molar volume of the depositant are known. Skriver et al. [105, 106] presented the surface energies for most elemental metals, both through solid-state theoretical calculations depending upon crystallographic orientation and experimental values. The values reported for silver is presented in table 3.1. The vapour pressure can be described by Eq. 3.14.

$$\log P = A - \frac{B}{T} \tag{3.14}$$

The coefficients A and B, for silver, are presented in table 3.1 as reported by Geiger et al. [107]. The molar volume, V_{mc}, for silver can be calculated from the molar mass, M, and density, ρ, of silver in the solid phase as shown in table 3.1. By inserting the values presented in this table into Eq. 3.9 it is possible to calculate the critical nucleation radius, r^*, for silver for a given combination of pressure, p, and temperature, T. Given a vacuum pressure of 4×10^{-3} mBar, r^* is equal to 3.8 Å at 300 K, for the same pressure r^* is equal to 1 nm at 560 K and 10 nm at 1096 K. For a vacuum pressure of 3×10^{-6} mBar, r^* becomes 4.2 Å at 300 K and is equal to 1 nm at 495 K and 10 nm at 872 K. Fig. 3.17 plots the critical nucleation radius for silver against temperature at various pressures. Considering that silver has a crystallographic lattice constant of 4.090 Å, the critical nucleation radius at 300 K indicate that the minimum grain seed size will not be limited by thermodynamical considerations.

Parameter	Value
ρ_{solid}	10,490 kg/m^3
ρ_{liquid}	9,320 kg/m^3
Molar weight, M	107.8682 g/mol
$V_{mc} = M/\rho_{solid}$	1.0283×10^{-5} m^3/mol
T_m (1 atm.)	1234.93 K
T_b (1 atm.)	2435 K
A	5.4870
B	13342
Crystal structure	fcc
Lattice constant, a	4.090 Å
Atomic radius	144 pm
γ_{100}	1.200 J/m^2
γ_{110}	1.238 J/m^2
γ_{111}	1.172 J/m^2
γ_{exp}	1.246-1.250 J/m^2

Table 3.1: Material parameters for silver.

Once a significant amount of depositant material has been deposited and the coverage of the substrate increases a significant drop in diffusion length would be expected. This drop would be due to the much higher metallic bonding energy between silver atoms compared to the silver-dielectric van Der Waal's bonding. For a representative diffusion energy barrier, for a chemisorped species, of 200 kJ/mol [86], the diffusion length is found to be in ther order of 10^{-20} m/s$^{1/2}$ at 300 K. As such the diffusion length during the structural growth stage can be considered negligible and the growth can be considered quenched. Consequently Z1 structural zone morphology is expected for films grown through thermal evaporation. For films deposited through RF magnetron sputtering, the enhanced kinetic energy of the depositant species should result in morphology characteristic of the ZT structural zone.

For films with Z1 morphology a statistical figure for surface roughness can be expressed as a function of film thickness as shown in Eq. 3.13. The crystal structure of bulk silver is face-centered-cubic with a lattice constant, α, of 4.090 Å. Depending upon crystallographic orientation the inter-plane spacings for the [100], [110] and [111] planes are

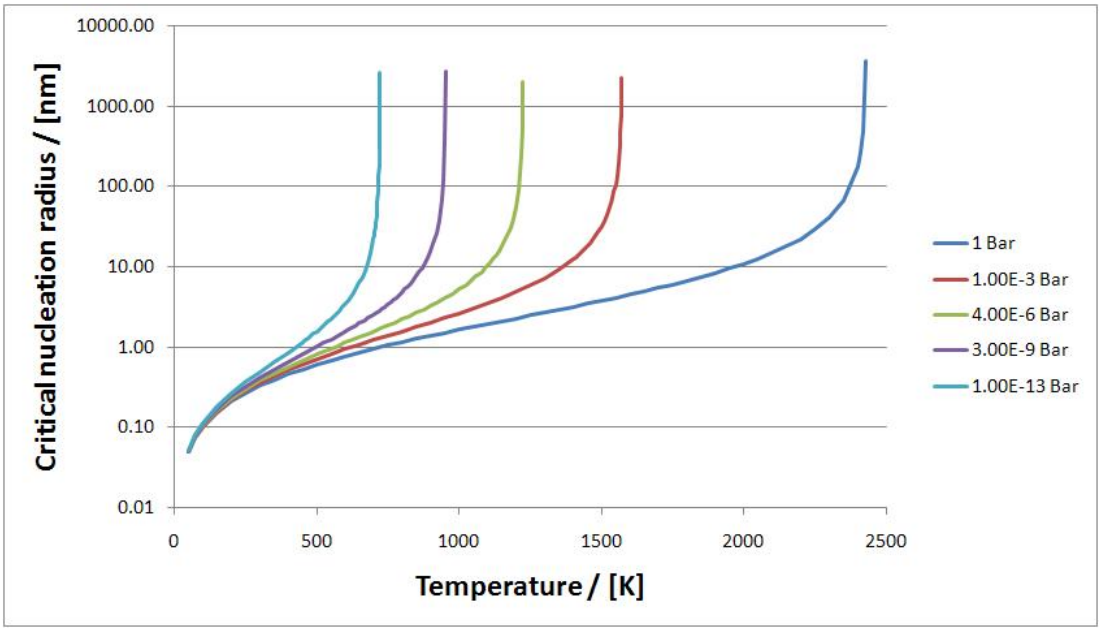

Figure 3.17: Plot of the critical nucleation radius for silver against temperature at various pressures. Calculated from Eq. 3.9 using the data presented in table 3.1.

$\frac{1}{2}\alpha$, $\frac{1}{\sqrt{2}}\alpha$ and $\frac{1}{\sqrt{3}}\alpha$ respectively. Thus, the minimum surface roughness figure, relevant to quenched growth of thin silver films, is obtained by setting a in Eq. 3.13 equal to $\frac{1}{2}\alpha$. As discussed in 3.2.4 a value of 0.75 for β has been shown to be characteristic of experiments in groing Z1 films.

As illustrated by Fig. 3.13, the kinetic energy imparted by sputtered species will produce a ZT morphology with reduced surface roughness compared to Z1 morphology. Consequently, films deposited through RF magnetron sputtering may potentially exhibit lower surface roughness than dictated by the statistical limit discussed above. Species produced by thermal evaporation typically have kinetic energies <0.1 eV compared to 5 eV for plasma sputtering generated species.

Deposition technologies at UCNFL

In regards to this project, silver thin-film deposition was limited to two PVD processes: thermal evaporation and RF magnetron sputtering. The experiments were undertaken in the laboratories at the Department of Electrical and Computer Engineering at the

University of Canterbury, Christchurch, New Zealand. Prior experiences at this laboratory had already identified thermal evaporation and RF sputtering as the most viable approaches to depositing smooth silver films [20, 108, 109]. DC sputtering and electron beam evaporation deposition were also available but were known to produce silver thin-films of inferior quality.

For thermal evaporation the Balzers thermal evaporator, shown in Fig. 3.18, was used. Ceramically coated tantalum evaporation boats were used to contain the silver evaporant. The source material used for thermal evaporation were 6 mm silver pellets with a purity of 99.99% from Goodfellow, Cambridge, UK. The deposition rate, determined by the energy input to the evaporation boat, was controlled by an analog potentiometer. Deposition thicknesses were estimated by tuning a frequency generator to match the frequency of the quartz microbalance and then correlate the change in frequency, Δf, of the beat signal measured during the deposition process with the height by consideration of data obtained from prior experiments. Shutter control was done manually. Samples were mounted in a sample holder mounted in the top of the chamber, with samples facing downwards.

Magnetron sputtering was performed using the Edwards Auto 500 deposition system shown in Fig. 3.19(left). The system at UCNFL features three different deposition sources: an RF magnetron source, a DC magnetron source and an electron beam evaporation source. The RF magnetron source was chosen for silver deposition. A 3" sputtering target, with a silver purity of 99.99%, from Kurt J. Lesker Company, Pittsburg, PA, USA, was used for the magnetron sputtering deposition. Sputtering was facilitated by an argon plasma generated at a frequency of 13.56 MHz. Samples were mounted to a sample holder using silver tape and the sample holder placed face-down in the top of the deposition chamber. Experiments were conducted using both rotating and stationary sample holders. In the stationary case the sample was mounted directly above the RF magnetron source. In the rotating case the holder would rotate steadily throughout the deposition process, resulting in a homogeneous deposition profile for all samples mounted at a given radius. The rotational frequency, 1.2 Hz, can be considered high relative to the duration of even the shortest thin-film deposition runs conducted in this investigation. Film thickness during deposition was monitored using a quartz

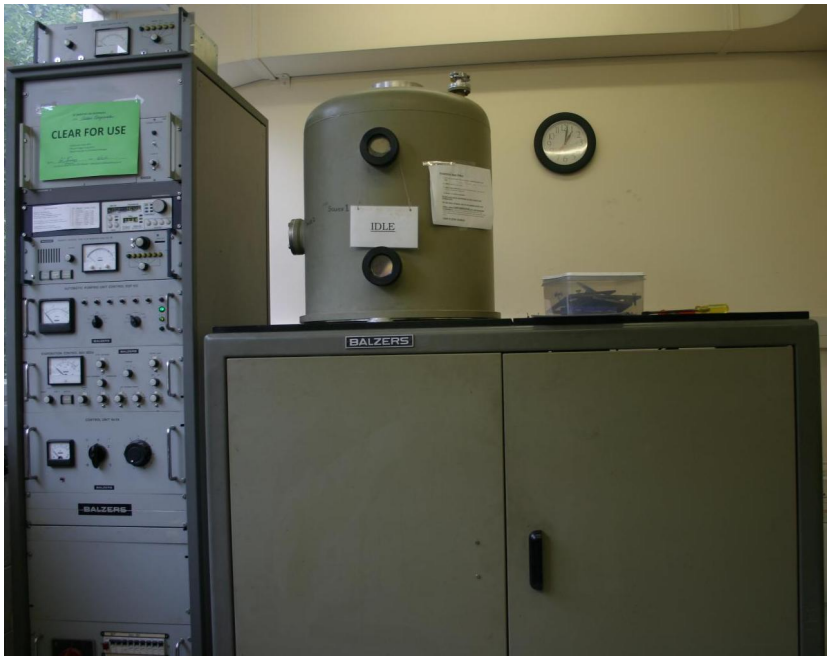

Figure 3.18: The Balzers thermal evaporation system.

microbalance connected to a digital shutter control box. If so desired a manual shutter override could be used instead.

Both deposition systems suffered from two common issues that complicated deposition experiments. The layout of the deposition chambers meant that shutters shut off the sources rather than the deposition substrates. Consequently it is not possible to measure the deposition rate prior to initiating the deposition run itself. Further, neither system were equipped with a rate-power feedback controller to automatically adjust the deposition rate to a desired preset. Thus, significant variations in deposition rate during the experiment may occur. Even more problematic, the lack of data logging of the deposition rate during the run means that it is very difficult (and here very difficult implies impossible) to precisely record and quantify the deposition rate for a given deposition run. Consequently it is only possible to measure the deposition time and the resulting film thickness and then calculate the average deposition rate for the process. Alas, this figure does not provide any insight into the potential variations in deposition rate throughout the run.

Figure 3.19: Photographs of (left) the Edwards Auto 500 magnetron sputtering and e-beam evaporation deposition system. (right) the Edwards Auto 500 control interface.

3.4 Experimental method

This section describes the deposition experiments undertaken to achieve the goals outlined in the beginning of this chapter. All experimental work was undertaken using the UCNFL facilities described above.

All silver thin-film deposition experiments was carried out using 1x1 cm^2 silicon chips with thermally grown silicon dioxide surfaces. The chips were cleaved from 4" silicon wafers using a diamond scriber. Wafers were covered in a protective layer of photoresist prior to scribing in order to reduce silicon dust contamination on the substrate surfaces. Prior to deposition all substrates were cleaned using a rinse-cycle consisting of acetone, methanol and isopropanol.

For thermal evaporation experiments the substrates were placed in the sample holder and then mounted into the deposition chamber. The thermally assisted pump-down cycle consisted of an initial 30 min pump-down while the chamber walls were being heated, followed by a 30 min cycle where the chamber walls were being cooled. During the last part of the pump-down sequence the film thickness monitor was initialised by matching the signal from the quartz microbalance with that of a frequency generator. Once a satisfactory base pressure, in the order of $5 - 9 \times 10^{-7}$ mBar, had been achieved the power was slowly ramped up to the desired setting in order to avoid thermal shocking of the evaporation boat. As the temperature of the evaporant increased the vapour pressure increased as well, as described by Eq. 3.14. Once the vapour pressure exceeded that of the deposition chamber an increase in chamber pressure was observed and evaporation began. Typical process pressures were within the range of $2 - 8 \times 10^{-6}$ mBar, which according to Eq. 3.1 yields a mean free path length of 50-200 m. Given a characteristic length scale for the system of 1 m this corresponds to a Knudsen number of 50-200 as given by Eq. 3.2. At this point the shutter was opened and the deposition took place. Once the desired Δf was reached the shutter was closed and the power turned off. Alas, deposition times and rates were not measured for the thermally evaporated samples. The vacuum pumps were then set on standby mode and once the chamber pressure reached a certain point the high-vacuum valve to the diffusion pump closed. Then the chamber was vented with nitrogen until atmospheric pressure was

reached. Once fully vented the chamber was opened and the samples removed. The control interface and deposition chamber for the Balzers thermal evaporator are shown in Fig. 3.20.

Figure 3.20: Photographs of (left) the control interface and (right) deposition chamber of the Balzers system.

For magnetron sputtering deposition the silver sputtering target was installed into the RF magnetron gun. Using silver tape, the samples were mounted on the circular sample holder a couple of centimetres from the edge. The sample holder was then fitted to the drive-axle within the deposition chamber. Two different sample holders were used and two different deposition experiments were undertaken; static and rotating. The difference in source-substrate geometry between the two sample holders is illustrated by Fig. 3.21. In the static case the sample holder was rotated to a position where the samples were situated directly above the RF magnetron source and then left in this

position for the duration of the experiment. In the rotating case the sample holder was mounted in the chamber and set to rotate at a constant speed until the thin-film deposition had been concluded. Once both target and sample were mounted in the chamber the door was sealed and the automated pump-down sequence initiated. Typical base pressures achieved in the Edwards Auto 500 system were within the range $4 - 40 \times 10^{-6}$ mBar. During the pump-down cycle the film-thickness monitor was programmed with the material parameters for the depositant, the relevant tooling factor and desired film thickness. Following the pump-down, argon gas was introduced to the chamber and a process pressure in the order of 4×10^{-3} mBar was established. At this pressure the mean free path length is in the order of 10 cm which corresponds to a Knudsen number of approximately 0.7 given a characteristic system length of 15.5 cm (as seen in Fig. 3.21). Then the plasma would be ignited, with the power supply set at the desired power. Power figures between 15 and 100 W were used in these experiments yielding deposition rates between 0.3 and 7 Å/s depending upon sample holder and whether the holder was rotating or stationary. A 5 min cleaning cycle of the target was performed prior to initiating the deposition run by starting the shutter control. Once the film reached the desired thickness, as measured by the film thickness monitor, the shutter was closed automatically. Then the power and argon supply was turned off and a short pump-down cycle was performed to empty the chamber. Finally the venting cycle was initiated and the samples removed from the chamber.

A few experiments were conducted to investigate whether reductions in surface roughness of the silver films could be achieved by introducing a germanium wetting layer between substrate and silver film. These were conducted using the Edwards Auto 500 deposition system, using the electron beam (EB) evaporation source to deposit the germanium layer and then RF magnetron sputtering to deposit the silver film. The large sample holder was used in rotating mode for these experiments in order to ensure homogeneous deposition during both deposition processes. Deposition of germanium through use of EB evaporation was characterised and the tooling factor established. Once this process had been characterised, an initial germanium wetting layer with an expected thickness of 10 nm was deposited followed by the deposition of an approximately 30 nm thick film of silver.

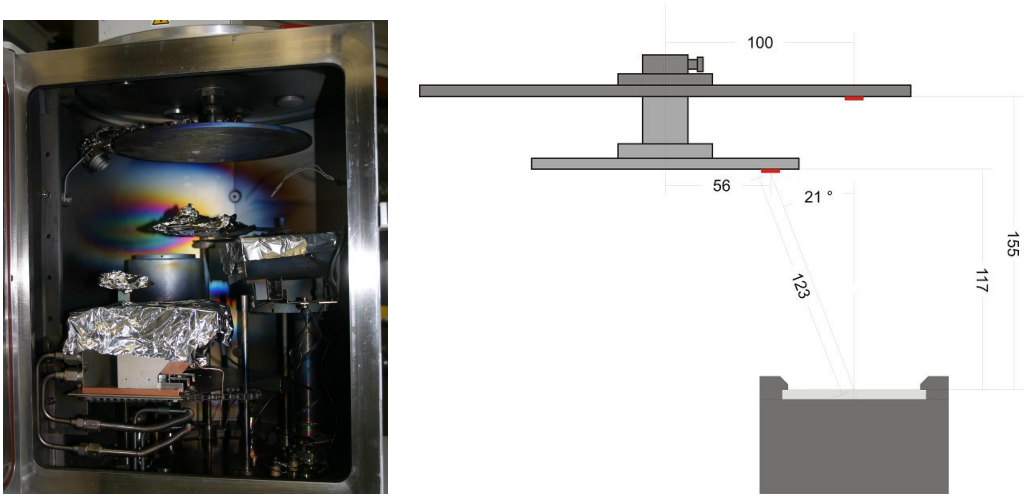

Figure 3.21: Left: The deposition chamber of the Edwards Auto 500. Right: Schematic overview of the source-sample geometry for magnetron deposition with dimensions in mm. The two different sample holders, large and small, are displayed in dark and light grey respectively. The red rectangle indicates the position of the substrate on either holder.

Following the thin-film deposition the samples were analysed using AFM. Experience gained through the early thermal evaporation experiments indicated that the film surfaces degraded over time, resulting in increased surface roughness. The mechanism behind this film degradation is not clear, however, it is known that silver will tarnish upon contact with either air or water containing either ozone or hydrogen sulfide. Experimental procedures were therefore changed during the RF magnetron experiments. For these experiments the samples were analysed immediately upon removal from the deposition chamber, unlike what was the case for the thermal evaporation samples where several samples were deposited inside a short time frame and subsequently analysed over the course of the following week.

Surface analysis was carried out using a Digital Instruments Nanoscope Dimension 3100 atomic force microscope operated in tapping mode. NCS11(B) AFM tips (μmasch, Tallinn, Estonia) were used for post-deposition surface characterisation. The tips were n-type silicon probes with typical tip radii of 10 nm and full cone angles of 40°. The analysis procedure used was as follows: 1) scan size was set to zero and the z-axis limit set to the minimum to increase vertical resolution, 2) the tip was brough into contact

the surface, 2) the integral and proportional gains were kept at very low values (∼0.01) and only increased as high as absolutely necessary to properly maintain the correlation between trace and re-trace curves, 3) the scan-size was then gradually increased in increments from 0 nm to 500 nm while the z-axis data range was increased as necessary to continually monitor the scan quality, 4) scans with a resolution of 256x256 pixels were recorded for scan sizes of 500x500 nm^2 and 1x1 μm^2, 5) film thickness was measured by recording 2x2 μm^2 AFM maps across the edge of trenches scratched into the silver film using the tip of a tweezer.

The AFM surface maps obtained in this manner were subjected to a post-processing procedure consisting of a 1st order X-Y-planefit and a 1st order flattening as performed by the Digital Instruments Nanoscope software V5.31r1. The RMS surface roughness was then measured across the entire sample unless significant surface features, e.g. dust particles, were present. In the case of such features, as large an area as possible, excluding the relevant feature, was used to calculate the surface roughness. The film thickness was measured from the 2x2 μm^2 maps through use of the Nanoscope program's step-height function.

3.5 Experimental results

The results on thin silver film deposition presented in this chapter were gained from the deposition of 42 films using thermal evaporation (17 depositions) and RF magnetron sputtering (25 depositions).

The thicknesses of the deposited films considered here covered the range of 10-72 nm, with thermally evaporated films having thicknesses in the range 10-45 nm and sputtered films in the range 20-72 nm. For thermal evaporation depositions, process pressures were in the range $0.8 - 6.7 \times 10^{-6}$ mBar. Deposition durations were not recorded for the thermal evaporation experiments and consequently the average deposition rate is unknown for these samples. For the sputtered silver films, process pressures were within the range $4.2 - 4.6 \times 10^{-3}$ mBar and average deposition rates spanned the range of $0.2 - 6.5$ Å/s.

In some cases very significant variations in surface roughness values were observed across a single sample; e.g. one RF magnetron deposited film exhibited surface roughness values between 0.6 and 4.8 nm. Such significant outliers have been removed from the results presented below and do not factor into the analysis of the results in general. Other results were discarded due to lacking or dubious logging of experimental parameters.

Plots of average deposition rate versus power for RF sputter deposition of thin silver film on silicon dioxide using three different sample holders, are shown in Fig. 3.22. The plot shows positive linear correlation between power and average deposition rate.

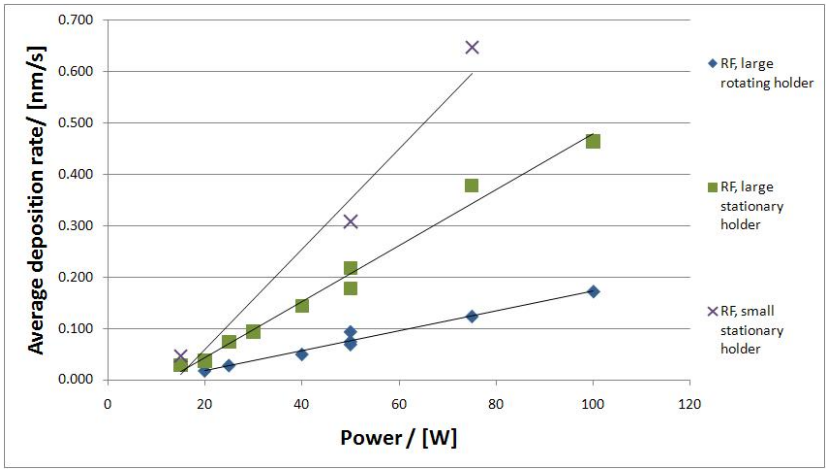

Figure 3.22: Average deposition rate versus power for RF magnetron sputtering of silver.

There was significant variation in the observed slope depending upon which of the three different sample holders were used. This variation can be attributed to the significant differences in source-sample geometries as illustrated in Fig. 3.21. Given the process conditions, characteristic of these RF magnetron sputtering depositions, the mean free path, l, can be estimated to be $\sim$3 cm. This yields a Knudsen number, Kn, as given by Eq. 3.2 of $\sim$0.2 which would indicate a transport mechanism in the intermediate regime between high vacuum and fluid flow. This fits well with the observed difference in deposition rates between static samples held by large and small sample holders, as the deposition rate at the large holder is lower than would be expected by assumption

of an inverse square relationship. The non-zero intercept ($P \approx 12$ W), between deposition rate and power, indicates the threshold for striking a plasma in the magnetron gun and also illustrates why depositions were not performed using power below 15 W.

For each sample, the RMS surface roughness and its standard deviation were calculated from several AFM measurements performed across the sample. These sample-averaged surface roughnesses fell within the range 0.7 to 3.3 nm RMS. Representative screenshots of AFM roughness analysis are shown in Fig. 3.23. Most of the deposition experiments were aimed at depositing silver films with a thickness on the order of 30 nm. Most films deposited with significantly different thicknesses were from depositions that were conducted while the necessary experience to predict film thickness with reasonable accuracy and consistency was gained. The thicknesses of the films deposited onto germanium wetting layers were not measured due to the multi-layered structure of these samples.

Fig. 3.24 shows a compilation of observed RMS surface roughness, from the various deposition experiments, plotted against the thickness of the thin-film. For the thermally evaporated film a positive correlation between film thickness and surface roughness was observed (red triangles). For RF magnetron deposition, using stationary sample holders, a negative correlation could be inferred, disregarding one outlying data point (green squares - larger holder and purple crosses - small holder). In the case of the rotating sample holder some degree of positive correlation was seen (blue diamonds). The film thicknesses of the silver layers deposited in the germanium wetting layer experiments were not measured due to the multi-layered structure. The thickness aimed for was 30 nm for all three samples and the data is included here to illustrate the potential variation for nominally identical processes with a given film thickness.

Fig. 3.25 depicts RMS surface roughness against deposition rates. The thermally evaporated films are not included in this plot for the reasons mentioned in the beginning of this section. As for the roughness versus thickness plot, differing behaviour was observed when comparing the rotating with the static sample holder experiments. For films deposited using the large rotating sample holder an apparent positive correlation between deposition rate and surface roughness was observed (blue diamonds). For the

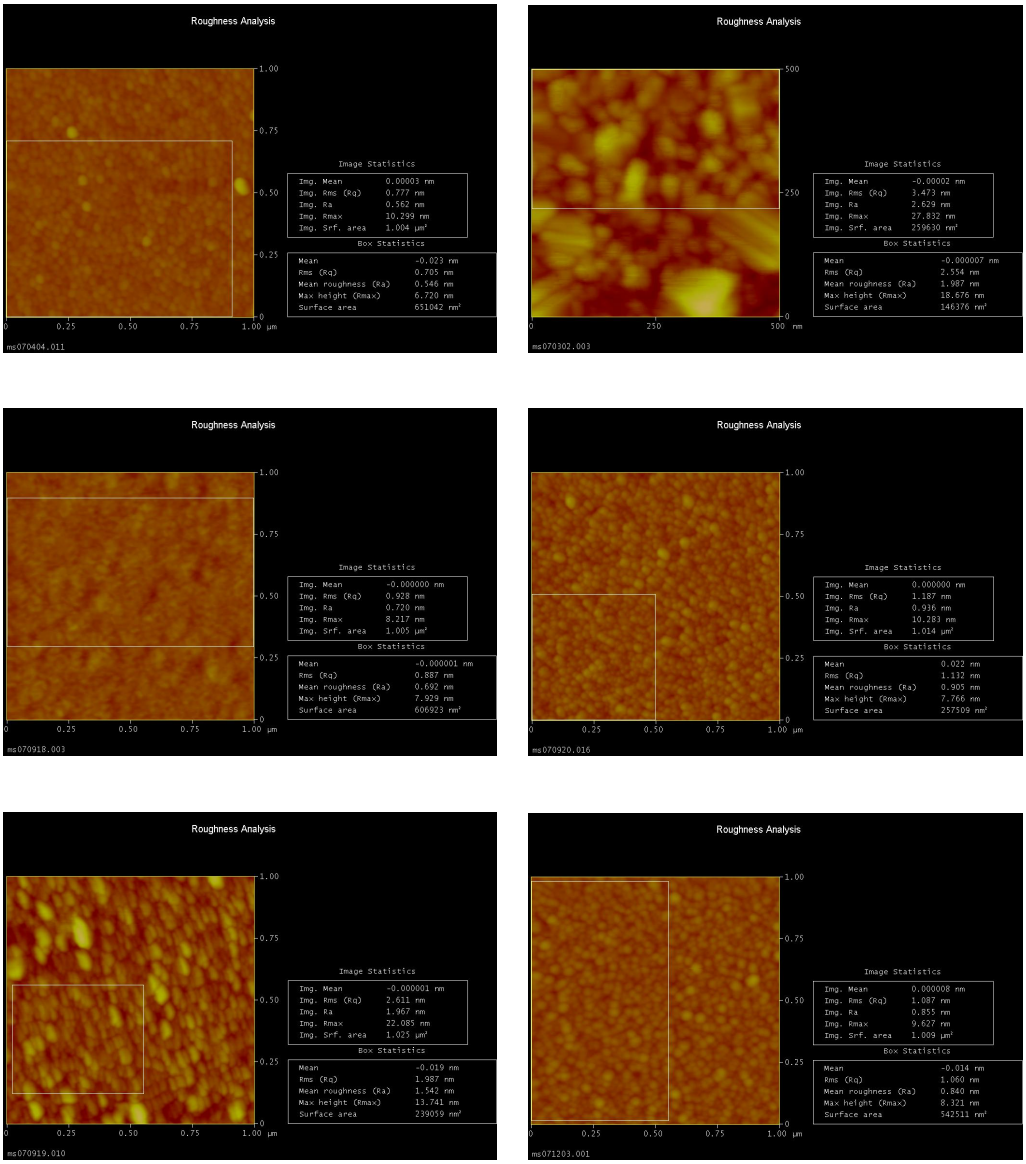

Figure 3.23: AFM surface maps of silver thin films. All maps have a z-scale of 30 nm. Top Left: Thermal evaporation, 12.7 nm thick, 0.705 nm RMS. Top Right: Thermal evaporation, 32.2 nm thick, 3.473 nm RMS. Middle Left: RF magnetron sputtering, 24.7 nm thick, 0.906 nm RMS. Middle Right: RF magnetron sputtering, 25.7 nm thick, 1.187 nm RMS. Bottom Left: RF magnetron sputtering, 32.4 nm thick, 2.611 nm RMS. Bottom Right: RF magnetron sputtering, ∼10 nm germanium wetting layer, ∼30 nm thick silver film, 0.909 nm RMS.

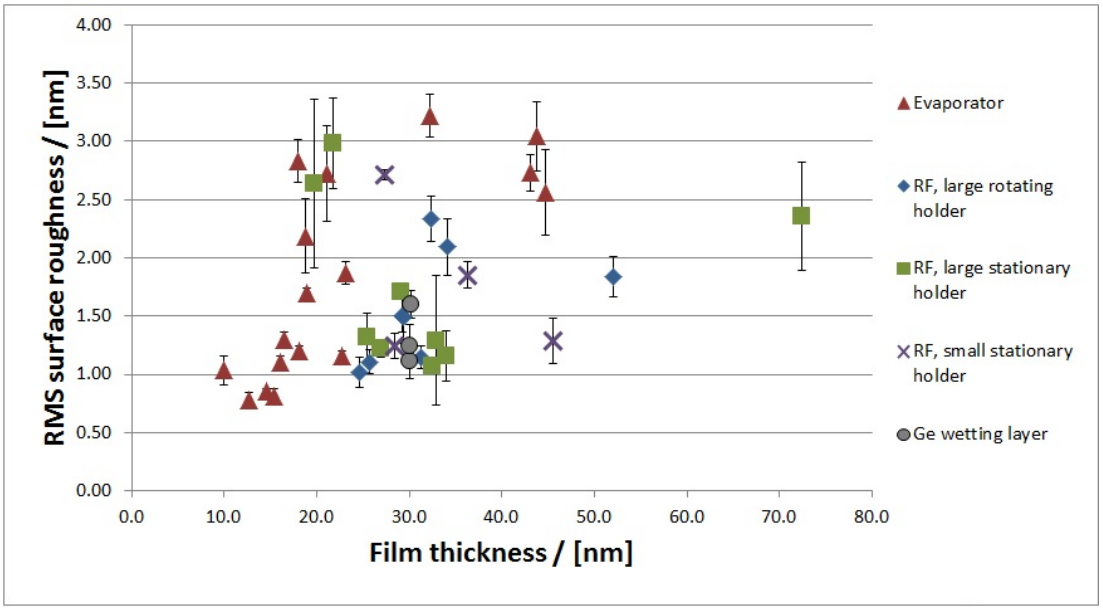

Figure 3.24: RMS surface roughness versus film thickness.

large stationary holder the correlation, if any, appeared negative (green squares). For films deposited using the small stationary sample holder a parabolic behaviour could be inferred (purple crosses), however more data would be needed to verify this.

3.6 Summary, outlook and conclusion

As shown in Section 3.5 the lowest RMS surface roughness figure obtained for any film deposited using the UCNFL facilities was 0.78 nm. However, this was for a 12.7 nm thick film which is less than half the desired thickness of 30 nm. As discussed in Section 3.2.4 statistical effects are expected cause increasing roughness with increased thickness.

The smoothest film with a thickness close to the desired 30 nm, had a surface roughness of 1.07 nm RMS for a thickness of 32.5 nm. This film was deposited using RF magnetron sputtering, a deposition technique which does reduce the impact of statistical roughening due to the enhanced kinetic energy of species supplied by the source.

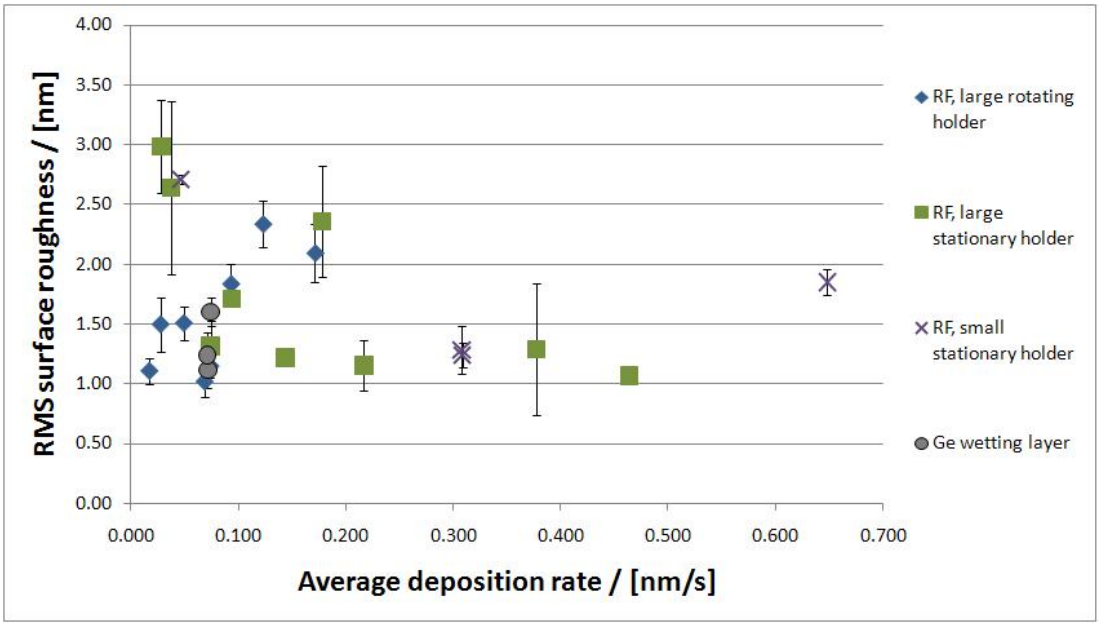

Figure 3.25: RMS surface roughness versus average deposition rate.

Fig. 3.24 shows that surface roughness will increase with film thickness and for the thermal evaporation experiments there is reasonable correlation between the results and the statistical model. Sample-averaged surface roughness figures for silver films in the thickness range from 10 to 80 nm fell within the range of 0.7 to 3.5 nm RMS. This surface roughness range does not constitute a significant nor consistent improvement of past results [20, 108].

As illustrated by the scatter plots in Fig. 3.24 and Fig. 3.25 achieving consistent improvements in film surface roughness proved difficult. This problem could be attributed to several issues; e.g lack of feedback controlled deposition rates, lack of substrate temperature control, memory effects in deposition systems used for many different experiments, etc. However, even disregarding the issue of achieving consistent experimental control of the surface roughness parameter, none of the results indicate that significant improvement of surface roughness (i.e. $<$1.0 nm RMS) in 30 nm thick silver films is achievable using the experimental techniques available.

Depositions using germanium wetting layers did not exhibit the 10-fold reduction in surface roughness reported by Logeeswaran et al. [100, 101]. Using the germanium wetting layer, surface roughnesses between 1.11 and 1.60 nm RMS were observed compared to 1.05 to 2.34 nm RMS for films deposited without a wetting layer. However, it should be noted that the surface roughness of the films deposited here already exhibited much lower surface roughness without the germanium layer than that of similar films (∼7-10 nm) as reported by Logeeswaran et al [100, 101]. While achieving better wetting between depositant and substrate will improve the seeding of the layer, this effect will become less important with increasing film thickness as structural growth effects begin to dominate.

3.6.1 Outlook

One way of improving film morphology of silver films would be by depositing onto a semiconductor substrate where the dissimilarity between the two materials should improve initial wetting between the layers. In order to still fulfil the requirement that the non-silver layers be transparent at the exposure wavelength it would be necessary to choose a semi-conductor material which exhibits the desired photonic behaviour. One example would be zinc oxide which has a bandgap energy of 3.4 eV at 300 K, which corresponds to a wavelength of 364.9 nm. This is just short of the wavelength for the mercury lamp I-line at 365.4 nm, alternatively the H-line at 404.7 nm could be used instead, although this would alter the plasmonic response of the silver layers. J. Chai investigated this particular subject, demonstrating that such films could be formed with surface roughness below 1 nm RMS, as well as achieving image transfer of sub-diffraction limited information through superlenses based on the Ag/ZnO material combination [109].

A different approach could be choosing an exposure wavelength different from the mercury I-line, thereby allowing a superlens to be fabricated from a different material combination. As mentioned in Section 3.3.1 stacks consisting of alternating layers of Mo/Si and Nb/Si with very low interfacial roughness have already been fabricated. Depending upon the dielectric properties of such materials it might be conceivable that an exposure wavelength could be found for which such a stack would act as a superlens.

Another conceivable way of reducing the surface roughness of superlens layers would be through deposition of an amorphous plasmonic material. Amorphous materials, unlike polycrystalline materials, have no grain boundaries and consequently a more homogeneous composition. Deposition of amorphous compound materials from metals can potentially be achieved through quenched growth deposition of eutectic alloys from constituents with large lattice mismatches and differing crystal symmetries. Finding such an alloy with the desired plasmonic frequency could potentially enable the fabrication of superlenses with superior imaging characteristics compared to lenses based on polycrystalline materials. However, there are indications that the plasmonic properties of non-crystalline materials may be inferior due to large Drude phenomenological scattering [79].

It is possible to envision a deposition system in which most critical deposition parameters are controllable. Cathodic arc discharge sources produce a high fraction ($\sim$0.7) of ionised species. Through the application of an electric field it would be possible to accelerate such ionised species and subsequently select the desired mass-to-charge distribution through use of a mass spectrometer such as in the Aksenov Quarter-torus [110]. By applying a reverse bias between spectrometer and substrate it would be possible to control the kinetic energy of the species impinging upon deposition substrate as well as vary this kinetic energy throughout the deposition process. Substrate temperature control capable of both maintaining cryogenic and high temperatures would allow in situ heat treaments during film deposition depending upon need. A substrate holder mounted on a rotational pivot stage would provide the opportunity of varying the angle of incidence during the experiment as well as ensuring uniformity across the sample. Additionally an independent ion-beam could be included and utilised to further manipulate the growth mechanisms. However, comparable systems are not currently available at the UCNFL or through known collaborators, and their development is beyond the scope of this project.

3.6.2 Conclusion

The goals stated in the beginning of this chapter were not met with success, and consequently the expriments proposed, that relied upon the achievement of these goals, must be deemed infeasible for reasons discussed above. While the achievement of these goals

was not feasible with the available equipment, several suggestions have been presented on how to achieve smooth superlenses as well as depositing smooth metal-dielectric stacks.

However, there is a question that has not been considered: What level of surface roughness can be tolerated, if a certain imaging resolution is to be achieved, using a planar superlens? It must be concluded that the answer to this question can not be found experimentally, given the resources at hand, due to the lack of control over the surface roughness parameter. Hence the next phase of the project was to seek to answer this question through full-field electromagnetic modelling techniques, as described in the next two chapters.

4

Finite Element Method simulations of surface roughness effects in planar superlenses

This chapter presents the methodology and results obtained from finite element method (FEM) modelling of the impact of interfacial surface roughness upon the imaging characteristics of planar superlenses. The chapter begins with an introduction outlining the motivation for and the purpose of this investigation. Then follows a presentation of the methodology of the simulations describing the basic model; the modelling domain, boundary conditions, material parameters and numerical data interpretation. The results obtained from the FEM simulations for various geometries are then presented and discussed. Finally a summary of the findings and a conclusion is presented. The work presented in this chapter has been published as "Simulations of surface roughness effects in planar superlenses" in Journal of Optics A: Pure and Applied Optics **11** (10) 105503 [21].

4.1 Introduction

As discussed in Chapter 3, it proved difficult to achieve consistent experimental control of surfrace roughness in thin-film deposition given the available technologies at the University of Canterbury. Alas, the inability to achieve this goal in turn hampers the quantitative investigation of how such surface roughness would affect the imaging

performance of silver superlenses. Consequently, a mathematical modelling approach to such an investigation was proposed. Using the FEM it is possible to solve Maxwell's equations numerically for complex geometries. Line traces from authentic AFM surface maps of silver thin-films were extracted and used to represent realistic surface roughness profiles for use in these simulations. The amplitude data of these profiles was scaled to match the desired RMS roughness value and the subsequent impact upon image quality was extracted from simulated intensity distributions.

In order to quantify the performance of planar superlenses as a function of the interfacial roughness it is necessary to establish what quantities to measure and how to evaluate these measures. One important quality of any imaging system is the correspondence between object and image, i.e. how well does the image represent the object? The image used in these simulations consists of a binary grating with a given period, Λ, and aperture width, w, as shown in Fig. 4.1 together with the single-layer superlens geometry. Comparing the the linewidth of the image with the linewidth of

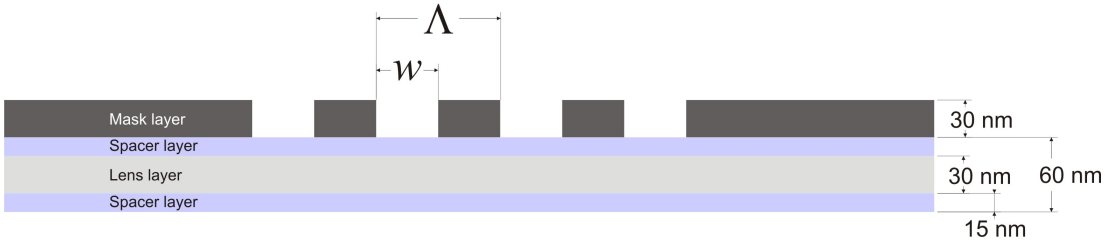

Figure 4.1: Schematic overview of the shadow mask and single-layer superlens geometry.

the object will give some indication of how the imaging system performs. For lithographic applications statistical consistency is of great importance. Consequently the variation of the linewidth in the image, also known as the line-width roughness (LWR), is a very important quantity for any lithography system. The typical figure used to represent LWR is three times the standard deviation (3σ) of the image linewidth. The 3σ interval represents the maximum error within which 99.7% of a normal distribution will occur. Thus, mean linewidth, $\bar{w}$, and LWR, 3σ, were chosen as the two figures on which to evaluate the superlens imaging performance.

Simulations were performed across a surface roughness range of 0.1 to 1.5 nm RMS for single- and dual-layer superlenses. For single-layer superlenses the influence of asymmetric surface roughness profiles was also investigated. The modelling results suggested a positive linear relationship between surface roughness, on the lens interfaces, and line width roughness in the resulting image. Dual-layer superlenses were observed to be more sensitive to the magnitude of interfacial surface roughness than single-layer superlenses. Results from asymmetric roughness profiles indicated that the imaging characteristics of planar superlenses is independent of which interface the roughness is concentrated on.

4.2 Methodology

This section describes the modelling domains and material parameters used in the FEM simulations. First a description of the general modelling domain including material parameters, boundary conditions and superlens geometries is presented. Then follows a description of the procedures involved with imposing the desired roughness profiles on the superlens interfaces. This leads to a discussion of the necessary considerations in meshing the model prior to finding the numerical solution. The section concludes with a description of the numerical output provided by these simulations.

The simulations described herein are two-dimensional (2D) finite element method (FEM) simulations, performed for different superlens geometries, within a range of surface roughness magnitudes. All simulations were performed using the commercial FEM tool Comsol Multiphysics© 3.4 (COMSOL). Simulations were performed using the module "'RF Module - In-Plane TM Waves (rfweh)"' using idealised material parameters as described below.

4.2.1 Modelling domain overview

Simulations were performed on two superlens geometries, a single-layer and a dual-layer superlens, as shown schematically in Fig. 4.2. Common to both simulated geometries is the presence of a shadow mask consisting of a 40-nm thick shadow masking layer ($\epsilon_r = \mu_r = 1$ and $\sigma = 3.8 \cdot 10^7$ S/m) with four 50-nm wide apertures placed symmetrically around the center of the mask at a pitch of 100 nm in a modelling domain of 1.2

μm by 1 μm. The modelling domain is bounded by perfectly conducting ($\mathbf{n} \times \mathbf{E} = 0$) boundaries along the y-axis and by transparent (perfectly matched layers) boundaries along the x-axis. For these simulations a free-space wavelength of 365 nm was used, which means that the size of the features being imaged is approximately $\frac{\lambda}{7}$. This geometry was chosen to approximately match the systems that have been used to demonstrate silver superlensing to date [17, 18, 66].

The single-layer superlens, as shown in Fig. 4.2(a), is represented by a sandwich consisting of three alternating layers: spacer, lensing layer and spacer. Both spacer layers are considered free space ($\epsilon_r = \mu_r = 1$) while the lensing layer is a metallic material with a degree of loss ($\epsilon_r = -1 - 0.2j$ and $\mu_r = 1$ corresponding to a complex refractive index $\tilde{n} = \sqrt{\epsilon_r \mu_r} = \pm(0.1 - 1.0j)$. The layers have thicknesses of 15 nm for the spacer layers and 30 nm for the lensing layer. This geometry is referred to as a [15-30-15] geometry.

The dual-layer superlens, seen in Fig. 4.2(b), consists of five layers: spacer, lens, spacer, lens and spacer. The material parameters are the same as for the single-layer geometry and the thicknesses are [15-30-30-30-15] nm, respectively. The object plane is the near-side of the given lens stack (x=0 nm) and conversely the image plane is the far-side of the lens stack (x=60 nm for the single-layer lens and x=120 nm for the dual-layer lens).

Idealised material parameters were chosen to avoid effects caused by lack of index-matching at material interfaces. The loss component, $-0.2j$ in the electric permittivity for the lensing layer is similar to the loss component (0.23-0.27 [62, 63]) observed in silver for EM waves with wavelengths of 365 nm (3.40 eV).

4.2.2 Modelling surface roughness

Data extracted from atomic force microscope (AFM) scans of thin silver films was used to generate geometry objects replicating surface roughness profiles for the lensing layer interfaces. For each roughness profile a line trace was extracted at random from a representative 1x1 μm^2 AFM map, with a resolution of 256x256 pixels corresponding to a resolution of 3.9 nm/pixel. An example of such a line trace is shown in Fig. 4.3 together with part of the entire AFM map. The height data of the trace, consisting

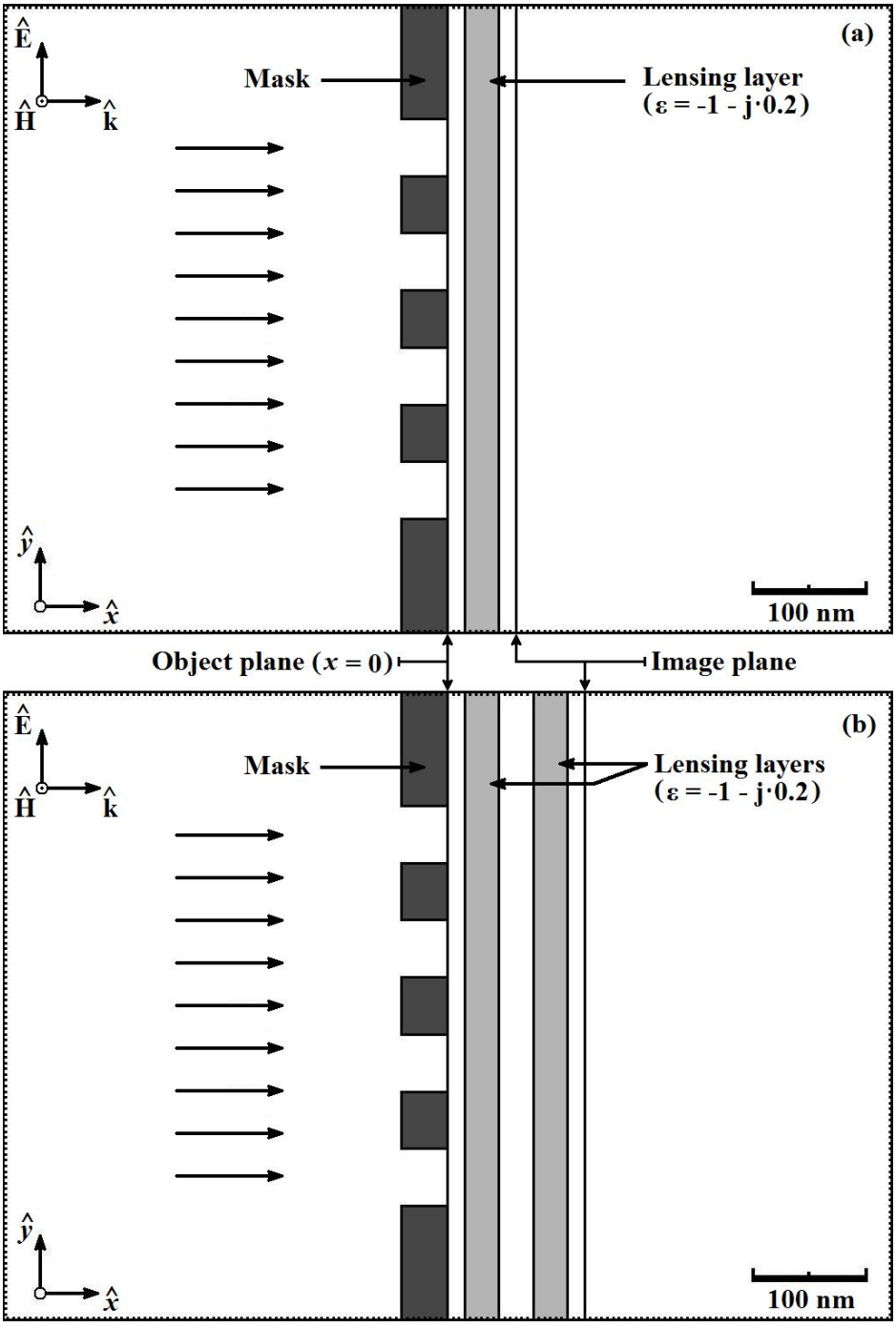

Figure 4.2: Schematic overview of analysed superlens geometries. (a) Single layer superlens geometry. (b) Dual-layer superlens geometry.

of 256 data points, was subsequently scaled to exhibit the RMS value representing the desired surface roughness. Geometry objects consisting of an arbitrary number of interfaces with arbitrary spacing and specified RMS roughness were produced using a Matlab program written by Ciaran P. Moore. Once generated, the geometry object was imported into COMSOL, as seen in Fig. 4.4(a).

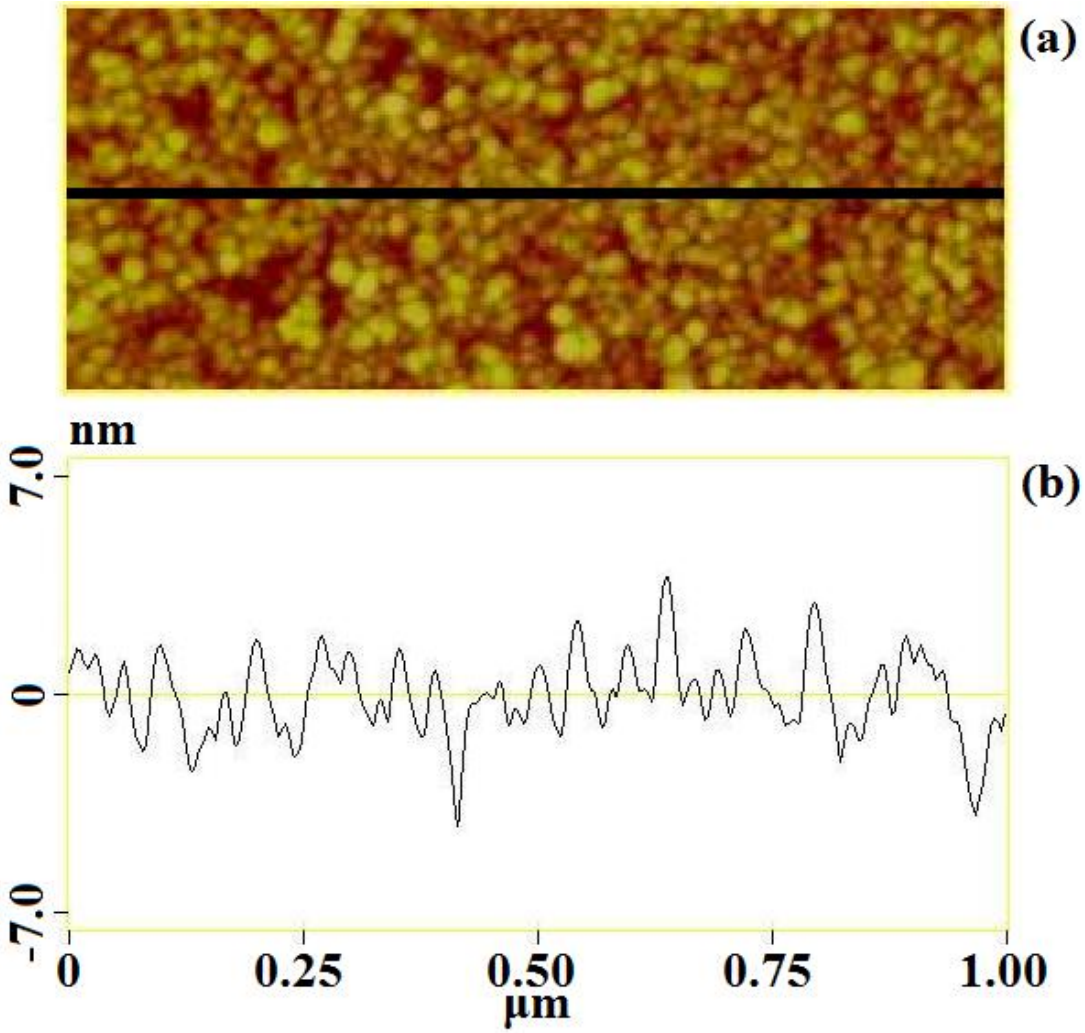

Figure 4.3: (a) A part of a 1x1 μm^2 AFM surface map. (b) The surface roughness profile indicated by the black line in (a).

Once the desired geometry had been imported the domain was meshed. The number of mesh elements used in these simulations varied from $\sim$ 350,000 elements for single-layer geometries to $\sim$500,000 elements for dual-layer geometries. An example of a relatively low-density meshing for a [15-30-15] system with 1 nm RMS interfacial roughness is shown in Fig. 4.4(b). COMSOL's built-in meshing tool automatically creates meshes with high density in the areas of interest for the problems considered in this paper. Higher mesh densities (1,400,000 elements) were modelled, however, the increase in resolution did not change the result significantly while the modelling time was increased dramatically as computer memory limitations were reached. This memory limitation also ruled out the viability of conducting modelling of comparable 3D geometries. The requirement for high meshing density coupled with the memory constraint meant that 3D simulations would have be limited to extremely small modelling domains. In the 2D case the number of degrees of freedom scales approximately as $2N$, where N is the number of elements in the model. For 3D models the degrees of freedom will scale as $\sim 3N$. The computer's memory resources (8 Gb of RAM) were exhausted when trying to solve the model for $\sim$ 3 million degrees of freedom - for the 3D case this would correspond to approximately 1 million elements or 100^3. If a meshing density equivalent to the average of that used here was to be achieved in a 3D model the domain size would be limited to $\sim$170x170x170 nm^3. However, it must be noted that for the meshing density varies across the domain and that the density in the regions of interest is significantly higher than the average as is illustrated by Fig. 4.4(b).

For the single-layer geometry both symmetric and asymmetric roughness profiles were analysed. In this case symmetric infers that the interfacial surface roughness is of equal magnitude on both interfaces. Conversely, by asymmetric it is implied that the roughness magnitude of the near-side spacer-lensing layer interface is significantly different from that of the far-side interface. Specifically, the geometries analysed here had one virtually flat interface (roughness magnitude $<$0.001 nm RMS) and one rough interface (roughness magnitude 0.1-1.5 nm RMS). These geometries were characterised by the RMS surface roughness of the rough surface and on which interface the roughness was concentrated. The near-side is defined as the lens interface closest to the object plane ($x = 0$).

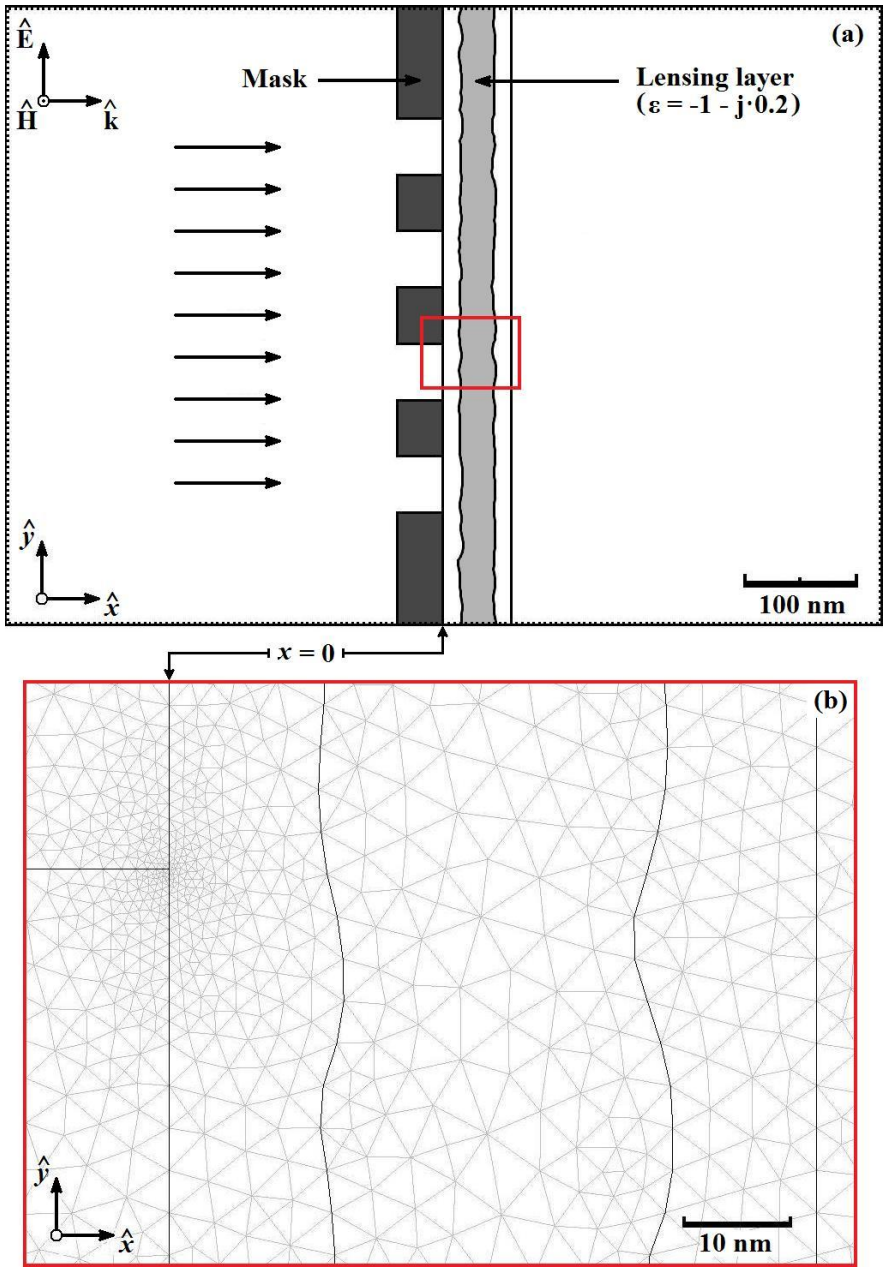

Figure 4.4: (a) A 1 nm RMS surface roughness single-layer lens geometry in COMSOL. The box indicates the area shown in the close up in Fig. 4.4(b). (b) Details of the meshing of a 1 nm RMS roughness single-layer superlens. This mesh consists of 22,263 elements, a typical mesh used for the actual simulations contain approximately 350,000 elements. Meshing was performed using the built-in meshing function. This image illustrates how the mesh density varies in the region of interest around the superlensing layer.

4.2.3 Simulation output data

Simulations were performed for surface roughnesses in the range from 0.1 to 1.5 nm RMS in 0.1 nm intervals. Following each simulation run, a plot of the norm of the electric field, $\|\mathbf{E}\|$, was saved for easy access during data analysis. Data analysis was performed in Matlab© (The MathWorks Inc.) using the COMSOL/Matlab interface. An ensemble, consisting of fifteen simulation runs, was performed for each of the fifteen surface roughness magnitudes evaluated.

From each simulation run two linewidth figures werFle calculated, yielding a total of thirty data points for each simulation ensemble. A larger sample population would improve the statistical weight of the findings presented in Section 4.4, however time and data storage limitations meant that $n = 30$ was considered a reasonable compromise.

4.2.4 Robustness of the model

In order to ensure that the results obtained from the FEM simulations are valid, it is important that the model itself is robust. In order to guarantee the robustness of the model two issues must be considered: convergence and symmetry.

At low meshing densities FEM simulations may produce significantly varying solutions depending upon the exact meshing geometry. In this regime the model is considered divergent and the results obtained from such calculations must be disregarded. As the meshing density is increased the ensuing solutions will converge towards the model's true solution. Consequently, it is important to demonstrate that the meshing density of the model is sufficiently high that no significant variation in the output data is observed.

Fig. 4.5 presents three different levels of meshing intensity and their corresponding simulation output data. As can be seen by considering these, the model is convergent within this range of meshing densities as no significant variation is observed in the output data. The results presented in Sec. 4.4 were obtained from models with meshing densities approximately equal to that of the bottom case in Fig. 4.5. Higher meshing densities of up towards 1.5 million elements were attempted. At this meshing density no solution was found due to the computer running out of resources, at that point it

was using 7 Gb of physical memory and a 11 Gb page file. Table 4.1 presents the average mesh element size, degrees of freedom and time to solve relative to the number of elements.

Number of elements	Average element size nm^2	Degrees of Freedom	Time to solve s
22263	54	44680	2
89052	13	178411	9
356208	3	713029	47

Table 4.1: FEM simulation element size, degrees of freedom and run times versus number of elements.

When modelling systems featuring wave phenomena it is important to ensure that the dimensions and boundary conditions of the modelling domain do not introduce any resonance effects to the system. The model utilised here was evaluated in this regard by changing the modelling domain size along both the x and y axes. As shown in Fig. 4.6, no significant variation was observed in the output data due to changes in domain size and symmetry along either axis.

Based upon these observations the FEM model used here may be considered robust in regards to both convergence and symmetry effects.

4.3 Data analysis

This section describes how the mean linewith, $\bar{w}$, and 3σ line width roughness, LWR, were calculated for each of the simulation ensembles.

As mentioned above, the output data from the simulations was the norm of the electrical field, $\|\mathbf{E}\|$. Evaluation of the optical image was performed by analysis of optical intensity profiles. The optical intensity, I, was calculated as $I = \|\mathbf{E}\|^2$. Fig. 4.7 show examples of intensity plots for a perfectly smooth (4.7a) and a 1 nm RMS surface roughness (4.7b) superlens. The impact the surface roughness has upon the intensity along the surfaces of the lensing layer in the form of asymmetries and irregular intensity

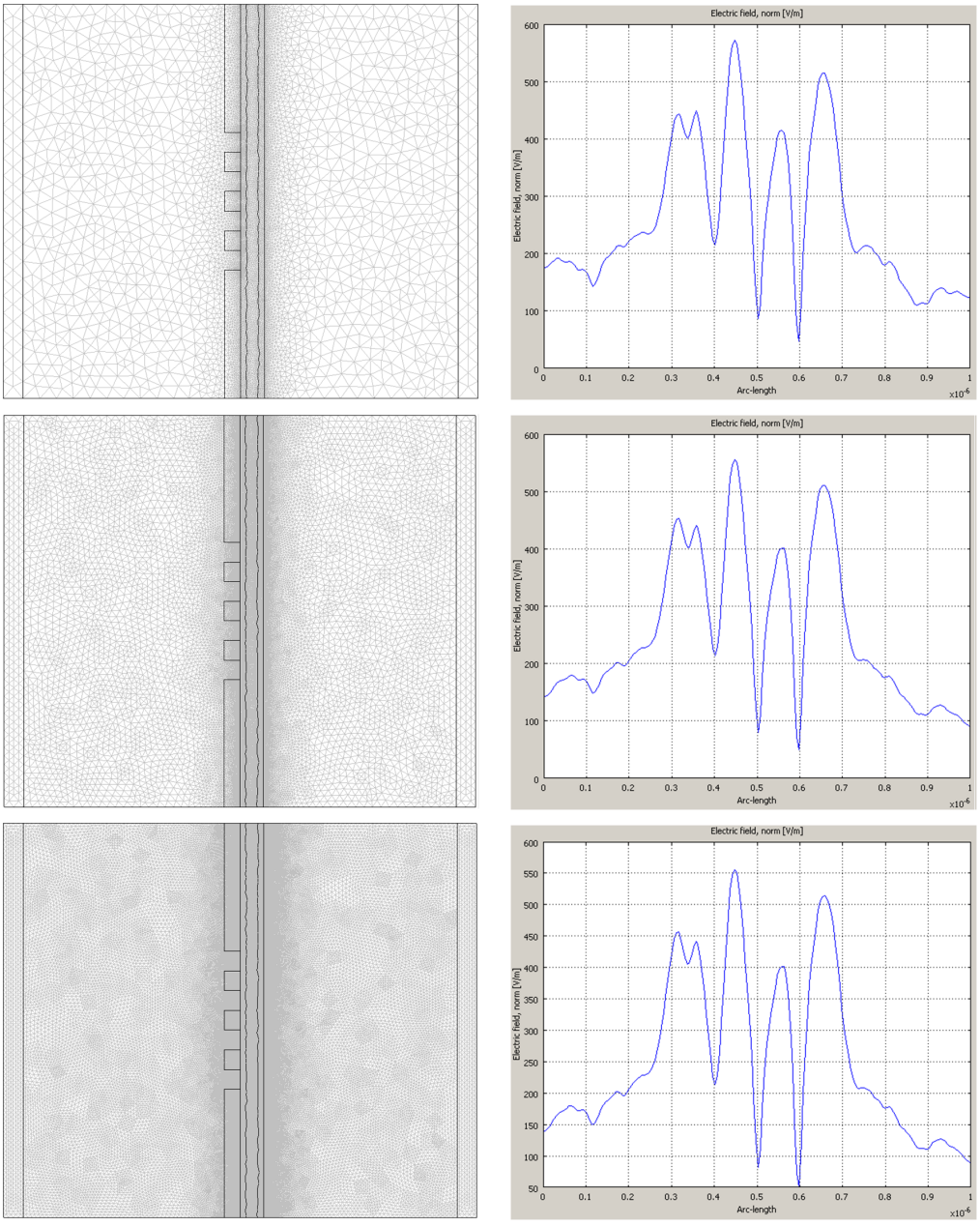

Figure 4.5: Screenshots showcasing three different meshing densities (left) for the same model geometry and the corresponding plots (right) of the norm of the electric field along the image plane (x=60 nm) for the respective solutions. From top to bottom, number of mesh elements, degrees of freedom and time required to solve. Top to bottom: 22263, 89052 and 356208 elements respectively. The bottom meshing density is representative of the simulations analysed in Sec. 4.4.

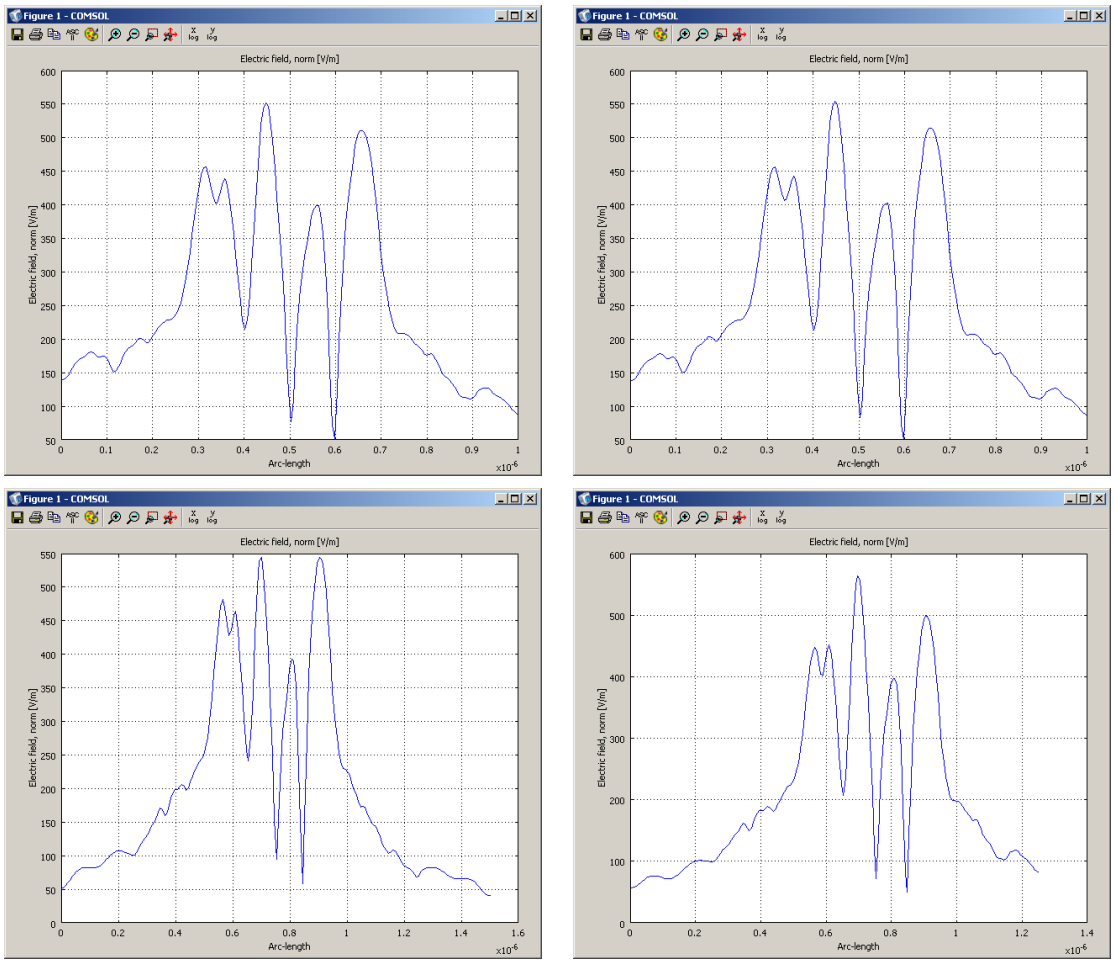

Figure 4.6: Output data from the FEM model with varying domain sizes and symmetries. As seen from these plots of the norm of the electrical field, no significant variation is observed within the region of interest due to such variations in domain size and symmetry. Top left: symmetrical 3x1 μm^2 domain with 350592 elements. Top right: asymmetrical 2.2x1 μm^2 domain with 351536 elements. Bottom left: symmetrical 1.2x1.5 μm^2 domain with 382112 elements. Top right: asymmetrical 1.2x1.25 μm^2 domain with 373520 elements.

variations is seen by comparing 4.7a and 4.7b.

Data analysis was performed by evaluation of the optical intensity profile along the image plane for each simulation. An example of the optical intensity at the image plane for a perfectly smooth superlens is shown in Fig. 4.8. However, in order to calculate the linewidth, and the variation thereof, for a given ensemble, it is necessary to first establish a common denominator.

4.3.1 Calculating the baseline intensity

The image plane intensity profile was extracted for each of the fifteen traces making up an ensemble. The mean of these fifteen intensity profiles was then used to establish the baseline intensity, I_0, subsequently used to evaluate each individual intensity profile. I_0 was found by taking the mean of the peaks and troughs for the average intensity profile ($I_0 = \frac{1}{2}(I_{max} - I_{min})$). I_{max} was found by taking the mean intensity of the central 10 nm in each of the two central apertures. Likewise I_{min} was found by taking the mean of the intensity in 10-nm regions around the two troughs on the outside of the central peaks as illustrated in Fig. 4.8. The central trough was disregarded since the symmetry of the system ensures very low intensity and variation at this point, which would have the potential to unrealisticly reduce the observed variations. Averaging over 10 nm for each peak and trough was done to reduce the impact of sharp peaks in the intensity profile due to width diffraction at sharp features on the lens surface.

It must be noted that the choice of method for calculating I_0 will affect the simulations results. The method here was chosen for two reasons: it was reasonably manageable to implement and it evaluates each individual intensity profile based upon an average metric for the entire ensemble. It is difficult to quantify to which extent the choice of I_0 affects the results for LW and LWR. It would stand to reason that the LW results would be quite susceptible to the choice of I_0, whereas LWR should be less sensitive, provided the intensity profiles are evaluated at a threshold intensity where the steepness of the slope is high.

Fig. 4.9 shows a comparison between the intensity profiles for a perfectly smooth and a 1 nm RMS surface roughness single-layer superlens. The horizontal line marks

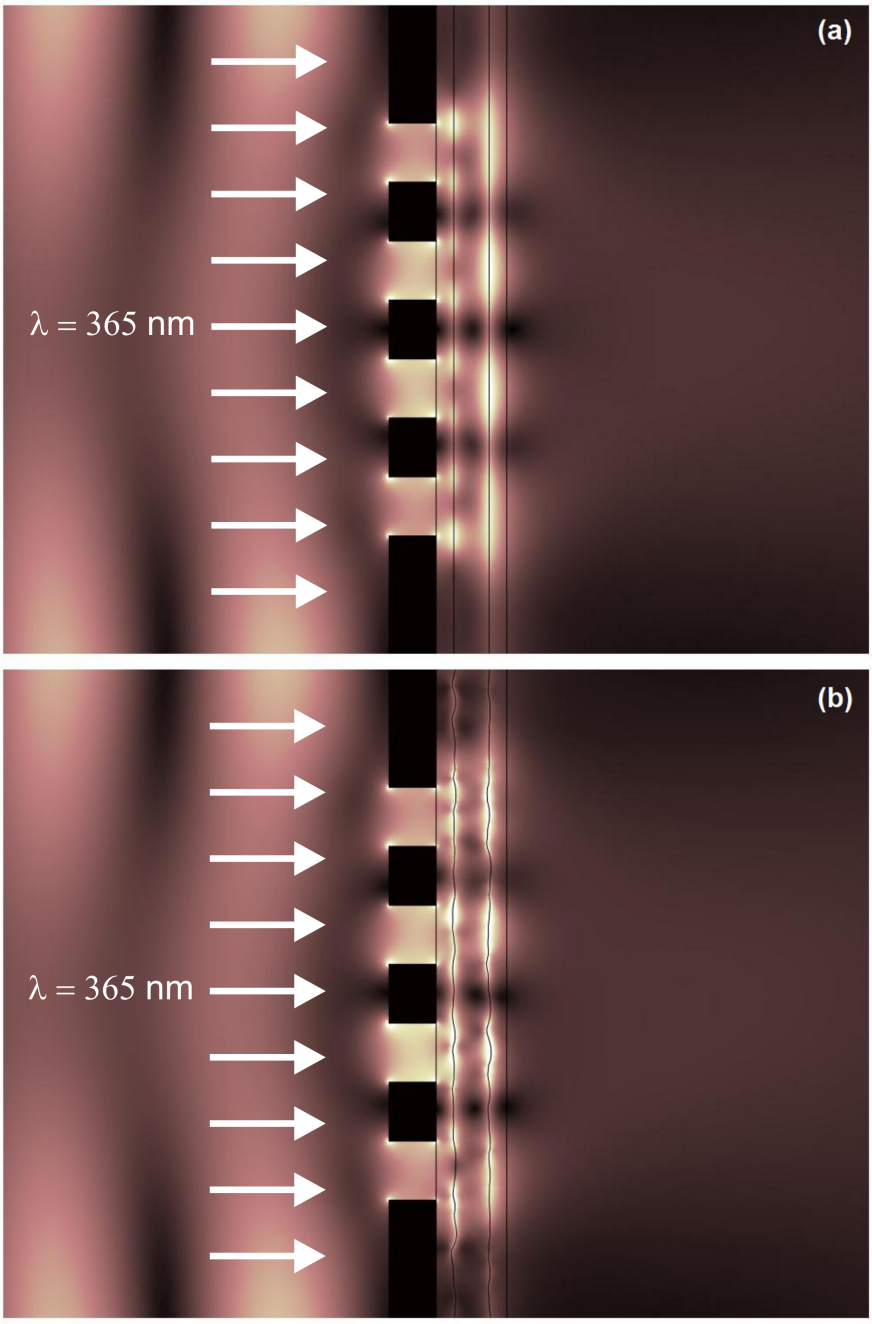

Figure 4.7: COMSOL plots of the optical intensity for [15-30-15] superlens geometries: (a) Zero surface roughness on the lens interfaces. (b) Interfacial surface roughness equal to 1 nm RMS. Arbitrary intensity scale with brighter indicating higher optical intensity.

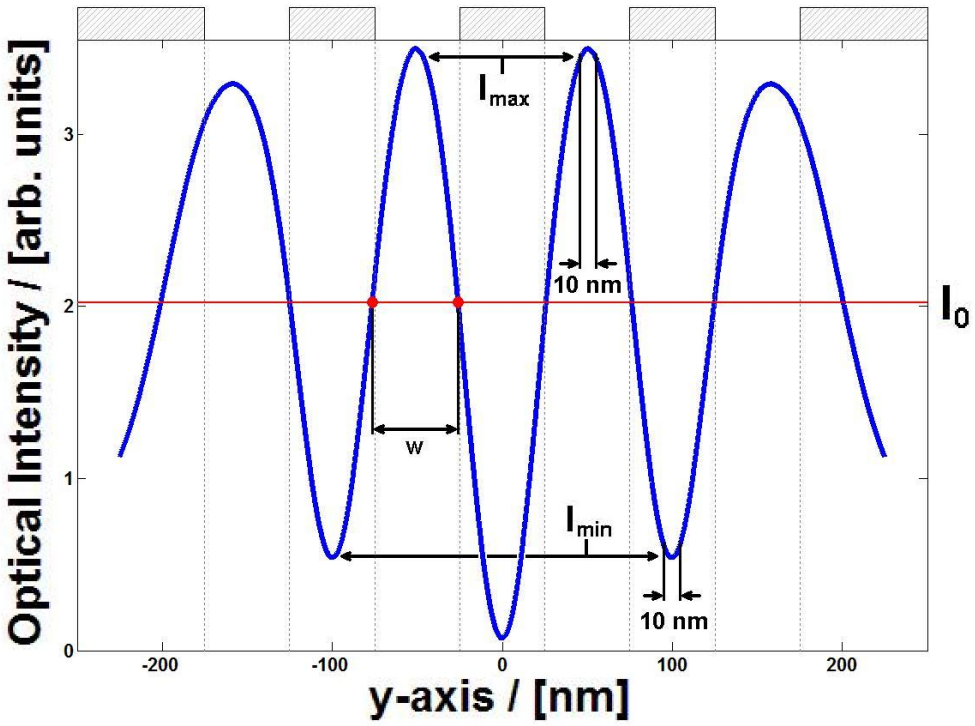

Figure 4.8: Line trace of the optical intensity along the image plane (x=60 nm) from the intensity plot shown in Fig. 4.7(a). Dashed blocks along the figure's top illustrate the profile of the shadow mask. Labels identify the locations of the intervals used in determining I_{min} and I_{max} used to calculate I_0. I_0 is represented by the horizontal line, (I_0=2.02). The linewidth, w, is given by the horizontal distance between the intercepts between the intensity trace and I_0. Note that the x-axis in this figure is mapping the y-axes in Fig. 4.7.

the baseline intensity, I_0, where the 1 nm RMS intensity profile is evaluated. A significant asymmetry is imposed upon the intensity profile, by the presence of surface roughness, due to considerable localised dampening. Significant suppression of intervals, in which I_{min} is evaluated, means that Michelson Contrast calculations ($C_M = (I_{max} - I_{min})/(I_{max} + I_{min})$) lose consistency. As a consequence, resulting contrast figures do not convey significant information regarding image fidelity.

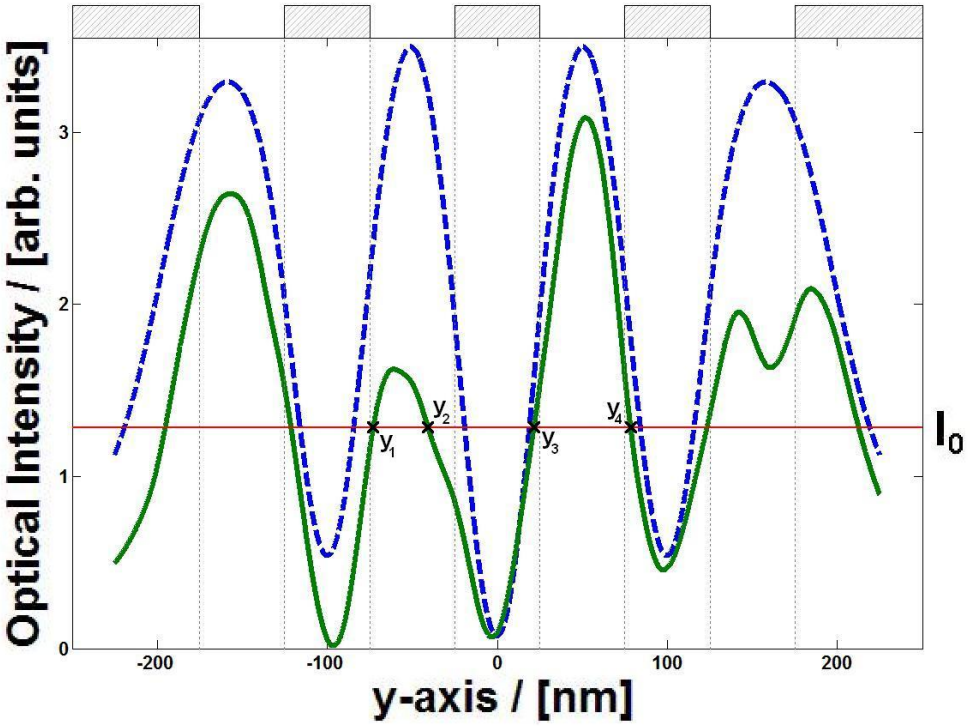

Figure 4.9: Linetrace of the optical intensity along the image plane (x=60 nm) from the intensity plots shown in Fig. 4.7. The dashed graph represents the intensity profile for the smooth case as shown in Fig. 4.7(a). The solid graph represents for the case with 1 nm RMS surface roughness as shown in Fig. 4.7(b). I_0 for the rough case is represented by the horizontal line, (I_0=1.29).

4.3.2 Linewidth and LWR calculation

After having established I_0 for the ensemble, each of the 15 intensity profiles were evaluated at this intensity and the corresponding linewidths calculated. This was done by subtracting I_0 from each individual intensity profile and finding the y-axis intercepts (y_1, y_2, y_3, y_4) as illustrated by Fig. 4.9. Each of the 15 intensity profiles yielded two linewidths ($w_n = y_{2n} - y_{2n-1}, n = [1, 2]$). The average of these 30 linewidths and the corresponding standard deviation were then calculated. The LWR was calculated as 3 times the standard deviation. This proceedure was performed for each of the ensembles. Ultimately the data analysis program yielded the mean linewidth and the corresponding standard deviation for each evaluated surface roughness value. Standard statistical

analyses were used to determine error bars for these values, assuming the values are normally distributed.

The χ^2-distribution was used in order to evaluate the statistical confidence of the found σ. The 95% confidence interval for the standard deviation, σ, and a given sample population, n, was calculated as shown in Eq. 4.1 [111].

$$\sigma\sqrt{\frac{n-1}{\chi^2_{0.025}}} < \sigma < \sigma\sqrt{\frac{n-1}{\chi^2_{0.975}}} \tag{4.1}$$

For $n = 30$ this yields a 95% confidence interval for σ of $(1 - 0.2036)\sigma < \sigma < (1 + 0.3443)\sigma$.

4.4 Modelling results

This section presents the results obtained from the FEM simulations of different superlens geometries.

4.4.1 Single-layer superlenses

Data for the [15-30-15] single-layer superlens was extracted from the intensity plots as described above. In Fig. 4.10 the mean linewidth, $\bar{w}$, is plotted against the interfacial surface roughness. The error bars represent the true standard deviation of the mean, calculated as $SD_{\bar{w}} = \sigma/\sqrt{n}$, $n = 30$. The linewidth remains relatively constant, if slightly dilated compared to the 50-nm wide apertures, until the surface roughness reaches ≈1 nm RMS. At higher values a slightly decreasing trend is evident.

Fig. 4.11 shows the correlation between LWR and RMS surface roughness. The error bars represents the 95% confidence interval as calculated according to the χ^2-distribution. The data shows that the optical intensity distribution LWR scales in direct proportion to the lens surface rougness magnitude within the surface roughness range studied here. Linear regression yielded a trendline with a slope of 19 nm/nm and a coefficient of determination (R^2) of 0.92. These results are for a 2D simulation of the ideal case. Three dimensional simulations using realistic material parameters should be performed in order to extract quantitative results. Here, no considerations have been

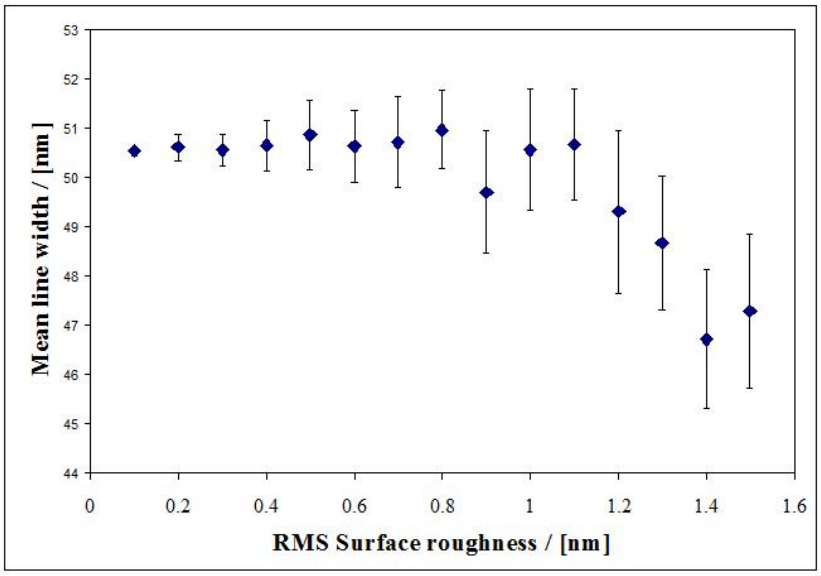

Figure 4.10: Mean line width versus lens RMS surface roughness magnitude for a [15-30-15] single-layer ideal superlens. Error bars represent the true standard deviation of the mean, $\frac{\sigma}{\sqrt{n}}$, $n = 30$.

given to factors such as bandwidth and intensity profile of the radiation source, resist chemistry, substrate reflections and imperfect shadow masking. As a consequence, it would be expected that the real LWR would be larger than those reported here. Experimental results demonstrating $\frac{\lambda}{12}$ resolution, through a 15-nm thick silver layer with surface roughness of ∼0.8 nm, have been reported by Chaturvedi et al. [5]. Some degree of feature broadening, from $w = 30$ nm to $\bar{w} = 37$ nm, is reported in this study. Alas, no LWR data is provided making a direct comparison between simulation and experimental image fidelity difficult. However, it must be noted that other non-ideal effects, not considered by this model, will also have an impact upon experimental results.

Only one shadow mask geometry was considered in this work. It has not been explored what impact adding additional apertures or varying their individual spacings would have on image quality. From the intensity profiles (Fig. 4.7) it appears that resonance effects affect the resulting image and variations of the shadow mask profile could have a significant impact upon the quality of the resulting image. This will be explored in greater detail in Chapter 5.

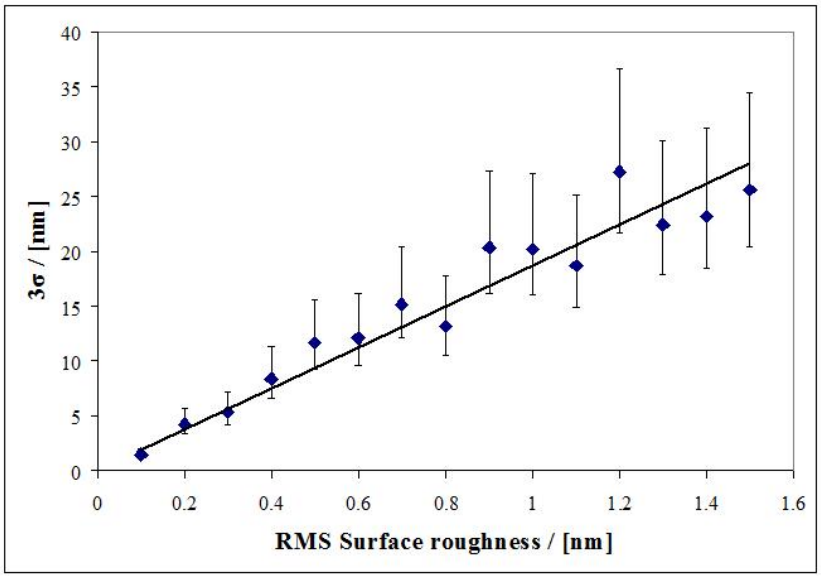

Figure 4.11: Line width roughness, 3σ, versus lens RMS surface roughness magnitude for a [15-30-15] single-layer ideal superlens. Error bars represent the 95% confidence interval for the LWR as given by the χ^2-distribution. The linear trendline has a slope of 18.7 nm/nm and intercepts the y-axis at y=0.

Asymmetric single-layer superlenses

The impact of asymmetry in regards to interfacial roughness distribution was also investigated. When depositing thin films onto a substrate it is a reasonable assumption that the film-substrate interfacial roughness profile will, to a degree dependent upon wetting and nucleation behaviour, conform to the substrate surface roughness profile. On the other hand, the topology of the free film surface will be dictated by statistical and thermodynamical factors. In the case of a smooth deposition substrate a large disparity between roughness profiles at the interface and surface may persist. If such asymmetry were to have any significant impact upon the imaging performance of superlenses, it would be conceivable to achieve superior performance by only slightly altering the fabrication process.

Results for the two different asymmetric configurations are presented in Fig. 4.12 where LWR is plotted against surface roughness. As for the symmetric single-layer case the error bars represents the 95% confidence interval. The diamond shaped markers repre-

sents the case where the surface roughness is concentrated on the interface closest to the object plane. Conversely the triangular markers represent the case where surface roughness is concentrated on the far-side interface nearest to the image plane. The trendline for the symmetric single-layer case is included as a reference and is represented as the dashed line. Trendlines for the asymmetric cases are represented by the solid and dash-dot-dotted line for the near-side and far-side cases respectively. The slope of these trendlines are 11 nm/nm for the near-side and 12 nm/nm for the far-side, with coefficients of determination of 0.89 and 0.93, respectively.

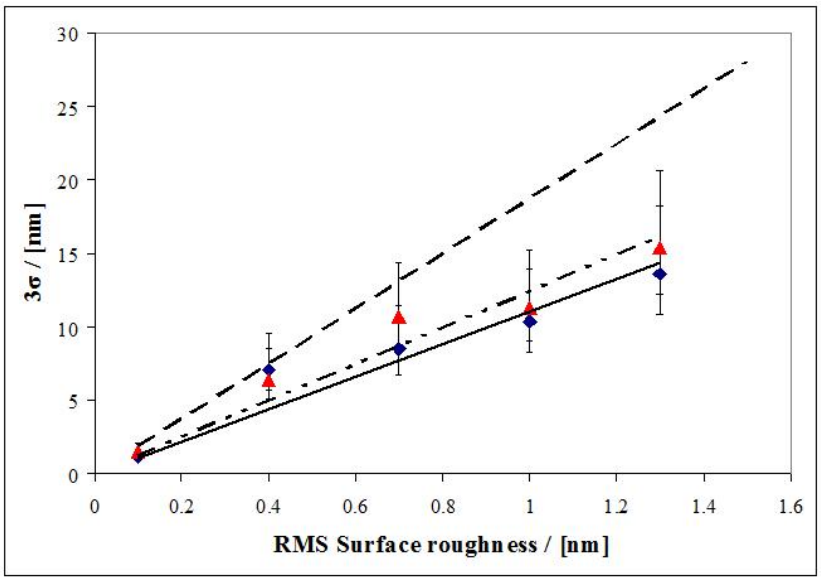

Figure 4.12: Line width roughness, 3σ, versus lens surface roughness for [15-30-15] single-layer ideal superlenses with asymmetric roughness profiles. The diamond markers represent the case where the roughness is concentrated on the near-side interface of the lensing layer and the triangular markers represent the data for the far-side case. Error bars represent the 95% confidence interval as given by the χ^2-distribution. The trendline for the symmetric case (as shown in Fig. 4.11) is included for easy reference and is represented by the dashed line. The linear trendline for the near-side case is given by the solid line and has a slope of 11.0 nm/nm while the trendline for the far-side case is represented by the dash-dot-dotted line and has a slope of 12.4 nm/nm.

The impact upon LWR of the asymmetric surface roughness is less than for the symmetric case, as would be expected considering that the total amount of surface roughness

is about half of that for the symmetric case. It does not appear to matter whether the surface roughness is concentrated on the near- or the far-side of the lensing layer. These results for the asymmetric roughness profiles suggests that no discernible gain is achieved by concentrating the surface roughness towards or away from the object plane.

4.4.2 Dual-layer superlenses

Data for the [15-30-30-30-15] dual-layer superlens was extracted from the intensity plots and Fig. 4.13 shows the correlation between LWR and RMS surface roughness. The error bars represents the 95% confidence interval as calculated according to the χ^2-distribution. The data suggests a directly proportional correlation between LWR and surface rougness. Linear regression yielded a trendline with a slope of 24 nm/nm and a coefficient of determination of 0.87.

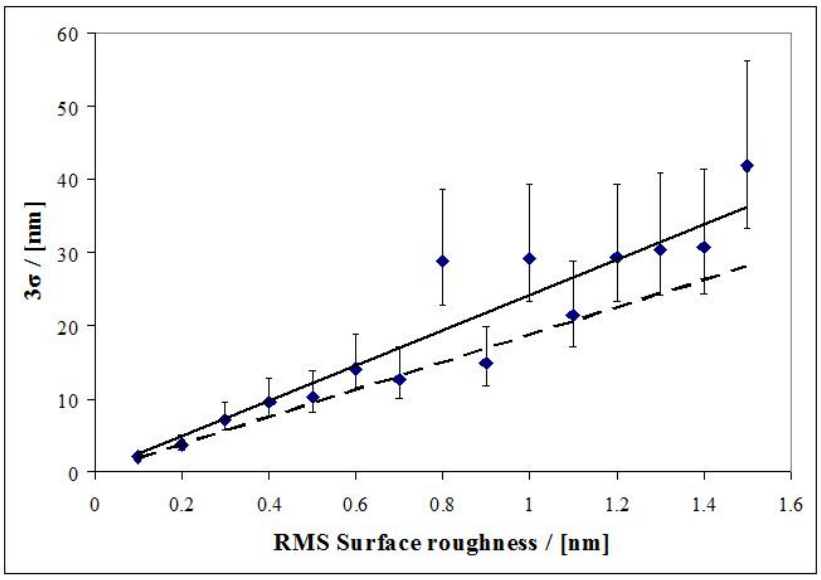

Figure 4.13: Line width roughness, 3σ, versus lens surface roughness for a [15-30-30-30-15] dual-layer ideal superlens. Error bars represent the 95% confidence interval as given by the χ^2-distribution. The trendline for the single-layer case (see Fig. 4.11) is included for easy reference and is represented by the dashed line. The linear trendline for the dual-layer lens has a slope of 24.1 nm/nm.

Results obtained from from dual-layer superlens simulations in COMSOL indicate that the LWRs for the single and dual-layer systems are comparable for surface roughness below 0.8 nm RMS. Beyond that point the dual-layer lens exhibit significantly more varying behaviour compared to the single-layer lens. Experimental results for dual-layer superlenses with ∼1 nm RMS roughness also showed much greater variability in line quality compared to single-layer imaging [70].

Line widths appears to be slightly increased compared to both the imaged object and the single-layer lens in the surface roughness range of 0.1 to 0.7 nm RMS. Additionally, the linewidth decrease observed for the single-layer lens when roughnesses exceed 1 nm RMS is even more markedly observed for the dual-layer lens, as shown in Fig. 4.14.

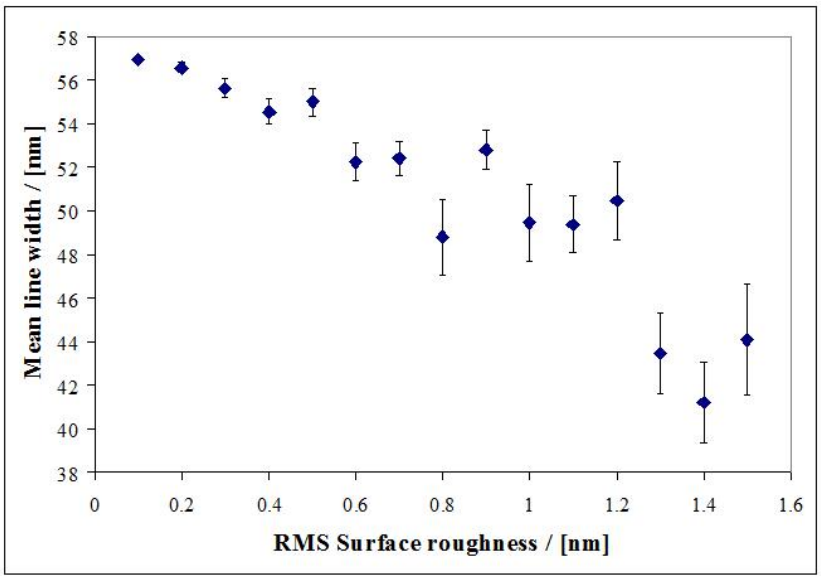

Figure 4.14: Mean line width versus lens surface roughness for a [15-30-30-30-15] dual-layer ideal superlens. Error bars represent the true standard deviation of the mean, $\frac{\sigma}{\sqrt{n}}$, $n = 30$.

4.5 Conclusion

The results of simulating surface roughness effects suggests that interfacial surface roughness has a significant impact upon the imaging characteristics of superlens systems, both in terms of image fidelity and in regards to image-to-object correspondance. A positive linear relationship between surface roughness and line width roughness is observed for both single- and dual-layer lenses within the surface roughness range considered here. Dual-layer lenses have been shown to be more sensitive to surface roughness compared with their single-layer counterparts.

Imaging properties for both superlens geometries appear to become less predictable when the roughness approaches approximately 0.8 nm RMS. This fact is particularly interesting since it is very close to the surface roughness currently achievable using standard physical vacuum deposition techniques. This supports the hypothesis that significant gains in superlens imaging performance could be achieved by even moderate reductions interfacial surface roughness.

The results for the asymmetric versus symmetric roughness profiles indicate that the imaging characteristics are independent on the localisation of the roughness. For surface roughness, the imaging characteristics are mainly dependent on the total amount of surface roughness at the lensing layer interfaces. These results indicate that a robust fabrication technique for depositing consistently smooth thin films is a prerequisite for realising useful planar superlenses. Additionally, it appears that no significant gain is achieved by selective localisation of the roughness within the lensing system which means that special considerations in fabrication approach in regards to this subject are unnecessary.

Comparing the results obtained here with experimental results it must be concluded that other parameters besides interfacial roughness affects superlens imaging performance. Many factors could be imagined to have a significant impact upon the imaging performance of a superlens imaging system as a whole, e.g. index-mismatching at interfaces, planarisation of spacer layers, mask layer fabrication fidelity, resist performance, etc.

Thus, the impact of the magnitude of interfacial roughness upon superlens imaging performance has been analysed. Given that plasmonic coupling is a resonant interaction, it would be worthwhile to consider more fundamental issues. One such issue to consider is the effect of the spatial frequency of the interfacial roughness. Chapter 5 describes such a study.

5

Resonant Surface Roughness Interactions in Planar Superlenses

This chapter describes FEM modelling work undertaken to characterise resonant behaviour in the imaging performance of superlenses. First, a brief introduction describes the motivation behind this investigation. This is followed by a review of other work dealing with the subject of plasmonic interference. Finally the methodology and results of this study are presented. The work described in this chapter was published as "Resonant surface roughness interactions in planar superlenses" in Microelectronic Engineering **87** (5-8) pp. 887-889 2010 [22].

5.1 Introduction

As identified in Section 4.5 there is reason to assume that other factors besides the interfacial roughness magnitude in superlenses have a detrimental impact upon the systems imaging performance. Consequently, simulations were performed to investigate how various spatial frequencies of surface roughness, in planar superlenses, affect imaging performance. Resonant behaviour was observed and increases between 110 and 267%, in image line width roughness (LWR), were observed at the peaks relative to the average image LWR observed outside these resonant frequencies. This investigation suggests that the position of these resonance peaks is dependent upon the periodic character

of the object being imaged, implying that a resonant coupling between shadow mask features and surface roughness takes place.

Finite element method (FEM) modelling provides an opportunity for analysing how surface roughness impacts upon superlens imaging performance by solving Maxwell's equations for the complex geometries involved in superlens imaging systems, using arbitrary surface roughness profiles at the metal-dielectric interfaces. The investigation of the impact of surface roughness magnitude upon superlens imaging performance was described in Chapter 4.

These initial investigations demonstrated a positive linear relationship between RMS surface roughness magnitude and line width roughness (LWR) in the resulting image. The object imaged was a set of 50 nm wide apertures set at a pitch of 100 nm, imaged using an exposure wavelength of 365 nm. The slope of the linear correlation was found to be approximately 20 nm of LWR per nanometre of RMS surface roughness on the superlens interfaces. As discussed in Section 4.5, these results suggest that the performance witnessed in superlens experiments to date is inferior to what could ideally be achieved using silver thin films with realistically achievable interfacial roughness magnitudes ($\sim$ 1 nm RMS). These simulations were performed in two dimensions using idealised material parameters and real surface roughness profiles extracted using atomic force microscopy (AFM). Here we extend this FEM analysis to study the spatial-frequency dependence of the surface roughness effects.

5.2 Resonance effects in plasmonic lithography

Plasmons, which are collective charge oscillations, are in their very nature resonant phenomena. Whether unbound SPPs or locally confined LSPs, this resonant character means that coupling and interference effects play an important role in any system relying on plasmonic interactions. Various interference effects from both SPPs and LSPs have been studied and described in the literature.

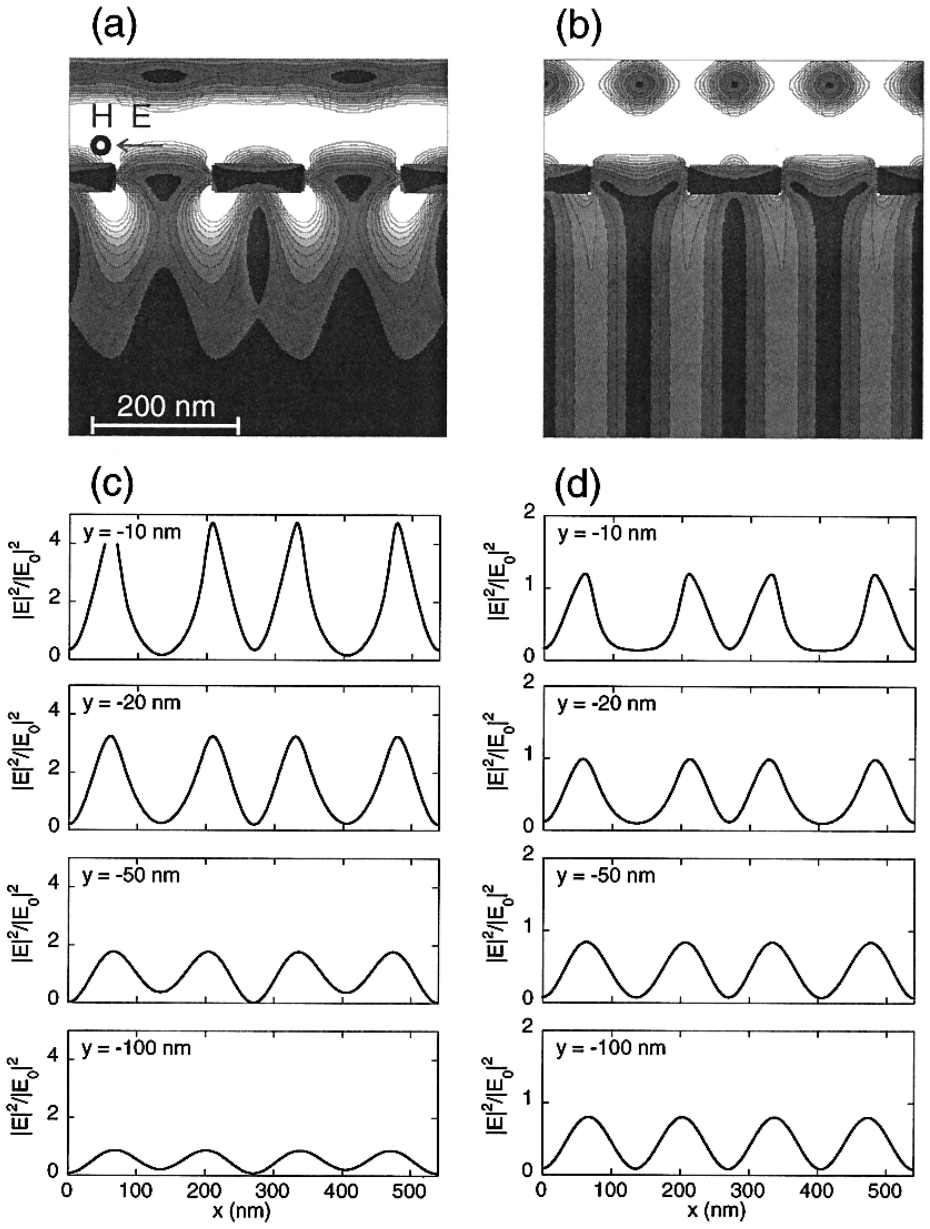

Figure 5.1: Evanescent interferometric lithography simulations illustrating interferometric coupling of LSPs on the corners of shadow mask absorbers. 270-nm period, 40-nm thick chrome gratings are illuminated by a TM-polarised plane wave with freespace wavelengths of (a) 454 nm and (b) 432 nm. The line scans in (c) and (d) represent the electrical field intensity profiles in the space beyond the object plane. Figure reproduced from [112].

5. RESONANT SURFACE ROUGHNESS INTERACTIONS IN PLANAR SUPERLENSES

One example of plasmonic interference is that of evanescent interferometric lithography (EIL). Simulation studies of metallic gratings around the cut-off wavelength for 1st diffraction order propagation illustrate that significantly enhanced contrast can be achieved within the near-field region [112, 113]. Further, the resulting image consists of a spatially frequency-doubled pattern relative to the mask as illustrated by Fig. 5.1. This EIL effect can be achieved through carefully tuning of the exposure wavelength to match the imaging system. The concept of EIL has been experimentally verified, e.g. by Luo in 2004 who produced frequency-tripled line patterns [114]. Via 435.8-nm wavelength exposure through a silver mask, featuring 60-nm wide line apertures with a periodic spacing of 300 nm, a 100-nm period half-pitch grating structure was formed in a 50-nm thick resist layer, as shown in Fig. 5.2.

Another example of plasmonic intereference effects was presented in a simulation study by Liu in 2005 [115]. Here propagating SPPs, formed through light-grating coupling, were caused to interfere and cause periodic standing interference patterns in areas beyond the grating-couplers. By causing several of such interference regions to overlap, 2D periodic standing interference patterns were produced. An image of electrical field intensity distribution arising from the overlap of two such interference patterns is shown in Fig. 5.3.

These are all examples of how resonant interactions play an important role in plasmonic applications. In the case of superlenses, SPPs act as an information transfer mechanism and it is unclear which resonant-coupling effects play a significant role in this regard and how they would affect the information transfer capabilities of such systems. In Section 2.3.4 it was discussed how surface roughness affects the loss mechanisms for SPPs. Eqs. 2.31 and 2.32 shows that these roughness induced losses depend not only on surface roughness magnitude, δ, but also on the correlation length, σ, of the surface roughness.

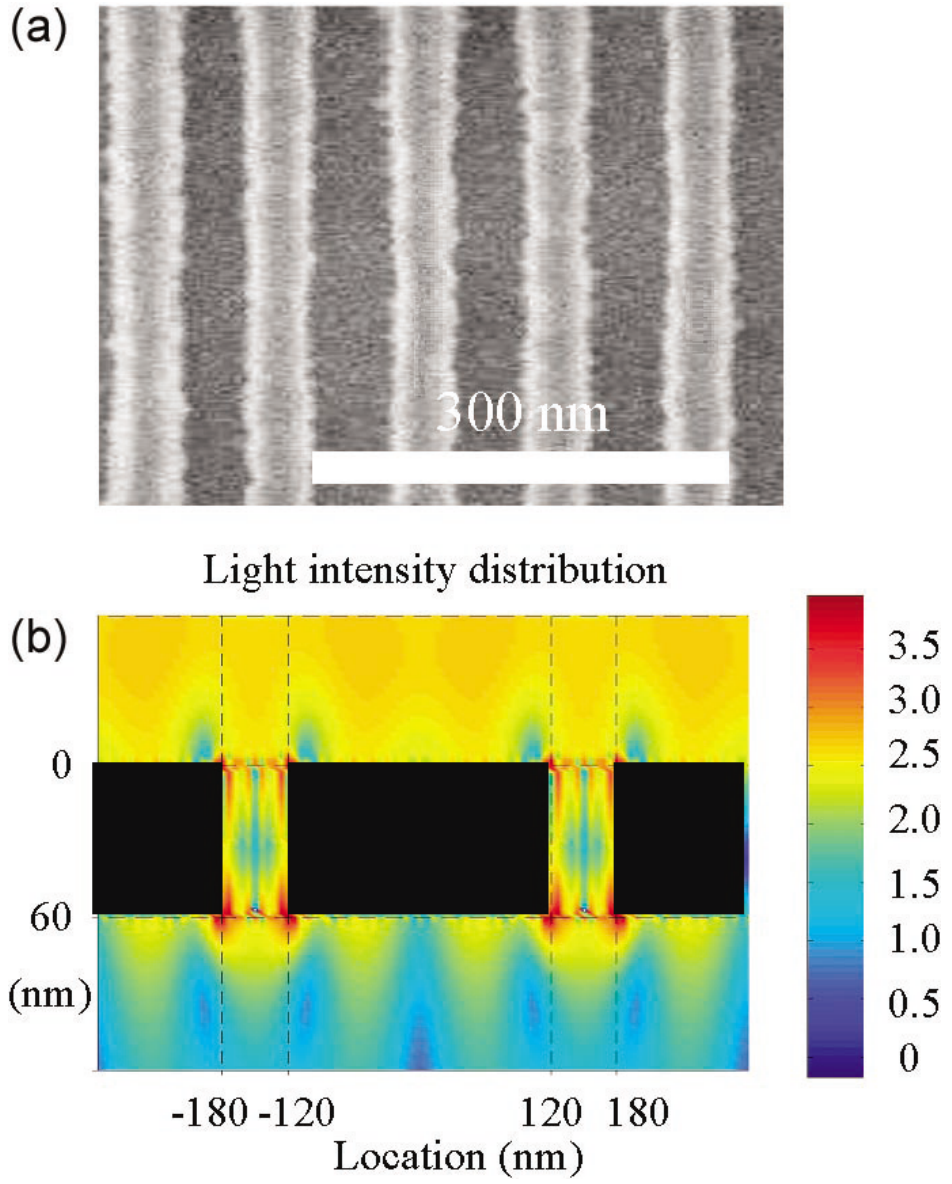

Figure 5.2: Spatial frequency tripling produced using a low duty cycle (dc=0.2) shadow mask with sub-wavelength apertures. A silver mask featuring 60-nm wide apertures were spaced at 300 nm were illuminated by light with a freespace wavelength of 435.8 nm. Experimental results are shown in (a) while (b) present a simulated near-field optical intensity plot for a similar geometry. Figure reproduced from [114].

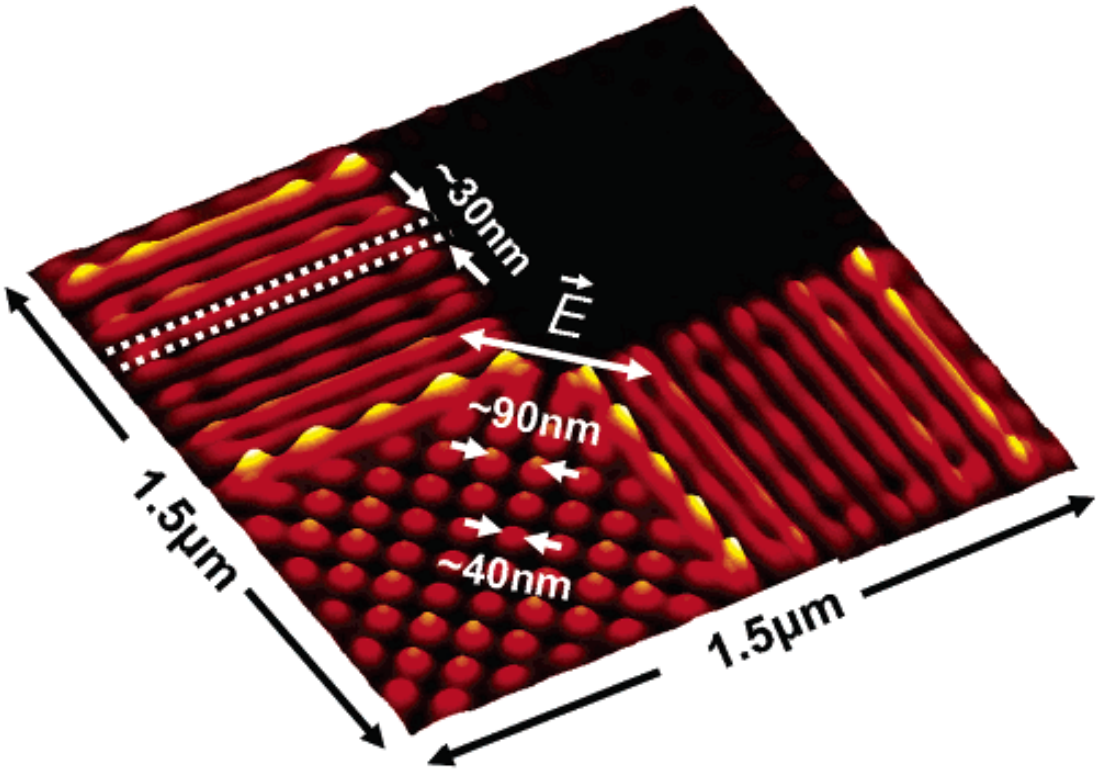

Figure 5.3: Simulation study of standing interference patterns arising from 2D coupling between propagating SPPs. The SPPs here were induced by 266-nm light coupling via 130-nm period aluminium line gratings. Propagating SPPs can form standing interference patterns in a space between two grating couplers. The dot pattern array here was formed by causing two such interference patterns to overlap perpendicularly. Figure reproduced from [115].

Considering these facts, an analysis of how information transfer in superlenses is affected by varying spatial frequencies of surface roughness is of interest. If resonant behaviour is observed, identifying the dominant coupling mechanism would further increase understanding of superlens imaging systems in general and in particular which role surface roughness plays in this regard. To investigate this subject, superlenses with periodic surface rougness profiles, having identical characteristic magnitudes and varying spatial frequencies, were studied through FEM simulations.

5.3 Methodology

In order to investigate how different spatial frequencies, contained within a typical surface roughness profile, affect the LWR, FEM simulations were performed for a single layer plasmonic superlens system, consisting of a 30-nm thick silver film sandwiched between two 15-nm thick spacer layers, illuminated at 365 nm, with sinusoidal surface roughness profiles introduced on both silver-dielectric interfaces, as shown in Fig. 5.4.

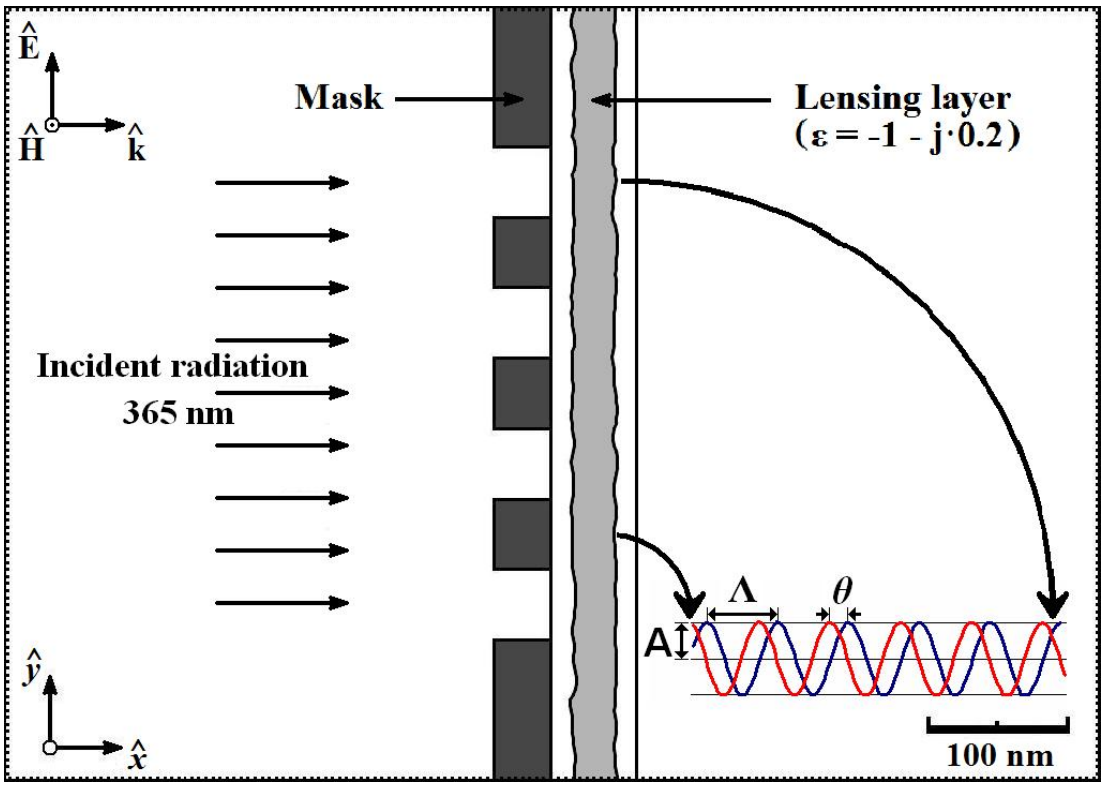

Figure 5.4: A schematic of the modelling domain, illustrating the position of the various elements and the unit axes for both the frame of reference and polarisation vectors. The modelling domain is 1.2 μm by 1.0 μm.

An mask feature, consisting of four 50-nm wide apertures spaced periodically at 100 nm, defined in a representative high-conductivity material ($\sigma = 3.774 \cdot 10^7$ S/m and $\epsilon_r = \mu_r = 1$), was used as the test object. Intensity profiles at the image plane, 60 nm beyond the object plane, were used to determine image quality. The superlens layer

($\epsilon_r = -1 - 0.2j$ and $\mu_r = 1$) was positioned symmetrically between the object and image planes. The spacer layers were given electromagnetic properties identical to free space ($\epsilon_r = \mu_r = 1$).

The details of the FEM simulation method, used in this investigation, have been described in Section 4.2. Typically ~350,000 elements were used across the 1 μm x 1.2 μm modelling domain. Convergence tests were performed to ensure that this did not affect the accuracy of the results obtained. Perfectly Matched Layers (PMLs) were employed at the x-axis boundaries to ensure that end reflections did not affect the results either. The period, Λ, of the sinusoidal roughness profiles was varied, in 35 steps (variation between 10 and 50% per step), from 10 nm to 1 μm throughout the simulations while the amplitude, A, was fixed at $\sqrt{2}$ nm (equalling 1 nm RMS). A set of 15 simulations was performed at each period of the surface roughness, with the phase, θ, picked at random for each individual roughness profile. For each lens object a roughness profile with random phase was chosen for each of the interfaces.

5.4 Results

The LWR was estimated for each constant-period ensemble, and Fig. 5.5 shows LWR as a function of the spatial frequency of the roughness, $k_y = 2\pi/\Lambda$, where the error bars indicate the 95% confidence interval as per the χ^2-distribution. Also shown in Fig. 5.5, by the dashed line, is a typical power spectral density plot for the roughness of a thermally-evaporated silver film, obtained from atomic-force microscopy (AFM) analysis.

The simulation data indicates resonant behaviour with three resonance peaks inside the range of typical spatial frequencies present in silver thin film surface roughness. These three resonance peaks are centred at spatial frequencies of 51, 93 and 165 μm^{-1}($\pm$ <5%). In order to evaluate the bandwidth affected by this resonant behaviour their approximate full width at half maximum (FWHM) were estimated. The FWHM were found to be 14, 28 and 19 μm^{-1} for the three respective peaks. Compared to the non-resonant baseline the LWR magnitude is increased by 110%, 267% and 172% for the respective

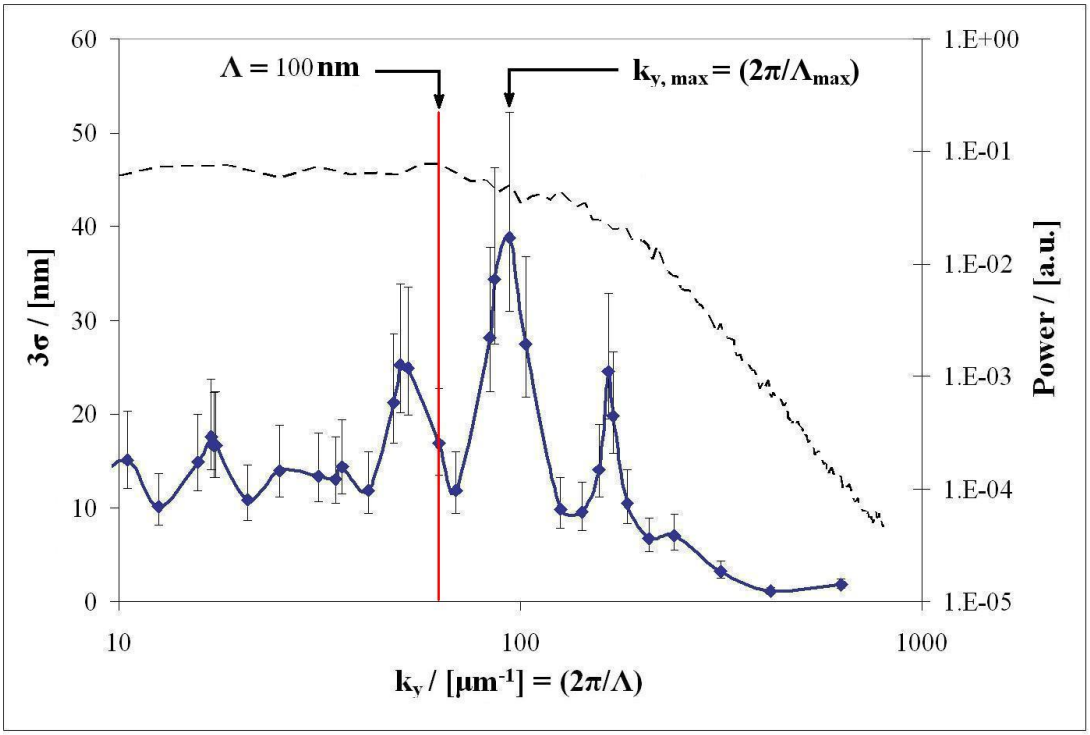

Figure 5.5: Line width roughness, 3σ, (solid line and symbols) as a function of the surface roughness wave vector, k_y. The error bars represent the 95% confidence interval as per the χ^2-distribution. Three resonance peaks are present inside the central interval of the plot. The dashed line represents the power spectral density (PSD) for a typical silver thin film.

peaks. This implies that across the spatial frequency band, where the resonant behaviour is observed, approximately one third of the band is affected by the resonant LWR increase to significant degree.

In order to identify the causes of the resonant coupling, that the peaks in Fig. 5.5 imply, additional simulations were performed while varying either the wavelength of the incident radiation, λ, or the period of the apertures in the shadow mask, p, each by $\pm 20\%$ around their nominal values (λ=365 nm, p=100 nm). The impact of changing the wavelength, λ, to 292 and 438 nm respectively, was negligible and neither was a measurable shift in resonant peak position nor a significant change in peak height observed. Simulations with the aperture period, p, set to 80 and 120 nm respectively, caused a considerable and apparently linear shift in the position of the central resonance peak

as is illustrated in Fig. 5.6, with no discernable change in peak amplitude. This shows a linear variation of the peak position (surface roughness period at which the LWR was greatest) with regards to p, with the peak position occurring at approximately 65% of the grating period. The reason for this non-unity scaling factor is not known at present, but it could be related to the finite domain size in which these simulations were performed.

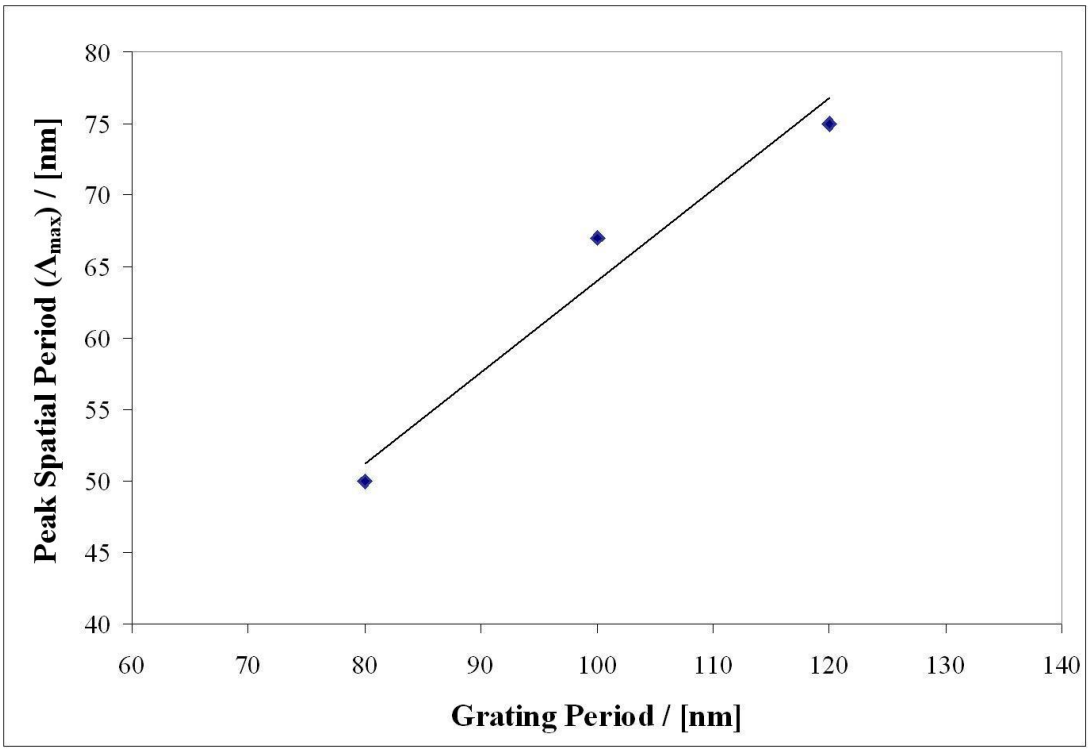

Figure 5.6: Position of the central resonance peak as a function of grating period, p. As a guideline a trendline representing a directly proportional fit has been introduced to the plot. This trendline has a correlation coefficient of 0.64 nm/nm with a coefficient of determination, R^2, of 0.96.

5.5 Potential Implications in Superlens Imaging

This resonant interaction constitutes an additional consideration in regards to superlens enhanced ENFOL. For exposure patterns with features inside a narrow spatial frequency bandwidth it is potentially possible to tailor the metallo-dielectric interfaces

to minimise LWR in the image. This would necessitate excellent control of deposition characteristics such as grain size, and consequently surface roughness spatial frequency, distribution. Conversely, patterns comprised of features with a wide spatial frequency distribution will experience inhomogeneous LWRs. In this case minimising the surface roughness magnitude would become even more important in order to achieve homogeneous imaging characteristics across the entirety of the exposure pattern.

An analysis of superlens images presented in relation to successful superlens lithography experiments yields a LWR figure of more than 100 nm for lines approximately 225 nm wide [20, Fig. 6.19]. This figure is about five times larger than the figure of 19 nm predicted by the FEM simulations for a single layer superlens with interfacial surface roughness of around 1 nm RMS. This implies that the contributions to LWR from other factors, such as the resist and LWR in the mask being imaged, are also of importance. Until these factors can be controlled, a systematic experimental study of the resonant surface roughness interactions presented here is not warranted.

5.6 Conclusions

The results presented here show that there are resonant interactions between superlens surface roughness and LWR when imaging grating-like objects. The resonance peaks, observed for an object consisting of four 50-nm wide apertures spaced periodically at 100 nm, are situated in the surface roughness period range of 30-150 nm, which, unfortunately, falls well within the PSD distribution for a typical thermally deposited silver thin film. Control of grain size during film deposition (whilst maintaining low RMS roughness amplitude) is one possible avenue to mitigating these effects by ensuring that the features being imaged do not strongly resonate with the dominant film roughness interaction modes. Experimental verification of these roughness resonances will only be possible once precise control of surface roughness parameters, in silver thin-film deposition, has been achieved.

6

Calixarene-based photoresist development

This chapter details the development and basic characterisation of a calixarene-based molecular glass photoresist for applications in near-field lithography studies. Most conventional photoresists are polymer-based and as a result their resolution and line edge roughness (LER) potentials are limited by the size of their polymeric constituents. Furthermore, resist manufacturers have no real incentive to develop molecular glass resist for the near-UV.The aim of this work is therefore to investigate the potential use of calixarene-based photoresists for high-resolution, low LER super-resolution patterning at exposure wavelengths in the near-UV part of the electromagnetic spectrum.

Optimisation of resist-schemes for evanescent near-field optical lithography (ENFOL) has already demonstrated impressive performance [4, 46]. Utilising a multi-layer resist scheme consisting of three distinct layers, T. Ito et al. achieved resolution of 22-nm half-pitch line gratings and pattern transfer of 32-nm half-pitch line gratings using a mercury lamp with an I-line (365 nm) band pass filter as the exposure source.

Considering these facts together with the results and conclusions gained from modelling studies of superlens systems, presented in Chapters 4 and 5, there is good reason to assume that ENFOL and superlens imaging can be improved through novel high-performance resists.

Calixarene-based resists have been demonstrated to yield very high resolution and low LER in electron beam lithography (EBL) [116–118], albeit at the cost of sensitivity. Calixarene-based molecular resists have also been investigated for use in extreme ultra-violet (EUV) photolithography [119–121]. By inclusion of an appropriate photo-acid generator (PAG) such resists may be formulated to be sensitive to radiation of a desired photonic energy, allowing the development of a calixarene-based resist sensitive at ultra-violet wavelengths.

While other studies of calixarene-based resists have been conducted [122–124] there are no reports of any investigations of either the particular calixarene, tetramethyl calix[4]resorcinarene (TMC4R), used in this study or the combination of crosslinking agent and PAG utilised here.

6.1 Photoresist chemistry

Fundamentally, a resist is a recording medium in which the medium's physical and/or chemical properties may be altered through selective exposure, e.g. electromagnetic radiation, electrons, etc. The term photoresist specifically covers resists sensitive to electromagnetic radiation. Through this selective exposure, precise and repeatable patterning may be achieved. The ultimate precision of the resulting pattern depends upon a number of factors, the most important of which are the fundamental limitations of the radiation source used in the particular application. Other factors include the limitations of the equipment used (e.g. imperfect optics), atmospheric influences (e.g. noise) and the lithographical performance of the resist scheme used. The fundamental limitations of diffraction-limited optics were covered in Chapter 1. For a given resist scheme the lithographical performance can be quantified by a number of factors:

- Resolution - the smallest achievable feature for a given resist.
- Line Edge Roughness - expected statistical variation in resist features, due to inherent resist and optic characteristics.
- Sensitivity - what energy density is required to clear the resist.

For a given resist scheme these factors may be adjusted in order to reach an optimum compromise which is dictated by the specific application of the resist. The RLS tradeoff is a description of the interdepence of these three factors, see Eq. 8 in Steenwinckel et al.[125]. Eq. 6.1 describes the approximate relation between these three factors, where R is the resolution, L the LER, S the sensitivity and k is a material constant dependent upon the resist scheme and exposure tool in question. Adjusting these factors can be achieved by varying the relative ratios of the resist compounds and process parameters [126].

$$R^3 \cdot L^2 \cdot S = k, \tag{6.1}$$

The resist investigated in this project was a negative tone, chemically amplified, molecular glass resist which operated in the near-UV part of the spectrum. The resist scheme consisted of the following compounds:

- Base molecule - a modified tetramethyl calix[4]resorcinarene (TMC4R).
- Crosslinker - hexakis[methoxymethyl]melamine (HMMM).
- Photoacid generator - Ciba Irgacure PAG103 (PAG).
- Solvent - propylene glycol monomethyl ether acetate (PGMEA).
- Developer - PGMEA.

The calixarene molecule was synthesised at the Department of Chemistry at the University of Canterbury and the synthesis process is described in Section 6.1.1. Calixarene molecules have a characteristic bowl-like structure (calix means chalice in Greek) and, in the case of the calix[4]resorcinarene the, "chalice" consists of four benzene rings, see Fig. 6.1.

The crosslinker, HMMM, was procured from Tokyo Chemical Industry Co., Ltd., Japan, and reacts, in the presence of sulfonic acid, with calixarene to form large intertwined supramolecular structures. HMMM is also known as 2,4,6-Tris[bis(methoxymethyl)amino]-1,3,5-triazine or N,N,N',N',N",N"-Hexakis(methoxymethyl)melamine. A schematic diagram of the molecule is shown in Fig. 6.2 together with a 3D model.

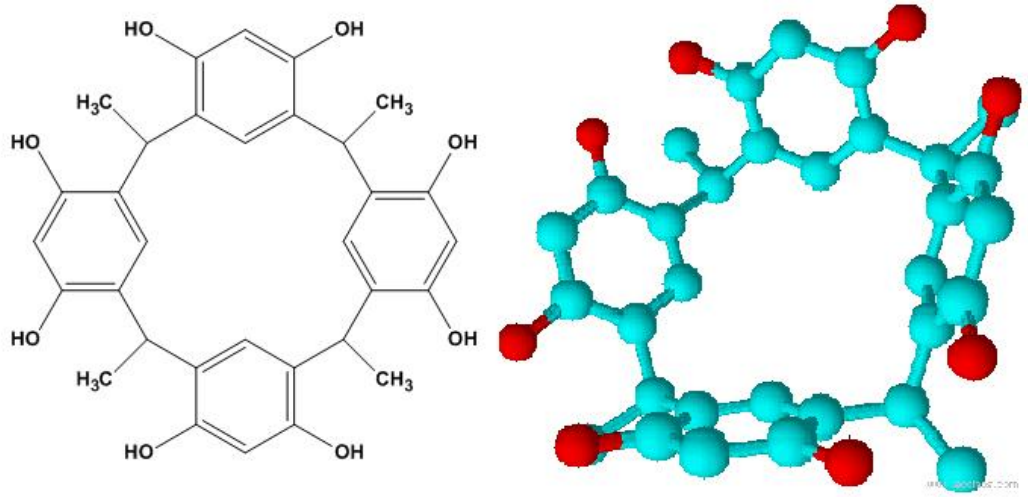

Figure 6.1: Tetramethyl calix[4]resorcinarene schematic diagram and 3D representation.

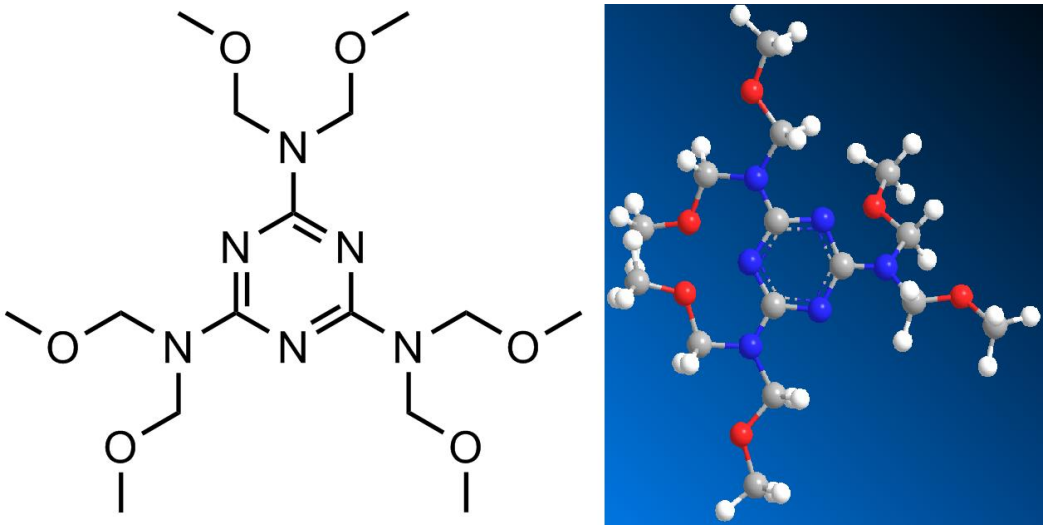

Figure 6.2: Hexakis(methoxymethyl)melamine schematic diagram and 3D representation.

The photoacid generator (PAG), Irgacure PAG103 [127] was bought from the New Zealand agent for Ciba, which is part of the BASF corporation, Ludwigshafen, Germany. It is sensitive across the spectral range from 190 to 450 nm. Upon photo-exposure the compound liberates n-propane sulfonic acid, as shown in Fig. 6.3, which then catalyses the crosslinking of calixarene and HMMM.

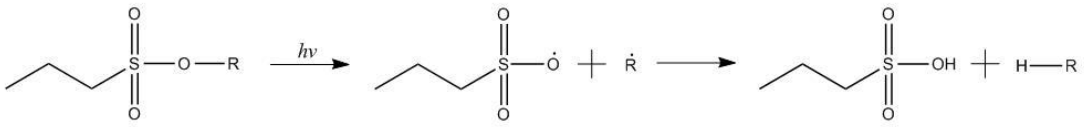

Figure 6.3: Schematic diagram of the photo-initiated liberation of n-propane sulfonic acid from the PAG molecule [127]. No details are available regarding the actual photo-active component of PAG103 as such the R-group is merely included to illustrate where the photoactive component attaches to the sulfonic acid. Initial photonic interaction releases the sulfonic acid radical from the photoactive group. Following their release, the radical components will strip hydrogen atoms from their environment, in this case the most likely donor will be left-over PGMEA.

The solvent PGMEA is a widely used as a resist solvent combining a low evaporation rate with a very low tendency to form particles at high resist dilution rates. Since this is a negative tone resist, no change occurs in the unexposed regions of the resist which, therefore, remain readily soluble in PGMEA. As a consequence PGMEA may be utilised as both resist solvent and as a developer in this resist scheme.

6.1.1 Calixarene synthesis

The calixarene used in this resist was a modified tetramethyl calix[4]resorcinarene (m-TMC4R). The TMC4R molecule was synthesised through condensation of resorcinol with acetaldehyde. While the exact details of the chemical process is beyond the scope of present thesis, molecular diagrams of the constituents and product are shown in Fig. 6.4.

The synthesis followed the procedure outlined below.

1. Resorcinol dissolved in a 50% ethanol-water solution.
2. Acetaldehyde added and mixture heated to 75°C using a silicone oil bath.
3. Concentrated hydrochloric acid added to the heated mixture, to catalyse reaction.
4. Mixture left at 75°C for one hour, then removed and left to cool at room temperature for another hour.

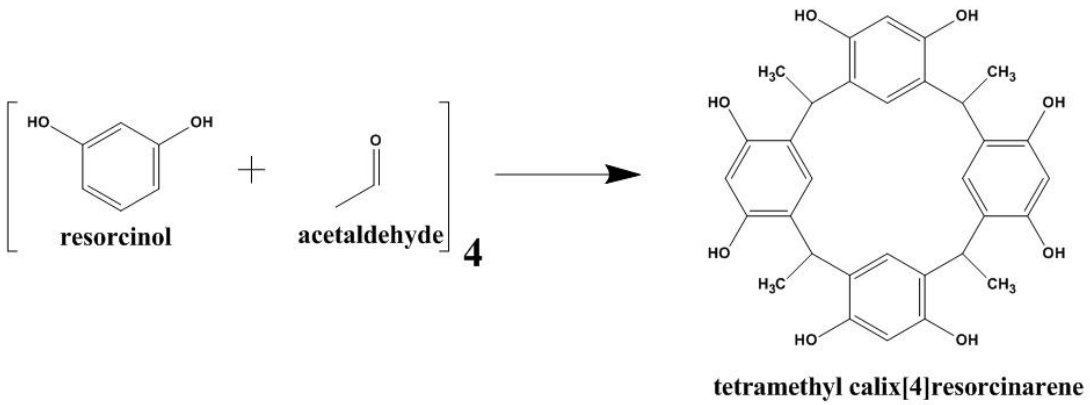

Figure 6.4: Tetramethyl calix[4]resorcinarene synthesis from resorcinol and acetaldehyde.

5. TMC4R filtered from mixture using glass filter under vacuum.

6. TMC4R washed with DI water to remove reaction residues.

7. Resulting clean TMC4R-water slurry left to dry out in a 60°C oven for 48+ hours.

The process outlined above yielded a very pure product, see the TMC4R hydrogen nuclear magnetic resonance (NMR) spectrum in Fig. 6.5, albeit at the cost of low yield, approximately 22%.

The resulting TMC4R will, when dissolved in PGMEA, tend to form aggregate supramolecular structures which precipitate from the solution [128]. This precipitation occurs within hours of initial mixing of TMC4R in PGMEA and consequently reduces the practical shelf life of resists based on such solutions to zero. This phenomenon can be prevented by breaking the TMC4R's molecular symmetry. Disruption of the TMC4R's symmetry can be achieved by attaching an additional sidegroup to a fraction of the hydroxyl groups. In this case a methylbenzene group was added to approximately 25% of the hydroxyl groups through condensation with benzyl bromide, see Fig. 6.6.

This modified TMC4R (m-TMC4R) was produced using the procedure presented below. Sodium hydride was used to provide the alkaline reaction environment to facilitate the condensation. Due to the hydrophilic and reactive nature of sodium hydride the

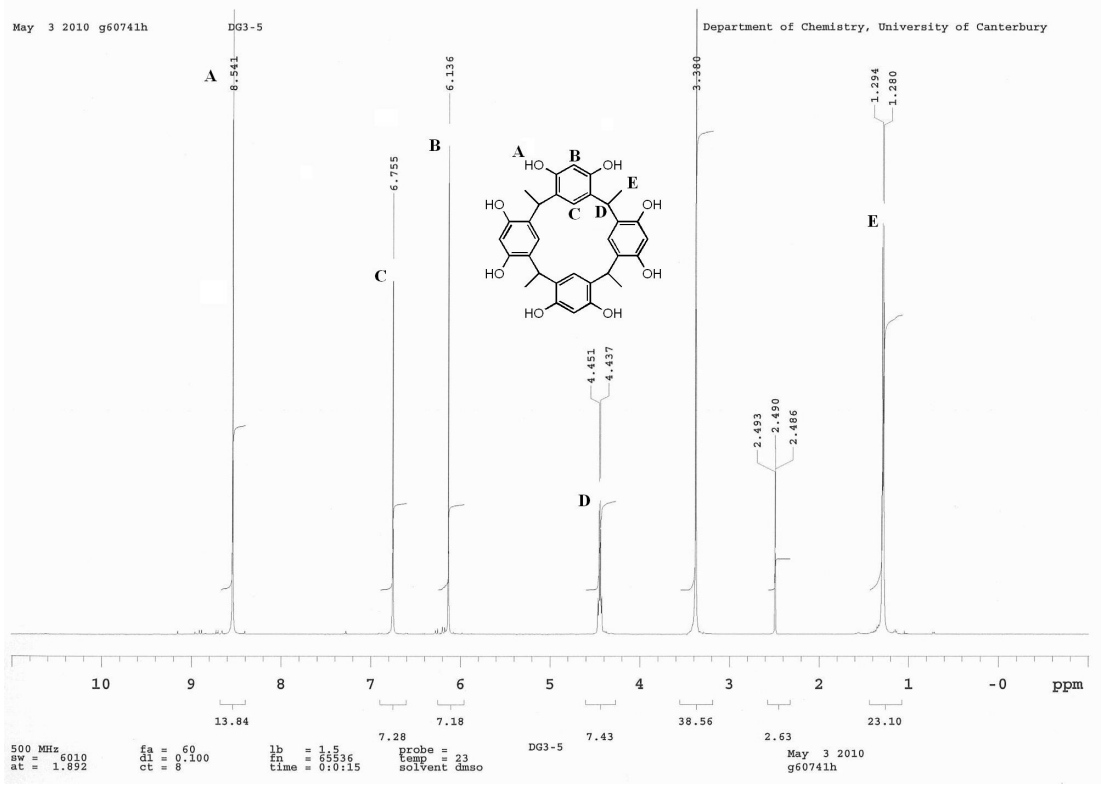

Figure 6.5: Hydrogen NMR of tetramethyl calix[4]resorcinarene. No unexpected peaks were observed, indicating good purity. The two unlabeled peaks were due to the DMSO solvent used in NMR sample preparation.

procedure was performed in a nitrogen atmosphere. Due to the toxicity of benzyl bromide great care was taken in the handling and weighing of this substance.

1. Sodium hydride cleaned with petroleum ether in a nitrogen atmosphere to strip protective oil from the sodium hydride.
2. TMC4R added to the clean and dry sodium hydride powder.
3. Add reaction solvent - Dimethylformamide (DMF) - to the mix.
4. Benzyl bromide added to the mixture.
5. Reaction left to stir at 50°C overnight.

Once the reaction had run its course the m-TMC4R was separated from the solution. Separation was achieved using the following procedure.

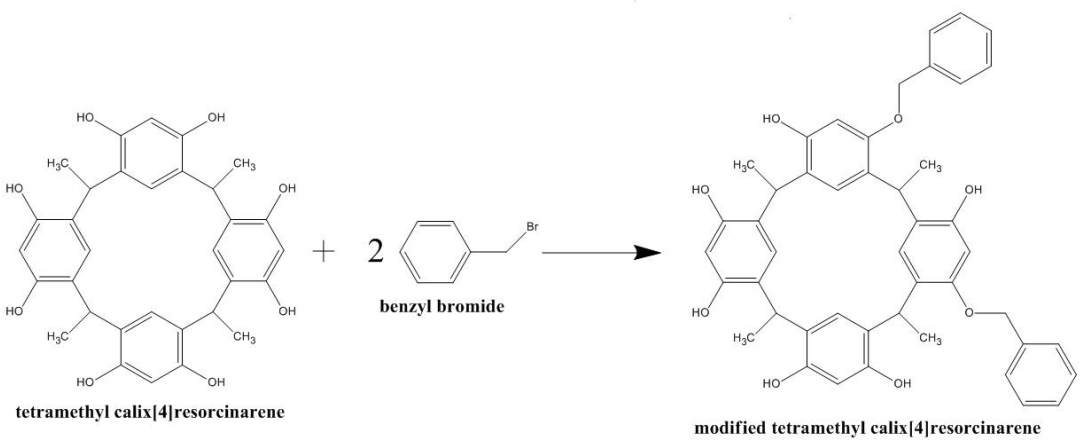

Figure 6.6: Tetramethyl calix[4]resorcinarene is modified, by reaction with benzyl bromide, to break the molecule's symmetry.

1. Saturated ammonium chloride aqueous solution added to the mixture.

2. Mixture washed repeatedly with ethyl acetate to move calixarene out of the DMF/water mixture. Following each consequtive wash, separate and set aside ethyl acetate. Once thoroughly washed, discard DMF/water mixture.

3. m-TMC4R/ethyl acetate solution washed several times with DI water to remove water soluble impurities.

4. Mixture washed with saturated sodium chloride aqueous solution to improve separation between water and ethyl acetate.

5. Mixture dried using sodium sulfate leaving a clean anaqueous calixarene/ethyl acetate solution.

6. Ethyl acetate evaporated by heat and vacuum to leave concentrated solution of m-TMC4R in ethyl acetate.

7. m-TMC4R precipitated from the concentrated calixarene-ethyl acetate solution by adding it slowly to petroleum ether reservoir.

8. Product filtered from the mixture using a glass filter under vacuum.

The yield of the modification process was approximately 80%. Resists based upon m-TMC4R have shown no tendency to form supramolecular precipitates, even after more than 6 months the resists remain clear with no precipitation forming on the bottom.

6.1.2 Chemical amplification and crosslinking

In conventional, non-chemically-amplified, photoresists the change in physical and chemical properties of the resist medium is typically caused by direct interaction between incoming photons and the resist material itself. However, in chemically amplified resists photonic interaction liberates catalytic components which then instigate either the deprotection or crosslinking of the photoresist depending upon resist tone. The catalyst will typically be a strong acid liberated from a larger photosensitive group when the photo-acid generator (PAG) interacts with a photon, as shown in Fig. 6.3. By choosing an appropriate PAG, chemically amplified resists may be tailored to suit various lithographical applications utilising a wide range of exposure sources (e.g. EBL, UVL, DUV and EUV)[117, 121].

The rate of the chemical reaction catalysed by the acid is sensitive to temperature, as such a post-exposure bake (PEB) is a crucial step for chemically amplified resists. The PEB parameters, temperature and time, have a significant impact upon the resulting image. Since the acid itself is not consumed in the reaction, each acid may cause several reactions and consequently acid diffusion will have an impact upon both resolution and LER. Conversely, if the temperature is kept too low or the time too short resist inversion will be incomplete even in fully exposed areas, which will result in poor pattern transfer.

In the resist investigated in this project the PAG liberates propane sulfonic acid which in turn catalyses the crosslinking process between m-TMC4R and HMMM. During this process methoxyl-groups are liberated from the HMMM molecule. The crosslinking mechanism itself occurs when the HMMM bonds to one of the benzene rings of the m-TMC4R molecule. The end result is a crosslinked m-TMC4R-HMMM connection, the acid catalyst and two methanol molecules per crosslinking reaction. See Fig. 6.7 for a diagram of this reaction. The methanol evaporates out of the film during the PEB and will contribute to the significant film thickness shrinkage described in Section 6.2.2.

Compound	**Chemical formula**	**Molar mass** [g/mol]
Resorcinol	$C_6H_6O_2$	110.04
Acetaldehyde	C_2H_4O	44.05
Benzyl bromide	C_7H_7Br	171.06
TMC4R	$C_32H_32O_8$	544.59
m-TMC4R	$C_46H_44O_8$	724.84
HMMM	$C_15H_30N_6O_6$	390.44
Propane sulfonic acid	$C_3H_7SO_3H$	124.16
PGMEA	$C_6H_12O_3$	132.16

Table 6.1: Tabel showing the names, chemical formulas and molar masses of compounds used in the TMC4R-based photoresist.

The continuous crosslinking of TMC4R and HMMM forms large supramolecular structures which form a highly chemically resistant film, see Fig. 6.8.

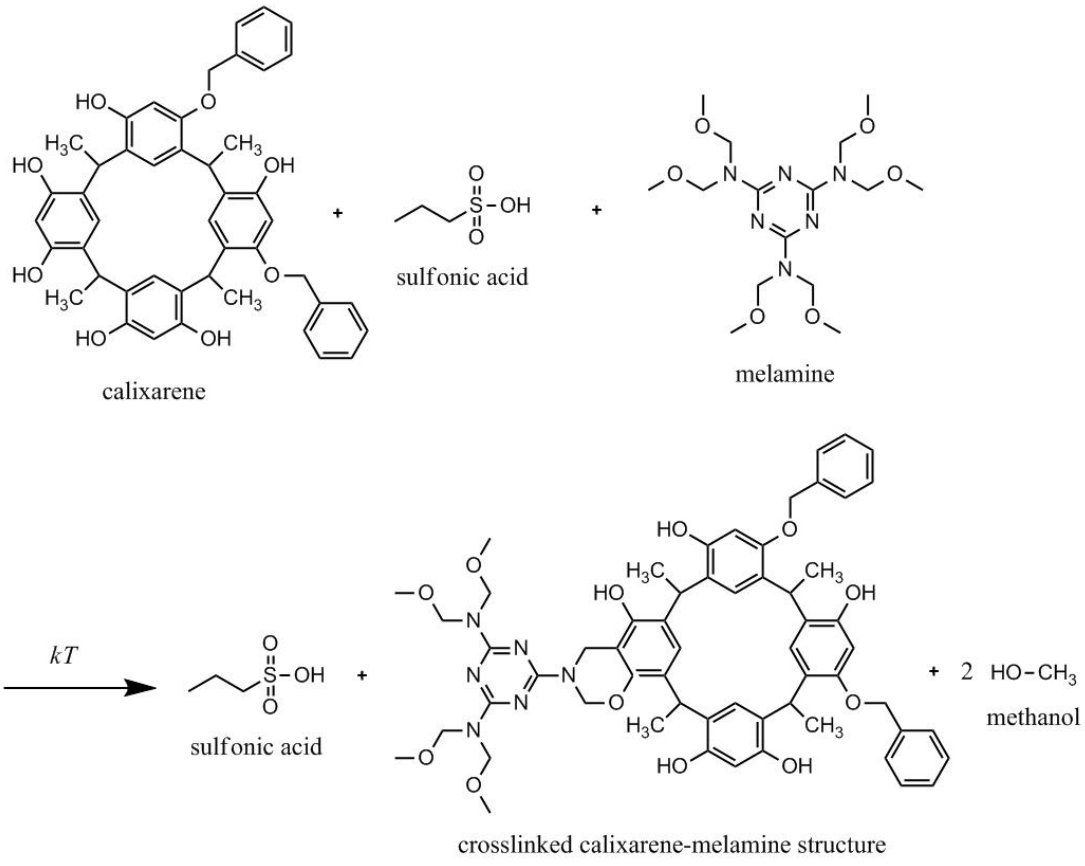

Figure 6.7: Crosslinking process: the sulfonic acid catalyses the liberation of methanol from the HMMM molecule which then forms a bond with the TMC4R. For 100% complete crosslinking each TMC4R molecule would bond to four HMMM molecules which in turn would each connect to three TMC4R molecules.

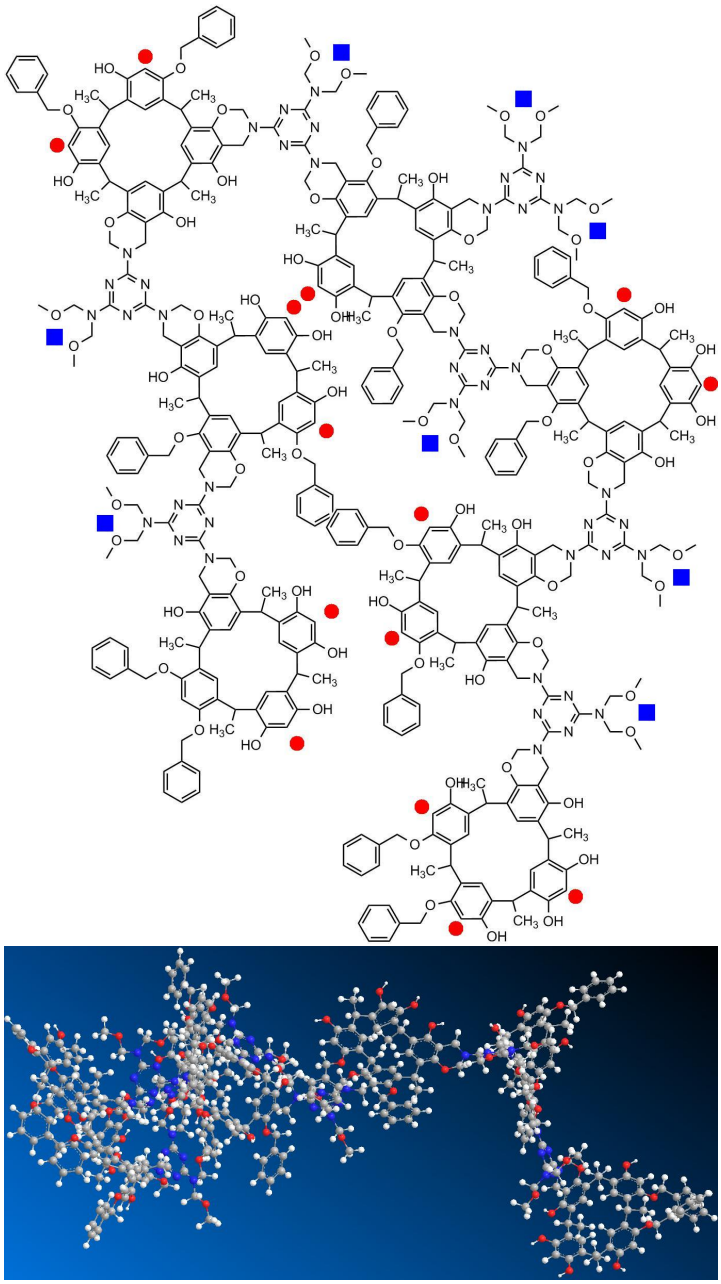

Figure 6.8: An example of a crosslinked TMC4R-HMMM structure. Top: 2D representation of the structure. Potential sites for further crosslinking connections are illustrated by blue squares (TMC4R) and red dots (HMMM). The actual structure is three dimensional and is not easily represented by a two dimensional illustration. Bottom: A 3D rendition of the 2D structure presented above.

6.2 Calixarene resist development

Section 6.1 covered the mechanisms and components of the TMC4R-based photoresist as well as the synthesis and modification of the TMC4R molecule. This section covers the experimental work undertaken to establish relative mixing ratios of the various constituents that produces a functional resist. The aim of this work was to establish a resist formulation that provided both high resolution as well as a low LER.

6.2.1 Spin characteristics

In order to characterise the spin-coating properties of the resist, initial tests were performed using a solution consisting of TMC4R and HMMM (in a 1:1 ratio) in PGMEA. These tests were performed using a Headway Research PWM32 spiner and no PAG was added to the resist mixture for these tests. Attempts at spin-coating clean silicon wafers indicated adhesion issues between the resist and substrate. Oxygen plasma surface treatments, 60 s at 100 W in an Emitech K1050X plasma asher, were found to improve adhension noticably, as shown in Fig. 6.9. It was also noticed that film coverage homogeneity improved with high spin-acceleration values.

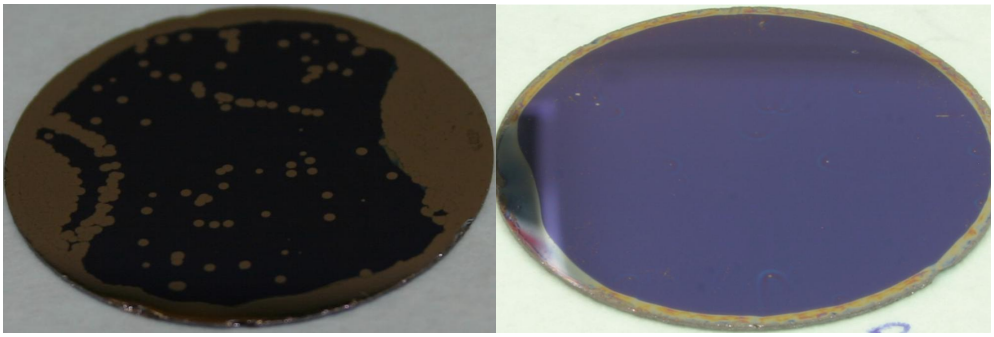

Figure 6.9: Photographs of 2" silicon wafers with TMC4R resist. Left: The untreated surface exhibits poor adhesion. Right: A 60 s oxygen plasma treatment at 100 W shows improved resist adhesion.

Due to the maleability of the soft unexposed molecular resist, getting consistent film thickness measurements from the Dektak profilometer proved difficult. A bottom anti-reflection layer (BARL), AZ©BARLi II 200 from AZ electronic materials UK, served the additional role as an adhesion layer allowing very good, homogeneous, resist film

coverage across the samples. Furthermore, the BARL facilitated formation of clean and well defined trenches, for film thickness measurements, when scratching the surface with a sharp implement. The BARL was spun onto the substrates at 4,000 RPM and subsequently baked at 200°C for 60 seconds. This resulted in smooth, homogeneous films with thicknesses in the range of 150-156 nm as found by profilometric measurements, performed using a Veeco Dektak 150 profilometer.

Spin testing was conducted using 2" silicon wafers, pre-coated with such BARLs, as substrates. For the tests, TMC4R resists, with a calixarene-to-melamine ratio (TMC4R:HMMM) of 1:1 and solid content in the range 3.8-10.3 wt%, were spin coated at rotational speeds between 1,000 and 5,000 RPM for 60 seconds using a rotational acceleration of 10,000 RPM/s. The samples were baked at 100°C for 60 seconds and subsequently measured. As illustrated by the spin-curves seen in Fig. 6.10 these parameters allow for the formation of resist films with thicknesses in the range of 50-300 nm. In Fig. 6.11 the same data is represented as film thickness plotted against resist solid-content given constant rotational speeds.

6.2.2 Dose tests

Dose tests for the TMC4R resists were carried out, using a Karl Suss MA6 mask aligner, by performing several sequential exposures on a single substrate per test-run. This approach was applied to reduce the variation in post-exposure processing parameters between tests. Such precautions were found to be necessary, after several inconsistent test runs, due to the high sensitivity of chemically amplified resists to post-exposure processing. Some inconsistencies were still observed for high-sensitivity resists (high TMC4R:HMMM ratio, low PAG content) due to the considerably longer exposure time. In these cases a measurable reduction in post-development resist thickness was observed as the time between exposure and PEB bake increased.

Resist sensitivity can be tuned by adjusting the PAG content, although too high a photo-acid concentration will affect the statistical imaging performance detrimentally as per the RLS tradeoff discussed in Section 6.1. However, resist sensitivity was also found to be strongly dependent upon the TMC4R:HMMM ratio as is illustrated by Fig. 6.12. The higher TMC4R:HMMM ratio, the higher the clearing dose. This ratio

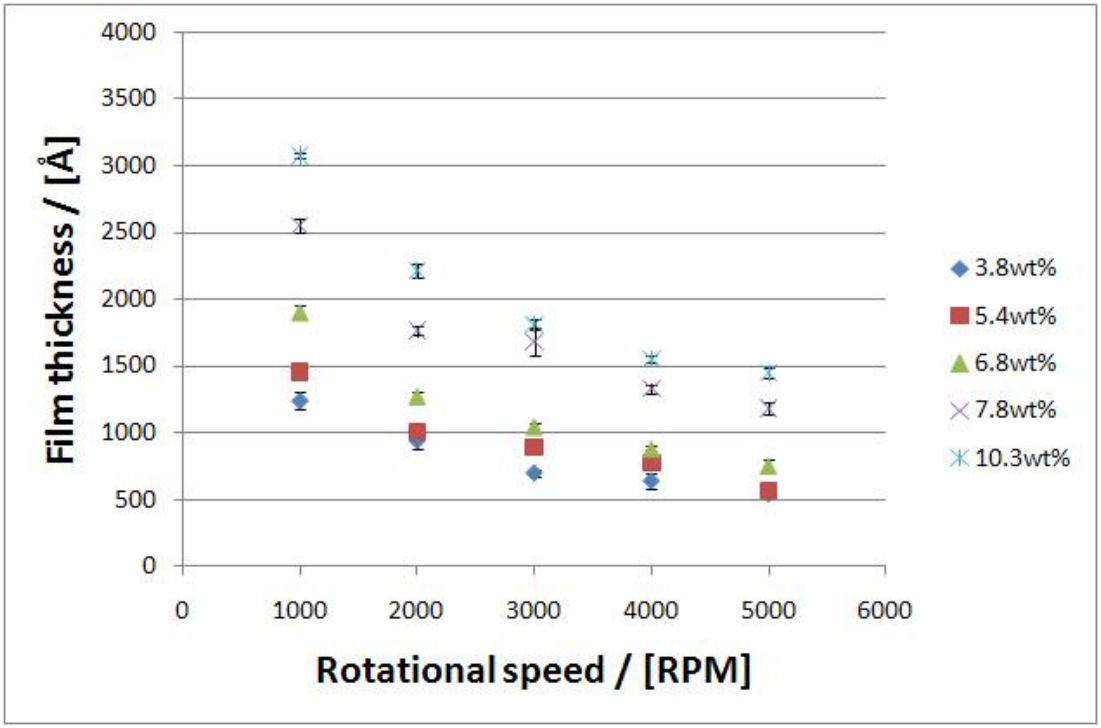

Figure 6.10: Film thickness versus rotational speed.

also has a significant influence upon the resolution of the resist as will be shown in Section 6.2.3.

All dose tests were conducted using silicon substrates coated with BARL. Resists were spun onto these substrates at 3,000 RPM for 60 seconds using an angular acceleration of 10,000 RPM/s. Following the spin coating step the substrates were baked on a hotplate at 100°C for 60 seconds. Exposures were then conducted and a PEB at 100°C for 60 seconds was performed. Later results using resists with TMC4R:HMMM ratios higher than 1 showed improved results by increasing the PEB time from 60 to 300 seconds.

Significant difference in resist thickness prior to, t_0, and following full exposure, t_t, was observed. The magnitude of this difference varied depending upon the TMC4R:HMMM ratio and was, at least in part, due to the liberation and evaporation of methanol that is

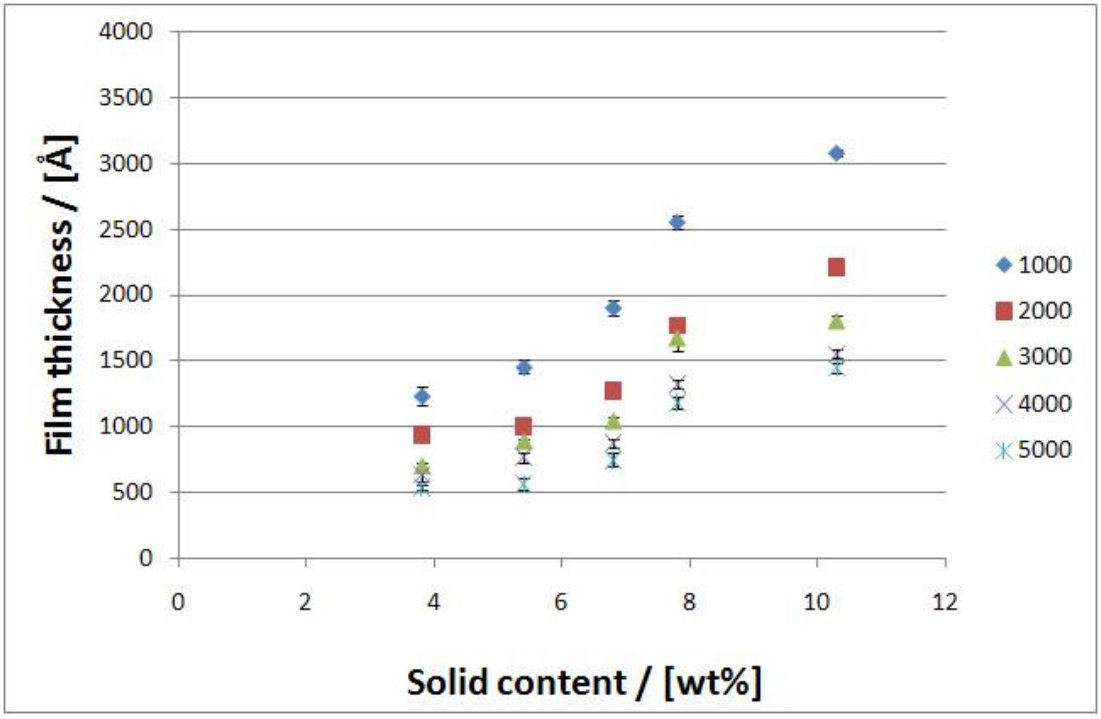

Figure 6.11: Film thickness versus solid content.

part of the crosslinking reaction as described in Section 6.1.2. The crosslinking reaction, and thus the liberation of methanol, only occurs when there are free interaction sites available on both the TMC4R and HMMM. Consequently the higher the crosslinking efficiency the larger the amount of liberated methanol and so the larger the volume loss observed. This is in accordance with the observations shown in Fig. 6.12 and reported in Table 6.2.

In order to evaluate imaging performance, photoresist contrasts were estimated from these exposure curves. The limitations inherent in the experimental procedure made it difficult to achieve ample data density in the critical parts of the dose curves. Consequently the contrasts presented here should merely be considered a viable metric for evaluating the relative imaging performance of the TMC4R resist with varying TMC4R:HMMM ratios. The constrast figures reported here were calculated as per

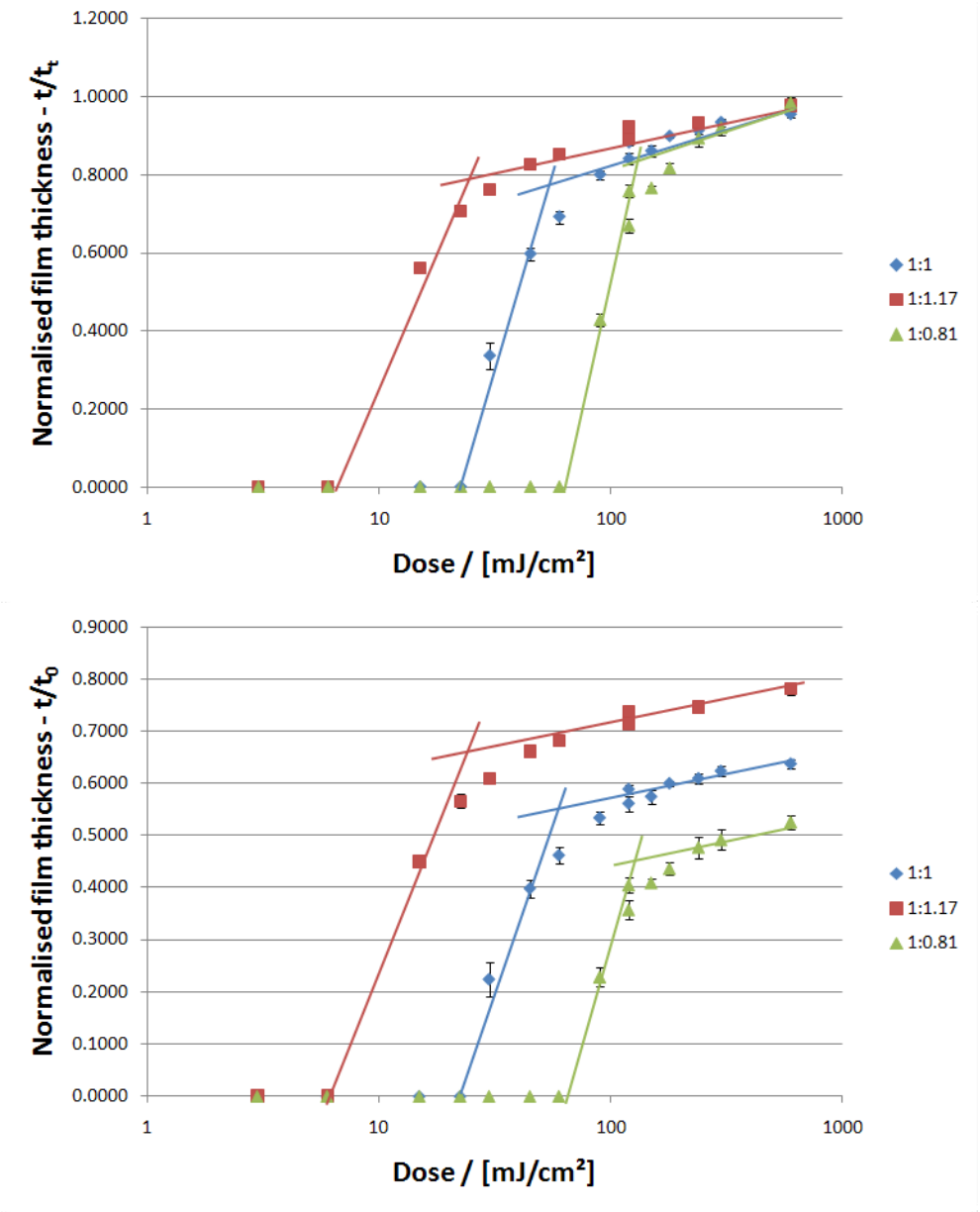

Figure 6.12: Normalised film thickness after development versus exposure dose for resist with three different TMC4R:HMMM ratios. Top: Post-development resist thickness measurements normalised to the thickness, t_t, of the fully crosslinked resist. Bottom: Post-development resist thickness measurements normalised to the thickness, t_0, of the resist prior to exposure.

TMC4R:HMMM	γ	**Gel dose** [mJ/cm^2]	$\mathbf{t_t/t_0}$
1:0.81	0.94	145	0.53
1:1	0.83	70	0.64
1:1.17	0.49	31	0.78

Table 6.2: Contrast, γ, and sensitivity measurements for TMC4R resists with a PAG-to-solid content ratio of 1:21. Contrasts were calculated through use of Eq. 6.2.

Eq. 6.2 [2], where ln is the natural logarithm.

$$\gamma = \pm \frac{1}{D} \frac{dz}{d \ln E}\bigg|_{E=E_0} = \frac{t_t}{t_0} \frac{1}{\ln\left(\frac{E_g}{E_0}\right)} \tag{6.2}$$

In Eq. 6.2 D is the pre-development resist thickness, dz is the variation in resist thickness, E_g is the clearing dose and E_0 is the onset dose at which the post-develoment resist thickness starts to change.

6.2.3 Coarse resolution tests

Initial resolution tests were carried out using conventional UVL shadow masks. The shadow masks were fabricated using a Heidelberg Instruments μPG101 mask writer and contained a number of different test-patterns as shown in Fig. 6.13, with representative lithography results shown in Fig. 6.14. These test-patterns included a 1x1 cm^2 square aperture, lines of text, 8-way crosses and line grating arrays. The 8-way crosses were composed of four rectangular lines, measuring 500x10 μm^2, intersecting each other at their centre. The line grating arrays featured linewidths (LW) of 3, 5, 10 and 20 μm with duty cycles of 25 and 50%. The 8-way crosses provided informative visual feedback when optimising dosage, PEB and development parameters. Due to the angle between the arms of the crosses, achieving sharp definition at these points is strongly dependent upon optimising process parameters. The various gratings were used to establish good mixing ratios between TMC4R and HMMM as well as exposure, PEB and development parameters. The text features were included to include rounded features with a range of pattern densities and curvatures. The 1x1 cm^2 aperture was included in case ellipsometric film characterisation was to be undertaken.

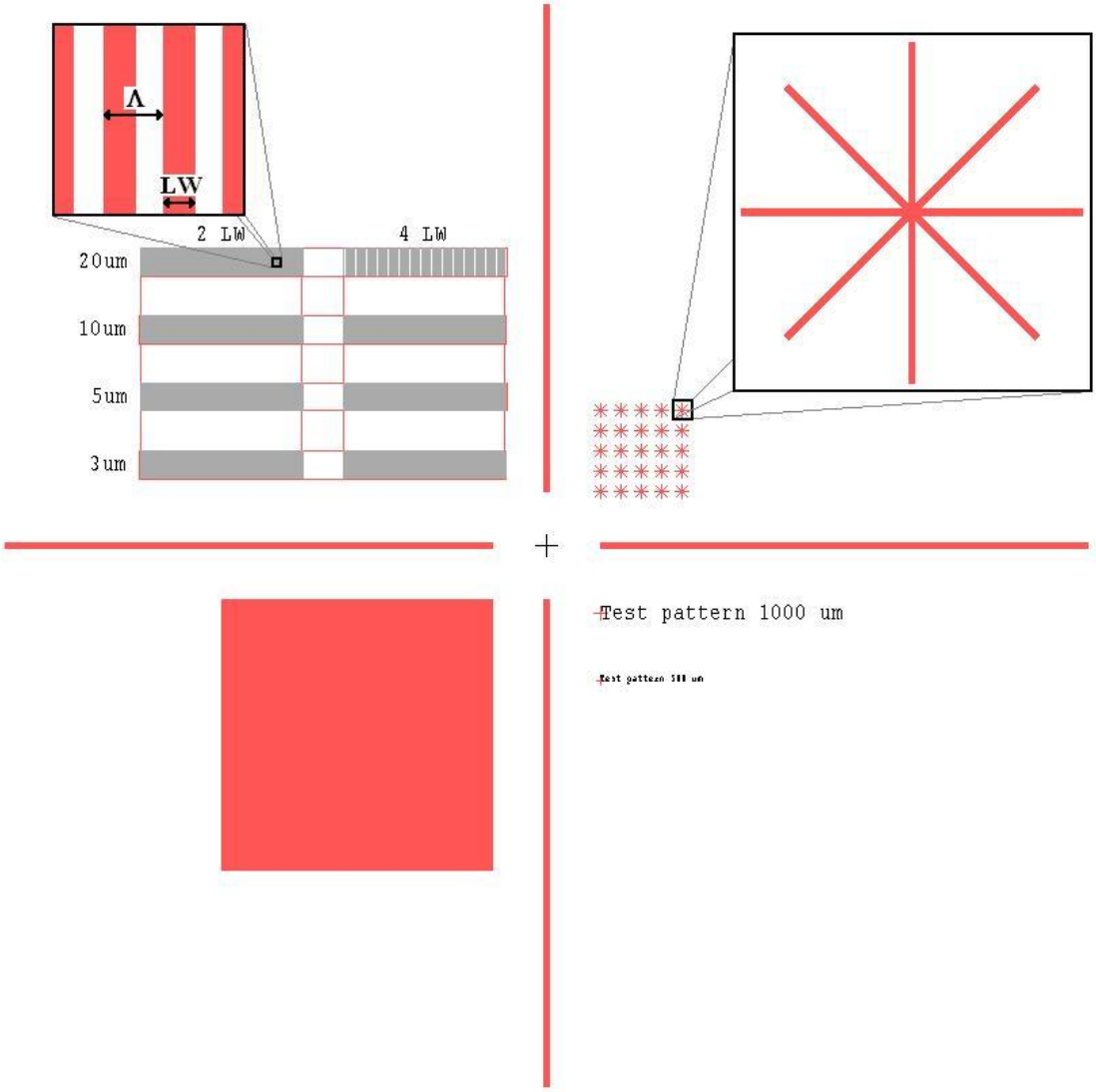

Figure 6.13: UVL resolution test pattern overview. The patterns types are divide by quandrants. In the first quadrant are the 8-way crosses. Line gratings are situated in the 2nd quadrant. The pattern in the 3rd quadrant consists of a 1x1 cm^2 aperture. In the 4th quadrant are several repeated lines of text at different font sizes.

As was initially observed in the dose-test, the calixarene-to-melamine (TMC4R:HMMM) ratio had a strong influence upon lithographic performance in regards to resolution. With a resist composition of TMC4R:HMMM 1:1, the resolution was adequate to resolve even the smallest and densest line grating (LW=3 μm, Λ=6 μm) at a dose where even the sparsest of patterns were still nicely formed, as illustrated by Fig. 6.14. In an attempt to reduce the magnitude of the film thickness shrinkage during processing, see Section 6.2.2, the relative HMMM content was increased. While this modification did both reduce the film shrinkage and lower the clearing dose it also had a detrimental impact upon resolution. At a TMC4R:HMMM ratio of 1:1.37 it was no longer possible to resolve either of the 3 μm line gratings or the 5 μm half-pitch grating, as illustrated by Fig. 6.14(column D). Furthermore, for isolated structures, like the 8-way crosses, it became very difficult to achieve high pattern resolution due to the variation of aerial exposure density across the pattern combined with the lower clearing dose. As a result the arms on the crosses would become tapered along their lengths while the central region of the pattern would become a shapeless blob with crescent shaped "corners". Based upon these observations another resist composition consisting of TMC4R:HMMM 1:0.81 was tested. A significant increase in clearing dose was observed for this resist, as shown in Table 6.2, as well as improved resolution which will be discussed in Chapter 7.

6.2.4 Summary

A UV sensitive photoresist scheme based upon TMC4R was developed and investigated in regards to:

- Mixing ratio of resist constituents (TMC4R:HMMM ratio).
- Dose curves.
- Coarse resolution imaging performance.
- Spin curves.

It was found that the TMC4R:HMMM ratio is crucial in regards imaging resolution, clearing dose and film thickness shrinkage during processing. Better image resolution and contrast was achieved for TMC4R:HMMM ratios larger than 1 at the cost of both

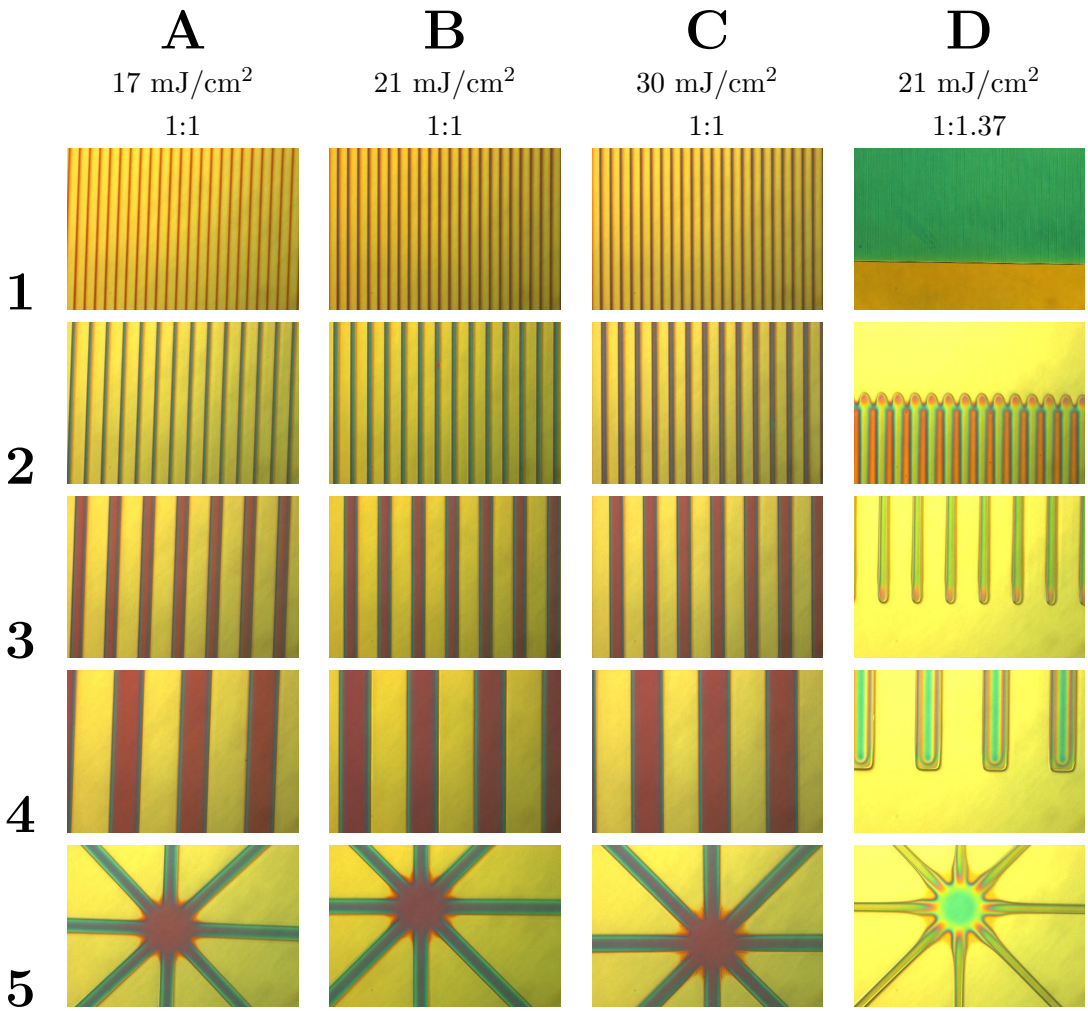

Figure 6.14: Microscope captures of coarse resolution tests. Columns A, B and C show results for resists with a TMC4R:HMMM ratio of 1:1 at exposure doses of 17, 21 and 30 mJ/cm^2 respectively. Column D shows the results from a resist with a TMC4R:HMMM ratio of 1:1.37 with an exposure dose of 21 mJ/cm^2. The contents of the rows are as follows: 1) 3 μm line width (LW), 50% duty cycle (dc), 2) 5 μm LW, 50% dc, 3) 10 μm LW, 50% dc, 4) 20 μm LW, 50% dc and 5) 8-way crosses, 10 μm LW.

increased film shrinkage and reduced photospeed. Conversely TMC4R:HMMM ratios less than 1 showed improved photospeed and less film shrinkage while exhibiting poorer image resolution and contrast.

Coarse resolution tests showed good resolution of 3 μm half-pitch gratings at exposure doses in the range of 20-30 mJ/cm^2 for resists with a TMC4R:HMMM ratio of 1:1.

Dose tests indicate clearing doses in the range of 30-150 mJ/cm^2 and contrasts in the range of 0.49-0.94 depending upon the TMC4R:HMMM ratio for resists with a PAG-to-solid content (PAG:SC) ratio of 1:21.

Spin coating tests showed that the resist forms smooth, uniform films in the range from 50 to 300 nm for resists with solid contents (SC) in the range from 3.8 to 10.3 wt% spun at rotational speeds between 1000 and 5000 RPM.

In order to properly characterise the high-resolution imaging performance of this resist scheme lithography techniques such as interference and near-field lithography must be applied, as is discussed in the following chapter.

7

Sub-wavelength resolution imaging using a calixarene-based photoresist

This chapter documents experimental work into super resolution imaging utilising the calixarene-based photoresist scheme described in chapter 6. While chapter 6 covered the fundamental characteristics of the resist, this chapter will provide a greater insight into its lithographic performance through subwavelength resolution imaging. The first section of this chapter will describe work conducted using an interference lithography (IL) setup, more precisely a Lloyd's mirror. The second section describes the work undertaken in order to realise near-field imaging using the calixarene-based resist as well as the results obtained from this work.

7.1 Interference lithography

Using a Lloyd's mirror interference lithography (IL) setup (see figure 7.1), with a helium cadmium (HeCd) laser, operating at a freespace wavelength, λ, of 325 nm, large area gratings were defined in the calixarene-based resist. A Lloyd's mirror setup is capable of defining gratings with periods down to a theoretical minimum of $\frac{\lambda}{2n}$, where n is the refractive index of the medium in which the interference occurs, (corresponding to a line width (LW) of $\frac{\lambda}{4n}$ in the case of a perfect half-pitch grating) at grazing incidence ($\theta = \frac{\pi}{2} = 90°$).

Line gratings with periods of 1000 nm, 500 nm and 250 nm were defined using this experimental setup. The resist patterns were subsequently characterised through scanning electron microscopy (SEM) and subsequent line-edge-roughness (LER) analysis.

7.1.1 Basic theory

Interference lithography relies on the interference of two, or more, coherent optical beams. The Lloyd's mirror setup used in these experiments consists of a mirror set at a right angle to a sample holder. The mirror setup is rotated at an angle, θ, relative to the optical axis of an incoming beam of light as shown in Fig. 7.1; the beam reflected by the mirror interferes with the incoming beam producing a standing wave interference pattern with nodes perpendicular to the sample surface.

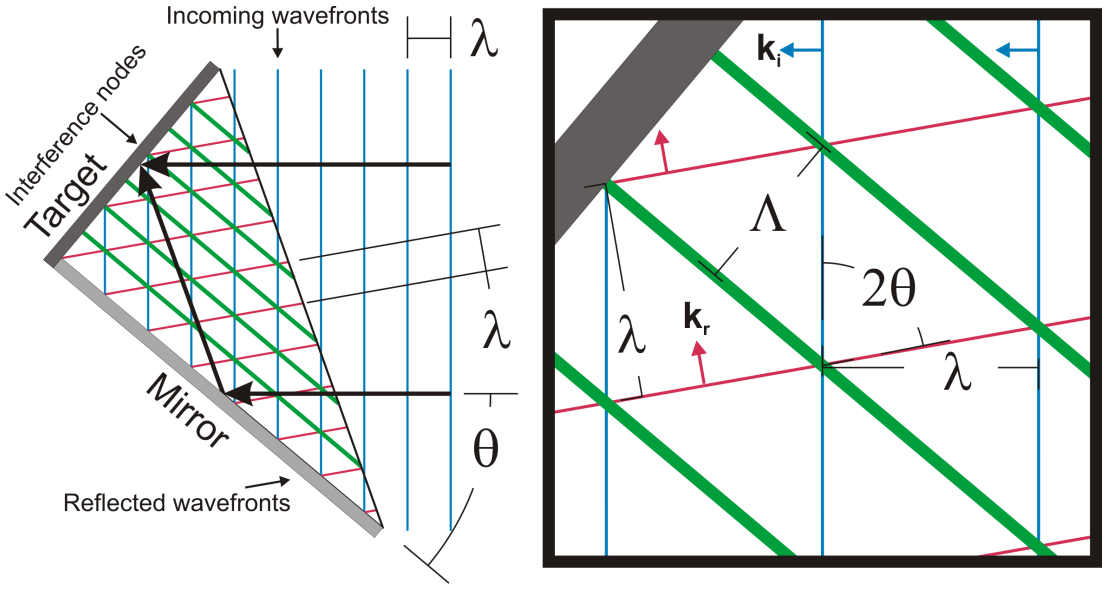

Figure 7.1: A Lloyd's mirror interference lithography setup. A substrate (dark grey slab) is set at an angle of 90° to a mirror (light grey slab). A plane wave (blue) propagating from the right hits the substrate at an incident angle of θ and reflects off the mirror at an angle of $\pi - \theta$. The reflected plane wave (red) interferes with the incident wave (blue) and causes a standing wave interference pattern (green) to arise.

Considering Fig. 7.1 it follows from basic geometric laws (the right-angled triangle and the law of sines) that the period, Λ of the interference pattern nodes can be found from the wavelength, λ, the angle of incidence, θ and the refractive index, n, of the medium occupying the space between the mirror and substrate, as:

$$\Lambda = \frac{\lambda}{2n\sin(\theta)} \tag{7.1}$$

From this point onwards it is assumed that experiment is performed in a medium with refractive index, n, equal to unity.

Consider a plane wave $\mathbf{E}_i$, with an optical intensity given by I_0, incident upon the Lloyd's mirror setup. The reflected plane wave $\mathbf{E}_r$ interferes with $\mathbf{E}_i$ to produce the standing wave interference pattern $\mathbf{E}_s$ given by Eq. 7.2.

$$\begin{aligned} \mathbf{E}_i &= E_0 e^{i(\mathbf{k}_i\cdot\mathbf{r}-\omega t)} \\ I_0 &= \langle|\mathbf{S}|\rangle = \frac{1}{2}\epsilon_0 c E_0^2 \\ \mathbf{E}_r &= rE_0 e^{i(\mathbf{k}_r\cdot\mathbf{r}-\omega t)} \\ \mathbf{E}_s &= \mathbf{E}_i + \mathbf{E}_r \end{aligned} \tag{7.2}$$

Assuming transverse electric (TE) polarisation, Eq. 7.2 yields the following expressions for the maximum and minimum magnitudes of the electric field in the interference pattern:

$$\begin{aligned} |\mathbf{E}_{s,max}| &= E_0(1+r) \\ |\mathbf{E}_{s,min}| &= E_0(1-r) \\ I_{max} &= \frac{1}{2}\epsilon_0 c|\mathbf{E_{s,max}}|^2 \Leftrightarrow I_{max} = I_0\cos\theta(1+r)^2 \qquad (7.3) \\ I_{min} &= \frac{1}{2}\epsilon_0 c|\mathbf{E_{s,min}}|^2 \Leftrightarrow I_{min} = I_0\cos\theta(1-r)^2 \qquad (7.4) \end{aligned}$$

Here I_{max} and I_{min} are the optical intensities at the peak and troughs of the standing wave interference pattern. Note that r is the reflection coefficient, which is related to the reflectance, R, as $R = r^2$. The Michelson contrast, C_m, of the interference pattern is given by Eq. 7.5.

$$\begin{aligned} C_m &= \frac{I_{max}-I_{min}}{I_{max}+I_{min}} = \frac{(1+r)^2-(1-r)^2}{(1+r)^2+(1-r)^2} \\ C_m &= \frac{2r}{1+r^2} \end{aligned} \tag{7.5}$$

7.1.2 Experimental setup

The Lloyd's mirror experimental setup used for the work presented here, with the setup schematic shown in Fig. 7.2, consisted of a Kimmon IK3501R-G HeCd laser emitting at a freespace wavelength, λ, of 325 nm. The electric field, $\mathbf{E}_i$, of the emission was linearly polarised in the vertical direction (i.e. TE polarised) at a polarisation ratio of >500:1. The laser had a coherence length of 30 cm, a beam diameter of 1.2 mm and beam divergence of 0.5 mrad [129]. Photos of the experimental setup are shown in Fig. 7.3

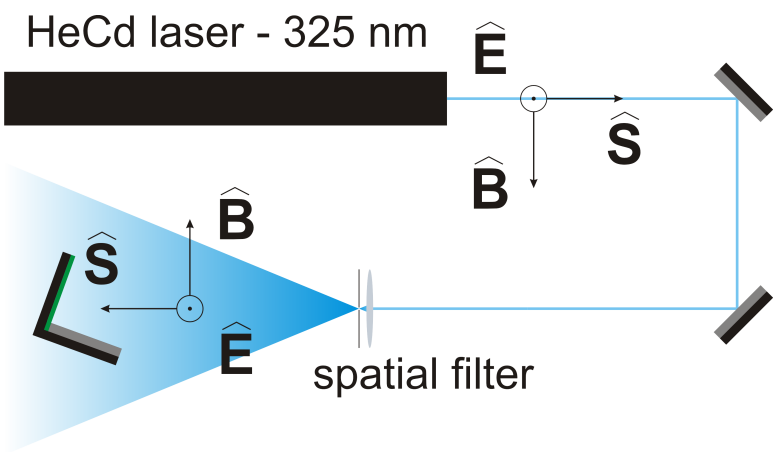

Figure 7.2: Diagram showing the Lloyd's mirror experimental setup and the polarisation orientation of the electric (**E**) and magnetic field (**B**) as well as the direction of the pointing vector (**S**).

The laser beam was, via two mirrors, directed through a spatial filter, consisting of a focusing lens with a focal length of 11 mm and a 5-μm diameter pinhole situated at the lens' focal point. There was no collimating lens beyond the pinhole resulting in a very wide Gaussian beam profile at the target which was situated 1 m from the pinhole. The beam power, P_0, at the target was measured using a Thorlabs PM100A power meter with a detector surface area, $A_{detector}$, of 0.708 cm^2. The optical intensity, I_0, of the incoming beam, at the target, was calculated using Eq. 7.6.

$$I_0 = \frac{P_0}{A_{detector}} = \frac{P_0}{0.708\ cm^2}. \tag{7.6}$$

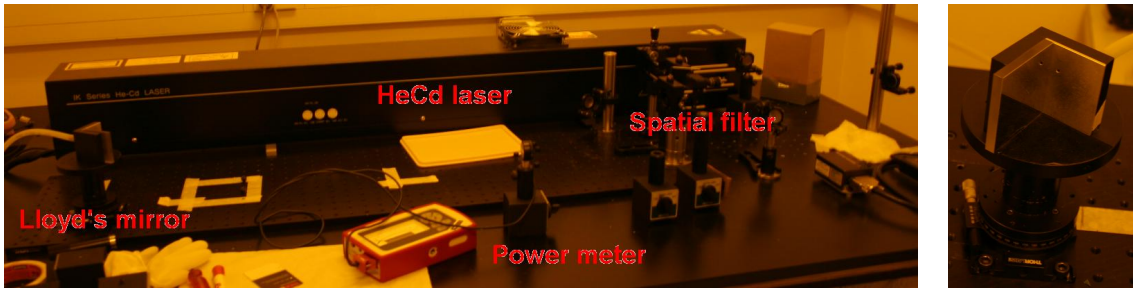

Figure 7.3: Left: The experimental IL setup featuring a HeCd laser, spatial filter, Lloyd's mirror and power meter. Right: Detail of the Lloyd's mirror consisting of a rotational stage with a sample holder and mirror mounted at 90°.

The target holder consisted of a right-angled bracket set on top of a rotational stage. One side of the bracket was a vacuum chuck connected to a vacuum pump, for holding the sample substrates, and the other side held an optically flat mirror with a reflectance, R, in the range of 92-93% at λ =325 nm depending upon the angle of incidence.

Sample preperation was performed by spin coating 4" diameter silicon wafers with a bottom anti-reflection layer (BARL), BARLi II 200, spun at a speed of 4,000 RPM for 60 seconds and subsequently baked at 200°C for 60 seconds. The 4" wafer was then spin coated with the tetramethyl calix[4]resorcinarene (TMC4R) based photoresist described in Chapter 6 and then cleaved into smaller pieces using a diamond scribing tool and tweezers. The spin-coating procedure was performed using a Headway Research PWM32 spinner.

Prior to every exposure the angle of incidence, θ, was set and the beam power, P_0, was measured. The exposure time, t, was controlled and measured using an improvised shutter and a stopwatch. The exposure dose, D_{exp}, was calculated as $D_{exp} = I_{max} \cdot t$ with I_{max} given by Eq. 7.3.

Following exposure the sample was transported from the laser lab to a separate resist-processing laboratory (the UCNFL 'yellow room') for post exposure baking (PEB) at 100°C for a period between 60 and 300 seconds. Initially a PEB of 60 seconds was applied, however, it was found that a 300-second PEB yielded better results. Fig. 7.4 illustrates the impact of short (left) versus long (right) PEB times.

The samples were then developed by immersion into propylene glycol monomethyl ether acetate (PGMEA) for 30 seconds followed by a 30-second isopropyl alcohol (IPA) rinse and finally dried using a nitrogen gun.

Subsequent inspection of the exposure was performed using an Olumpus BX60 optical microscope, although optical inspection became impractical for gratings with periods, Λ, smaller than $\sim$500 nm. See Fig. 7.5 for optical micrographs of line gratings with different grating periods.

7.1.3 Results

Characterisation of the line gratings, defined through interference lithography, was performed through scanning electron microscopy (SEM) and subsequent LER analysis. SEM was performed using a Raith 150 EBL-tool in imaging mode. LER analysis of SEM micrographs was performed using SuMMIT from EUV Technology [130].

Half-pitch line gratings were fabricated with grating periods, Λ, ranging from 250 nm to 1150 nm. These exposures were performed using resist with TMC4R:HMMM ratios of 1:0.81 and 1:0.74, with PAG to solid content ratios of 1:21. The pre-exposure resist film thicknesses were around 150 nm.

Definition of 250-nm period gratings was achieved through use of resists with TMC4R:HMMM ratios of 1:0.81 and 0.74 as shown in Figs. 7.6 and 7.7 respectively. Better imaging performance was observed for the 1:0.74 compared to the 1:0.81 resists, although at the cost of higher clearance dose, as illustrated by these two figures.

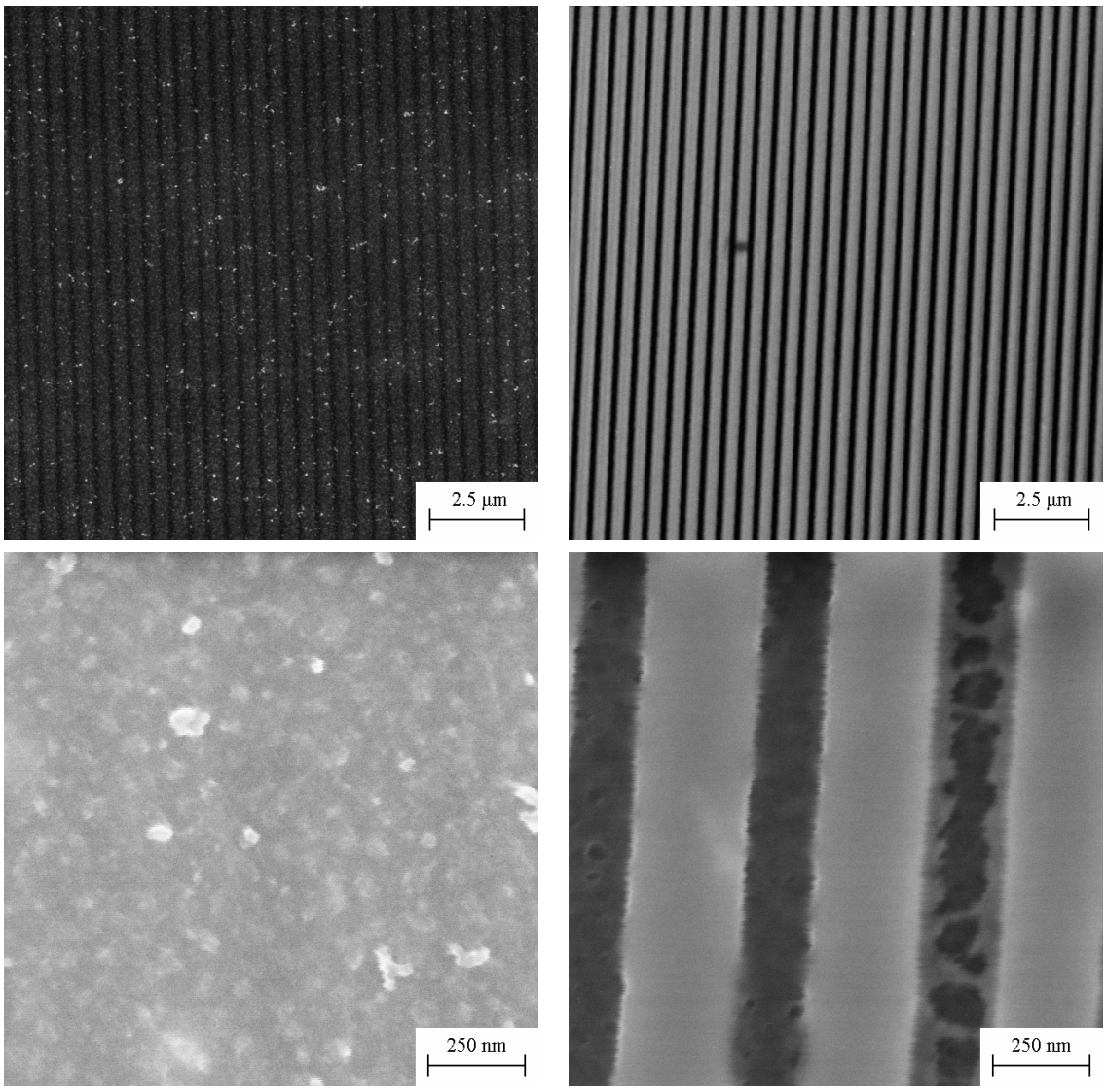

Figure 7.4: Impact of PEB time on 500-nm period half-pitch gratings. TMC4R:HMMM 1:0.81. PAG:SC 1:21. SC: 9.2 wt%. Top: Low magnification - x5k. Bottom: High magnification - x15k. Left: 1230 mJ/cm^2. t_{PEB} = 60 s. Right: 1292 mJ/cm^2. t_{PEB} = 300 s.

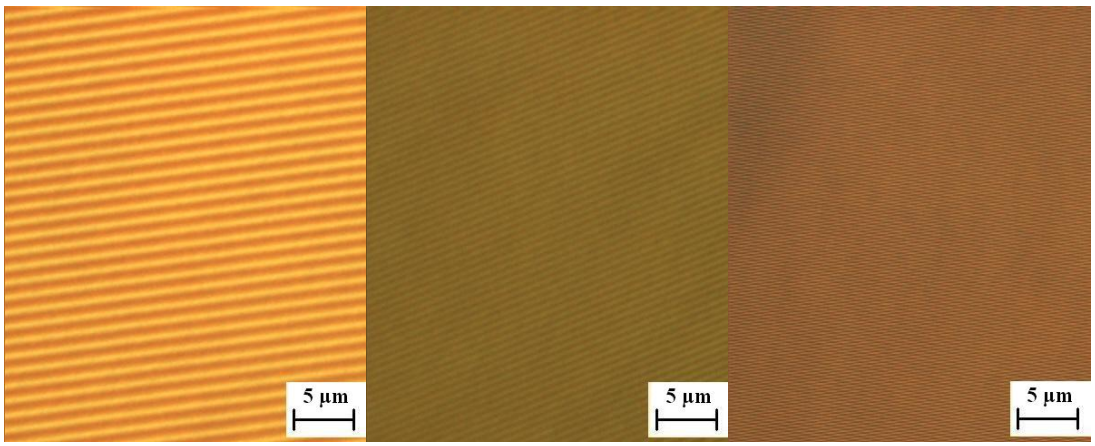

Figure 7.5: Optical microscope images of line gratings defined using IL. Resist composition: TMC4R:HMMM 1:1, PAG:SC 1:21, 9.0 wt%. All three samples were subjected to a PEB at 100°C for 60 seconds following exposure. Left: exposure parameters: θ =8° and D_{exp} =354 mJ/cm^2, yielding a half-pitch grating with a period of 1168 nm. Middle: exposure parameters: θ =16° and D_{exp} =344 mJ/cm^2, yielding a half-pitch grating with a period of 590 nm. Right: exposure parameters: θ =33° and D_{exp} =300 mJ/cm^2, yielding a grating with a period of 298 nm and a nominal duty cycle of 50%.

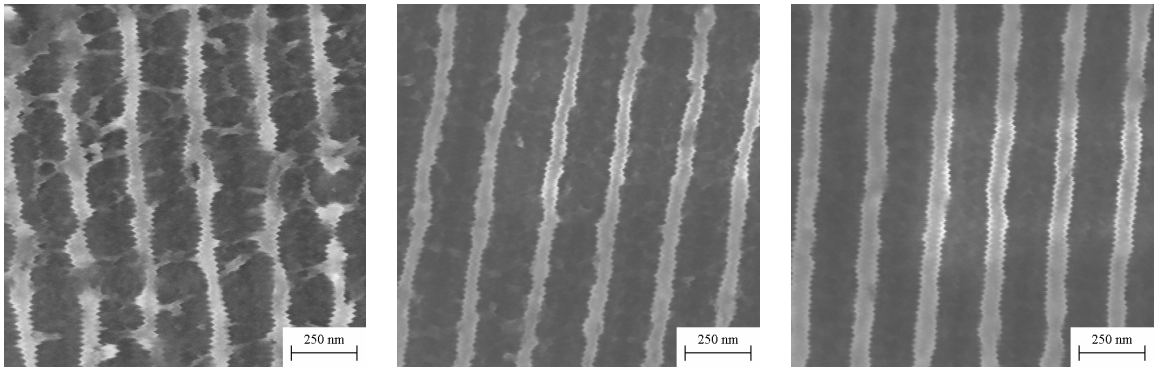

Figure 7.6: 250-nm period gratings. TCM4R:HMMM 1:0.81. PAG:SC 1:21. SC: 9.2 wt%. Left to right: 748 mJ/cm^2, 872 mJ/cm^2 and 997 mJ/cm^2.

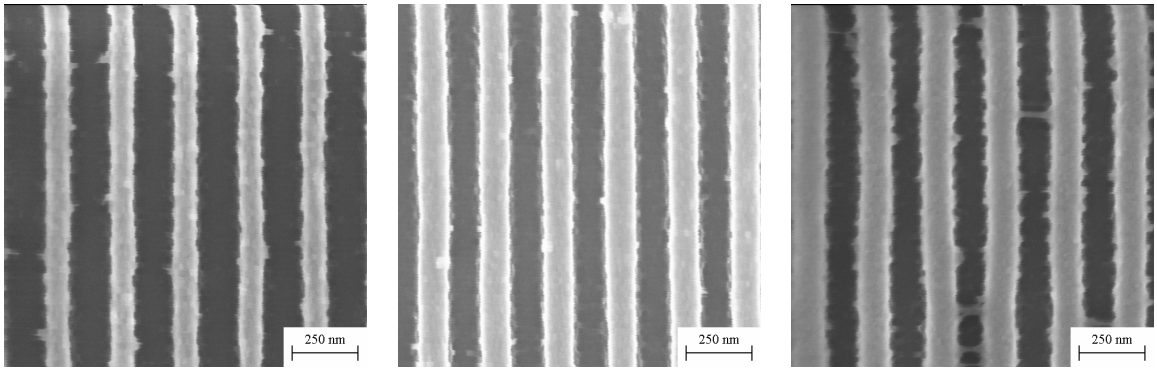

Figure 7.7: 250-nm period gratings. TCM4R:HMMM 1:0.74. PAG:SC 1:21. SC: 9.1 wt%. Left to right: 994 mJ/cm^2, 1866 mJ/cm^2 and 2243 mJ/cm^2.

While the imaging performance of TMC4R:HMMM 1:0.81 resists proved lacking for the 250-nm period gratings, they performed better in resolving 500-nm period gratings as seen in Fig. 7.8. However, the 1:0.74 resist still exhibited superior performance as seen in Fig. 7.9.

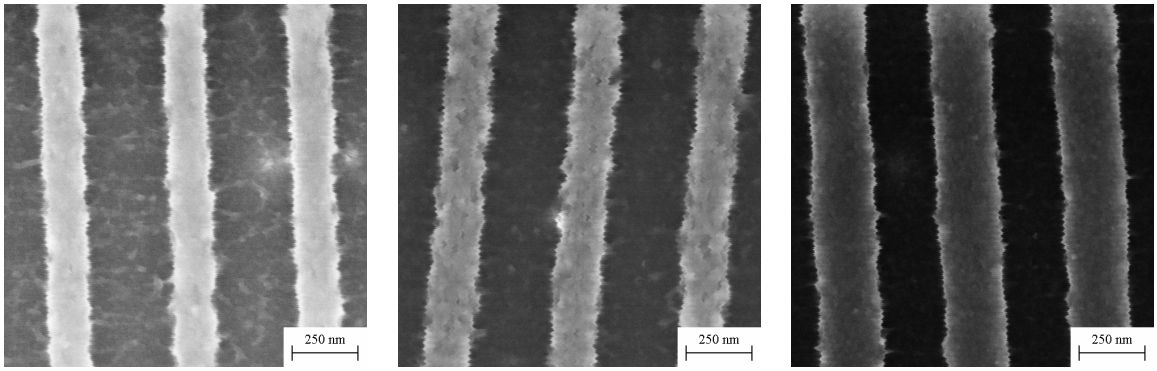

Figure 7.8: 500-nm period gratings. TCM4R:HMMM 1:0.81. PAG:SC 1:21. SC: 9.2 wt%. Left to right: 877 mJ/cm^2, 1176 mJ/cm^2 and 2491 mJ/cm^2.

For resists with higher HMMM content, formation of networks of fibrils connecting the primary resist features was observed (e.g. Fig. 7.6(left)). Furthermore, for these resists the primary features had lower structural density with apparent porosity in some cases. Examples of this phenomenon are presented in Fig. 7.10.

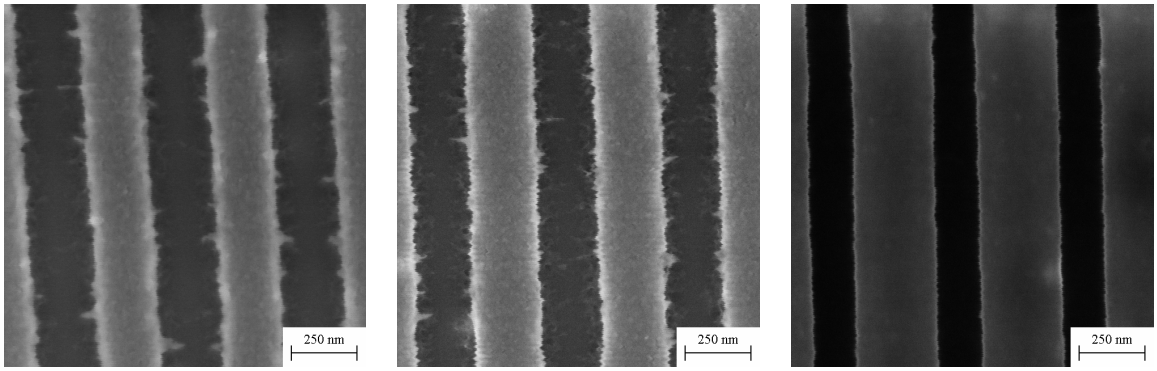

Figure 7.9: 500-nm period gratings. TCM4R:HMMM 1:0.74. PAG:SC 1:21. SC: 9.1 wt%. Left to right: 1753 mJ/cm^2, 2491 mJ/cm^2 and 3272 mJ/cm^2.

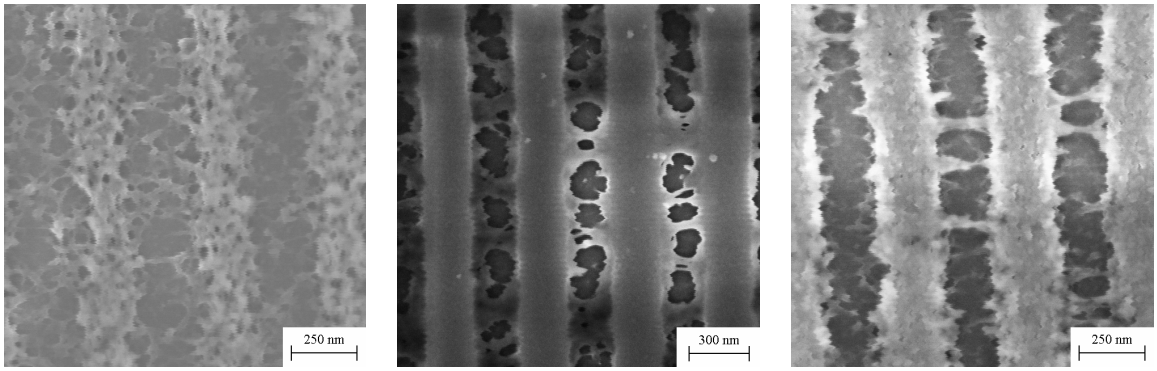

Figure 7.10: 500-nm period gratings. Illustration of structural porosity and fibril networks. PEB: 100°C for 60 seconds. Left: TMC4R:HMMM 1:1, 507 mJ/cm^2. Middle: TMC4R:HMMM 1:1, 877 mJ/cm^2. Right: TMC4R:HMMM 1:0.81, 2337 mJ/cm^2.

IL exposures in the commercial AZ1518 resist were also undertaken in order to compare resolution and LER with the calixarene resist. Both 500 nm and 250 nm period gratings were defined using this resist. In order to achieve a reasonably thin resist layer for defining sub-micrometer features the AZ1518 resist was diluted with PGMEA in a ratio of PGMEA:AZ1518 3:1. Fig. 7.11 shows 250 nm period gratings at varying exposure doses. The AZ1518 was a positive-tone photoresist while the TMC4R-resist was negative tone. Consequently over- and under-exposure characteristics for the two resists were very different.

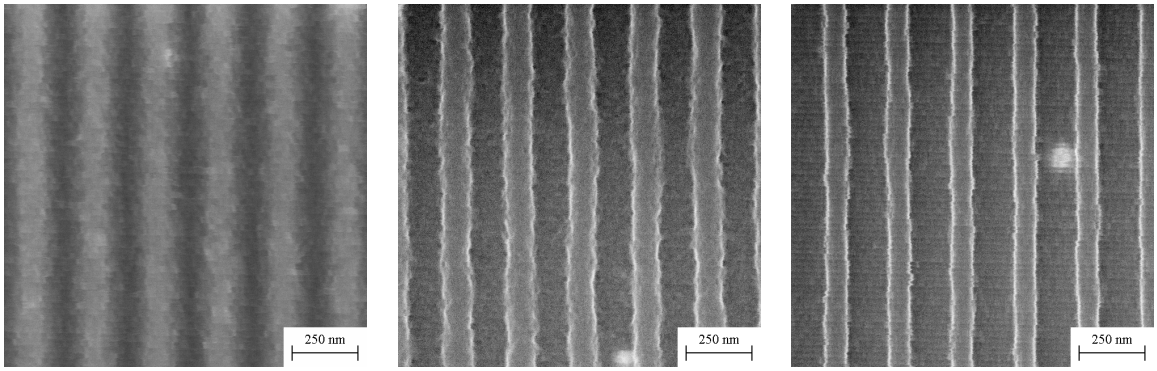

Figure 7.11: 250-nm period gratings defined in AZ1518 resist. To achieve a thinner resist layer the photoresist was thinned down with PGMEA in a ratio of PGMEA:AZ1518 - 3:1. Exposure doses from left to right: 209 mJ/cm^2, 449 mJ/cm^2 and 511 mJ/cm^2.

LER figures were calculated from the SEM micrographs using the SuMMIT software shown in Fig. 7.13. Micrographs were loaded into the program and subjected to post-processing: vertical alignment of line pattern by rotation, image cropping to excluded unwanted regions and image contrast adjustment. "Fences" are placed to identify the features to be analysed and an intensity threshold is specified at which to evaluate the features. The line features analysed here were evaluated at an intensity threshold of 50%. Spatial frequency bandpass filtering is available to reduce the impact of high- and low-frequency noise on the results.

Characteristic values for the line features are calculated automatically and includes: LW critical dimension (CD), line width roughness (LWR) and line edge roughness (LER), as well as their corresponding standard deviations. SuMMIT calculates LWR and LER

as the average 3σ of the line-width and line-edge variation, respectively, for all line features analysed. Each micrograph processed in this manner provided characteristic data for a specific number of lines, N. These data were collated in a spreadsheet and the N-weighted averages and standard deviations for each individual sample were calculated. Table 7.1 presents this data for 250- and 500-nm period gratings, for TMC4R-resists with TMC4R:HMMM ratios of 1:0.74 and 1:0.81 and the AZ1518 resist.

TMC4R: HMMM	Λ nm	D_{exp} mJ/cm^2	N	**LW** nm	**dc**	**LER** nm	σ_{LER} nm	**LWR** nm	σ_{LWR} nm
1:0.74	253	994	172	100.5	0.40	13.3	0.56	15.5	1.58
		1570	90	133.2	0.53	11.4	2.12	14.7	2.93
		1866	155	137.4	0.54	11.3	2.81	14.0	4.43
		2093	82	149.2	0.59	13.4	1.87	16.7	2.40
	499	1753	54	275.7	0.55	18.6	1.13	26.8	3.40
		2491	47	291.5	0.58	18.2	1.12	25.1	1.97
		3272	11	323.5	0.65	8.5	0.93	12.3	0.57
1:0.81	253	872	19	65.4	0.26	27.3	1.40	35.6	3.79
		997	43	72.7	0.29	17.8	1.94	21.6	3.46
	499	877	71	193.9	0.39	21.3	2.15	29.0	2.22
		2491	47	276.8	0.55	17.1	0.52	24.0	0.97
AZ1518	253	449	25	126.9	0.50	15.3	1.00	20.1	2.29
		511	27	97.7	0.39	11.2	0.69	14.7	0.79
	499	185	14	167.8	0.34	15.1	0.98	18.0	2.53
		258	12	150.7	0.30	13.3	0.35	18.3	0.63

Table 7.1: Table presenting experimental IL-results: resist composition, grating period (Λ), exposure dose (D_{exp}), number of resist lines analysed, line widths (LW), corresponding duty cycle (dc = LW / Λ), line edge roughness (LER = 3σ), LER standard deviation, line width roughness (LWR) and LWR standard deviation for calixarene resists, with TMC4R:HMMM ratios of 1:0.74 and 1:0.81, as well as the AZ1518 resist.

SEM imaging of the resist structures was performed at an acceleration voltage of 3 kV to ensure a relatively shallow interaction volume. The exposed grating patterns had a typical height variation smaller than 100 nm which, combined with the features being located on top of a polymeric BARL, resulted in very poor contrast at higher acceleration voltages. The fine fibril network structures mentioned above were not observable

at increased acceleration voltages.

A significant and varying level of noise in the Raith 150 system made SEM imaging difficult. When imaging 250-nm period gratings the noise hampered the effort, both by affecting the final image and by making optimisation of the electro-optical system parameters increasingly difficult. In some cases the combination of low contrast and high noise meant that obtaining clearly focused images was not possible inside a realistic timeframe. In Fig. 7.12 two SEM micrographs taken at 50k times magnification are shown. In the left image the stigmation settings of the electron optics is slightly off compared to the right image where the stigmation settings have been thoroughly optimised. When imaging several of such samples the stigmation settings must be optimised continually to retain imaging quality. However, the ability to perform this optimisation efficiently relies on the structure imaged; for poorly resolved structures the contrast is very low and the procedure becomes both more difficult and more time consuming. Note that even for the high-quality image significant noise remains in the image. The high-frequency line-edge noise is due to noise in the system and does not represent the actual LER of the resist pattern. A rough estimate of the impact of noise upon the measured LER figures indicates that an increase in observed LER of as much as 2 nm is probable.

7.1.4 Summary

Sub-micrometer period gratings were defined in the TMC4R-based photoresist and the commercial AZ1518 through interference lithography using a Lloyd's mirror setup. The best results were obtained using a resist with a TMC4R:HMMM ratio of 1:0.74 and a PAG:SC ratio of 1:21. Exposures, at an angle of incidence, θ, of 40° with an exposure dose, D_{exp}, of 1.9 J/cm^2, post-baked at 100°C for 300 seconds and developed in PGMEA for 30 seconds this resist produced well-defined 250-nm half-pitch line gratings with good structural density and LER (3σ) as low as 9 nm. A SEM micrograph of this grating is shown in Fig. 7.14(top left). Fig. 7.14(top and bottom right) also shows SEM micrographs illustrating the difference in imaging performance between resists with TMC4R:HMMM ratios of 1:0.81 and 1:0.74 when defining 500 nm period gratings.

7. SUB-WAVELENGTH RESOLUTION IMAGING USING A CALIXARENE-BASED PHOTORESIST

The imaging performance of the TMC4R-based photoresist is found, in comparison with the commercially available AZ1518 resist, to be approximately similar, if not slightly superior as can be seen from Fig. 7.14(top and bottom left). However, it must be noted that the AZ1518 resist is not a state-of-the-art high contrast resist.

Resist image characterisation by SEM was complicated due to two issues: the low contrast of polymer-on-polymer structures as well as inherent noise in the SEM itself.

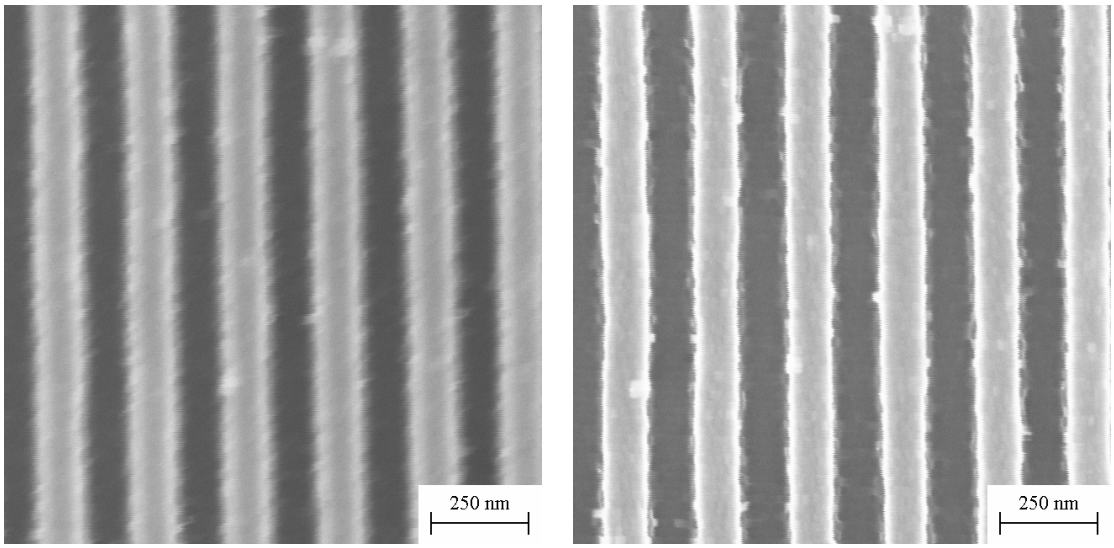

Figure 7.12: Variation in SEM imaging quality - x50k magnification. 250-nm period half-pitch gratings. TMC4R:HMMM 1:0.74. PAG:SC 1:21. SC: 9. wt%. 1866 mJ/cm^2 Left: Stigmation setting slightly off. Right: Exactly the same region with almost perfect stigmation setting.

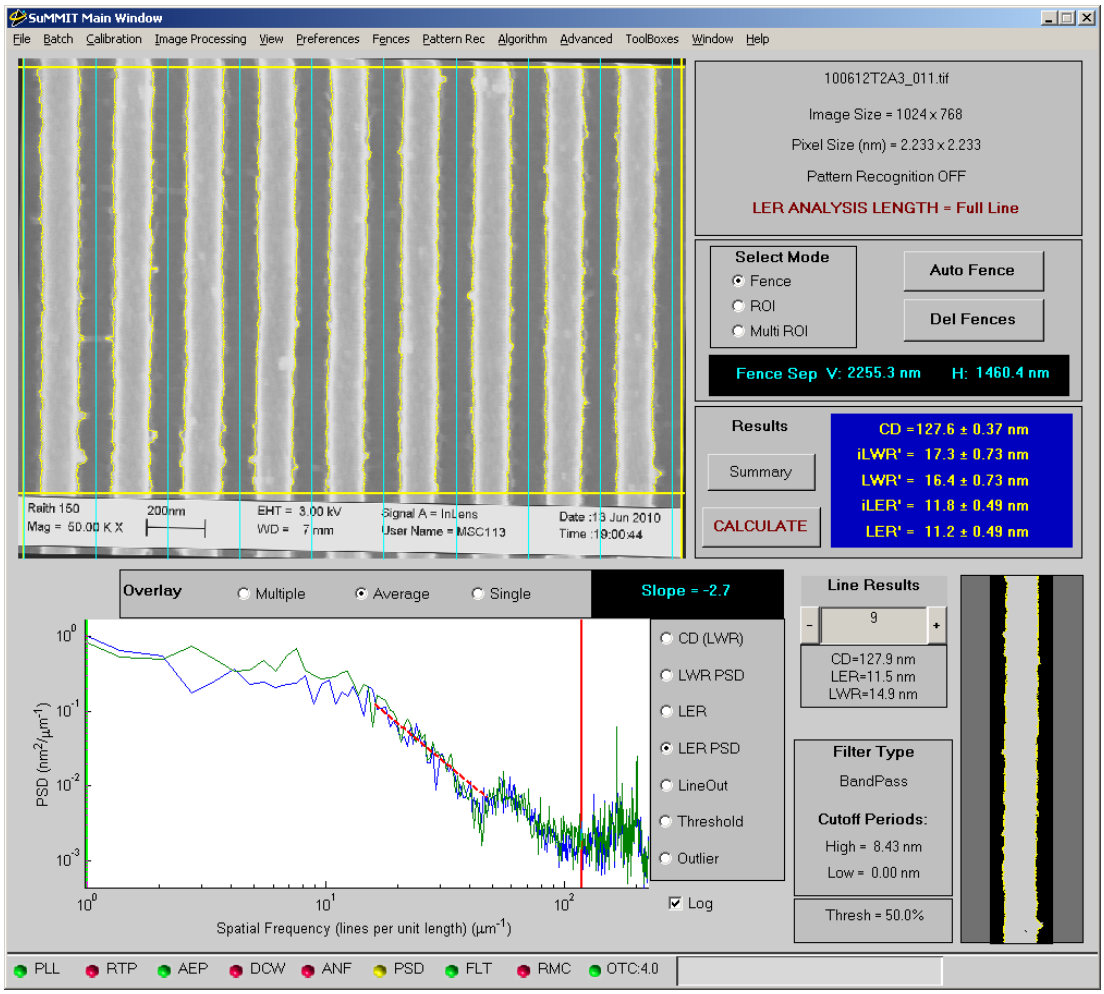

Figure 7.13: Screenshot from the SuMMIT application analying a SEM micrograph of an IL defined grating. The region of interest is defined by sliding the yellow borders of image in the upper left-hand corner. "Fences" can be placed automatically or manually as desired. The desired intensity threshold for line profile evaluation is shown near the lower right-hand corner. The calculated parameters and their standard deviations are shown in the blue box along the right-hand side of the GUI. The number of lines analysed is shown immediately below the results-box. The lower left-hand region shows the PSD as a function of spatial frequencies and the bandpass filtering can be set by sliding the green and red lines to exclude noisy regions.

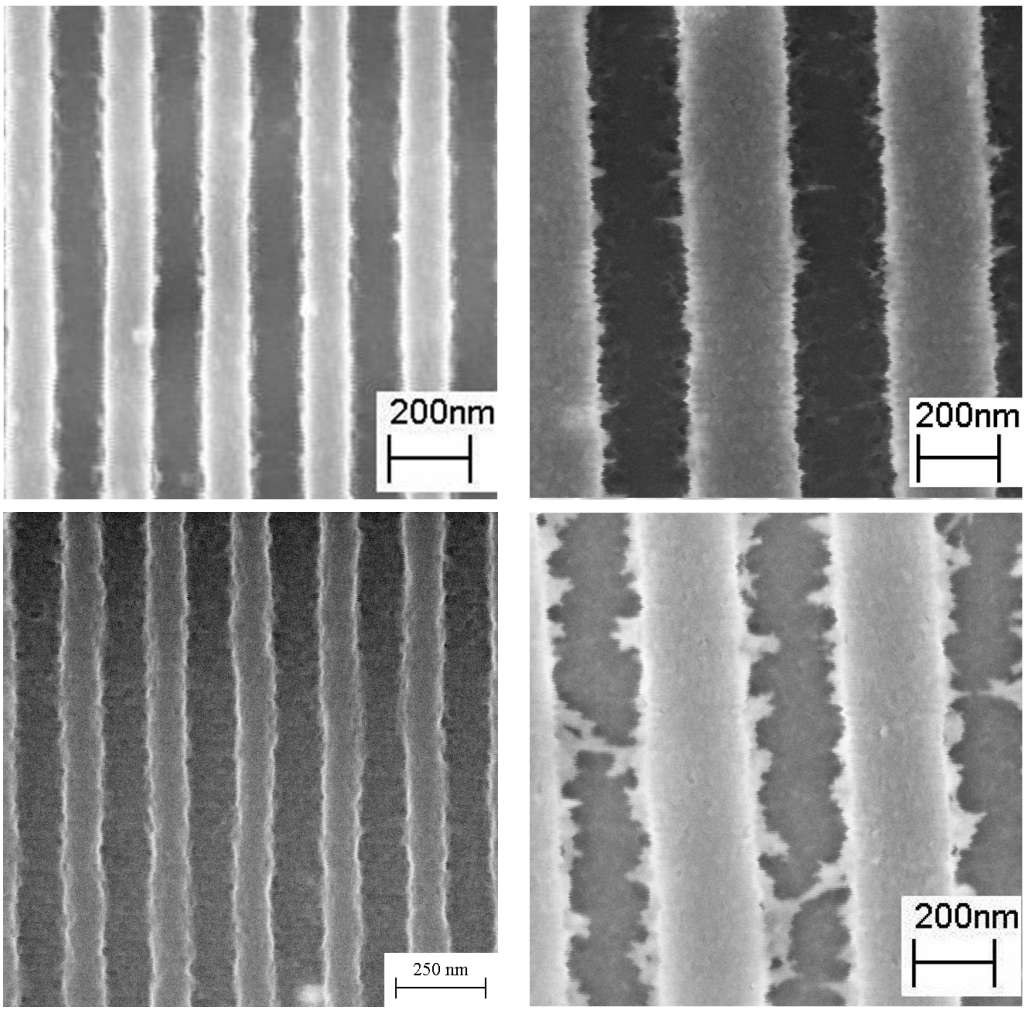

Figure 7.14: SEM micrographs of line gratings defined through IL. Top left: 250-nm period half-pitch grating in a calixarene resist with a TMC4R:HMMM ratio of 1:0.74 and a PAG:SC ratio of 1:21 subjected to an IL exposure of 1.9 J/cm^2. The duty cycle of this grating was 0.54 and it had a LER of 12.1 nm. Bottom left: 250-nm period line grating defined in AZ1518 resist. The exposure dose for this resist structure was 499 mJ/cm^2. The duty cycle of this grating was 0.49 and it had a LER of 15.0 nm. Top right: 500-nm period half-pitch grating in a calixarene resist with a TMC4R:HMMM ratio of 1:0.74 and a PAG:SC ratio of 1:21 subjected to an IL exposure of 2.5 J/cm^2. The duty cycle of this pattern is 0.57 and it had a LER of 18.8 nm. Bottom right: 500-nm period half-pitch grating in a calixarene resist with a TMC4R:HMMM ratio of 1:0.81 and a PAG:SC ratio of 1:21 subjected to an IL exposure of 2.5 J/cm^2. The duty cycle of this pattern is 0.55 and it had a LER of 28.2 nm.

7.2 Near-field imaging

While the interference lithography technique presented in Section 7.1 enabled quick patterning of large area, sub-wavelength resolution line gratings, it was still limited in some regards. As for resolution the theoretical limit is a period of 162.5 nm, as shown in Eq. 7.1, and in regard to patterning, only two dimensional superpositions of line gratings is possible. To further characterise the calixarene-based photoresists imaging capacity below this resolution limit and for more complex patterns, evanescent near-field optical lithography (ENFOL) experiments were conducted. These experiments were performed using shadow masks made from quartz substrates with tungsten UV absorbers. The following section presents the mask fabrication process, experimental methodology and results obtained from this investigation.

7.2.1 Mask fabrication

The ENFOL shadow masks used in these experiments were fabricated on 2" quartz substrates through thin-film deposition of tungsten, reactive ion etching (RIE) and mix-and-match of ultra-violet photolithography (UVL) and electron beam lithography (EBL). The fabrication process is presented in Fig. 7.15 which illustrate the individual process steps:

1. Thin-film deposition of tungsten onto the quartz substrate.
2. Spin-coating of the substrate with AZ1518 UV photoresist.
3. Definition of alignment marks and large scale structures by UVL to facilitate easy navigation around the substrate during subsequent characterisation.
4. Development of UVL defined pattern.
5. Pattern transfer into tungsten through RIE and subsequent UV photoresist strip.
6. Spin-coating the substrate with poly(methyl methacrylate) (PMMA) EB resist.
7. Selective removal of PMMA layer to facilitate grounding of the tungsten layer to prevent localised charge build-up on the substrate during EBL.
8. EBL definition of high-resolution patterns.

9. Development of EBL defined pattern.

10. Pattern transfer into tungsten through RIE.

11. Stripping of EB resist.

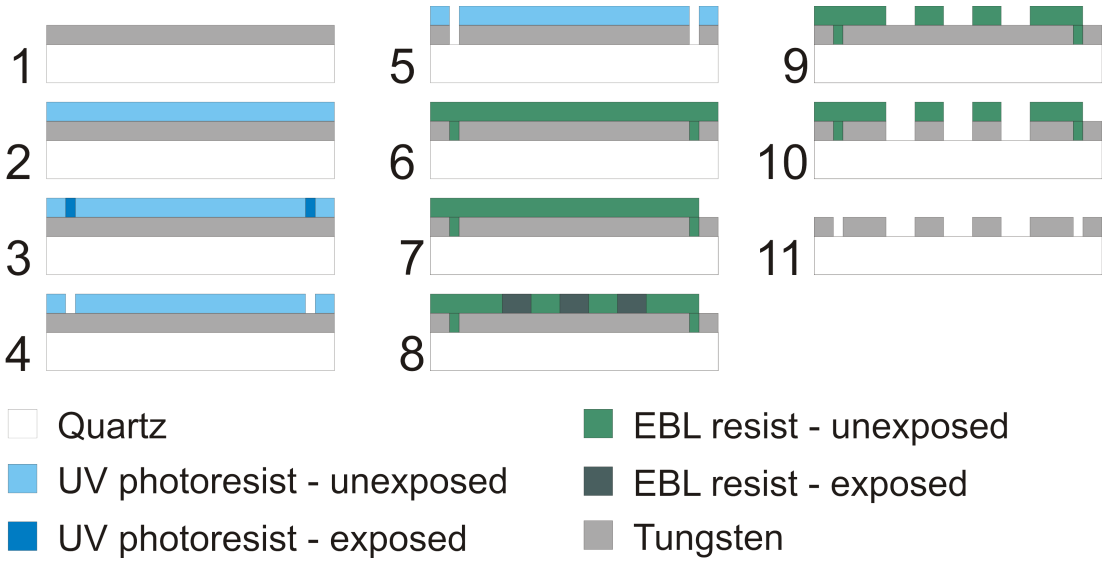

Figure 7.15: Fabrication process for ENFOL shadow masks.

Initial mask fabrication attempts were made using amorphous silicon (a-Si) instead of tungsten as Ito et al. has identified this material as a good ENFOL shadow mask absorber material [8]. However, even fairly thick (>50 nm) layers of a-Si proved inadequate as charge dissipation layers during EBL. Attempts were made to use a water soluble conducting polymer (PEDOT) spun on top of the PMMA, however the hydrophobicity of PMMA severely complicated this approach and no satisfactory results were obtained. In an attempt to improve the wetting characteristics of PMMA, experiments with short oxygen plasma treatments were carried out. The results of these experiments were unsatisfactory insofar that the PMMA layer had to be subjected to the plasma so long that significant film degradation occurred. Ultimately the a-Si approach was abandoned in favour of using tungsten which provides good charge dissipation, under the provision that the layer itself is electrically grounded.

The substrates used for the ENFOL shadow mask fabrication were double-side polished, 500-μm thick, 2" diameter quartz substrates from Mark Optics. Quartz substrates were used due to their high UV transparency and double-side polishing was specified to avoid optical scatting at either interface.

Tungsten was deposited upon the quartz substrate through DC magnetron sputting using an Edwards Auto 500 magnetron sputtering system (see Fig. 3.19). Tungsten films with thicknesses in the range of 35-50 nm were deposited at a DC power of 300 W.

The UVL fabrication step was performed using a Karl Suss MA6 mask aligner and shadow masks fabricated using a Heidelberg Instruments μPG101 mask writer. AZ1518 photoresist was spin-coated onto the tungsten thin-film, using a Headway Research PWM32 spinner operating at 5000 RPM for 60 seconds, and subsequently baked for 90 seconds at 100°C. An exposure dose of 60 mJ/cm^2 was applied and the pattern subsequently developed in MF-322 developer for 30 seconds.

To allow for easy navigation and identification of the various features on the ENFOL shadow masks, the shadow masks used in this fabrication step contained alignment marks and quadrant divisions. Each quadrant contained 22 quadratic cells for defining high-resolution patterns through EBL as well as numerical identification marks for both quadrant and cell identification. The UVL defined pattern is shown in Fig. 7.16. Note the dashed quadrant separators and cell borders, this is to prevent electrical insulation of "islands" within the charge dissipation layer.

High-resolution patterning of the ENFOL shadow masks was performed using a Raith 150 EBL system. High molecular weight (HMW) PMMA was spin coated onto the tungsten surface of the substrate at 3000 RPM for 60 seconds. The PMMA film was subsequently baked in a 185°C oven for a minimum of 30 minutes. Exposure was performed using an acceleration voltage of 10 kV and an aperture size of 10 μm. For area exposures, exposure doses ranging from 100 to 320 μC/cm^2 were applied depending on pattern density. For line exposures, doses ranged from 420 to 720 pC/cm.

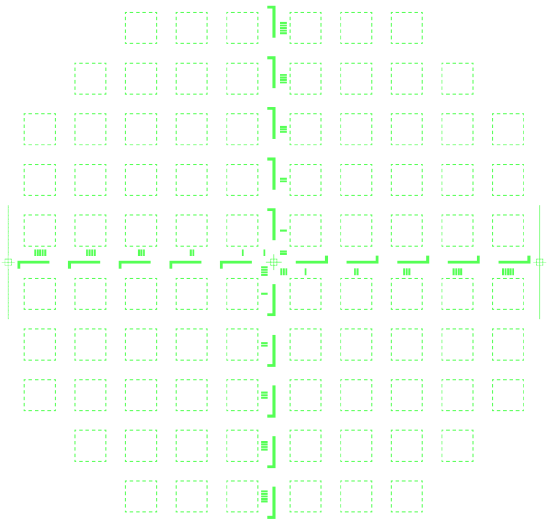

Figure 7.16: L-edit layout for UVL layer.

Several different EBL exposure patterns were attempted:

- Line gratings.
- Nested-Ls containing variations in pattern density.

Fig. 7.17 show schematic overviews of the line grating and nested-L patterns used in for the mask fabrication. The figure highlights the critical dimensions (Λ and LW) of the various patterns as well as their sizes.

Line gratings were included to allow easy comparison with IL results and also to potentially achieve higher resolution. Nested-Ls contain sharp corners, variations in pattern density: 50%, 25% and 17% fill factor, and isolated line features. Furthermore, nested-Ls are very challenging patterns for EBL and thus provides a good measure of the quality of the EBL process step. The Raith system used for these exposures is often subject to significant acoustic noise. The noise is evident during SEM imaging and manifests itself as superimposed waveforms propagating at a speed dependent upon the SEM scan-rate. The amplitude of the noise varies, however noise on the order of $\sim$50 nm was observed on a few occassions. It must be assumed that this significant noise is also present during EBL, which would have a significant, but not easily quantifiable, impact upon EBL pattern fidelity. Several different exposure approaches were

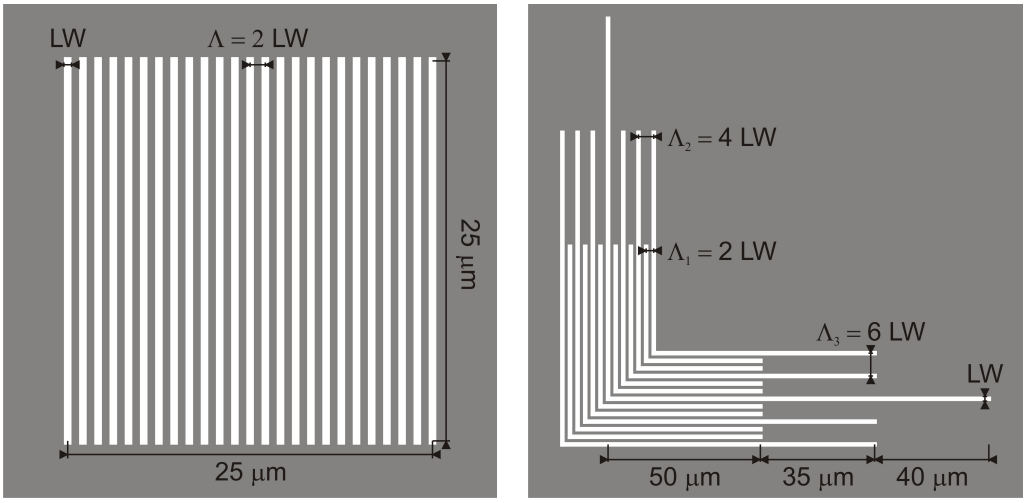

Figure 7.17: EBL exposure patterns for ENFOL mask fabrication. Left: 25 μm x 25 μm equal line/space grating array characterised by period Λ. Right: Nested-Ls with varying line densities characterised by linewidth LW.

attempted to minimize the impact of the noise upon the resulting pattern. Single-pixel lines have yielded good results in the past but are very noise-sensitive. In an attempt to counter this, experiments were performed to investigate if several consecutive exposures of single-pixel line features, each with a comparatively lower dose (so that the total exposure dose remained constant), would yield better results. These experiments were performed for $n = [1, 5, 10]$, where n is the number of consecutive line passes each with a line dose, D_l, equal to D_T/n, where D_T is the total exposure dose. A comparison of EBL results using different exposure profiles for a 150-nm period half-pitch grating is shown in Fig. 7.18. The best of both types of exposure approaches were used in fabricating the final ENFOL shadow masks - i.e. consequetively written lines with $n = 5$ as well as area dose exposures with a 25% duty cycle.

Pattern transfer into the tungsten layer, for both UVL and EBL defined patterns, was achieved through RIE using an Oxford Plasmalab 80 plus. The etch process used the parameters presented in Table 7.2. As can be seen from the etching times they were very short. As a consequence the plasma did not have time to stabilise properly and as such process repeatability was compromised. Rigorous process optimisation for the tungsten RIE step was found not to be worthwhile, partly due to the vast range of very

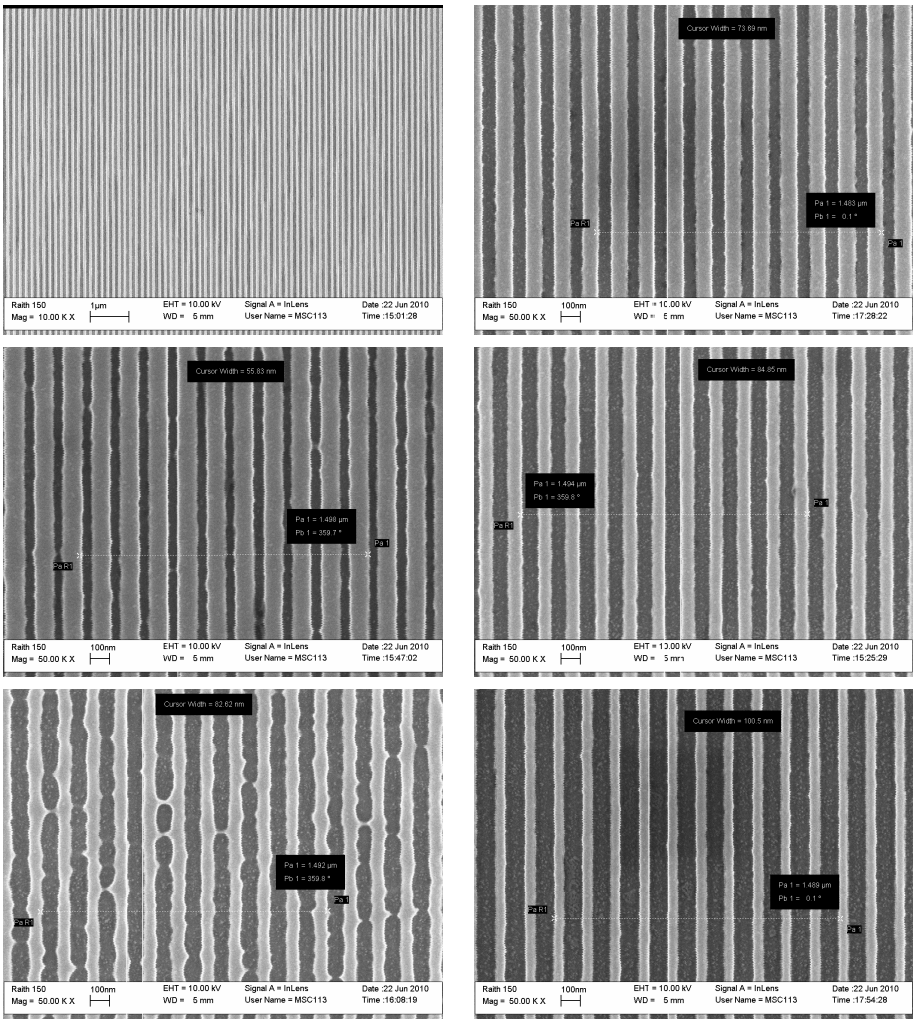

Figure 7.18: Comparison of EBL exposure methods for realising a 150-nm period half-pitch grating. The left-hand column shows the resulting resist image for exposure profiles utilising single-pixel line exposures. Top: Shows single line-pass exposure with a line dose of 720 pC/cm. Middle: 5 consecutive line-passes with 1 nm offsets and a combined line dose of 420 pC/cm. Bottom: 10 consecutive line-passes with 1 nm offsets and a combined line dose of 600 pC/cm. The right-hand column shows the resist image for area exposures with varying dose and fill factors. Top: Exposure with a fill factor of 10% and an area dose of 320 μC/cm^2. Middle: Exposure with fill factor of 25% and an area dose of 140 μC/cm^2. Bottom: Exposure with fill factor of 40% and an area dose of 100 μC/cm^2.

Tungsten etch	
Pressure	150 mTorr
Power	200 W
Gases	SF_6
Temperature	313 K
Etching time	20 s

Table 7.2: RIE recipe for tungsten etch.

different processes performed using this equipment, thus making it diffcult to achieve process-to-process consistency. Furthermore the resulting pattern transfer was deemed satisfactory in most cases.

In Fig. 7.19 several SEM micrographs of mask features fabricated through the approach outlined above are shown. This figure also presents statistical LW and LER results as calculated by SuMMIT.

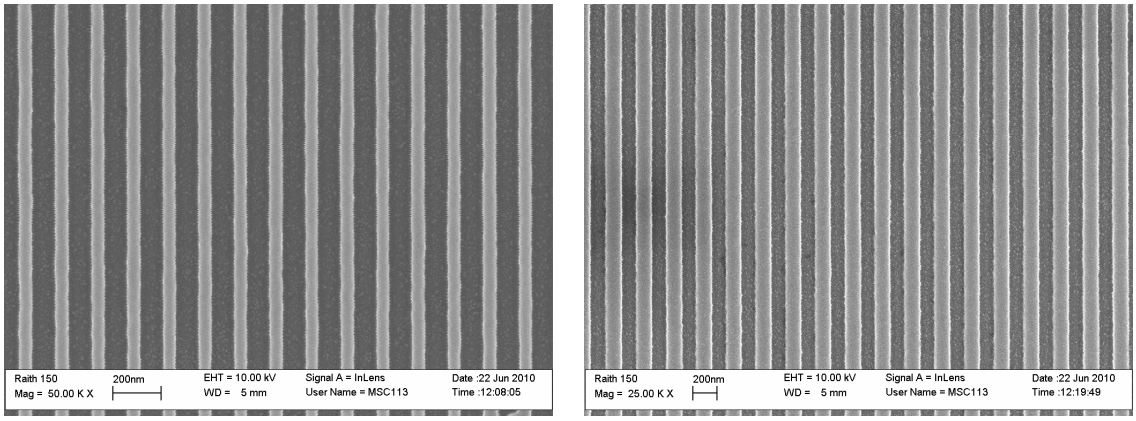

Figure 7.19: ENFOL shadow mask features after pattern transfer into tungsten by RIE. Left: 150-nm pitch, area dose 100 μC/cm^2, fill factor 40%. Average LW 57.8 nm and LER 3.4 nm. Right: 250-nm pitch, single-pixel lines, 5 consecutive passes, combined dose 900 pC/cm. Average LW 137.8 nm and LER 6.5 nm.

7.2.2 Experimental method

Near field exposures were conducted using shadow mask fabricated as described in Section 7.2.1. For grating fabrication the EBL area dose exposure approach, utilising a fill factor of 10%, was chosen. The TMC4R resist, described in Chapter 6, was used for these exposures. A schematic representation of the steps used during these ENFOL exposures is presented in Fig. 7.20.

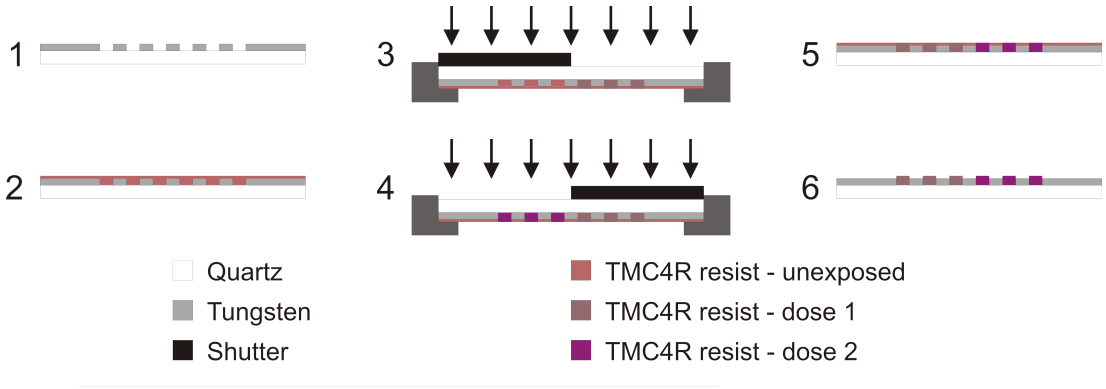

Figure 7.20: Schematic outline of the process steps involved in the ENFOL exposure experiments: 1) Sample: shadow mask with sub-wavelength features, 2) the sample was coated with TMC4R resist, 3) sample turned upside down, placed in sample holder and partially exposed to UV, 4) subsequent partial UV exposures with varying doses, 5) sample removed from sample holder and subjected to a PEB, 6) pattern developed in PGMEA.

The steps outlined by the schematic in Fig. 7.20 corresponds to the following six steps:

1. Sample: a shadow mask with sub-wavelength features, fabricated from quartz and tungsten using mix-and-match UV and EB lithography.

2. The sample was coated with TMC4R resist. Very low rotational speeds (approx. 500 RPM) were utilised to ensure good coverage over pattern features.

3. The sample was turned upside-down and placed in the sample holder. A plastic shutter plate was placed ontop of this setup to facilitate selective UV exposure of different sample regions.

4. Subsequent UV exposure of additional regions with varying doses through rotation of shutter plate.

5. The sample was removed from sample holder and subjected to a PEB of 100°C for 300 seconds.

6. The exposure pattern was then developed by a 30-second PGMEA wash and a subsequent 30-second IPA rinse.

The TMC4R resist was applied directly onto the top-side of the shadow mask used for the exposure to avoid complications associated with achieving intimate conformal contact between mask and substrate as required for ENFOL exposures. This approach is viable when using a negative tone resist such as the TMC4R-resist, since the resulting resist features will adhere to the mask itself. This allows approximate mapping of the isodose surface where the dose equals the gel dose.

To ensure good resist coverage across the mask features, low rotational speeds of approximately 500 RPM were used during the spin coating process. Due to the exposure method and negative tone resist, resist thickness in this case was considered less important provided the resist layer was of an adequate thickness.

A custom made sample holder was used to fix the coated shadow mask in the Karl Suss MA6 mask aligner. The sample was placed bottom up in the custom holder and the holder subsequently inserted into the standard 3" mask-holder plate for the mask aligner. A rotational plastic shutter, positioned on top of the sample, allowed for segmented exposures by the mercury lamp. In this way, several separate quarter segment exposures, with different exposure doses were possible per EBL defined shadow mask. The sample holder is shown in Fig. 7.21, which also shows how the sample holder was mounted into the MA6 mask aligner.

Following exposure the sample was subjected to a PEB of 100°C for 300 seconds to ensure resist crosslinking. Then the exposure pattern was developed by submersion in PGMEA for 30 seconds and a subsequent IPA rinse.

Due to the sample consisting of shallow resist features upon a substrate consisting of patterned tungsten and quartz, SEM analysis of the resulting resist structures was impractical. Instead, structures were imaged using a Digital Instruments Dimension

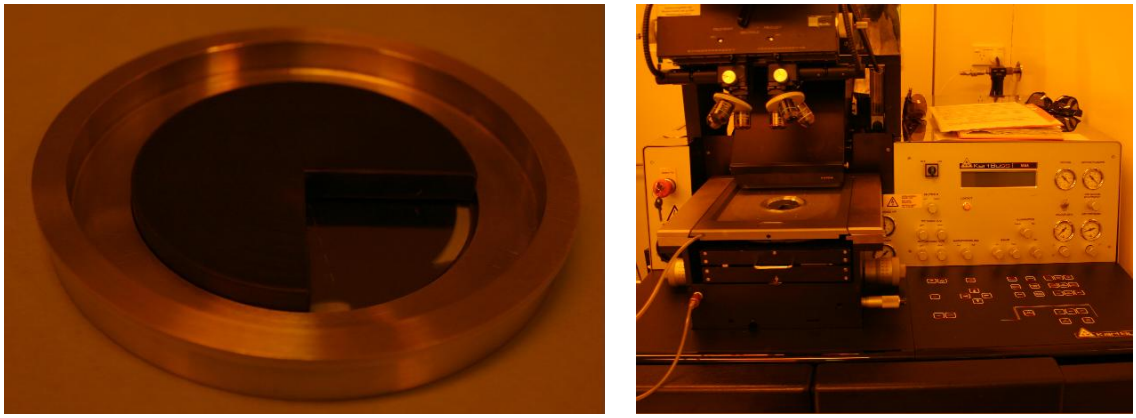

Figure 7.21: Left: The ENFOL sample holder with a quartz wafer inserted and the rotational shutter in place. Right: The ENFOL sample holder mounted in the Karl Suss MA6 mask aligner.

3100 AFM and the resulting surface maps were subsequently used for LER analysis in SuMMIT.

7.2.3 Results

Using the experimental method outlined in Section 7.2.2 line gratings and nested-L patterns were defined in the TMC4R-based photoresist through ENFOL. Here follows a presentation of the results obtained from ENFOL exposures of two fundamental patterns as illustrated by Fig. 7.17: 250-nm period half-pitch line gratings and 150-nm line-width nested-Ls. Exposures were perfomed at four doses: 75, 150, 300 and 600 mJ/cm^2. The patterns analysed here were all defined in a TMC4R-resist with TMC4R:HMMM of 1:0.74 and a PAG:SC of 1:21. All samples were subjected to a 300-s PEB at 100°C prior to development in PGMEA.

Line gratings

Fig. 7.22 show 2x2 μm^2 AFM surface maps of 250-nm period gratings exposed at various UV exposure doses. With increasing doses, line widening is observed as well as a gradual loss of vertical definition.

Fig. 7.23 shows cross-sectional profiles of the gratings presented in Fig. 7.22 together with peak-to-peak (PtP) and full-width half-maximum (FWHM) measurements. From

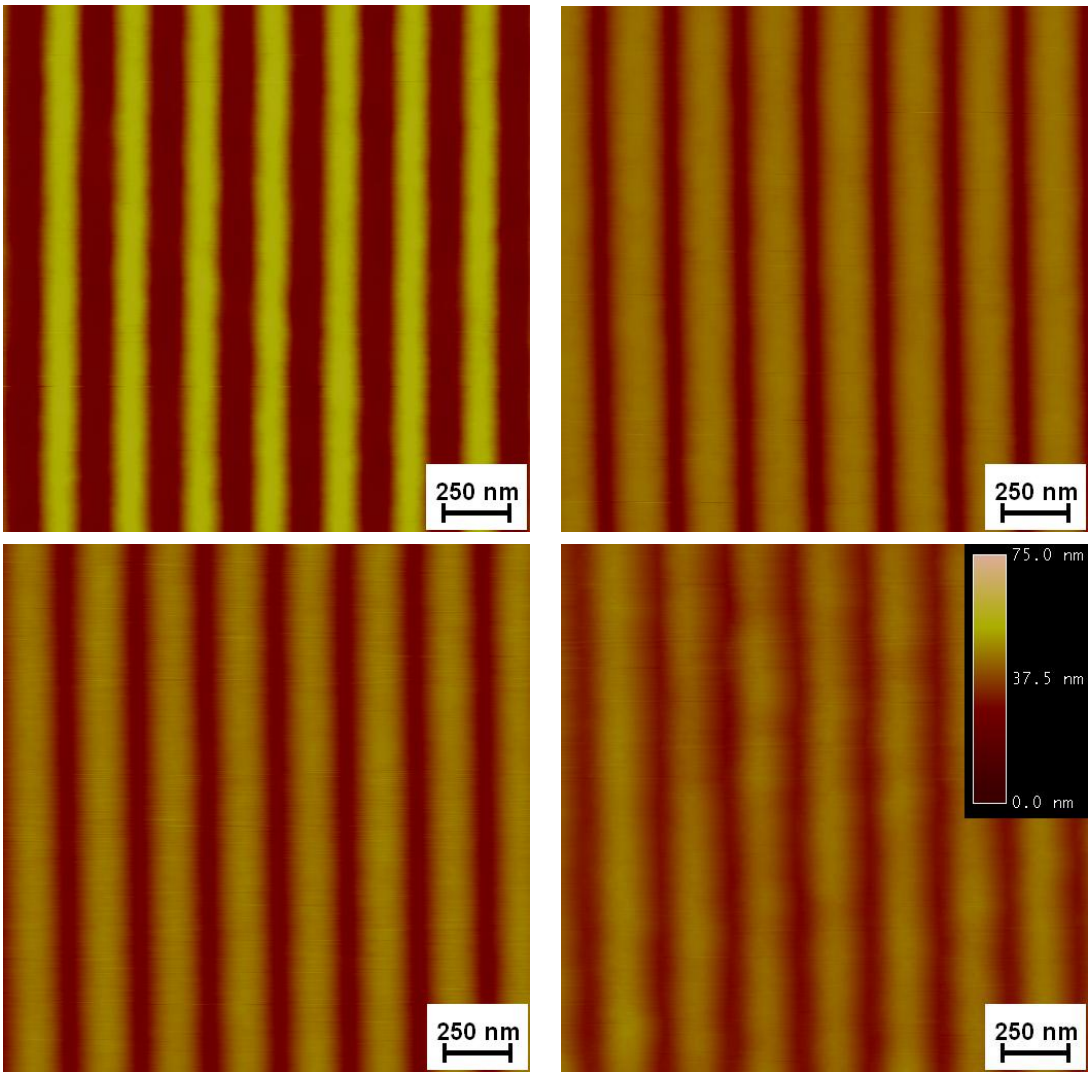

Figure 7.22: AFM surface maps of ENFOL defined 250-nm period half-pitch gratings with different exposure doses. These gratings were defined in a TMC4R-resist with TMC4R:HMMM of 1:0.74 and PAG:SC of 1:21 spun onto a single substrate which was subjected to a 300 s PEB at 100°C prior to development. All surface maps have a vertical scale of 75 nm. Line statistics were calculated using the SuMMIT image processing software and are presented in Table 7.3. Top left: exposure dose: 75 mJ/cm^2. Bottom left: exposure dose: 150 mJ/cm^2. Top right: exposure dose: 300 mJ/cm^2. Bottom right: exposure dose: 600 mJ/cm^2.

these cross-sections it is evident that PtP decreases with increasing exposure dose. The lowest dose has a significantly higher vertical definition compared with higher doses. This observation is, in part, due to finite tip-effects in AFM with increasing LW reducing the extent to which the tip is able to probe the trench.

Fig. 7.24 shows cross-sectional profiles of the gratings presented in Fig. 7.22 at the edge of the exposure pattern. The area imaged by Fig. 7.24 is the area at the very edge of the shadowmask grating pattern as illustrated by Fig. 7.25. It can be seen that for the lowest dose of 75 mJ/cm^2 the resist is not exposed within the shadow mask apertures, resulting in trenches below the surface zero-plane. The tungsten layer had a thickness of ∼50 nm and it can be seen that finite tip-effects limits the depth resolution of the features. However, while the resist in the trenches is clearly under-exposed, a resist profile remains on the dark-field features of the shadow mask, effectively forming a reverse image of the expected grating. Variation in the exposure dose profile close to the edge can be observed with resist features projecting approximately 25 nm above the zero-plane.

At an exposure dose of 150 mJ/cm^2 the height definition of the grating approximately doubles relative to the zero-plane of the scan. The increased LW further reduces the vertical resolving power of the AFM. With an increased exposure dose of 300 mJ/cm^2 a reduction in FWHM LW is observed as well as a decrease in measured PtP. This indicates that an actual rounding of the features, a loss of sharpness, occurs at this higher dose. The amplitude of the features relative to the zero-plane is still increased, however a slope is beginning to present itself at the edge of the exposure field indicating residual exposure. This effect is obvious when considering the profile resulting from a 600 mJ/cm^2 exposure. Here the PtP and FWHM LW are both decreased substantially and a significant slope is observed in the scan-profile in the dark-field area of the image increasing towards the edge of the exposure pattern.

The results obtained from LER-analysis of the 250-nm period gratings performed in SuMMIT, extracted using the procedure outlined in Section 7.1.3, are summarised in Table 7.3. As seen, LER figures of approximately 7 nm were obtained for all except the highest exposure dose.

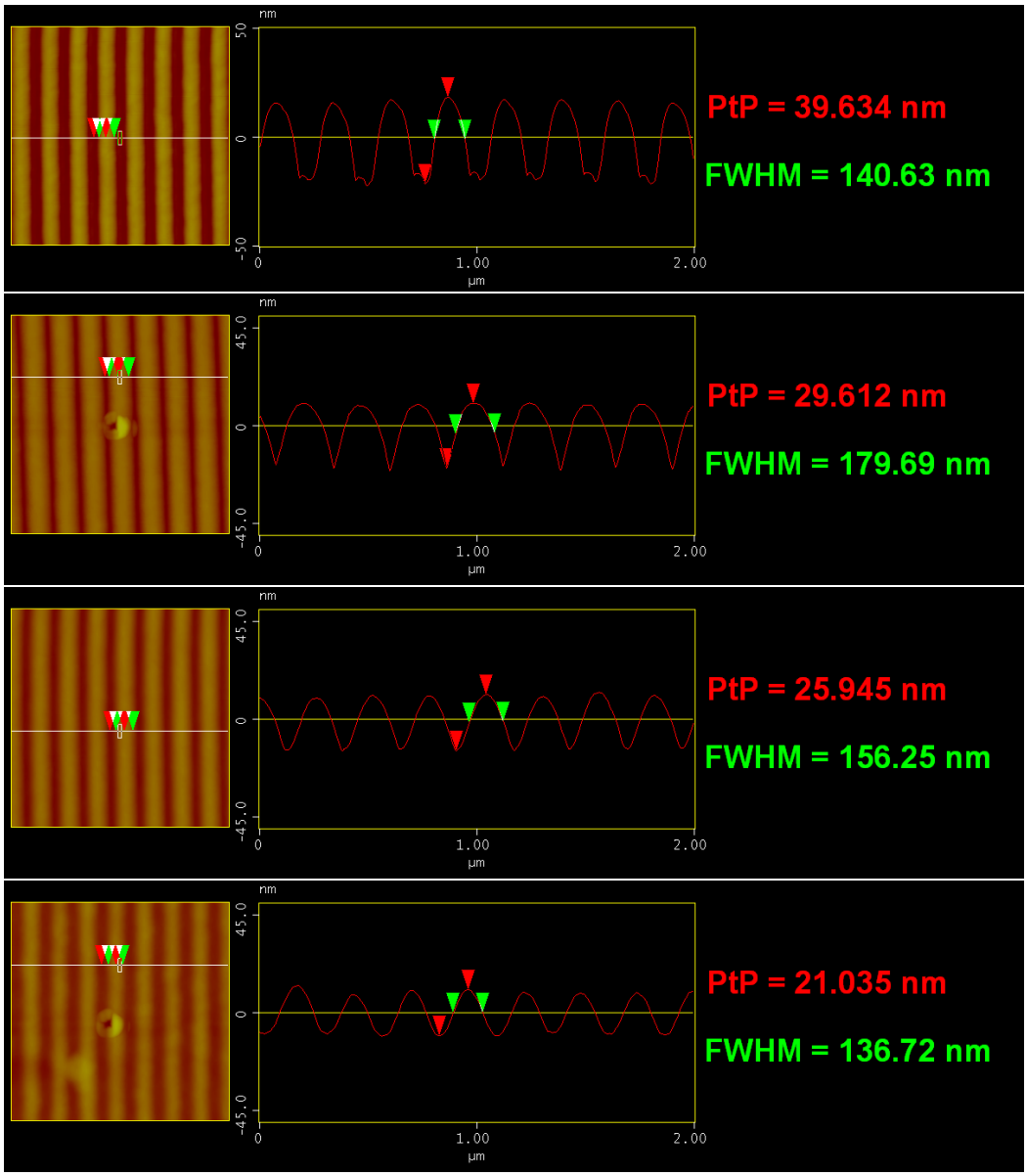

Figure 7.23: ENFOL defined 250-nm period half-pitch gratings with exposure doses of (top to bottom): 75, 150, 300 and 600 mJ/cm^2. These figures show cross-sections of AFM map profiles as well as PtP and FWHM data for the samples.

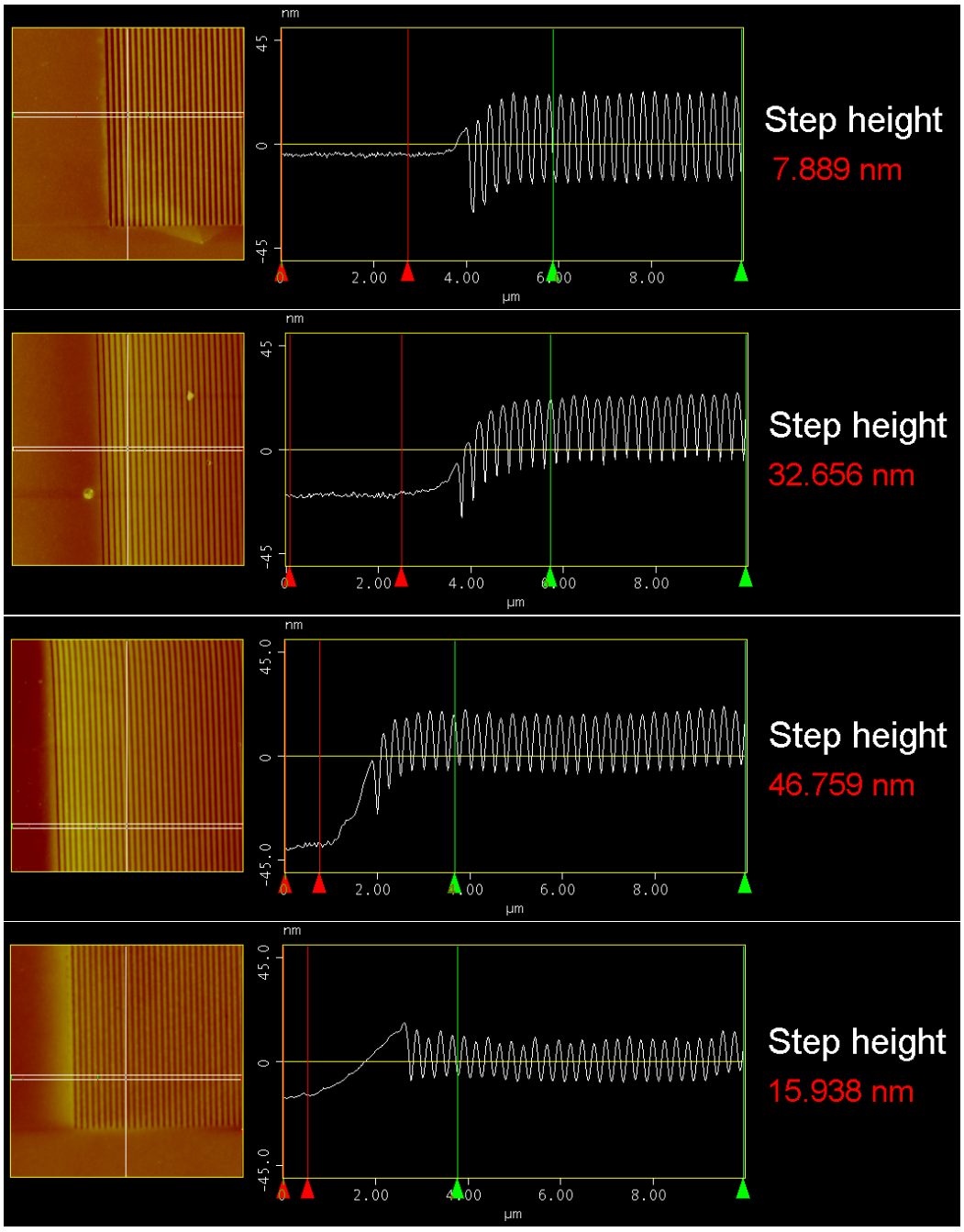

Figure 7.24: ENFOL defined 250-nm period gratings at different exposure doses. These AFM maps show the edge of the grating pattern and the transition from the unexposed to the exposed region. Step height is measured as the difference between the average heights of the unexposed and exposed regions, measured between the red and green cursors respectively. Exposure doses from top to bottom: 75, 150, 300 and 600 mJ/cm^2.

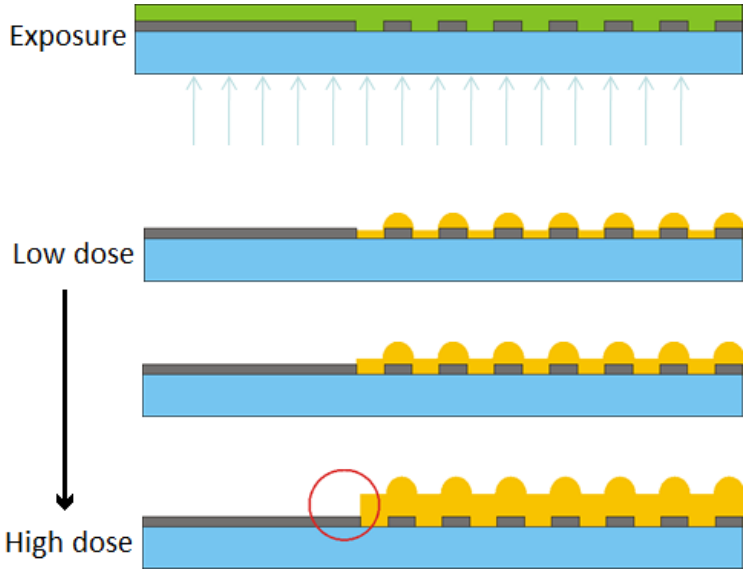

Figure 7.25: Schematic illustratoin of the resist profile for ENFOL grating exposures. As the exposure dose increases the resist image of the grating is superimposed upon a residual background resist exposure.

Nested-L patterns

Nested-L exposure patterns, as shown in Fig. 7.17(right), with characteristic LW of 150 nm were produced through ENFOL exposure. Here follows AFM analysis from two specific regions of these structures: the isolated single-line region and the region with seven parallel lines at a period of 4LW.

AFM scans of the isolated line structures are presented in Fig. 7.26. As can be seen from these scans, at an exposure dose of 75 mJ/cm^2 there are no protruding structures along the mask aperture, instead a 10-nm deep trench is observed. At an exposure dose of 150 mJ/cm^2 two 3.5-nm high, parallel lines with a spacing of approximately 500 nm are observed. When comparing this inter-line spacing with the ∼325-nm wide trench observed at 75 mJ/cm^2, feature widening is evident. A dramatic increase in feature height is observed at 300 mJ/cm^2 as well as a pronounced asymmetry in the line profiles. A small decrease in FWHM is also observed, indicating no further feature widening. However, lateral definition of the isolated pattern feature has almost disappeared at the highest exposure dose of 600 mJ/cm^2.

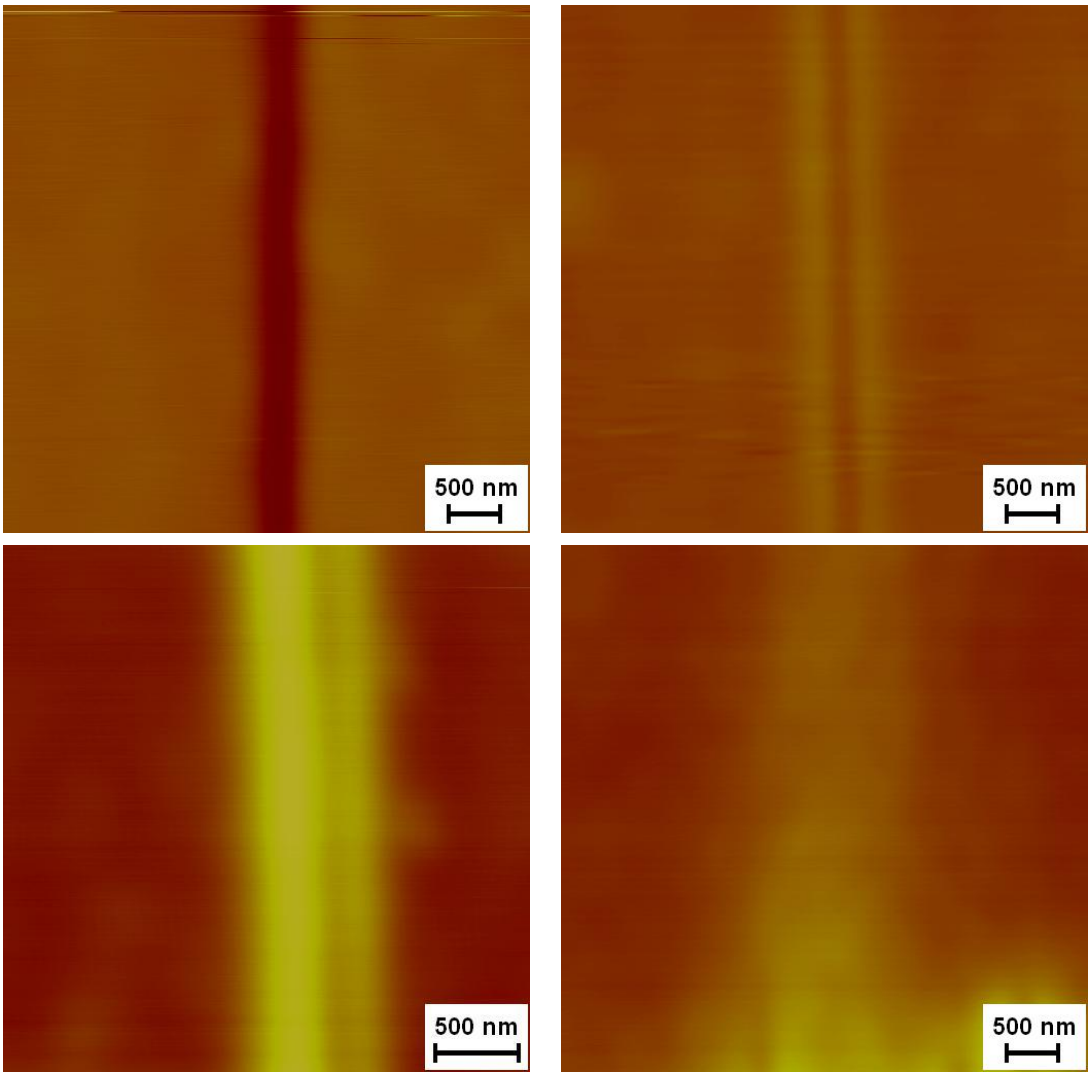

Figure 7.26: AFM surface maps of ENFOL defined isolated lines from nested-Ls with nominal linewidth of 150 nm. All surface maps have a vertical scale of 40 nm and were taken from the single-line area of the nested-L pattern. Top left: ENFOL exposure of 75 mJ/cm^2. Bottom left: ENFOL exposure of 150 mJ/cm^2. Top right: ENFOL exposure of 300 mJ/cm^2. Bottom right: ENFOL exposure of 600 mJ/cm^2.

D_{exp} mJ/cm^2	N	**LW** nm	**dc**	**LER** nm	σ_{LER} nm	**LWR** nm	σ_{LWR} nm
75	20	128.6	0.51	7.7	1.62	9.5	1.62
150	17	180.6	0.72	7.0	0.30	10.7	1.26
300	19	157.1	0.63	7.7	1.14	10.0	1.77
600	21	145.9	0.58	15.0	1.33	25.3	3.32

Table 7.3: LER for ENFOL defined 250-nm period line gratings. Data from left to right: Exposure dose (D_{exp}), number of lines analysed (N), line width (LW), corresponding duty cycle (dc), LER (average and standard deviation) and LWR (average and standard deviation).

Fig. 7.27 presents cross-sectional profiles of the isolated line structures shown in Fig. 7.26. This figure contains the height of the features, Δz, relative to the scan zero-plane and FWHM measured from the scan profiles.

The nested-L regions featuring seven parallel lines, spaced at 4LW, were also analysed by AFM. Fig. 7.28 shows a schematic representation of the 4LW region shadow mask along with AFM maps of the resulting resist profiles for three different exposure doses: 150, 300 and 600 mJ/cm^2. The nested-L structure imaged here had a characteristic LW of 150 nm corresponding to a line spacing of 600 nm. Comparison of the resist images with the underlying shadow mask pattern shows that the resist presents a reverse image of the masks bright-field, as was also observed for the line gratings presented in Fig. 7.24.

Fig. 7.29 presents cross-sectional scan profiles of the 4LW structures shown in Fig. 7.28 along with three characteristic measures. The red cursors measure the maximum feature height, Δz, above the sample zero-plane. The green cursors measure the horizontal distance equal to 5 Λ = 20 LW, which here is nominally equal to 3 μm. The white cursors measure the PtP value for the central peaks.

7.2.4 Summary

Line gratings with a period of 250 nm and LER (3σ) of less than 10 nm have been demonstrated at various exposure doses. The grating patterns were well defined across

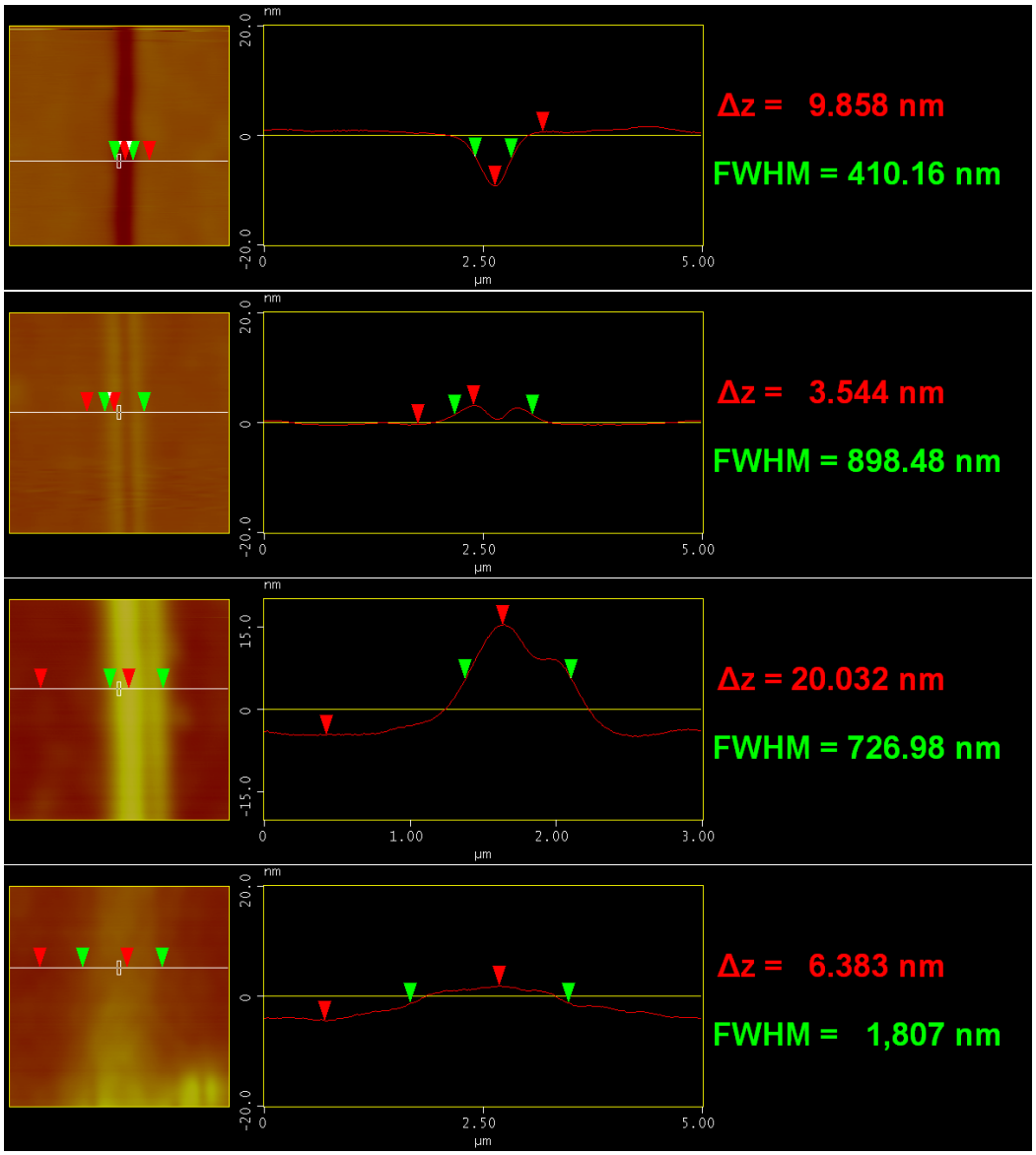

Figure 7.27: AFM profile scans of ENFOL defined isolated lines. The vertical scale for all four scans is 40 nm, notice that the lateral scan length is not equal for all four scans. Exposure doses, from top to bottom: 75, 150, 300 and 600 mJ/cm^2.

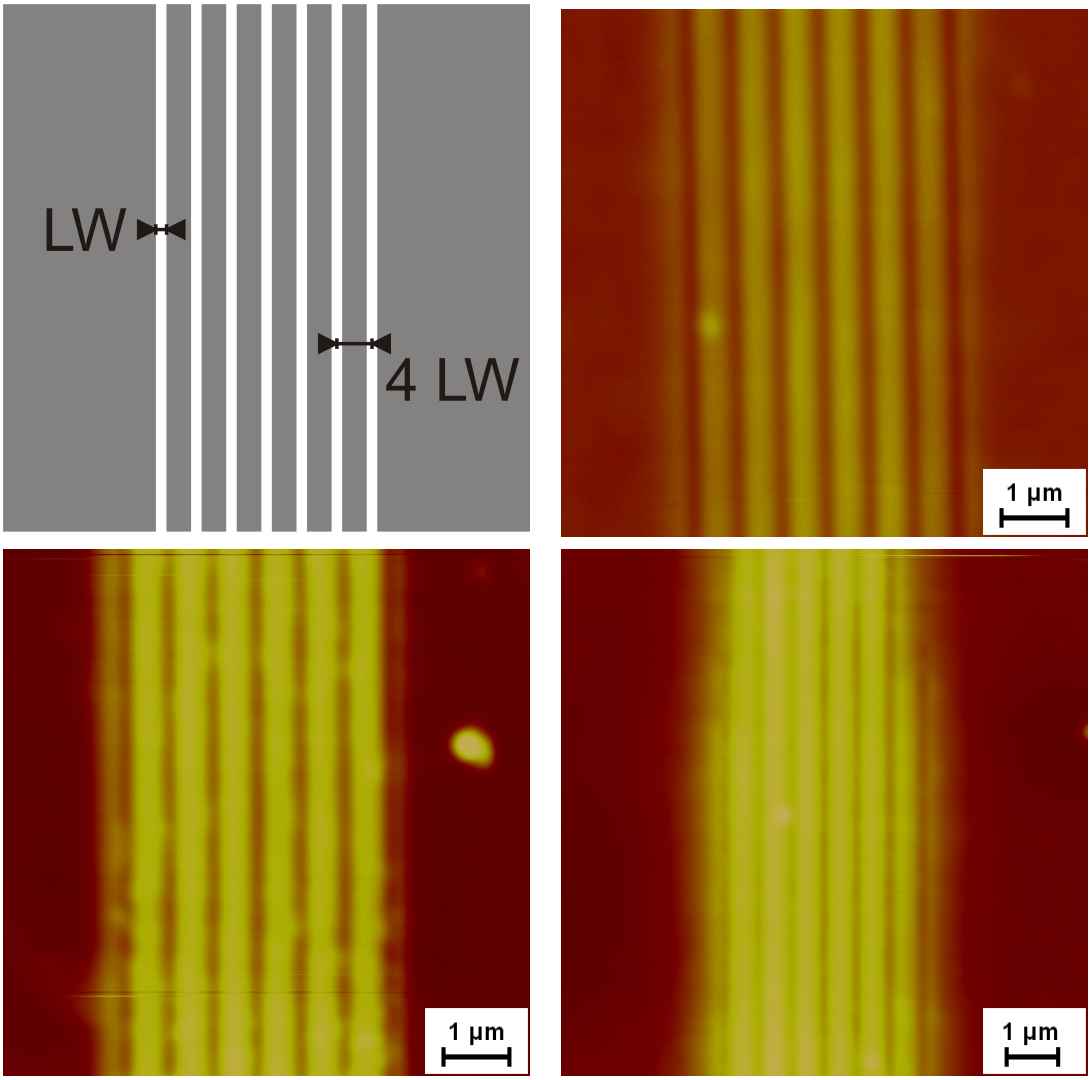

Figure 7.28: AFM maps of 4LW-period region from the nested-L geometry and a schematic representation of the shadow mask profile through which the exposure was performed. Vertical scale is 50 nm in all three AFM maps. Top left: Schematic representation of the shadow mask in the 4LW region. Here LW is equal to 150 nm. Top right: Exposure dose: 150 mJ/cm^2. Bottom left: Exposure dose: 300 mJ/cm^2. Bottom right: Exposure dose: 600 mJ/cm^2.

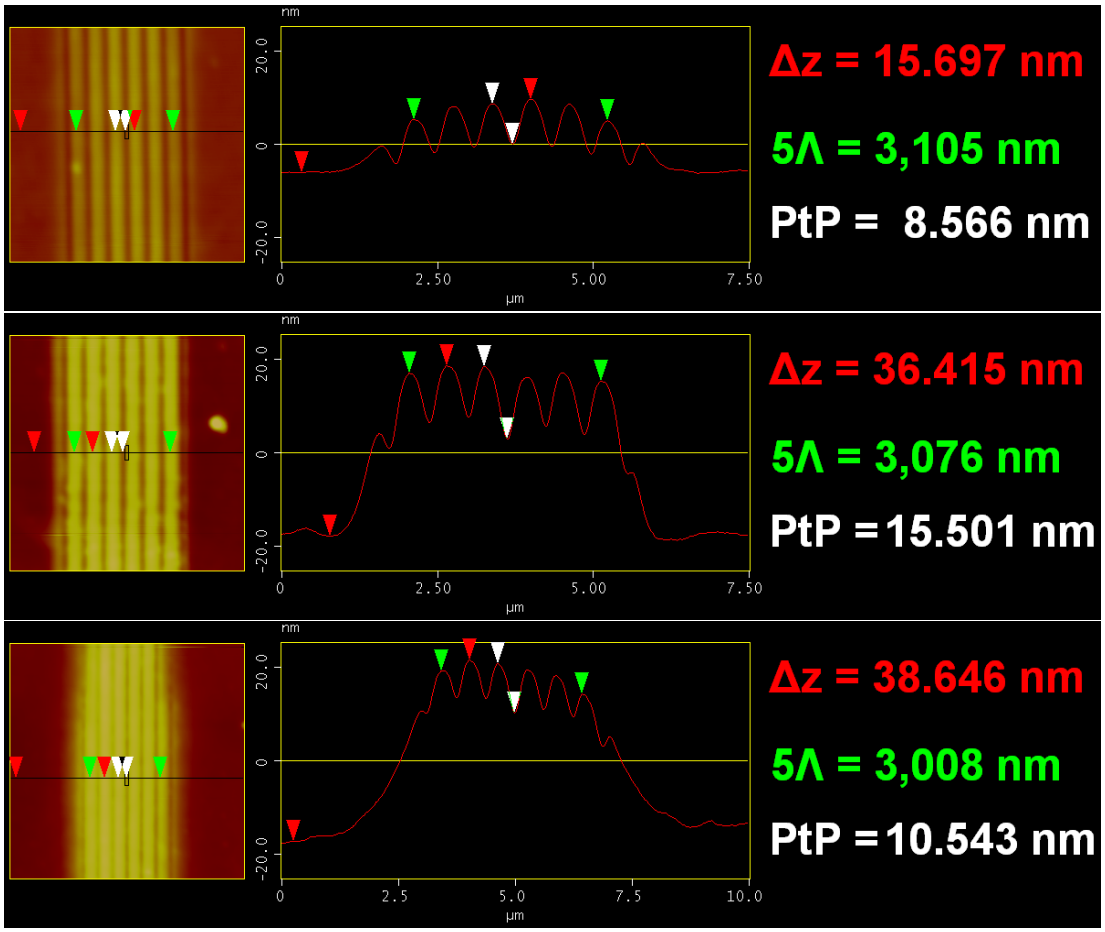

Figure 7.29: AFM cross-sections of the 4LW-period region from the 150-nm line-width nested-L geometry. The images presents maximum vertical range, Δz, the lateral distance of five periods, 5Λ, and the vertical definition of the central lines, PtP. Exposure doses, from top to bottom: 150, 300 and 600 mJ/cm^2.

the entire 25x25 μm^2 exposure fields. AFM scans of exposure-field edge-regions show that for low exposure doses the mask apertures remain free of resist and that protruding resist features forms on the mask absorbers. This is contrary to expectations of image formation in negative-tone photoresists. At higher exposure doses the overall resist-image height projects further beyond the mask-plane, however a reduction in vertical definition, PtP, of the high spatial frequency pattern is also observed.

Nested-L geometries were used to investigate the formation of isolated line structures as well as periodic line-structures. The nested-L structures were characterised by a nominal line width of 150 nm. The size of the geometry, 125x125 μm^2, complicated AFM analysis due to the large time requirement on navigating from one region of the geometry to another. Consequently two regions were analysed: isolated single lines and the 4LW region. The 150-nm wide isolated line features produced a resist-image consisting of twin parallel lines separated by approximately 600 nm. The seven lines in the 4LW region produced resist-images consisting of eight periodic peaks with loss of definition of the outer peaks observed at higher exposure doses. A general increase in vertical projection of the resist-image was observed at higher doses accompanied by reduction in PtP definition.

In both the case of the gratings and the nested-L geometries unexpected resist-image formation was observed. Resist features appeared to form predominantly on the dark-field of the periodic structures. This would indicate that significant field-enhancement, due to edge-diffraction, occured at the sharp corners of shadow-mask features resulting in an enhanced optical intensity in the, supposedly unexposed, dark-field region. With increasing exposure doses a loss of vertical definition in the resist-image was observed. This could indicate residual exposure from ambient far-field radiation and is seen as a general vertical shift of the resist-image away from the object-plane. As the resist image is projected further away from the object-plane, evanescent loss of spatial high-frequency components, resulting in loss of image resolution, is expected.

7.3 Dicussion and conclusion

Sections 7.1 and 7.2 presented experiments and results for IL and ENFOL respectively. Here follows a discussion of the results obtained through these super-resolution lithography experiments conducted using the TMC4R-resist. A comparison of ENFOL results achieved using the TMC4R-resist with ENFOL results achieved in earlier studies is presented to illustrate the enhanced imaging capability of the TMC4R-resist.

7.3.1 Discussion

The performance of the TMC4R-resist in IL and ENFOL is most easily evaluated by consideration of the 250-nm period grating structures described above. An immediate comparison of these results show that a significant improvement in LER was observed for the ENFOL-defined structures when compared to those defined through IL. In this regard there are several factors that need to be taken into account: 1) the patterns defined through IL were analysed by SEM not AFM, 2) fluctuations in air-flow, accoustic vibrations and air-borne dust will introduce noise into the IL exposure, 3) IL experiments were carried out outside the cleanroom and samples had to be transported into the yellow-room for PEB and development.

The importance of choice of microscopy technique should not be underestimated when comparing IL and ENFOL results. For structures with steep side-walls imaged through SEM, feature variation along the vertical plane will have an impact upon the resulting micrograph. Conversely, in AFM only LW-variations along the top edge of the structure can be evaluated due to the very nature of scanning probe microscopy. On the other hand the finite tip effect in AFM significantly limits the grating depth that can be evaluated, which in turn will indicate a lower aspect ratio than what might actually have been achieved.

Considerations 2) and 3) means that the IL experiment is more prone to noise-effects than the ENFOL experiment. In ENFOL the resist is spun directly onto the shadow mask, consequently noise should be effectively non-existant during the exposure step assuming that the exposure source is stable. For the ENFOL exposures sample substrates never left the yellow-room until after PEB and development. Samples used in

the IL-experiment were cleaved, cleaned, coated and transported to the laser-lab prior to exposure. Following exposure the samples were again transported back into the yellow-room for PEB and development. Consequently the risk of sample contamination was much higher in the IL experiment when compared to ENFOL.

A comparison the exposure doses required to form well-defined resist-images through IL and ENFOL shows that the TMC4R-resist is significantly more sensitive to the broad-band mercury-lamp exposure when compared to the HeCd laser exposure wavelength of 325 nm. In comparison, the best IL result was achieved at 1.9 J/cm^2 compared to the 150 mJ/cm^2. Furthermore, the intensity of the ENFOL exposure source was significantly higher than that of the IL source. This meant that very high exposure times were necessary in the IL experiments, which further compounds the sensitivity to noise.

7.3.2 ENFOL results comparison

ENFOL experiments undertaken by McNab around 2001 [113] were performed using exposure patterns comparable to the line gratings described above. McNab's ENFOL experiments were undertaken using a significantly different procedure; NiCr formed on thin silicon nitride membranes were brought into conformal contact with a Shipley S1805 positive tone photoresist via pressure-driven inflection in a vacuum-chuck. An unfiltered mercury lamp was used as the exposure source. A 270-nm period grating pattern was exposed into a thick resist layer using a bright-field mask, producing a resist-image consisting of a grating structure situated on top of a raised mesa as shown in Fig. 7.30(left). The near-field defined grating pattern was characterised by a modulation depth, a, of $\sim$45 nm and the total pattern depth, d, was $\sim$200 nm. For comparison Fig. 7.30(right) presents a 250-nm period grating, exposed at 150 mJ/cm^2, into a negative tone TMC4R-resist, with TMC4R:HMMM of 1:0.74. The resulting resist-image features a modulation depth of $\sim$30 nm and a total pattern depth of $\sim$45 nm. This is the sample which was shown in Fig. 7.22(bottom left), presented in a manner to facilitate easy comparison. Note that the z-scale varies by a factor of ten between the two images.

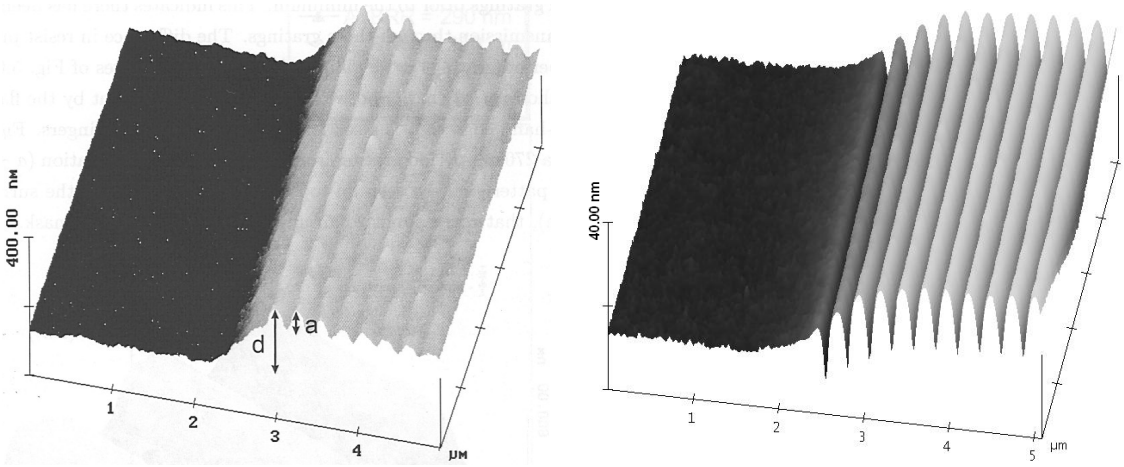

Figure 7.30: Comparison of ENFOL resist-images. Left: ENFOL exposure of a 270-nm period grating into a 470-nm thick layer of Shipley S1805 photoresist. Modulation depth, a, of ∼45 nm and pattern depth, d, of ∼200 nm. This result was achieved by McNab in 2001 [113]. Right: ENFOL definition of a 250-nm period grating in the TMC4R resist at an exposure dose of 150 mJ/cm^2. For this sample a is ∼30 nm and d is ∼45 nm.

Comparison of high-resolution AFM scans of resist-images is presented in Fig. 7.31. Here 3D- and 2D-plots of 2x2 μm^2 surface scans are presented side-by-side to allow comparison between ENFOL results achieved by McNab and those achieved through the TMC4R-resist. As also seen in Fig. 7.30(left), a significant difference in resist-image smoothness of the two samples is readily observed. The TMC4R-resist provides much smoother and homogeneous images compared with that produced using the Shipley S1805 photoresist. The Shipley resist-image displays an evidently granular structure which suggests that the resolution is approaching the grain-size characteristic for the resist. Consequently the Shipley resist-image exhibits a significantly higher LER than that of the TMC4R-resist. Although the experimental procedures utilised to obtain these resist-images are very different, a stricly qualitative comparison of the resist images suggests that the TMC4R-resist is capable of superior image formation relative to the Shipley resist for features of this size.

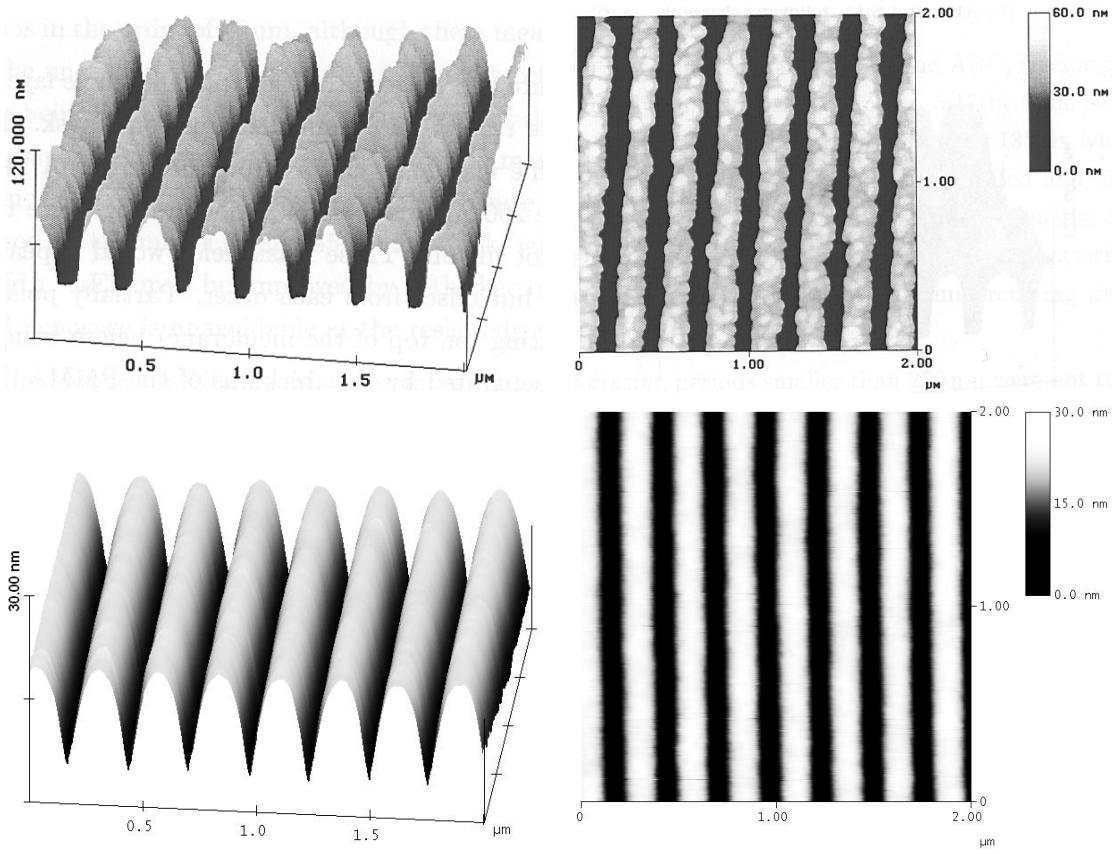

Figure 7.31: Comparison of AFM scans of ENFOL resist-images of 270-nm period gratings, 3D surface plots on the left and 2D plots on the right. Top: Results achieved by McNab using a 45-nm thick layer of Shipley S1805 photoresist [113]. Bottom: Results achieved using the TMC4R-resist.

7.3.3 Conclusion

The results obtained from the IL experiments provided a deeper insight into the high-resolution imaging capabilities of the TMC4R-resist. In particular, the importance of the TMC4R:HMMM ratio upon resist imaging performance was demonstrated. Significant increases in resolution, image fidelity and clearance dose were observed for higher TMC4R:HMMM ratios. Large area line gratings with periods of 250, 500 and 1000 nm were defined using the IL setup. These line gratings were characterised by good image fidelity with LER of approximately 10 nm for the 250-nm period gratings. The experimental IL protocol presented here proved to be a capable and rapid testing approach for analysing the high-resolution imaging capabilities of different photoresist formulations. The imaging capabilities of the TMC4R was found to match, if not surpass, that of the commercial AZ1518 photoresist, albeit at the cost of an approximately four times as high clearance dose.

Resist images exposed through ENFOL, utilising EBL-defined tungsten shadow masks, were produced. Two exposure patterns were analysed using AFM: 250-nm period gratings and nested-L patterns with 150-nm LW. Gratings defined through ENFOL exhibited very low LER down to 7 nm. The bright-dark-field reversal observed in the resist-images suggests that localised field-enhancement at the corners of shadow mask features plays a dominant role in the exposure mechanism for the samples analysed here. This effect could potentially be reduced by utilisation of a different UV-absorber material, such as a-Si. Comparison of the results achieved here with earlier ENFOL results clearly demonstrates the superior imaging characteristics of the TMC4R-resist relative to those of conventional UV-photoresists. Consequently the TMC4R-resist protocol constitutes a viable approach for improving future experimental results in super-resolution UV-lithography. Furthermore, this illustrates the importance of considering the capabilities and limitations of any resist-protocol utilised in lithographic studies.

8

Summary, outlook & conclusion

This chapter summarises the key findings of the thesis and evaluates these results relative to the project aims stated in Section 1.2. The summary is followed by an outlook discussing the ramifications and potential gains for future investigations. Finally the conclusion recaps the most important findings of this project.

8.1 Summary

As stated in Section 1.2, the initial aim of the project was to conduct an experimental investigation to evaluate how surface roughness affects superlens imaging performance. In order to facilitate such an investigation it was necessary to first realise a fabrication protocol in which surface roughness in silver thin films is both controllable and consistent. The milestones necessary to achieve this goal were identified in the introduction to Chapter 3. A series of process optimisation experiments were carried out through thermal evaporation and RF magnetron sputtering deposition of silver films. The results of these experiments illustrated the relationship between deposition parameters and film roughness, but also demonstrated the inherent difficulty in attaining both control and consistency of surface roughness parameters in the deposition of thin silver films on dielectric substrates. Since the necessary process control could not be achieved, an investigation of surface roughness effects upon superlens imaging performance was conducted through numerical modelling studies. Controlling surface roughness was straightforward in this case and atomic force microscopy surface roughness data, obtained from real silver thin-films, was extracted, scaled and applied as

roughness profiles.

These numerical investigations of surface roughness effects in superlens imaging were carried out through finite element method (FEM) simulations. The background and methodology behind this investigation were described in Chapter 4. Results achieved through these simulations indicated that the 3σ line edge roughness (LER) increases proportionally with the magnitude of the roughness profile of the metal-dielectric interfaces in superlenses. Evaluating LER as a function of RMS surface roughness magnitude produced a scaling factor of 19 nm/nm for single-layer superlenses. Other results from this investigation showed that dual-layer superlenses, having more interfaces, are more sensitive to surface roughness and that it is irrelevant whether surface roughness is concentrated on the near or far side of the superlens relative to the object plane.

Superlens imaging relies on plasmonic mechanisms to achieve image transfer. Since plasmons are inherently resonant phenomena, the potential implications of resonant coupling with surface roughness profiles were also investigated through FEM simulations. Chapter 5 presented the premise and outcome of this investigation. Through simulation of periodic roughness profiles with varying spatial frequencies resonant behaviour was identified. The dominant coupling mechanism was found to be between the shadow mask pattern and surface roughness profile.

The results of the simulation studies further indicated that other effects than surface roughness are likely to have had a detrimental effect upon image transfer fidelity in superlens experiments reported to date. The use of conventional, and consequently relatively low-resolution, UV photoresists in super-resolution UV-lithography was identified as a factor likely to negatively impact upon experimental results. The formulation of new high-performance resist schemes for electron-beam lithography and extreme UV-lithography has been the focus of rigorous investigation in recent years. Calixarenes are a group of molecules which have shown promise within this field. Consequently a chemically amplified, negative-tone calixarene-based photoresist scheme was developed and characterised as described in Chapter 6. Initial characterisation demonstrated good resolution and contrast potential and also identified the importance of optimising resist composition.

Super-resolution lithography experiments, carried out using the calixarene-based resist scheme, were described in Chapter 7. Interference lithography (IL) proved an effective approach for evaluating the high-resolution capabilities of the resist. Through IL well-defined 250-nm period line gratings were formed over large areas using an optimised resist composition. The imaging performance of the calixarene resist was found to match, or even exceed, that of the conventional AZ1518 photoresist at this resolution. Resist features produced in the calixarene resist via IL were found to exhibit low 3σ LER values of $\sim$10 nm. Further super-resolution experiments were carried out through evanenscent near-field optical lithography. The images resulting from these experiments exhibited very good pattern fidelity as well as very smooth surface characteristics. ENFOL-defined resist images of 250-nm period gratings exhibited superior fidelity when compared to gratings defined through IL, having LER as low as $\sim$7 nm. Comparison with results achieved through use of a conventional UV-photoresist illustrated the promising imaging characteristics of the calixarene resist.

8.2 Outlook

Results obtained through 2D FEM simulations showed a linear dependence of image LER on surface roughness RMS magnitude. This result means that there is no threshold at which surface roughness magnitude becomes insignificant. Consequently, continuous improvement in superlens imaging fidelity imposes a demand for continuous reduction of surface roughness on the lens interfaces. However, it also illustrates that measurable improvements in superlens imaging are achievable through optimising film deposition. The combined results from the two FEM studies presented indicate that image fidelity can be improved both by reducing roughness magnitude as well as film grain-size. These are important considerations to bear in mind for future investigations. While even atomically smooth surfaces are characterised by finite surface roughness, the spatial frequency of such periodic modulation is high enough that reduced loss of image fidelity would be expected according to the FEM study of resonance effects pertaining to surface roughness. In regards to simulation work it would be interesting to also conduct such investigations through full 3D simulations. However, such an investigation would impose hardware requirements beyond those fulfilled by desktop computers.

The thin film deposition experiments undertaken in this project highlights the inherent complications in realising smooth metal-dielectric interfaces through common deposition techniques. Consequently other approaches must be considered if superlenses with smooth interfaces are to be produced. Various methods for achieving this particular goal were discussed in Sections 3.3 and 3.6, including the use of wetting layers, post-deposition processing and increased control of process parameters. The issue of surface roughness constitutes a real and fundamental obstacle if superlens imaging is to be improved. Identifying a robust and pratical solution for achieving smooth interfaces in metal-dielectric stacks is a requirement for further advances within this field of research.

Future high-resolution lithography experiments are still possible through IL. First, resolution was not pushed to its limit in the IL experiments conducted here. Secondly, by conducting IL experiments using a high refractive index prism as a solid immersion medium it is possible to further increase the potential resolution. Increasing the resolution of conventional IL experiments is a simple matter and enables sub-200-nm resolution. Application of the calixarene photoresist to solid immersion IL experiments produces unresolved issues; e.g. use of index-matching liquids and adhesion during resist-prism contact. Experiments using such high-index prisms, conducted at the University of Canterbury, have demonstrated sub-100-nm resolution capabilities [131].

In regards to ENFOL experiments, noise during the EBL step of mask fabrication was identified as an issue. Optimisation of the EBL process would enable the formation of masking patterns with both finer features as well as reduced LER. A transistion to embedded-amplitude masks [40, 41] would ease optimisation of calixarene-resist thickness for future ENFOL exposures. Establishing a mask fabrication protocol using amorphous silicon as mask absorbers could also potentially improve ENFOL results [8].

Resist-optimisation encompasses a vast parameter-space. Consequently it can not be concluded that the resist-optimisation presented here is exhaustive. Optimisation of the TMC4R:HMMM ratio is of primary concern as identified in Chapters 6 and 7. However the PAG-to-solid content ratio was barely considered in this investigation, a

specific ratio was found to yield reasonable results and was then used forthwidth. Acid-diffusion during PEB is of great importance in chemically-amplified photo-resists. As a result the PEB constitutes a crucial process step for such resists and the end-results are very sensitive to PEB parameters. Additionally it is possible to add a quenching component to the resist, which will act to reduce acid diffusion length during the PEB. However, adding this extra component would require an optimisation of the quencher-to-PAG ratio and thereby adding an additional dimension to the parameter space and thus further complicating the optimisation process.

The negative-tone resist-scheme developed here have several undesirable characteristics if it was to be applied in a fabrication protocol. In its unexposed state the resist is a viscous layer formed from a molecular gel. As a result the resist is very maleable and prone to mechanical damage if subjected to physical contact with a solid implement. Film thickness shrinkage was observed during exposure tests and found to be more pronounced for resists with high TMC4R:HMMM ratios. Such shrinkage would reduce the effectiveness of the resist in lift-off applications. Finally, cross-linked resist features are very durable and at the current stage no removal procedure has been established. However, it is possible to formulate positive tone resist schemes based upon calixarene as well. One approach to achieve this is a photo-deprotection scheme using t-BOC-protected calixarenes as the resist base, for a positive-tone calixarene resist for EUVL see [132]. This formulation was also considered, however the negative tone approach was chosen since it enables lithographic imaging of a resist-layer spun directly onto the shadow mask.

Super-resolution studies presented in Chapter 7 demonstrated the TMC4R-resist's capacity to resolve sub-200-nm resist features with 3σ LER of less than 10 nm. Thus, superlensing experiments performed using this resist would facilitate improved experimental evaluation of the impact of surface roughness upon superlens near-field image projection. Evaluation of the actual interfacial roughness profiles within the superlens stack could be performed through transmission electron microscopy of lens cross-sections. Correlating measured roughness profile characteristics with observed resist-images would represent a viable method of experimentally establishing a quantitative

relationship between these two quantities. This also presents an opportunity to verify the FEM simulation results presented in Chapters 4.

8.3 Conclusion

Thin film deposition, of silver films onto silicon dioxide substrates, produced silver films with root mean square surface roughness as low as 0.8 nm. These experiments improved the understanding of the technical requirements necessary for achieving very smooth silver-dielectric interfaces in metal-dielectric stacks. Part of this increased knowledge was a realisation that achieving consistently smooth silver-dielectric interfaces poses a fundamental challenge. Since it is inherently difficult to achieve this goal using conventional thin film deposition equipment, numerical FEM simulations were undertaken to investigate how interfacial surface roughness affects superlens imaging performance.

Results from numerical modelling studies highlighted that interfacial surface roughness in superlenses does indeed have a significant detrimental impact upon imaging fidelity in such systems. It was estimated that in order to properly evaluate the statistical image-degradation due to surface roughness effects, it would be necessary to establish an experimental protocol capable of producing resist-images with characteristic 3σ line edge roughness of less than 20 nm.

A calixarene-based resist-scheme capable of high-resolution imaging was developed and characterised. This resist-scheme proved capable of producing high-resolution line gratings with 3σ below 10 nm through both interference and evanescent near-field optical lithography. Qualitative comparison of results achieved during these experiments with past results achieved using a conventional photoresist illustrates the improved imaging performance of the calixarene-based resist developed here. This demonstrates both the importance of resist-optimisation for super-resolution lithography and presents a powerful tool for future superlens investigations.

References

[1] G. E. Moore. Cramming more components onto integrated circuits. *Electronics*, 38(8):114, 1965.

[2] C. Mack. *Fundamental Principles of Optical Lithography: The Science of Microfabrication*. John Wiley & Sons, Ltd, 2007. ISBN: 978-0-470-72730-0.

[3] "itrs: 2010 update". `http://www.itrs.net/Links/2010ITRS/2010Update/ToPost/2010_Update_Overview.pdf`, 2010.

[4] T. Ito, A. Terao, Y. Inao, T. Yamaguchi, and N. Mizutani. Photo-deprotection resist based on photolysis of o-nitrobenzyl phenol ether; challenge to half-pitch 22 nm using near-field lithography. *Proceedings of the SPIE*, 6519:65190J–1–65190J–8, 2007.

[5] P. Chaturvedi, W. Wu, V. J. Logeeswaran, Z. Yu, M. S. Islam, S. Y. Wang, R. S. Williams, and N. X. Fang. A smooth optical superlens. *Applied Physics Letters*, 96:043102, 2010.

[6] M. M. Alkaisi, R. J. Blaikie, S. J. McNab, R. Cheung, and D. R. S. Cumming. Sub-diffraction-limited patterning using evanescent near-field optical lithography. *Applied Physics Letters*, 75(22):3560–3562, 1999.

[7] T. Ito, M. Ogino, T. Yamada, Y. Inao, T. Yamaguchi, N. Mizutani, and R. Kuroda. Fabrication of sub-100 nm patterns using near-field mask lithography with ultra-thin resist process. *Journal of Photopolymer Science and Technology*, 18(3):435–441, 2005.

[8] T. Ito, T. Yamada, Y. Inao, T. Yamaguchi, N. Mizutani, and R. Kuroda. Fabrication of half-pitch 32 nm resist patterns using near-field lithography with a-si mask. *Applied Physics Letters*, 89:033113, 2006.

[9] T. Ito, A. Terao, Y. Inao, T. Yamaguchi, and N. Mizutani. Molecular design of o-nitrobenzyl phenol ether for photo-deprotection resist; challenge to half-pitch 22 nm using near-field lithography. *Journal of Photopolymer Science and Technology*, 20(4):591–598, 2007.

[10] Y. Inao, S. Nakasato, R. Kuroda, and M. Ohtsu. Near-field lithography as prototype nano-fabrication tool. *Microelectronic Engineering*, 84:705–710, 2007.

[11] J. B. Pendry. Negative refraction makes a perfect lens. *Physical Review Letters*, 85(18):3966–3969, 2000.

[12] V. G. Veselago. Electrodynamics of substances with simultaneously negative values of ϵ and μ. *Soviet Physics Uspekhi - USSR*, 10(4):509–514, 1968.

[13] R. A. Shelby, D. R. Smith, S. C. Nemat-Nasser, and S. Schultz. Microwave transmission through a two-dimensional, isotropic, left-handed metamaterial. *Applied Physics Letters*, 78(4):489–491, 2001.

[14] R. A. Shelby, D. R. Smith, and S. Schultz. Experimental verification of a negative index of refraction. *Science*, 292(5514):77–79, 2001.

[15] X. H. Hu and C. T. Chan. Photonic crystals with silver nanowires as a near-infrared superlens. *Applied Physics Letters*, 85(9):1520–1522, 2004.

[16] S. Zhang, W. J. Fan, N. C. Panoiu, K. J. Malloy, R. M. Osgood, and S. R. J. Brueck. Experimental demonstration of near-infrared negative-index metamaterials. *Physical Review Letters*, 95(13):4, 2005.

[17] D. O. S. Melville and R. J. Blaikie. Super-resolution imaging through a planar silver layer. *Optics Express*, 13(6):2127–2134, 2005.

[18] N. Fang, H. Lee, C. Sun, and X. Zhang. Sub-diffraction-limited optical imaging with a silver superlens. *Science*, 308(5721):534–537, 2005.

[19] D. R. Smith, W. J. Padilla, D. C. Vier, S. C. Nemat-Nasser, and S. Schultz. Composite medium with simultaneous negative permeability and permittivity. *Physical Review Letters*, 84(18):4181–4187, 2000.

[20] D. O. S. Melville. *Planar Lensing Lithography: Enhancing the Optical Near Field*. PhD thesis, University of Canterbury, 2006.

[21] M. Schøler and R. J. Blaikie. Simulations of surface roughness effects in planar superlenses. *Journal of Optics A - Pure and Applied Optics*, 11(10):105503, 2009.

[22] M. Schøler and R. J. Blaikie. Resonant surface roughness interactions in planar superlenses. *Microelectronic Engineering*, 87(5-8):887–889, 2010.

[23] P. B. Meggs. *A History of Graphic Design*. John Wiley & Sons, Inc., 1998. ISBN: 0-471-291-98-6.

[24] J. D. Plummer, M. Deal, and P. D. Griffon. *Silicon VLSI Technology*. Prentice Hall, 2000. ISBN: 0-13-085037-3.

[25] A. E. Grigorescu and C. W. Hagen. Resists for sub-20-nm electron beam lithography with a focus on hsq: state of the art. *Nanotechnology*, 20(29):292001, 2009.

[26] H. Schift. Nanoimprint lithography: An old story in modern times? a review. *Journal of Vacuum Science & Technology B*, 26(2):458–480, 2008.

[27] L. G. Rosa and J. Liang. Atomic force microscope nanolithography: dip-pen, nanoshaving, nanografting, tapping mode, electrochemical and thermal nanolithography. *Journal of Physics - Condensed Matter*, 21(48):483001, 2009.

[28] Wikipedia. `en.wikipedia.org`.

[29] T. Yamamote, N. Ooishi, and K. McKay. Using in-design physical verification to reduce tapeout schedules. `http://www.design-reuse.com/articles/24046/in-design-physical-verification.html`.

REFERENCES

[30] K. Jain, C. G. Willson, and B. J. Lin. Ultrafast deep uv lithography with excimer lasers. *Electron Device Letters*, 3(3):53–55, 1982.

[31] B. Wu and A. Kumar. Extreme ultraviolet lithography: A review. *Journal of Vacuum Science & Technology B-Vacuum Surfaces and Films*, 25(6):1743–1761, 2007.

[32] D. Bratton, D. Yang, J. Dai, and C. K. Ober. Recent progress in high resolution lithography. *Polymers for Advanced Technologies*, 17:94–103, 2006.

[33] E. Y. Lam and A. K. Wong. Computational lithography: virtual reality and virtual virtuality. *Optics Express*, 17(15):12259–12268, 2006.

[34] D. P. Sanders. Advances in patterning materials for 193 nm immersion lithography. *Chemical Reviews*, 110:321–360, 2010.

[35] E. K. Abbe. The relation of aperture and power in the microscope (continued). *Journal of the Royal Microscopical Society*, 3(1):790–812, 1883.

[36] N. P. Mahalik, editor. *Micromanufacturing and Nanotechnology*. Springer-Verlag, Germany, 2005. ISBN: 3-540-25377-7.

[37] H. I. Smith. Fabrication techniques for surface-acoustic-wave and thin-film optical devices. *Proceedings of the IEEE*, 62(10):1361–1387, 1974.

[38] H. I. Smith, N. Efremow, and P. L. Kelley. Photolithographic contact printing of 4000å linewidth patterns. *Journal of The Electrochemical Society*, 121(11):1503–1506, 1974.

[39] U. Ch. Fischer and H. P. Zingsheim. Submicroscopic pattern replication with visible light. *Journal of Vacuum Science & Technology*, 19(4):881–885, 1981.

[40] J. G. Goodberlet. Patterning 100 nm features using deep-ultraviolet contact photolithography. *Applied Physics Letters*, 76(6):667–669, 2000.

[41] J. G. Goodberlet and B. L. Dunn. Deep-ultraviolet contact photolithography. *Microelectronic Engineering*, 53:95–99, 2000.

[42] J. G. Goodberlet and H. Kavak. Patterning sub-50 nm features with near-field embedded-amplitude masks. *Applied Physics Letters*, 81(7):1315–1317, 2002.

[43] R. J. Blaikie, M. M. Alkaisi, S. J. McNab, D. R. S. Cumming, R. Cheung, and D. G. Hasko. Nanolithography using optical contact exposure in the evanescent near field. *Microelectronic Engineering*, 46:85–88, 1999.

[44] M. Paulus, H. Schmid, B. Michel, and O. J. F. Martin. Contrast mechanisms in high-resolution contact lithography: A comparative study. *Microelectronic Engineering*, 57-58:109–116, 2001.

[45] H. Schmid, H. Biebuyck, and B. Michel. Light-coupling masks: An alternative, lensless approach to high-resolution optical contact lithography. *Journal of Vacuum Science & Technology B*, 16(6):3422–3425, 1998.

[46] T. Yamaguchi, T. Yamada, A. Terao, T. Ito, Y. Inao, N. Mizutani, and R. Kuroda. Fabrication of hp 32 nm resist patterns using near-field lithography. *Microelectronic Engineering*, 84(5-8):690–693, 2007.

[47] J. B. Pendry, A. J. Holden, W. J. Stewart, and I. Youngs. Extremely low frequency plasmons in metallic mesostructures. *Physical Review Letters*, 76(25):4773–4776, 1996.

[48] J. B. Pendry, A. J. Holden, D. J. Robbins, and W. J. Stewart. Low frequency plasmons in thin-wire structures. *Journal of Physics: Condensed Matter*, 10:4785–4809, 1998.

[49] C. G. Parazzoli, R. B. Greegor, K. Li, B. E. C. Koltenbah, and M. Tanielian. Experimental verification and simulation of negative index of refraction using Snell's law. *Physical Review Letters*, 90(10):107401, 2003.

[50] D. R. Smith, J. B. Pendry, and M. C. K. Wiltshire. Metamaterials and negative refractive index. *Science*, 305:788–792, 2004.

[51] P. M. Valanju, R. M. Walser, and A. P. Valanju. Wave refraction in negative-index media: Always positive and very inhomogeneous. *Physical Review Letters*, 88(18):187401, 2002.

[52] D. R. Smith, D. Schurig, and J. B. Pendry. Negative refraction of modulated electromagnetic waves. *Applied Physics Letters*, 81(15):2713–2715, 2002.

[53] J. B. Pendry and D. R. Smith. Comment on "wave refraction in negative-index media: Always positive and very inhomogeneous". *Physical Review Letters*, 90(2):029703, 2003.

[54] N. Garcia and M. Nieto-Vesperinas. Left-handed materials do not make a perfect lens. *Physical Review Letters*, 88(20):207403, 2002.

[55] J. B. Pendry and S. A. Ramakrishna. Near-field lenses in two dimensions. *Journal of Physics: Condensed Matter*, 14:8463–8479, 2002.

[56] D. R. Smith, D. Schurig, , M. Rosenbluth, S. Schultz, S. A. Ramakrishna, and J. B. Pendry. Limitations on subdiffraction imaging with a negative refractive index slab. *Applied Physics Letters*, 82(10):1506–1508, 2003.

[57] S. A. Ramakrishna and J. B. Pendry. Removal of absorption and increase in resolution in a near-field lens via optical gain. *Physical Review B*, 67:201101, 2003.

[58] N. Garcia and M. Nieto-Vesperinas. Is there an experimental verification of a negative index of refraction yet? *Optics Letters*, 27(11):885–887, 2002.

[59] P. Markoš, I. Rousochatzakis, and C. M. Soukoulis. Transmission losses in left-handed materials. *Physical Review E*, 66:045601, 2002.

[60] J. S. Lih, Y. S. Wang, M. C. Lu, Y. C. Huang, K. H. Chen, J. L. Chern, and L. E. Li. Experimental realization of breaking diffraction limit by planar negative-index metamaterials in free space. *Europhysics Letters*, 69(4):544–548, 2005.

[61] V. M. Shalaev. Optical negative-index metamaterials. *Nature Photonics*, 1:41–48, 2007.

[62] G. B. Irani, T. Huen, and F. Wooten. Optical constants of silver and gold in the visible and vacuum ultraviolet. *Journal of the Optical Society of America*, 61:128–129, 1970.

[63] P. B. Johnson and R. W. Christy. Optical constants of noble metals. *Physical Review B*, 6(12):4370–4379, 1972.

[64] R. J. Blaikie and S. J. McNab. Simulation study of 'perfect lenses' for near-field optical nanolithography. *Microelectronic Engineering*, 61-62:97–103, 2002.

[65] Z. Liu, N. Fang, T. Yen, and X. Zhang. Rapid growth of evanescent wave by a silver superlens. *Applied Physics Letters*, 83(25):5184–5186, 2003.

[66] D. O. S. Melville, R. J. Blaikie, and C. R. Wolf. Submicron imaging with a planar silver lens. *Applied Physics Letters*, 84(22):4403–4405, 2004.

[67] D. O. S. Melville and R. J. Blaikie. Near-field optical lithography using a planar silver lens. *Journal of Vacuum Science & Technology B*, 22(6):3470–3474, 2004.

[68] R. J. Blaikie and D. O. S. Melville. Imaging through planar silver lenses in the optical near field. *Journal of Optics a-Pure and Applied Optics*, 7(2):S176–S183, 2005.

[69] H. Lee, Y. Xiong, N. Fang, W. Srituravanich, S. Durant, M. Ambati, C. Sun, and X. Zhang. Realization of optical superlens imaging below the diffraction limit. *New Journal of Physics*, 7:255, 2005.

[70] D. O. S. Melville and R. J. Blaikie. Experimental comparison of resolution and pattern fidelity in single- and double-layer planar lens lithography. *Journal of the Optical Society of America B-Optical Physics*, 23(3):461–467, 2006.

[71] S. Tripathi, R. Brajpuriya, A. Sharma, and S. M. Chaudhari. Surface and interface effects on plasmon loss features in ge thin films and si/ge multilayers. *Journal of Electron Spectroscopy and Related Phenomena*, 151(3):165–169, 2006.

[72] J. B. Pendry. Perfect cylindrical lenses. *Optics Express*, 11(7):755–760, 2003.

[73] S. A. Ramakrishna and J. B. Pendry. Spherical perfect lens: Solution of maxwell's equations for spherical geometry. *Physical Review B*, 69:115115, 2004.

[74] Z. Liu, H. Lee, Y. Xiong, C. Sun, and X. Zhang. Far-field optical hyperlens magnifying sub-diffraction-limited objects. *Science*, 315:1686, 2007.

[75] I. I. Smolyaninov, Y.-J. Hung, and C. D. Christopher. Magnifying superlens in the visible frequency range. *Science*, 315:1699–1701, 2007.

[76] E. E. Narimanov and V. M. Shalaev. Beyond diffraction. *Nature*, 447(17):266–267, 2007.

[77] H. Lee, Z. Liu, Y. Xiong, C. Sun, and X. Zhang. Development of optical hyperlens for imaging below the diffraction limit. *Optics Express*, 15(24):15886–15891, 2007.

[78] J. Zhang, H. Jiang, B. Gralak, S. Enoch, G. Tayeb, and M. Lequime. Towards -1 effective index with one-dimensional metal-dielectric metamaterial: a quantitative analysis of the role of absorption losses. *Optics Express*, 15(12):7720–7729, 2007.

[79] M. G. Blaber, M. D. Arnold, and M. J. Ford. A review of the optical properties of alloys and intermetallics for plasmonics. *Journal of Physics: Condensed Matter*, 22:143201, 2010.

[80] P. Nagpal, N. C. Lindquist, and D. J. Norris. Ultrasmooth patterned metals for plasmonics and metamaterials. *Science*, 325:594–597, 2009.

[81] M. D. Arnold and R. J. Blaikie. Subwavelength optical imaging of evanescent fields using reflections from plasmonic slabs. *Optics Express*, 15(18):11542–11552, 2007.

[82] L. Tonks and I. Langmuir. Oscillations in ionized gases. *Physical Review*, 33(2):195–210, 1929.

[83] E. N. Economou. Surface plasmons in thin films. *Physical Review*, 182(2):539–554, 1969.

[84] H. Raether. *Surface plasmons on smooth and rough surfaces and on gratings*. Springer-Verlag Berlin Heidelberg, 1988. ISBN: 3-540-17363-3.

[85] Y. Liu, D. F. P. Pile, Z. Liu, D. Wu, C. Sun, and X. Zhang. Negative group velocity of surface plasmons in thin metallic films. *Proceedings of SPIE*, 6323:63231M, 2006.

[86] D. L. Smith. *Thin-Film Deposition Principles and Practice*. McGraw-Hill Inc., 1995. ISBN: 0-07-058502-4.

[87] S. A. Scott and S. A. Brown. Three-dimensional growth characterisation of antimony aggregates on graphite. *Eureopean Physical Journal D*, 39:433–438, 2006.

[88] R. Messier and R. A. Roy. Preparation physical structure relations in sic sputtered films. *Journal of Vacuum Science & Technology A*, 2(2):312–315, 1984.

[89] R. Messier and J. E. Yehoda. Geometry of thin-film morphology. *Journal of Applied Physics*, 58(10):3739–3746, 1985.

[90] A. Y. Cho and J. R. Arthur. Molecular beam epitaxy. *Progress in Solid State Chemistry*, 10:157–192, 1975.

[91] R. France, C. S. Jiang, and A. J. Ptak. In situ strain relaxation comparison between gaasbi and gainas grown by molecular-beam epitaxy. *Applied Physics Letters*, 98:101908, 2010.

[92] W. H. Wang, W. Han, K. Pi, K. M. McCreary, F. Miao, W. Bao, C. N. Lau, and R. K. Kawakami. Growth of atomically smooth mgo films on graphene by molecular beam epitaxy. *Applied Physics Letters*, 93:183107, 2008.

[93] A. Ballestad, B. J. Ruck, J. H. Schmid, Adamcyk. M., E. Nodwell, C. Nicoll, and T. Tiedje. Surface morphology of gaas during molecular beam epitaxy growth: Comparison of experimental data with simulations based on continuum growth equations. *Physical Review B*, 65:205302, 2001.

REFERENCES

[94] K. Hiruma, S. Miyagaki, H. Yamanashi, Yuusuke. Tanaka, and I. Nishiyama. Performance and quality analysis of mo-si multilayers formed by ion-beam and magnetron sputtering for extreme ultraviolet lithography. *Thin Solid Films*, 516:2050–2057, 2007.

[95] I. Nedelcu, R. W. E. van de Kruijs, A. E. Yakshin, F. Tichelaar, E. Louis, H. Enkisch, S. Muellender, and F. Bijerk. Interface roughness in mo/si multilayers. *Thin Solid Films*, 515:434–438, 2006.

[96] K. Hiruma, S. Miyagaki, A. Yamaguchi, and I. Nishiyama. Effect of interface treatment with assisted ion beam on mo-si multilayer formation for mask blanks for extreme ultraviolet lithography. *Journal of Vacuum Science & Technology B*, 25(5):1554–1559, 2007.

[97] H. J. Voorma, E. Louis, and F. Bijkerk. Angular and energy dependence of ion bombardment of mo/si multilayers. *Journal of Applied Physics*, 82(4):1876–1881, 1997.

[98] E. E. Fullerton, J. Pearson, C. H. Sowers, S. D. Bader, X. Z. Wu, and S. K. Sinha. Interfacial roughness of sputtered multilayers: Nb/si. *Physical Review B*, 48(23):17432–17446, 1993.

[99] M. U. Guruz, V. P. Dravid, and Y. W. Chung. Synthesis and characterization of single and multilayer boron nitride and boron carbide thin films grown by magnetron sputtering of boron carbide. *Thin Solid Films*, 414:129–135, 2002.

[100] V.J. et Al. Logeeswaran. Smooth ag film deposited using e-beam evaporated ge as an intermediate layer for applications in nanoscale devices and optical superlens. In *Materials Research Society Symposium*, page 5, 2007.

[101] V.J. et Al. Logeeswaran. Ultrasmooth silver thin films deposited with a germanium nucleation layer. *Nano Letters*, 9(1):178–182, 2009.

[102] M. J. Roberts, A. Guenthner, and S. Feng. Evidence for inhibited diffraction of light propagating through nanolaminate metallodielectric material. *Optics Express*, 15(19):11999–12004, 2007.

[103] V.J. et Al. Logeeswaran. Ultra-smooth metal surfaces generated by pressure-induced surface deformation of thin metal films. *Applied Physics A*, 87(2):187–192, 2006.

[104] J. M. Warrender and M. J. Aziz. Effect of deposition rate on morphology evolution of metal-on-insulator films grown by pulsed laser deposition. *Physical Review B*, 76:045414, 2007.

[105] H. L. Skriver and N. M. Rosengaard. Surface energy and work function of elemental metals. *Physical Review B*, 46(11):7157–7168, 1992.

[106] L. Vitos, A. V. Ruban, H. L. Skriver, and J. Kollar. The surface energy of metals. *Surface Science*, 411:186–202, 1998.

[107] F. Geiger, C. A. Busse, and R. I. Loehrke. The vapor pressure of indium, silver, gallium, copper, tin and gold between 0.1 and 3.0 bar. *International Journal of Thermophysics*, 8(4):425–436, 1987.

[108] L. Ling. *Optical Manipulation Using Planar/Patterned Metallo-dielectric Multilayer Structures*. PhD thesis, University of Canterbury, 2008.

[109] J. H. J. Chai. *Combining Zinc Oxide and Silver for Potential Optoelectronic Applications*. PhD thesis, University of Canterbury, 2010.

[110] I. I. Aksenov, V. A. Belous, V. G. Padalka, and V. M. Khoroshikh. Transport of plasma streams in a curvilinear plasma-optics system. *Soviet Journal of Plasma Physics*, 4:425, 1978.

[111] A. M. Mood, F. A. Graybill, and D. C. Boes. *Introduction to the Theory of Statistics*. McGraw-Hill, 3rd edition, 1974. ISBN: 0-07-042864-6.

[112] R. J. Blaikie and S. J. McNab. Evanescent interferometric lithography. *Applied Optics*, 40:1692–1698, 2001.

[113] S. J. McNab. *Evanescent Near-Field Optical Lithography: Overcoming the Diffraction Limit*. PhD thesis, University of Canterbury, 2001.

[114] X. Luo and T. Ishihara. Surface plasmon resonant interference nanolithography technique. *Applied Physics Letters*, 84(23), 2004.

[115] Z. Liu, Q. Wei, and X. Zhang. Surface plasmon interference nanolithography. *Nano Letters*, 5(5):957–961, 2005.

[116] M. Ishida, J. Fujita, T. Ogura, E. Ochiai, E. Ohshima, and J. Momoda. Sub-10-nm-scale lithography using p-chloromethyl-methoxy-calix[4]arene resist. *Japanese Journal of Applied Physics*, 42:3913–3916, 2003.

[117] H. Sailer, A. J. Ruderisch, W. Henschel, V. Schurig, and D. P. Kern. High resolution electron beam lithography using a chemically amplified calix[4]arene based resist. *Journal of Vacuum Science & Technology B*, 22(6):3485–3488, 2004.

[118] B. Bilenberg, M. Schøler, P. Shi, M. S. Schmidt, P. Bøggild, M. Fink, C. Schuster, F. Reuther, C. Gruetzner, and A. Kristensen. Comparison of high resolution negative electron beam resists. *Journal of Vacuum Science & Technology B-Vacuum Surfaces and Films*, 24(4):1776 – 1779, 2006.

[119] S. W. Chang, R. Ayothi, D. Bratton, D. Yang, N. Felix, H. B. Cao, H. Dengb, and C. K. Ober. Sub-50 nm feature sizes using positive tone molecular glass resists for euv lithography. *Journal of Materials Chemistry*, 16:1470–1474, 2006.

[120] H. H. Solak, Y. Ekinci, P. Kser, and S. Park. Photon-beam lithography reaches 12.5 nm half-pitch resolution. *Journal of Vacuum Science & Technology B*, 25(1):91–95, 2007.

[121] H. Oizumi, T. Kumise, and T. Itani. Development of new negative-tone molecular resists based on calixarene for euv lithography. *Journal of Photopolymer Science and Technology*, 21(3):443–449, 2008.

[122] T. Nakayama, M. Nomura, K. Haga, and M. Ueda. A new three-component photoresist based on calix[4]resorcinarene derivative, a crosslinker, and a photo-acid generator. *Bull. Chem. Soc. Jpn.*, 71:2979–2984, 1998.

[123] T. Nakayama and M. Ueda. A new positive-type photoresist based on mono-substituted hydroquinone calix[8]arene and diazonaphthoquinone. *Journal of Materials Chemistry*, 9:697–702, 1998.

[124] O. Haba, K. Haga, M. Ueda, O. Morikawa, and H. Konishi. A new photoresist based on calix[4]resorcinarene dendrimer. *Chem. Mater.*, 11:427–432, 1999.

[125] D. van Steenwinckel, R. Gronheid, J. H. Lammers, A. M. Myers, F. Van Roey, and P. Willems. A novel method for characterizing resist performance. *Proceedings of SPIE*, 6519:65190V–1–65190V–11, 2007.

[126] D. van Steenwinckel, J. H. Lammers, T. Koehler, R. L. Brainard, and P. Trefonas. Resist effects at small pitches. *Journal of Vacuum Science & Technology B*, 24(1):316–320, 2006.

[127] "BASF The Chemical Company". "photoacid generator selection guide". http://www.dispersions-pigments.basf.us/p02/USWeb-Internet/pigments/en_GB/function/conversions:/publish/content/microsites/pigmentsdispersions/Brochures/2011_BASF_PhotoacidGeneratorSelGde_El.pdf, 2010.

[128] J. L. Atwood, L. J. Barbour, and A. Jerga. Organization of the interior of molecular capsules by hydrogen bonding. *Proceedings of the National Academy of Sciences*, 99:4837–4841, 2002.

[129] Ltd." "KIMMON Koha Co. "spec sheet for ik3501r-g". http://www.kimmon.com/cgi-bin/search/nph-ShowSpec.cgi?model_number=IK3501R-G&uid=763-66.249.65.4-1205946556.

[130] "euv technology summit software division". http://www.lithometrix.com/.

[131] P. Mehrotra, C. W. Holzwarth, and R. J. Blaikie. Solid-immersion lloyd's mirror as a testbed for plasmon-enhanced ultra-high numerical aperture lithography. *Journal of Micro/Nanolithography, MEMS and MOEMS*, Accepter for publication, 2011.

[132] D. Bratton, R. Ayothi, N. Felix, H. Cao, H. Deng, and C. K. Ober. Molecular glass resists for next generation lithography. *Proceedings of the SPIE*, 6153:61531D–1, 2006.